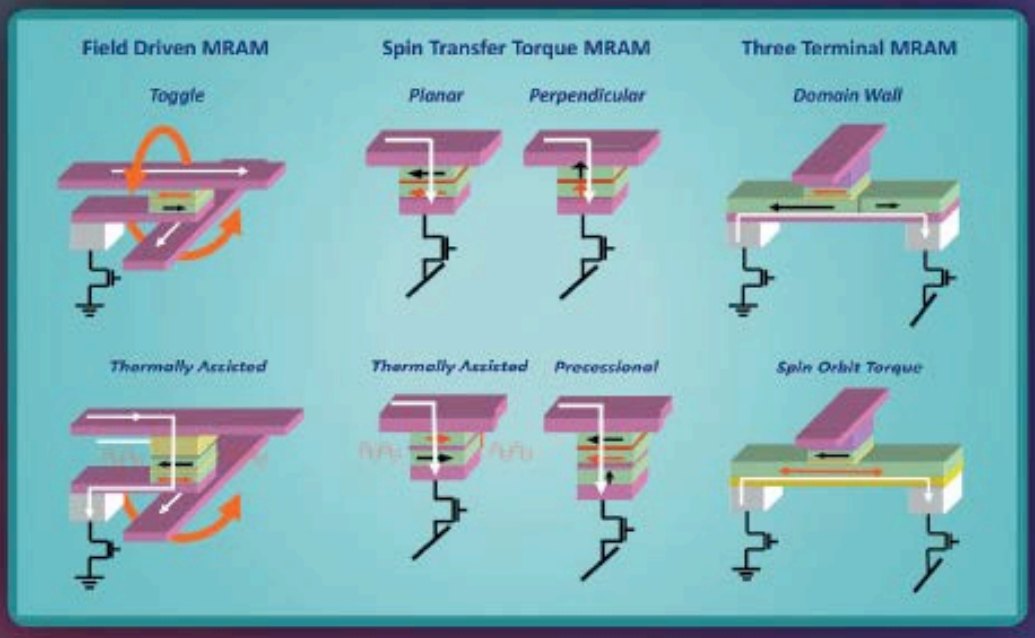
INTRODUCTION TO MAGNETIC RANDOM-ACCESS MEMORY



BERNARD DIENY, RONALD B. GOLDFARB, AND KYUNG-JIN LEE

IEEE PRESS

WILEY

WD EX1057
Western Digital v IP Bridge
Page (cover)

INTRODUCTION TO MAGNETIC RANDOM-ACCESS MEMORY

IEEE Press
445 Hoes Lane
Piscataway, NJ 08854

IEEE Press Editorial Board
Tariq Samad, *Editor in Chief*

George W. Arnold	Xiaoou Li	Ray Perez
Giancarlo Fortino	Vladimir Lumelsky	Linda Shafer
Dmitry Goldgof	Pui-In Mak	Zidong Wang
Ekram Hossain	Jeffrey Nanzer	MengChu Zhou

INTRODUCTION TO MAGNETIC RANDOM-ACCESS MEMORY

Edited by

BERNARD DIENY
RONALD B. GOLDFARB
KYUNG-JIN LEE





WILEY

WD EX1057
Western Digital v IP Bridge
Page iii

Copyright © 2017 by The Institute of Electrical and Electronics Engineers, Inc.

Published by John Wiley & Sons, Inc., Hoboken, New Jersey. All rights reserved
Published simultaneously in Canada

No part of this publication may be reproduced, stored in a retrieval system, or transmitted in any form or by any means, electronic, mechanical, photocopying, recording, scanning, or otherwise, except as permitted under Section 107 or 108 of the 1976 United States Copyright Act, without either the prior written permission of the Publisher, or authorization through payment of the appropriate per-copy fee to the Copyright Clearance Center, Inc., 222 Rosewood Drive, Danvers, MA 01923, (978) 750-8400, fax (978) 750-4470, or on the web at www.copyright.com. Requests to the Publisher for permission should be addressed to the Permissions Department, John Wiley & Sons, Inc., 111 River Street, Hoboken, NJ 07030, (201) 748-6011, fax (201) 748-6008, or online at www.wiley.com/go/permission.

Limit of Liability/Disclaimer of Warranty: While the publisher, editors, and authors have used their best efforts in preparing this book, they make no representations or warranties with respect to the accuracy or completeness of the contents of this book and specifically disclaim any implied warranties of merchantability or fitness for a particular purpose. No warranty may be created or extended by sales representatives or written sales materials. The advice and strategies contained herein may not be suitable for your situation. You should consult with a professional where appropriate. Neither the publisher nor the editors nor the authors shall be liable for any loss of profit or any other commercial damages, including but not limited to special, incidental, consequential, or other damages.

For general information on our other products and services or for technical support, please contact our Customer Care Department within the United States at (800) 762-2974, outside the United States at (317) 572-3993 or fax (317) 572-4002.

Wiley also publishes its books in a variety of electronic formats. Some content that appears in print may not be available in electronic formats. For more information about Wiley products, visit our web site at www.wiley.com.

Library of Congress Cataloging-in-Publication Data is available.

ISBN: 978-1-119-00974-0

Printed in the United States of America

10 9 8 7 6 5 4 3 2 1

CONTENTS

ABOUT THE EDITORS **xi**

PREFACE *A PERSPECTIVE ON NONVOLATILE MAGNETIC MEMORY TECHNOLOGY* **xiii**

CHAPTER 1 *BASIC SPINTRONIC TRANSPORT PHENOMENA* **1**

Nicolas Locatelli and Vincent Cros

1.1 Giant Magnetoresistance **2**
- 1.1.1 Basics of Electronic Transport in Magnetic Materials **2**
- 1.1.2 A Simple Model to Describe GMR: The "Two-Current Model" **5**
- 1.1.3 Discovery of GMR and Early GMR Developments **7**
- 1.1.4 Main Applications of GMR **8**

1.2 Tunneling Magnetoresistance **9**
- 1.2.1 Basics of Quantum Mechanical Tunneling **10**
- 1.2.2 First Approach to Tunnel Magnetoresistance: Jullière's Model **11**
- 1.2.3 The Slonczewski Model **14**
  - 1.2.3.1 The Model **14**
  - 1.2.3.2 Experimental Observations **15**
  - 1.2.3.3 About the TMR Angular Dependence **15**
- 1.2.4 More Complex Models: The Spin Filtering Effect **16**
  - 1.2.4.1 Incoherent Tunneling Through an Amorphous (Al_2O_3) Barrier **16**
  - 1.2.4.2 Coherent Tunneling Through a Crystalline MgO Barrier **17**
- 1.2.5 Bias Dependence of Tunnel Magnetotransport **19**

1.3 The Spin-Transfer Phenomenon **20**
- 1.3.1 The Concept and Origin of the Spin-Transfer Effect **20**
  - 1.3.1.1 The "In-Plane" Torque **20**
  - 1.3.1.2 The "Out-of-Plane" Torque **23**
- 1.3.2 Spin-Transfer-Induced Magnetization Dynamics **23**
  - 1.3.2.1 A Simple Analogy **24**
  - 1.3.2.2 Toward MRAM Based on Spin-Transfer Torque **25**
- 1.3.3 Main Events Concerning Spin-Transfer Advances **26**

References **27**

CHAPTER 2 *MAGNETIC PROPERTIES OF MATERIALS FOR MRAM* **29**

Shinji Yuasa

2.1 Magnetic Tunnel Junctions for MRAM **29**

2.2 Magnetic Materials and Magnetic Properties **31**

WD EX1057
Western Digital v IP Bridge
Page v

2.2.1 Ferromagnet and Antiferromagnet **31**
2.2.2 Demagnetizing Field and Shape Anisotropy **33**
2.2.3 Magnetocrystalline Anisotropy, Interface Magnetic Anisotropy, and Perpendicular Magnetic Anisotropy **35**
2.2.4 Exchange Bias **36**
2.2.5 Interlayer Exchange Coupling and Synthetic Antiferromagnetic Structure **37**
2.2.6 Spin-Valve Structure **38**
2.3 Basic Materials and Magnetotransport Properties **39**
2.3.1 Metallic Nonmagnetic Spacer for GMR Spin-Valve **39**
2.3.2 Magnetic Tunnel Junction with Amorphous AlO Tunnel Barrier **41**
2.3.3 Magnetic Tunnel Junction with Crystalline MgO(0 0 1) Tunnel Barrier **44**
2.3.3.1 Epitaxial MTJ with a Single-Crystal MgO(0 0 1) Barrier **44**
2.3.3.2 CoFeB/MgO/CoFeB MTJ with a (0 0 1)-Textured MgO Barrier for Device Applications **46**
2.3.3.3 Device Applications of MgO-Based MTJs **48**
References **51**

CHAPTER 3 *MICROMAGNETISM APPLIED TO MAGNETIC NANOSTRUCTURES* **55**

Liliana D. Buda-Prejbeanu

3.1 Micromagnetic Theory: From Basic Concepts Toward the Equations **55**
3.1.1 Free Energy of a Magnetic System **56**
3.1.1.1 Exchange Energy **56**
3.1.1.2 Magnetocrystalline Anisotropy Energy **57**
3.1.1.3 Demagnetizing Energy **57**
3.1.1.4 Zeeman Energy **60**
3.1.2 Magnetically Stable State and Equilibrium Equations **61**
3.1.3 Equations of Magnetization Motion **62**
3.1.4 Length Scales in Micromagnetism **63**
3.1.5 Modification Related to Spin-Transfer Torque Phenomena and Spin–Orbit Coupling **64**
3.1.6 Thermal Fluctuations **65**
3.1.7 Numerical Micromagnetism **66**
3.2 Micromagnetic Configurations in Magnetic Circular Dots **67**
3.3 STT-Induced Magnetization Switching: Comparison of Macrospin and Micromagnetism **70**
3.4 Example of Magnetization Precessional STT Switching: Role of Dipolar Coupling **73**
References **76**

CHAPTER 4 *MAGNETIZATION DYNAMICS* **79**

William E. Bailey

4.1 Landau–Lifshitz–Gilbert Equation **79**
4.1.1 Introduction **79**
4.1.2 Variables in the Equation **80**

4.1.3 The Equation 81
4.1.3.1 Precessional Term 82
4.1.3.2 Relaxation Term 83
4.2 Small-Angle Magnetization Dynamics 84
4.2.1 LLG for Thin-Film, Magnetized in Plane, Small Angles 84
4.2.2 Ferromagnetic Resonance 85
4.2.3 Tabulated Materials Parameters 87
4.2.3.1 Bulk Values 87
4.2.3.2 Finite-Size Effects 88
4.2.4 Pulsed Magnetization Dynamics 89
4.3 Large-Angle Dynamics: Switching 90
4.3.1 Quasistatic Limit: Stoner–Wohlfarth Model 90
4.3.2 Thermally Activated Switching 93
4.3.3 Switching Trajectory 94
4.4 Magnetization Switching by Spin-Transfer 95
4.4.1 Additional Terms to the LLG 95
4.4.2 Full-Angle LLG with Spin-Torque 96
Acknowledgments 97
References 97

CHAPTER 5 *MAGNETIC RANDOM-ACCESS MEMORY* 101

Bernard Dieny and I. Lucian Prejbeanu

5.1 Introduction to Magnetic Random-Access Memory (MRAM) 101
5.1.1 Historical Perspective 101
5.1.2 Various Categories of MRAM 102
5.2 Storage Function: MRAM Retention 104
5.2.1 Key Role of the Thermal Stability Factor 104
5.2.2 Thermal Stability Factor for In-Plane and Out-of-Plane Magnetized Storage Layer 106
5.3 Read Function 110
5.3.1 Principle of Read Operation 110
5.3.2 STT-Induced Disturbance of the Storage Layer Magnetic State During Read 111
5.4 Field-Written MRAM (FIMS-MRAM) 112
5.4.1 Stoner–Wohlfarth MRAM 112
5.4.2 Toggle MRAM 115
5.4.2.1 Toggle Write Principle 115
5.4.2.2 Improved Write Margin 117
5.4.2.3 Applications of Toggle MRAM 117
5.4.3 Limitation in Downsize Scalability 118
5.5 Spin-Transfer Torque MRAM (STT-MRAM) 118
5.5.1 Principle of STT Writing 119
5.5.2 Considerations of Breakdown, Write, Read Voltage Distributions 122
5.5.3 Influence of STT Write Pulse Duration 123
5.5.4 In-Plane STT-MRAM 124
5.5.4.1 Critical Current for Switching 124
5.5.4.2 Minimization of Critical Current for Writing 125
5.5.5 Out-of-Plane STT-MRAM 128

5.5.5.1 Benefit of Out-of-Plane Configuration in Terms of Write Current 130
5.5.5.2 Trade-off Between Strong Perpendicular Anisotropy and Low Gilbert Damping 131
5.5.5.3 Benefit from Magnetic Metal/Oxide Perpendicular Anisotropy 131
5.5.5.4 Downsize Scalability of Perpendicular STT-MRAM 133
5.6 Thermally-Assisted MRAM (TA-MRAM) 135
5.6.1 Trade-off Between Retention and Writability; General Idea of Thermally-Assisted Writing 135
5.6.2 Self-Heating in MTJ Due to High-Density Tunneling Current 136
5.6.3 In-Plane TA-MRAM 136
5.6.3.1 Write Selectivity Due to a Combination of Heating and Field 136
5.6.3.2 Reduced Power Consumption, Thanks to Low Write Field and Field Sharing 138
5.6.4 TA-MRAM with Soft Reference: Magnetic Logic Unit (MLU) 140
5.6.4.1 Principle of Reading with Soft Reference 141
5.6.4.2 Content-Addressable Memory 143
5.6.5 Thermally-Assisted STT-MRAM 144
5.6.5.1 In-Plane STT Plus TA-MRAM 144
5.6.5.2 Out-of-Plane STT Plus TA-MRAM 145
5.7 Three-Terminal MRAM Devices 150
5.7.1 Field versus Current-Induced Domain Wall Propagation 150
5.7.2 Principle of Writing 152
5.7.3 Advantages and Drawbacks of Three-Terminal Devices 153
5.8 Comparison of MRAM with Other Nonvolatile Memory Technologies 153
5.8.1 MRAM in the International Technology Roadmap for Semiconductors (ITRS) 153
5.8.2 Comparison of MRAM and Redox-RAM 155
5.8.3 Main Applications of MRAM 155
5.9 Conclusion 157
Acknowledgments 157
References 158

CHAPTER 6 *MAGNETIC BACK-END TECHNOLOGY* 165

Michael C. Gaidis

6.1 Magnetoresistive Random-Access Memory (MRAM) Basics 165
6.2 MRAM Back-End-of-Line Structures 166
6.2.1 Field-MRAM 166
6.2.2 Spin-Transfer Torque (STT) MRAM 168
6.2.3 Other Magnetic Memory Device Structures 169
6.3 MRAM Process Integration 169
6.3.1 The Magnetic Tunnel Junction 169
6.3.1.1 Substrate Preparation 171
6.3.1.2 Film Deposition and Anneal 172

6.3.1.3 Device Patterning 174
6.3.1.4 Dielectric Encapsulation 179
6.3.2 Wiring and Packaging 183
6.3.2.1 Ferromagnetic Cladding 184
6.3.2.2 Packaging 186
6.3.3 Processing Cost Considerations 186
6.4 Process Characterization 187
6.4.1 200–300 mm Wafer Blanket Magnetic Films 187
6.4.1.1 Current-in-Plane Tunneling (CIPT) 188
6.4.1.2 Kerr Magnetometry 189
6.4.2 Parametric Test of Integrated Magnetic Devices 189
6.4.2.1 Magnetoresistance versus Resistance and Resistance versus Reciprocal Area 190
6.4.2.2 Breakdown Voltage 192
6.4.2.3 Device Spreads 194
Acknowledgments 195
References 195

CHAPTER 7 *BEYOND MRAM: NONVOLATILE LOGIC-IN-MEMORY VLSI* 199

Takahiro Hanyu, Tetsuo Endoh, Shoji Ikeda, Tadahiko Sugibayashi, Naoki Kasai, Daisuke Suzuki, Masanori Natsui, Hiroki Koike, and Hideo Ohno

7.1 Introduction 199
7.1.1 Memory Hierarchy of Electronic Systems 199
7.1.2 Current Logic VLSI: The Challenge 201
7.2 Nonvolatile Logic-in-Memory Architecture 203
7.2.1 Nonvolatile Logic-in-Memory Architecture Using Magnetic Flip-Flops 205
7.2.2 Nonvolatile Logic-in-Memory Architecture Using MTJ Devices in Combination with CMOS Circuits 207
7.3 Circuit Scheme for Logic-in-Memory Architecture Based on Magnetic Flip-Flop Circuits 209
7.3.1 Magnetic Flip-Flop Circuit 209
7.3.2 M-Latch 211
7.4 Nonvolatile Full Adder Using MTJ Devices in Combination with MOS Transistors 214
7.5 Content-Addressable Memory 217
7.5.1 Nonvolatile Content-Addressable Memory 217
7.5.2 Nonvolatile Ternary CAM Using MTJ Devices in Combination with MOS Transistors 220
7.6 MTJ-based Nonvolatile Field-Programmable Gate Array 224
References 227

APPENDIX *UNITS FOR MAGNETIC PROPERTIES* 231

INDEX 233

WD EX1057
Western Digital v IP Bridge
Page ix

ABOUT THE EDITORS

Bernard Dieny has conducted research in magnetism for 30 years. He played a key role in the pioneering work on spin-valves at IBM Almaden Research Center in 1990–1991. In 2001, he co-founded SPINTEC in Grenoble, France, a public research laboratory devoted to spin-electronic phenomena and components. Dieny is co-inventor of 70 patents and has co-authored more than 340 scientific publications. He received an outstanding achievement award from IBM in 1992 for the development of spin-valves, the European Descartes Prize for Research in 2006, and two Advanced Research Grants from the European Research Council in 2009 and 2015. He is co-founder of two companies, one dedicated to magnetic random-access memory, Crocus Technology, the other to the design of hybrid CMOS/magnetic circuits, EVADERIS. In 2011 he was elected Fellow of the Institute of Electrical and Electronics Engineers.

Ronald B. Goldfarb was leader of the Magnetics Group at the National Institute of Standards and Technology in Boulder, Colorado, USA, from 2000 to 2015. He has published over 60 papers, book chapters, and encyclopedia articles in the areas of magnetic measurements, superconductor characterization, and instrumentation. In 2004 he was elected Fellow of the Institute of Electrical and Electronics Engineers (IEEE). From 1995 to 2004 he was editor-in-chief of *IEEE Transactions on Magnetics*. He is the founder and chief editor of *IEEE Magnetics Letters*, established in 2010. He received the IEEE Magnetics Society Distinguished Service Award in 2016.

Kyung-Jin Lee is a professor in the Department of Materials Science and Engineering, and an adjunct professor of the KU-KIST Graduate School of Converging Science and Technology, at Korea University. Before joining the university, he worked for Samsung Advanced Institute of Technology in the areas of magnetic recording and magnetic random-access memory. His current research is focused on understanding the underlying physics of current-induced magnetic excitations and exploring new spintronic devices based on spin-transfer torque. He is co-inventor of 20 patents and has more than 100 scientific publications in the areas of magnetic random-access memory, spin-transfer torque, and spin–orbit torque. He received an outstanding patent award from the Korea Patent Office in 2005 and an award for Excellent Research on Basic Science from the Korean government in 2010. In 2013 he was recognized by the National Academy of Engineering of Korea as a leading scientist in spintronics, “one of the top 100 technologies of the future.”

WD EX1057
Western Digital v IP Bridge
Page xi

PREFACE

A PERSPECTIVE ON NONVOLATILE MAGNETIC MEMORY TECHNOLOGY

As context for this book, computer memory hierarchy ranges from cache (fastest and most expensive) to main memory, to mass storage (slowest and least expensive). Cache memory, immediately accessible by the central processing unit, is usually static random-access memory (SRAM). Main memory is usually dynamic random-access memory (DRAM); like SRAM, it requires power to maintain its memory state, but additionally must be electrically refreshed, typically every 64 ms (1). Mass storage is exemplified by nonvolatile flash memory (of the NAND and NOR varieties) and magnetic hard-disk drives.

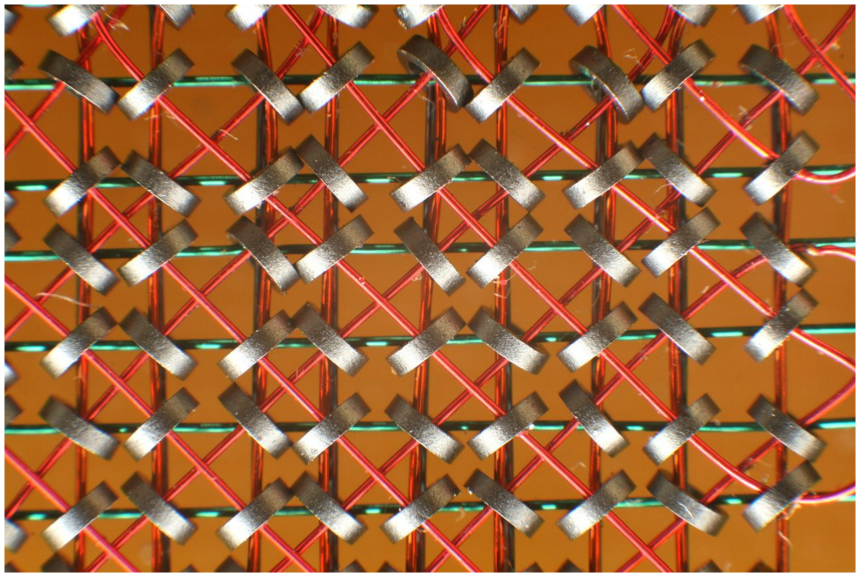
Although magnetic random-access memory (MRAM), in particular spin-transfer torque MRAM (STT-MRAM), has the potential to serve as a universal computer memory—cache, main memory, and mass storage—it will likely be most cost-effective as main memory. MRAM is already a commercial product, albeit expensive and of low density relative to DRAM, and several variations of STT-MRAM are in development. Particular interest is in the superior performance of STT-MRAM with perpendicular magnetic anisotropy. Still under research are three-terminal spin–orbit torque MRAM (2,3), which has high endurance and separate paths for read and write current, and voltage-controlled magnetoelectric MRAM (4–7), which has low energy requirements.

More generally, MRAM, the subject of this book, is characterized by nonvolatility, low energy dissipation, high endurance (repeated writing), scalability to advanced (sub-20 nm) technology nodes, compatibility with complementary metal–oxide semiconductor (CMOS) processing, resistance to radiation damage, and short read and write times. The most intriguing of these, nonvolatility and low energy dissipation, are the main drivers of the technology.

The preface is a contribution of the National Institute of Standards and Technology, not subject to copyright.

Introduction to Magnetic Random-Access Memory, First Edition. Edited by Bernard Dieny, Ronald B. Goldfarb, and Kyung-Jin Lee.
© 2017 The Institute of Electrical and Electronics Engineers, Inc. Published 2017 by John Wiley & Sons, Inc.

WD EX1057
Western Digital v IP Bridge
Page xiii



Details of a 1024 bit core plane memory module (11). When magnetic-core memory was introduced in the mid-1950s, toroid cores were about 2 mm in outer diameter.

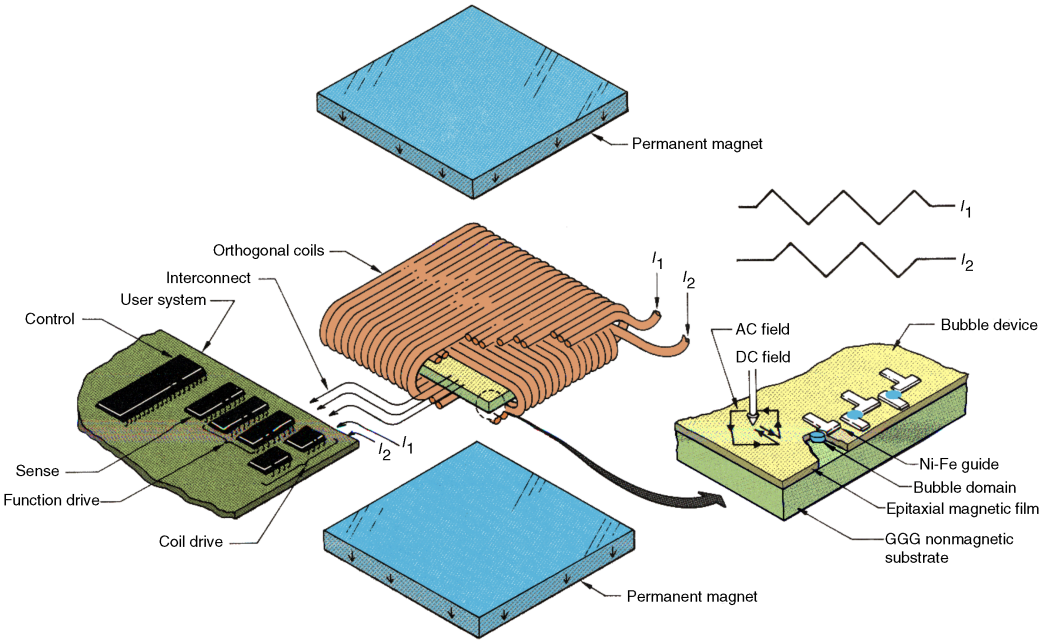
Nonvolatile MRAM is not really new. It was first developed in the early 1950s by Jay W. Forrester at Massachusetts Institute of Technology (8,9). As envisioned by Forrester, a three-dimensional magnetic-core memory module consisted of circumferentially magnetized toroids strung with *x*-, *y*-, and *z*-plane select wires and a fourth inductively driven output-signal wire. Switching times of the original material studied by Forrester, grain-oriented $Ni_{50}Fe_{50}$ "Deltamax," were on the order of 10 ms. He noted that nonmetallic magnetic ferrites would switch in less than 1 μs based on materials research by William N. Papian (10), and that is how the technology developed. The estimated cost per bit was $1 ($9 today, adjusted for monetary inflation).

Another form of nonvolatile magnetic memory was developed by Andrew H. Bobeck and colleagues at Bell Laboratories in the late 1960s and early 1970s for mass storage: magnetic bubble memory (12,13). It was based on sequential, not random, access. Magnetic bubble domains in synthetic garnets with perpendicular magnetic anisotropy were stabilized by bias fields from permanent magnets. The presence or absence of a bubble—a logic "1" or "0"—was detected with magnetoresistive sensors. Bubbles could be generated, propagated, transferred, replicated, stored, and annihilated. Two orthogonal drive coils provided an in-plane rotating magnetic field to control the magnetization of Ni-Fe bubble-propagation elements (14).

The advent of DRAM in the 1970s, which sacrificed nonvolatility for reduced size, higher speed, and reduced cost, made core memory obsolete for main memory. By the early 1980s, storage density advances and cost reductions in hard-disk drives made bubble memory obsolete for mass storage (although bubble memory continued to be used in military and aerospace applications that required ruggedness).

Besides MRAM, other forms of nonvolatile memory are subjects of intense research. They are based on binary state variables that include "spin, phase, multipole orientation, mechanical position, polarity, orbital symmetry, magnetic flux quanta, molecular configuration, and other quantum states" (15). Mechanisms

WD EX1057
Western Digital v IP Bridge
Page xiv



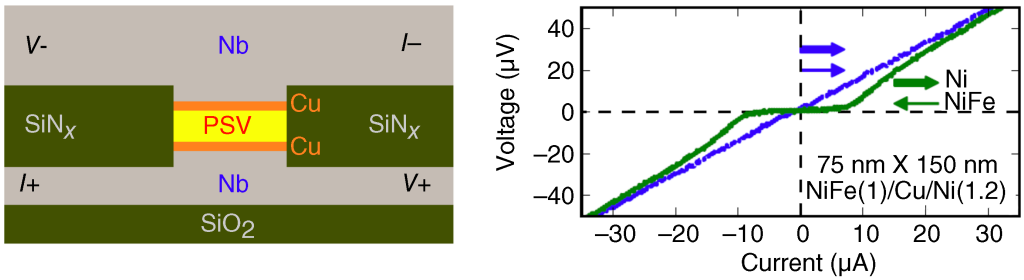
Schematic diagram of the first commercial magnetic bubble memory module, TIB0103, manufactured in 1977 (14). Shown are the bias magnets, drive coils, control and interface circuits, bubble chip, and Ni-Fe "T-bar" bubble-propagation pattern. (An asymmetric chevron pattern was used instead in the TIB0203 in 1978.) The magnetic bubble diameter was 5 μm. The chip had 92,000 bits, a storage density of 155,000 bits/cm^2, an access time of 2–4 ms, and a data transfer rate of 50,000 bits/s.

with great potential include resistive RAM ("memristors") (16) and phase-change RAM (17). One of these may eventually become the dominant technology for cache memory, main memory, or mass storage, but for now, MRAM seems the most promising for main memory. Nevertheless, alternatives to MRAM should not be discounted (18,19).

Coincident with the memory revolution is a rethinking of computer logic and architecture, particularly to address problems of energy consumption in supercomputers and massive data centers. For example, in the United States, the Intelligence Advanced Research Projects Activity (IARPA) has sponsored the development of a prototype cryogenic computer under its "Cryogenic Computing Complexity" program (20). Dramatic reductions are projected in both energy consumption and size (21). Such a computer would combine superconducting, single flux quantum (SFQ) logic with hybrid superconducting/magnetic RAM. Hybrid superconducting/magnetic Josephson junctions switched by spin-transfer torque, resulting in measureable changes in critical current, have been demonstrated (22).

Recent accelerated growth in data centers and their demand for energy are bringing the need for new computer logic and memory to a head. World Wide Web search engines have resorted to storing most of their data in energy-inefficient DRAM (23) because retrieval from mass storage is too slow. There is a need to prototype, test, and benchmark (24) the energy dissipation, high-speed performance, reliability, dimensional scalability, temperature margins, and fabrication reproducibility of MRAM materials, devices, and circuits. Inevitably, new physical phenomena arise as nanostructures shrink in size, and failures will be determined by unknown variables

WD EX1057
Western Digital v IP Bridge
Page xv



Nanopillar Josephson junction with a $Ni_{0.8}Fe_{0.2}$/Cu/Ni pseudo-spin valve (PSV) barrier (left) and voltage versus current at 4 K and zero applied field for parallel and antiparallel magnetic states (right) (22).

and the increased relative importance of uncontrolled edge properties with respect to the bulk (25).

This book is designed for microelectronics engineers who need a working knowledge of magnetic memory devices. As conceived by one of the editors, Bernard Dieny, it aims to promote synergy between researchers and developers working in the field of electron devices and those in magnetics and information storage.

The chapters in this volume cover basic concepts in spin electronics (spintronics); magnetic properties of materials; micromagnetic modeling; dynamics of magnetic precession and damping; different implementations of MRAM; the integration of MRAM with CMOS; and future hybrid logic-in-memory architectures.

The authors are leaders in their respective fields. Nicolas Locatelli and Vincent Cros are known for their major contributions in the field of spin torque nano-oscillators and nanodevices assembled in novel computer architectures (26,27). Shinji Yuasa is noted for his pioneering experimental work (28,29) on giant magnetoresistance in magnetic tunnel junctions with MgO barriers (30,31). Liliana Buda-Prejbeanu is expert in micromagnetic modeling and computational magnetics (32). Bill Bailey is an authority on magnetization dynamics and spin–orbit coupling (33). Bernard Dieny is famous for his key role in the discovery of giant magnetoresistance in spin valve structures (34,35). Lucian Prejbeanu is known for his work on thermally assisted MRAM (36). Michael Gaidis is a microwave engineer who has specialized in "back-end-of-line" integration of MRAM with CMOS (37). The chapter on non-volatile logic-in-memory (38,39) by Takahiro Hanyu, Hideo Ohno, and the team at Tohoku University represents one of the most complete compilations on this topical subject.

This book was sponsored by the IEEE Magnetics Society and published under the Wiley-IEEE Press imprint. The editor at Wiley-IEEE Press was Mary Hatcher.

RONALD B. GOLDFARB

National Institute of Standards and Technology
Boulder, Colorado, USA

WD EX1057
Western Digital v IP Bridge
Page xvi

REFERENCES

1. I. Bhati, M.-T. Chang, Z. Chishti, S.-L. Lu, and B. Jacob, "DRAM refresh mechanisms, penalties, and trade-offs," *IEEE Trans. Comput.* 65, pp. 108–121 (2016); doi: 10.1109/TC.2015.2417540.
2. I. M. Miron, K. Garello, G. Gaudin, P.-J. Zermatten, M. V. Costache, S. Auffret, S. Bandiera, B. Rodmacq, A. Schuhl, and P. Gambardella, "Perpendicular switching of a single ferromagnetic layer induced by in-plane current injection," *Nature* 476, pp. 189–194 (2011); doi: 10.1038/nature10309.
3. L.-Q. Liu, C.-F. Pai, Y. Li, H. W. Tseng, D. C. Ralph, and R. A. Buhrman, "Spin-torque switching with the giant spin Hall effect of tantalum," *Science* 336, pp. 555–558 (2012); doi: 10.1126/science.1218197.
4. S. Kanai, M. Yamanouchi, S. Ikeda, Y. Nakatani, F. Matsukura, and H. Ohno, "Electric field-induced magnetization reversal in a perpendicular-anisotropy CoFeB-MgO magnetic tunnel junction," *Appl. Phys. Lett.* 101, 122403 (2012); doi: 10.1063/1.4753816.
5. W.-G. Wang, M. Li, S. Hageman, and C. L. Chien, "Electric-field-assisted switching in magnetic tunnel junctions," *Nat. Mater.* 11, pp. 64–68 (2012); doi: 10.1038/nmat3171.
6. Y. Shiota, T. Nozaki, F. Bonell, S. Murakami, T. Shinjo, and Y. Suzuki, "Induction of coherent magnetization switching in a few atomic layers of FeCo using voltage pulses," *Nat. Mater.* 11, pp. 39–43 (2012); doi: 10.1038/nmat3172.
7. P. K. Amiri, J. G. Alzate, X. Q. Cai, F. Ebrahimi, Q. Hu, K. Wong, C. Grèzes, H. Lee, G. Yu, X. Li, M. Akyol, Q. Shao, J. A. Katine, J. Langer, B. Ocker, and K. L. Wang, "Electric-field-controlled magnetoelectric RAM: progress, challenges, and scaling," *IEEE Trans. Magn.* 51, 3401507 (2015); doi: 10.1109/TMAG.2015.2443124.
8. J. W. Forrester, "Digital information in three dimensions using magnetic cores," *J. Appl. Phys.* 22, pp. 44–48 (1951); doi: 10.1063/1.1699817.
9. J. W. Forrester,"Multicoordinate digital information storage device," U.S. Patent 2,736,880 (filed May 11, 1951, published February 28, 1956); https://www.google.com/patents/US2736880.
10. W. N. Papian, "A coincident-current magnetic memory cell for the storage of digital information," *Proc. IRE* 40, pp. 475–478 (1952); doi: 10.1109/JRPROC.1952.274045.
11. K. Lanzet, CC BY-SA 3.0; http://wikimedia.org/w/index.php?curid=7025574 (2009).
12. A. H. Bobeck, "Properties and device applications of magnetic domains in orthoferrites," *Bell Syst. Tech. J.* 46, pp. 1901–1925 (1967); doi: 10.1002/j.1538-7305.1967.tb03177.x.
13. A. H. Bobeck and H. E. D. Scovil, "Magnetic bubbles," *Sci. Am.* 224 (6), pp. 78–90 (1971); http://www.nature.com/scientificamerican/journal/v224/n6/pdf/scientificamerican0671-78.pdf.
14. D. Toombs, "An update: CCD and bubble memories," *IEEE Spectr.* 15 (4), pp. 22–30 (1978); doi: 10.1109/MSPEC.1978.6367665.
15. G. I. Bourianoff, P. A. Gargini, and D. E. Nikonov, "Research directions in beyond CMOS computing," *Solid-State Electron.* 51, pp. 1426–1431 (2007); doi: 10.1016/j.sse.2007.09.018.
16. E. Gale, "TiO_2-based memristors and ReRAM: materials, mechanisms and models (a review)," *Semicond. Sci. Technol.* 29, 104004 (2014); doi: 10.1088/0268-1242/29/10/104004.
17. M. Wuttig and N. Yamada, "Phase-change materials for rewriteable data storage," *Nat. Mater.* 6, pp. 824–832 (2007); doi: 10.1038/nmat2009.
18. Y. Fujisaki, "Current status of nonvolatile semiconductor memory technology," *Jpn. J. Appl. Phys.* 49, 100001 (2010); doi: 10.1143/JJAP.49.100001.
19. J. S. Meena, S. M. Sze, U. Chand, and T.-Y. Tseng, "Overview of emerging nonvolatile memory technologies," *Nanoscale Res. Lett.* 9, 526 (2014); doi: 10.1186/1556-276X-9-526.
20. Cryogenic Computing Complexity (C3) (2014), http://www.iarpa.gov/index.php/research-programs/c3 (accessed Sept. 15, 2016).
21. D. S. Holmes, A. L. Ripple, and M. A. Manheimer, "Energy-efficient superconducting computing: power budgets and requirements," *IEEE Trans. Appl. Supercond.* 23, 1701610 (2013); doi: 10.1109/TASC.2013.2244634.
22. B. Baek, W. H. Rippard, M. R. Pufall, S. P. Benz, S. E. Russek, H. Rogalla, and P. D. Dresselhaus, "Spin-transfer torque switching in nanopillar superconducting-magnetic hybrid Josephson junctions," *Phys. Rev. Appl.* 3, 011001 (2015); doi: 10.1103/PhysRevApplied.3.011001.

WD EX1057
Western Digital v IP Bridge
Page xvii

23. J. Ousterhout, "The volatile future of storage," *IEEE Spectr.* 52 (11), pp. 34 ff. (2015); doi: 10.1109/MSPEC.2015.7335899.
24. D. E. Nikonov and I. A. Young, "Benchmarking of beyond-CMOS exploratory devices for logic integrated circuits," *IEEE J. Exploratory Solid-State Comput. Devices Circuits* 1, pp. 3–11 (2015); doi: 10.1109/JXCDC.2015.2418033.
25. H. T. Nembach, J. M. Shaw, T. J. Silva, W. L. Johnson, S. A. Kim, R. D. McMichael, and P. Kabos, "Effects of shape distortions and imperfections on mode frequencies and collective linewidths in nanomagnets," *Phys. Rev. B* 83, 094427 (2011); doi: 10.1103/PhysRevB.83.094427.
26. N. Locatelli, V. Cros, and J. Grollier, "Spin-torque building blocks," *Nat. Mater.* 13, pp. 11–20 (2014); doi: 10.1038/NMAT3823.
27. N. Locatelli, V. V. Naletov, J. Grollier, G. de Loubens, V. Cros, C. Deranlot, C. Ulysse, G. Faini, O. Klein, and A. Fert, "Dynamics of two coupled vortices in a spin valve nanopillar excited by spin transfer torque," *Appl. Phys. Lett.* 98, 062501 (2011); doi: 10.1063/1.3553771.
28. S. Yuasa, T. Nagahama, A. Fukushima, Y. Suzuki, and K. Ando, "Giant room-temperature magnetoresistance in single-crystal Fe/MgO/Fe magnetic tunnel junctions," *Nat. Mater.* 3, pp. 868–871 (2004); doi: 10.1038/nmat1257.
29. S. Yuasa and D. D. Djayaprawira, "Giant tunnel magnetoresistance in magnetic tunnel junctions with a crystalline MgO(0 0 1) barrier," *J. Phys. D Appl. Phys.* 40, pp. R337–R354 (2007); doi: 10.1088/0022-3727/40/21/R01.
30. W. H. Butler, X.-G. Zhang, T. C. Schulthess, and J. M. MacLaren, "Spin-dependent tunneling conductance of Fe|MgO|Fe sandwiches," *Phys. Rev. B* 63, 054416 (2001); doi: 10.1103/PhysRevB.63.054416.
31. S. S. P. Parkin, C. Kaiser, A. Panchula, P. M. Rice, B. Hughes, M. Samant, and S.-H. Yang, "Giant tunneling magnetoresistance at room temperature with MgO(1 0 0) tunnel barriers," *Nat. Mater.* 3, pp. 862–867 (2004); doi: 10.1038/nmat1256.
32. L. D. Buda, I. L. Prejbeanu, U. Ebels, and K. Ounadjela, "Micromagnetic simulations of magnetisation in circular cobalt dots," *Comput. Mater. Sci.* 24, pp. 181–185 (2002); doi: 10.1016/S0927-0256(02)00184-2.
33. W. E. Bailey, L. Cheng, D. J. Keavney, C. C. Kao, E. Vescovo, and D. S. Arena, "Precessional dynamics of elemental moments in a ferromagnetic alloy," *Phys. Rev. B* 70, 172403 (2004); doi: 10.1103/PhysRevB.70.172403.
34. B. Dieny, V. S. Speriosu, S. S. P. Parkin, B. A. Gurney, D. R. Wilhoit, and D. Mauri, "Giant magnetoresistance in soft ferromagnetic multilayers," *Phys. Rev. B* 43, pp. 1297–1300 (1991); doi: 10.1103/PhysRevB.43.1297.
35. B. Dieny, "Giant magnetoresistance in spin-valve multilayers," *J. Magn. Magn. Mater.* 136, pp. 335–359 (1994); doi: 10.1016/0304-8853(94)00356-4.
36. I. L. Prejbeanu, M. Kerekes, R. C. Sousa, H. Sibuet, O. Redon, B. Dieny, and J. P. Nozieres, "Thermally assisted MRAM," *J. Phys Condens. Matter* 19, 165218 (2007); doi: 10.1088/0953-8984/19/16/165218.
37. M. C. Gaidis, E. J. O'Sullivan, J. J. Nowak, Y. Lu, S. Kanakasabapathy, P. L. Trouilloud, D. C. Worledge, S. Assefa, K. R. Milkove, G. P. Wright, and W. J. Gallagher, "Two-level BEOL processing for rapid iteration in MRAM development," *IBM J. Res. Dev.* 50, pp. 41–54 (2006); doi: 10.1147/rd.501.0041.
38. S. Matsunaga, J. Hayakawa, S. Ikeda, K. Miura, H. Hasegawa, T. Endoh, H. Ohno, and T. Hanyu, "Fabrication of a nonvolatile full adder based on logic-in-memory architecture using magnetic tunnel junctions," *Appl. Phys. Exp.* 1, 091301 (2008); doi: 10.1143/APEX.1.091301.
39. T. Hanyu, D. Suzuki, N. Onizawa, S. Matsunaga, M. Natsui, and A. Mochizuki,"Spintronics-based nonvolatile logic-in-memory architecture towards an ultra-low-power VLSI computing paradigm," *Proceedings of the Design, Automation & Test in Europe Conference* (2015), pp. 1006–1011; http://dl.acm.org/citation.cfm?id=2757048.

WD EX1057
Western Digital v IP Bridge
Page xviii

CHAPTER 1

BASIC SPINTRONIC TRANSPORT PHENOMENA

Nicolas Locatelli[1,2] *and Vincent Cros*[2]

[1]Unité Mixte de Physique, CNRS, Thales, Univ. Paris-Sud, Université Paris-Saclay, 91767 Palaiseau, France

[2]Centre de Nanosciences et de Nanotechnologies, CNRS, Univ. Paris-Sud, Université Paris-Saclay, 91405 Orsay France

SPINTRONICS is a merger of magnetism and electronics. Conventional electronics uses only the charge of the electrons. For instance, transistors are based on the modulation of the density of electrons in a semiconductor channel by an electric field. Semiconductor-based memory (e.g., DRAM, Flash) stores information in the form of an amount of charge stored in a capacitor. In contrast, spintronics uses the spin of the electrons in addition to their charge to obtain new properties and use these properties in innovative devices. The spin of the electrons is an elementary magnetic moment carried by each electron. It has a quantum mechanical origin. Magnetic materials can be used as polarizers or analyzers for electron spins. This is why most spintronic devices combine magnetic and nonmagnetic materials, which can be metals, semiconductors, or insulators.

Magnetism has been used for a long time for data storage applications. Indeed, information can be stored in some magnetic materials in the form of a magnetization orientation. This was developed for storage on magnetic tapes as well as in magnetic hard disk drives (HDDs). The increase in the demand for storage capacity has stimulated an increase by eight orders of magnitude in the areal density of information stored in HDDs over the past 50 years; the bit area has decreased by the same factor. In 2014, bit sizes are typically on the order of 40 nm × 15 nm. This decrease in bit size has required continual improvements in the storage medium, in the write head used to switch the magnetization in the medium, and in the read head used to read out the magnetic state. This field of magnetic recording has benefited strongly from research and development in the field of spintronics. In particular, the discoveries of giant magnetoresistance in 1988 (1) and tunnel magnetoresistance at room temperature in

Introduction to Magnetic Random-Access Memory, First Edition. Edited by Bernard Dieny, Ronald B. Goldfarb, and Kyung-Jin Lee.
© 2017 The Institute of Electrical and Electronics Engineers, Inc. Published 2017 by John Wiley & Sons, Inc.

WD EX1057
Western Digital v IP Bridge
Page 1

1995 (2,3) have been major breakthroughs from a scientific point of view, but they also helped recording technology keep moving forward. In 2010, a total of around 12,000 PB (10^{15} bytes) of storage capacity contained in 674.6 million HDDs were shipped worldwide.

Another type of spintronic devices that was proposed in the late 1990s is magnetic random-access memory (MRAM) (4). Indeed, solid state memory is of primary importance both for storage (the introduction of solid state drives in personal computers, tablets, and handheld devices) and for fast working memory between logic units and hard disk drives. In these applications, random-access memory based on devices involving magnetic materials, called magnetic tunnel junctions, are among the most promising technologies for future nonvolatile data storage, and may replace, in the near future, semiconductor-based memory (i.e., DRAM and SRAM), which represents a huge market.

This chapter is an introduction to the physical concepts required to understand how information is stored in a magnetic data cell, how this information can be detected, and how it is possible to modify the information by switching the magnetization from one state to another. First we introduce the basics of electronic transport in magnetic materials, a concept that is required for the comprehension of the physical mechanisms at the origin of magnetoresistive properties: giant magnetoresistance (GMR) and tunneling magnetoresistance (TMR), which is the magnetoresistive effect at play in spin-transfer torque (STT) MRAM devices. Then we describe how a spin-polarized current can exert a STT on the magnetizations in nanostructured spintronic devices by the interaction with local magnetic moments. Finally, we show how this novel effect can be used to modify the state of a magnetic element, leading to current-induced magnetization switching as the writing process in STT-MRAM.

1.1 GIANT MAGNETORESISTANCE

After introducing the basic concepts of electronic transport in ferromagnetic metals, a simple model of the GMR effect is presented, the so-called "two-current model" that was proposed to describe the dependence of the electrical resistance of magnetic multilayered stacks on their magnetic configuration. This model is helpful for the understanding of the basic principles of spin-dependent transport. Finally, the main applications of GMR are discussed.

1.1.1 Basics of Electronic Transport in Magnetic Materials

Magnetism, as produced by magnetite (Fe_3O_4), has been known from at least ancient Greek times. It was described as a force, either attractive or repulsive, that can act at distance. The origin of this force is due to a magnetic field that is created by some materials (called magnets), or is induced by the motion of electrons, that is, electrical currents. In magnetic materials, such as iron (Fe) or cobalt (Co), sources of magnetization are mainly the electrons' intrinsic magnetic moment associated with spin angular momentum, or simply "spin," and also to the electrons' orbital angular momentum. In Nature, other sources of magnetism are due to nuclear magnetic moments of the nuclei, typically thousands of times smaller than the

WD EX1057
Western Digital v IP Bridge
Page 2

electrons' magnetic moments. Consequently, these nuclear moments are negligible in the context of the magnetization of materials. However, they play an important role in nuclear magnetic resonance (NMR) and magnetic resonance imaging (MRI).

The spin magnetic moment $\vec{\mu}_S$ and spin angular momentum $\vec{S}$ are linked through the relationship $\vec{\mu}_S = -g\mu_B\vec{S}$, where g is a dimensionless number called the g-factor (or Landé factor) and $\mu_B = e\hbar/2m_e$ is the Bohr magneton. In this expression, $e = 1.60 \times 10^{-19}$C is the electron charge, $m_e = 9.31 \times 10^{-31}$ kg is the electron mass, and $\hbar = 1.05 \times 10^{-34}$ m^2 kg/s is the reduced Planck constant. Due to the quantum mechanical nature of the spin, measurement of the projection of the electron spin $\vec{S}$ on any direction can take only two values: $+1/2$ and $-1/2$.

In the context of spintronics, the main question is to understand how this fundamental characteristic property of the electrons, that is, the spin, influences the mobility of the electrons in materials. In fact, although it was suggested by N. Mott in 1936, the influence of spin on the transport properties in a ferromagnetic material was clearly demonstrated experimentally and described theoretically only in the late 1960s (for a review, see Ref. 5). The property of spin-dependent transport is at the heart of not only the GMR effect but also all related effects that have allowed the development of spintronic devices.

The ferromagnetic transition metals, such as Fe, Co, Ni, and their alloys, which are the key compounds in today's spintronic devices, have a specific electronic band structure compared to normal (nonmagnetic) metals. In transition metals, the two highest filled energy bands, which are the conduction bands, are occupied by 3*d* and 4*s* electrons. This nomenclature refers to atomic orbitals of the electrons. They are labeled *s*-orbital, *p*-orbital, *d*-orbital, and *f*-orbital referring to orbitals with angular momentum quantum number $l = 0$, 1, 2, and 3, respectively. These nomenclatures indicate the orbital shape and are used to describe the electron configuration. In a crystal, electrons with similar orbitals associate to fill a band of energy. More precise description on this topic can be found in any quantum mechanics textbook. In the case of ferromagnetic transition metals, each of these bands splits in two subbands corresponding to each spin configuration (see Fig. 1.1a). And in these magnetic materials, the interaction between spins, called the *exchange interaction*, energetically favors a parallel orientation of the electrons' spins.

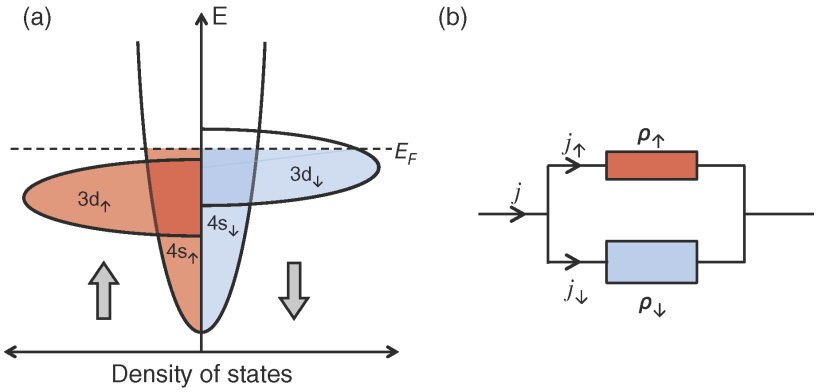


Figure 1.1 (a) Schematic representation of the band structure of a transition metal with strong ferromagnetic properties such as Co or Ni. (b) Equivalent circuit for the two-spin subbands in the "two-current" model.

WD EX1057
Western Digital v IP Bridge
Page 3

In the following, we will refer to electrons with a magnetic moment aligned parallel to the local magnetization as "spin-up" (↑) electrons, and to electrons with a magnetic moment aligned antiparallel to the local magnetization as "spin-down" (↓) electrons.

As for ferromagnetic metals, similar to a normal metal, the 4s band contains almost an equal number of spin-up and spin-down electrons. But the specificity of ferromagnetic metals lies in the structure of their 3*d* bands, for which the resulting lowest energy situation corresponds to a shift of the two subbands $3d_\uparrow$ and $3d_\downarrow$ (Fig. 1.1a). This offset generates an asymmetry for the number of electrons of each orientation, also responsible for the spontaneous magnetization. Consequently, they are also known as majority spin (↑) and minority spin (↓) electrons. It finally creates, for each spin orientation, a difference between spin-up and spin-down densities of states at the Fermi energy E_F. We remind here that the density of states (DOS) *D(E)* of a system describes the number of states *dn(E)* per interval of energy *dE* around each energy level *E* that are available to be occupied by electrons: $dn(E) = D(E)dE$. The Fermi level E_F corresponds to the highest energy level occupied by electrons in a system at a temperature $T = 0$ K. Electrons involved in the transport process lie at (or close to) the Fermi level.

In the low-temperature limit, one considers that the electron's spin is conserved during most scattering events. Under this assumption, transport properties associated with spin-up and spin-down electrons can be represented by two independent parallel conduction channels (Fig. 1.1b), and the mixing of these two conduction channels is then considered as negligible. In ferromagnetic metals, these two channels have different resistivities $\rho_\uparrow$ and $\rho_\downarrow$, which depend on whether the electron magnetic moment is parallel (↑) or antiparallel (↓) to the direction of the local magnetization.

In a first, simple approximation, we can consider that 4*s* electrons, which are fully delocalized in the metal because they belong to outer electronic shells, constitute the conduction electrons that carry most of the current. In contrast, 3*d* electrons are more localized and responsible for the magnetic properties of the metal. The overlapping of *s* and *d* bands at the Fermi level allows current-carrying 4*s* electrons to be scattered on the localized 3*d* states, on the condition that they have the same energy and the same spin. The difference between the density of states of (↑) and (↓) 3*d* electrons at the Fermi level, therefore, results in different scattering probabilities for 4*s* electrons with spin (↑) or (↓).

In the case of Co and Ni, materials with strong magnetization, the bands are filled such that the Fermi level lies above the $3d_\uparrow$ subband. This subband is then completely filled and the $3d_\uparrow$ density of states at the Fermi level is zero (as illustrated in Fig. 1.1a). As a result, $s \rightarrow d$ electron scattering is possible only for s (↓) electrons, while (↑) electrons are not scattered on 3*d* states. This results in a much larger diffusion rate and thus a larger resistivity for the minority spin channel (↓) as compared to the majority spin channel (↑): $\rho_\uparrow < \rho_\downarrow$. At low temperature and under this approximation of two independent channels, the total resistivity of a ferromagnetic metal is then given by the following simple expression (6):

$$\rho = \frac{\rho_\uparrow \rho_\downarrow}{\rho_\uparrow + \rho_\downarrow}. \tag{1.1}$$

WD EX1057
Western Digital v IP Bridge
Page 4

At high temperatures, some additional scattering of conduction electrons, for instance, by spin waves (propagating perturbations in the magnetic materials), can cause *spin-flip* events, that is, a mixing of the two conduction channels, but those can be ignored in first approximation up to room temperature.

Two definitions for the spin asymmetry coefficient of a given ferromagnetic material are used in the literature, $\alpha = \rho_{\downarrow}/\rho_{\uparrow}$ or $\beta = (\rho_{\uparrow} - \rho_{\downarrow})/(\rho_{\uparrow} + \rho_{\downarrow})$. In strong ferromagnets such as Co or Ni, $\rho_{\uparrow} < \rho_{\downarrow}$ and thus $\alpha > 1$.

A major consequence of the resistivity difference between conduction channels of minority and majority spin is that most of the current flows through the low resistivity spin (↑) channel. Consequently, an asymmetry in the current densities associated with (↑) and (↓) electrons appears. Hence, the current flowing in the ferromagnetic material is *spin polarized*. Calling $j_{\uparrow}$ and $j_{\downarrow}$ the current densities of spin (↑) and (↓) electrons, respectively, and p the current spin polarization, p is defined by $p = (j_{\uparrow} - j_{\downarrow})/(j_{\uparrow} + j_{\downarrow})$. Note that $p = \beta$ at low temperature.

1.1.2 A Simple Model to Describe GMR: The "Two-Current Model"

Historically, the *two-current model*, proposed by Mott and then by Fert and Campbell, was developed to explain the spin-dependent resistivity in materials doped with magnetic impurities. It allows the anticipation, in a rather simple way, of the GMR effect in magnetic multilayers. For this, we consider an archetypal multilayered stack consisting of thin layers of alternating ferromagnetic metals (F) and nonmagnetic (NM) metals. The magnetization of the ferromagnetic layers is supposed to be uniform within each layer. We also assume that the relative orientation of the magnetization in the successive F layers can somehow be changed from parallel (P) to antiparallel (AP) magnetic configuration, as illustrated in Fig. 1.3. The way this is achieved will be explained in more detail in the next section.

Two geometries to evaluate the resistance of this multilayered structure can be considered: either with current flowing parallel to the plane of the layers (known as "current-in-plane GMR," CIP-GMR) or with current flowing in the direction perpendicular to the plane of the layers (known as "current-perpendicular-to-plane GMR," CPP-GMR). The same model can be used to evaluate the magnetoresistive properties for both geometries, provided that the layers' thickness remains small compared to a characteristic length associated with each geometry.

For the CIP case, the characteristic length is actually the mean free path λ. For the CPP case, it is the spin-flip length or spin diffusion length l_{sf} (7).

As illustrated in Fig. 1.2, during their Brownian motion throughout the structure with an average drift along the electrical field direction, the electrons traverse successive ferromagnetic layers. We denote $r/2$ the resistance associated with traversing a F layer for the majority spin channel (same direction as the magnetization) and $R/2$ the corresponding resistance for the minority spin channel (opposite direction to the magnetization), with $r < R$. $r/2$ and $R/2$ are associated with the average resistance sensed by the electrons as they spend half of their total path, respectively, in the majority or minority spin channels. For the sake of simplicity, let us also assume that the resistance of the nonmagnetic separating layer is much smaller

WD EX1057
Western Digital v IP Bridge
Page 5

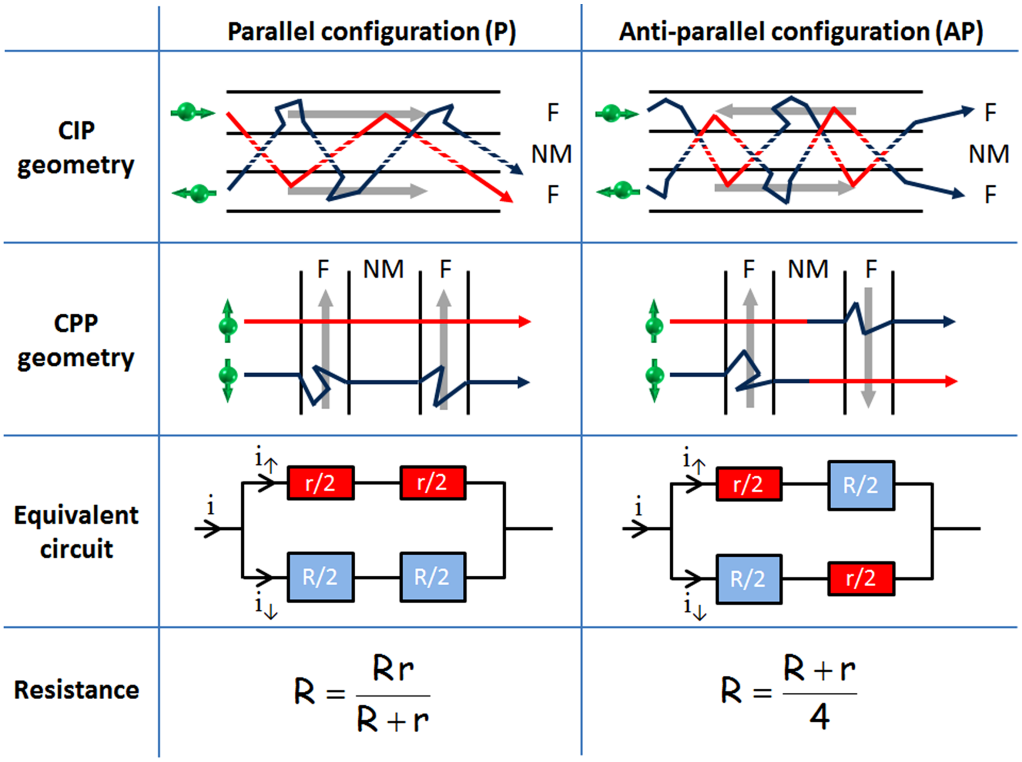


Figure 1.2 Illustration of the two-current model. The conduction paths of spin-up and spin-down electrons in a ferromagnetic metal/normal metal/ferromagnetic metal (F/N/F) multilayer, in the two cases of CIP and CPP transport. Conduction electrons with spin magnetic moment aligned antiparallel (blue paths) to the local magnetization experience more scattering events than those with parallel spin (red paths). The equivalent resistance circuit is represented for the two magnetic configurations: parallel and antiparallel.

than r and R. Then, in the P configuration, spin ($\uparrow$) and ($\downarrow$) electrons behave, respectively, as majority and minority electrons in all magnetic layers. As a result, the respective resistances of the two spin channels are $r_\uparrow = r$ and $r_\downarrow = R$. Since these two channels conduct the current in parallel, the equivalent resistance of the F/NM/F stack can be written as $r_P = rR/(r+R)$. In the case of materials with large spin asymmetry ($\alpha \gg 1$ and $r \ll R$), the multilayer can be considered short-circuited by the spin ($\uparrow$) channel; its equivalent resistance is $r_P \approx r$.

For the AP configuration, the electrons alternatively behave as majority or minority electrons as they propagate from one ferromagnetic layer to another. As a result, they are alternatively weakly and strongly scattered. Thus, the short-circuit effect previously mentioned in P configuration is here suppressed. In the AP configuration, the two channels have the same resistance $(R+r)/2$. The F/NM/F equivalent resistance is then $r_{AP} = (R+r)/4$, which is, in general, much larger than $r_P = r$.

Following this model, one can finally derive a simple expression for the amplitude of the GMR ratio:

$$\mathrm{GMR} = \frac{r_{AP} - r_P}{r_P} = \frac{(R-r)^2}{4Rr}. \tag{1.2}$$

WD EX1057
Western Digital v IP Bridge
Page 6

Let us mention that another definition of the GMR ratio is sometimes used in the literature, notably in theoretical articles. It consists of normalizing the resistance variation between P and AP configurations by the resistance in the AP configuration: $\mathrm{GMR} = (r_{AP} - r_P)/r_{AP}$. In this definition, the GMR amplitude has a maximum value of 100%, whereas the commonly used definition often leads to magneto-resistive ratios over 100%. The GMR ratio is of prime importance for the characterization of the resistance variation, which is measured to determine the magnetic state of the stack.

1.1.3 Discovery of GMR and Early GMR Developments

The characteristic length scale of spin-dependent diffusion in thin films is on the order of a few nanometers in magnetic materials and tens of nanometers in nonmagnetic materials. These numbers explain why it took almost 20 years between the first basic studies on spin-dependent transport carried out on magnetic alloys in the late 1960s and the GMR discovery. GMR could be observed only in multilayered stacks consisting of nanometer thick layers. The growth of such multilayers became possible in the 1980s, thanks to the development of a new growth technique adapted from semiconductor industry: molecular beam epitaxy (MBE). GMR was actually discovered in magnetic metallic multilayers consisting of alternating layers of iron and chromium (Fe/Cr). This discovery by Albert Fert in Orsay, France, and Peter Grünberg in Jülich, Germany, in 1988, consisted of a very large variation in the CIP electrical resistance of these stacks under the application of an external magnetic field. Due to an antiferromagnetic coupling that exists between the successive Fe layers across the Cr spacers, the magnetization in the successive Fe layers spontaneously orient themselves in an AP configuration in zero magnetic field, as represented in Fig. 1.3. Upon application of a large enough magnetic field to overcome this antiferromagnetic coupling, the magnetization of all Fe layers can be saturated in the direction of the field, resulting in a P magnetic configuration. The GMR consists in a very large drop of resistance of 80% at 4 K (50% at 300 K) between the AP and P configurations. In 1988, it has been named "giant magnetoresistance" because the GMR amplitude was much larger than all known magnetoresistance effects at room temperature at that time. This discovery of GMR is considered the starting point of spinelectronics or spintronics. Almost immediately, GMR attracted enormous interest both from the point of view of fundamental physics and also for its possible applications, especially in the fields of data storage and magnetic field sensors. Fert and Grünberg were awarded the Nobel Prize in Physics in 2007 for this discovery.

Research on magnetic multilayers and GMR rapidly became a very active topic. It is not our aim here to provide an exhaustive review of all experimental and theoretical results that followed the initial discovery. A more complete review can be found in Ref. 6. Here we will rather introduce some of the key advances in GMR that occurred in the first years of spintronics.

Parkin et al. first demonstrated in 1990 the existence of GMR in multilayers prepared by sputtering (8), a simpler and faster physical vapor deposition (PVD) technique: a technique that is compatible with industrial processes. In magnetic multilayers consisting of alternating ferromagnetic and nonmagnetic layers, they also demonstrated the existence of oscillations in the FM interlayer coupling across the

WD EX1057
Western Digital v IP Bridge
Page 7

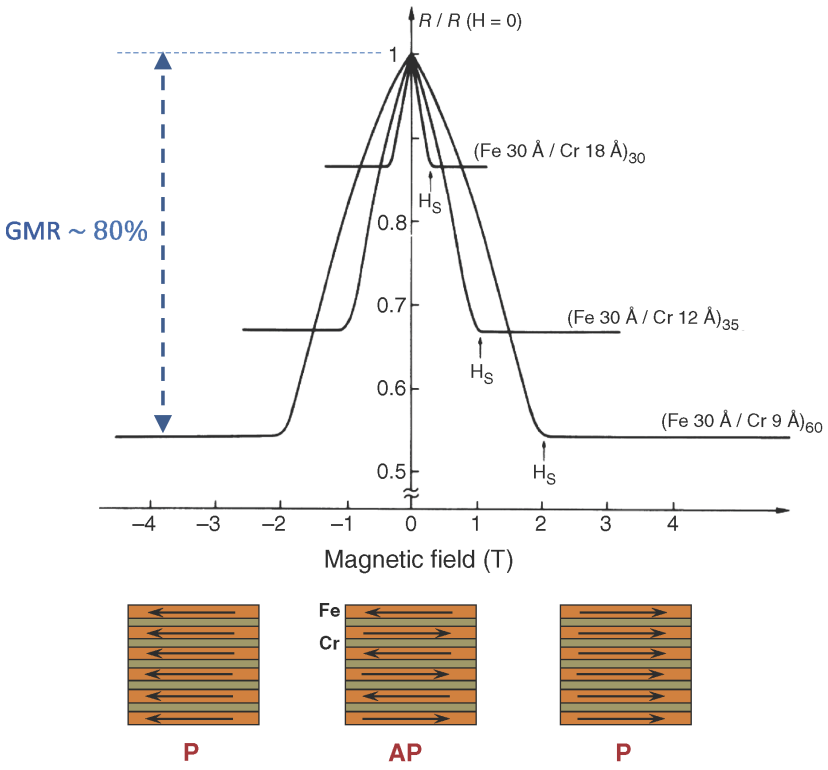


Figure 1.3 Normalized resistance as a function of external magnetic field $\mu_0 H$ for Fe/Cr multilayers, with different Cr intermediate layer thicknesses. The magnetic configuration is *AP* at zero external field and *P* at large applied fields (positive or negative). (Adapted from Ref. 1 with permission from American Physical Society.)

NM spacers as a function of the NM spacer thickness (see Chapter 2). This oscillatory coupling has been observed in a wide variety of multilayered systems, in particular (Fe/Cr) and (Co/Cu) multilayers. Another crucial step toward applications of GMR was also made in 1991 by Dieny et al., who developed trilayered ferromagnet/nonmagnetic metal/ferromagnet (F/NM/F) structures called *spin valves*, which exhibit GMR at low magnetic fields (a few millitesla instead of a few teslas for (Fe/Cr) multilayers (9). In these trilayers, the magnetization of one of the ferromagnetic layers is pinned in a fixed direction using a phenomenon called exchange bias, whereas the magnetization of the second ferromagnetic layer can be easily switched in the direction of the applied field. It is then possible to change the magnetic configuration of these spin valves from *P* to *AP* by applying a weak magnetic field (a few millitesla) parallel or antiparallel to the direction of magnetization of the pinned layer. These systems, which exhibit very high 'resistance versus field' sensitivity, were introduced as magnetoresistive heads in hard disk drives by IBM in 1998.

1.1.4 Main Applications of GMR

GMR has been primarily used as spin-valve magnetoresistive heads in HDDs between 1998 and 2004. It was subsequently replaced by TMR heads, which exhibit even

larger magnetoresistance amplitude. GMR sensors are being used in other types of applications in the automotive industry, robotics, as three-dimensional position sensors, and sensors for biotechnological applications.

Some attempts have been made to use CIP-GMR for memory applications (MRAM), but only low-memory densities of about 1 Mbit per chip could be achieved. This memory is used mainly for space applications because of its radiation hardness (10).

1.2 TUNNELING MAGNETORESISTANCE

The development of artificial magnetic systems based on magnetic tunnel junctions (MTJs) was a second major breakthrough in spin electronics. Magnetic tunnel junctions look like spin valves from a magnetic point of view (two ferromagnetic layers separated by a nonmagnetic spacer) but a major difference is that the nonmagnetic spacer consists of a very thin insulating layer. In these junctions, the current flows perpendicular to the plane of the layers so that the electrons have to tunnel from one ferromagnetic layer to the other one across the thin insulating barrier.

After the pioneering work of Jullière (11) on Fe–GeO–Co junctions at 4.2 K in 1973, it was not until the mid-1990s that the improvement of both growth techniques and lithography processes allowed the fabrication of reliable MTJs. The devices studied used amorphous aluminum oxide (Al_2O_3) as the insulating barrier (2,3). They led to the first measurements of large magnetoresistive effects (TMR) with ratios on the order of 10–70% at room temperature. A great advantage of TMR with respect to GMR is the much larger impedance of MTJs compared to GMR metallic structures in the CPP geometry. Indeed, in MTJs, the resistance of the structure is effectively determined by the thickness of the tunnel barrier. MTJs can be patterned in the form of deeply submicrometer pillars with resistance ranging from kilohms to megohms, depending on the barrier thickness. This makes MTJs easier to integrate with CMOS components such as transistors, which have typical resistance in conducting mode of a few kilohms. In contrast, GMR submicrometer pillars in CPP geometry have resistances on the order of a few tens of ohms, which is fine for sensor applications, but difficult to integrate with CMOS components, in particular for MRAM applications.

An important research effort was undertaken on the materials side to improve the TMR amplitude. In 2004, it was discovered that much larger TMR ratios of about 250% at room temperature could be obtained in MTJs containing a monocrystalline magnesium oxide (MgO) barrier instead of an amorphous alumina barrier (12,13), reaching up to 600% at room temperature. These improvements have allowed a large increase of the sensitivity of magnetic HDD heads, which are needed for increased bit density. Thanks to their higher impedance than CPP-GMR devices, they also enabled new types of MRAM that could be scaled down in size and ramped up in density. Magnetic tunnel junctions are today the core elements of all MRAM technology (see Chapter 5).

As already mentioned, the transport mechanism across MTJs is no longer Ohmic transport as in GMR but relies on the well-known quantum mechanical tunneling effect. We start our second section by summarizing the basics of quantum

WD EX1057
Western Digital v IP Bridge
Page 9

mechanical tunneling. This will allow us to introduce Jullière's model for TMR, giving an intuitive explanation of the magnetoresistive effect in magnetic tunnel junctions. This introduction will be completed by a description of a more accurate model (Slonczewski's model), and the spin filtering effect. Lastly, the important matter of voltage dependence of TMR will be discussed.

1.2.1 Basics of Quantum Mechanical Tunneling

In classical physics, charge transport through an insulating layer (even if it is ultra-thin) is forbidden. Hence, tunnel conduction through a potential barrier is a pure quantum mechanical phenomenon, called the *tunnel effect*. This effect, predicted in the early years of quantum physics, now has important applications in semiconductor devices such as the tunnel diodes. It is extensively described in elementary textbooks on quantum mechanics: we will only summarize here the main points relevant to MTJ physics.

In Fig. 1.4, the potential landscape for a (injector) metal–insulator–metal (collector) junction is schematically depicted. The main characteristics of the insulating barrier are its energy height Φ, and its thickness d. We consider an electron with an energy E, propagating in the metallic injector in the direction of the stack (perpendicular to the layers), with a wave vector amplitude $k_\perp = \sqrt{2m_eE/\hbar^2}$, where m_e is the electron effective mass and $\hbar$ is the reduced Planck constant. Based on the *free-electron approximation*, the resolution of Schrödinger's equation demonstrates that the electron has a nonzero probability of propagating through the insulating barrier and inside the collector electrode. We recall that in the free electron approximation, it is considered that the electrons are not subjected to any confining potential inside the metal or the barrier. The only potential variation is due to the insulating barrier. This model is well suited to 4*s* electrons, which are delocalized in the crystal.

Within the tunnel barrier, the electron wave function decays exponentially so that the probability for the electron to tunnel through the insulating barrier is given by

$$T(E) \propto e^{-2\kappa d}, \tag{1.3}$$

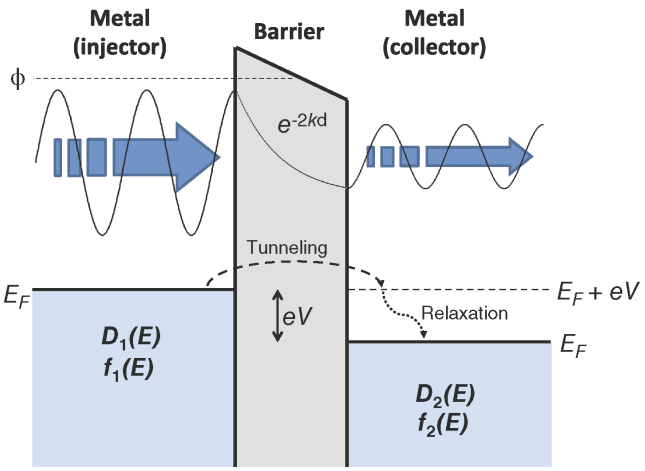


Figure 1.4 Schematics of the wave function of an electron tunneling between two metallic layers across a potential barrier.

WD EX1057
Western Digital v IP Bridge
Page 10

with the decay coefficient $\kappa(E) = \sqrt{2m_e(\Phi - E)/\hbar^2}$. A first conclusion from these expressions is that in order to limit the MTJ resistance with typically used materials (MgO, Al_2O_3), the thickness of the insulating layer has to be on the order of a nanometer, corresponding to a few atomic layers. As an illustration, considering that an electron has to cross a $(\Phi - E_F) = 1\ eV$ barrier, it would experience a decay length of $1/\kappa \approx 0.2$ nm.

In MTJs at zero bias voltage, the Fermi levels of the two electrodes align so that the same number of electrons are steadily tunneling from one side of the barrier to the other and vice versa. In order to obtain a net nonzero current flow, a bias voltage has to be applied between the two metallic electrodes. When a bias voltage V is applied, the collector electrode's Fermi level is lowered by eV relative to the injector's, so that electrons tunnel from injector to collector (see Fig. 1.4). The resulting current then depends on the barrier properties, but also on the states accessible on both sides of the barrier. Indeed, according to the Fermi's golden rule, the probability for an electron having an energy E to tunnel through the barrier from metal 1 to metal 2 is proportional to the number of unoccupied electron states in 2 (collector) at this energy. In addition, the number of electrons that are candidates for tunneling is proportional to the number of occupied state in 1 (injector) at E. Therefore, the tunneling current from 1 to 2 due to electrons with energy E can be written as

$$I_{1\to2}(E) \propto D_1(E) f_1(E)\, T(E)\, D_2(E + eV)(1 - f_2(E + eV)), \tag{1.4}$$

where $D_1(E)$ and $D_2(E + eV)$ are the density of states (DOS), respectively, in electrode 1 at the energy E and in electrode 2 at $(E + eV)$, and the functions $f_1(E)$ and $f_2(E)$ are the Fermi–Dirac distributions, which give the occupation probabilities of states in electrodes 1 and 2. Consequently, the product $D_1(E) f_1(E)$ represents the probability, in electrode 1, of having an electron with the energy E and $D_2(E + eV)(1 - f_2(E + eV))$ the probability, in electrode 2, of having an unoccupied state at the energy $(E + eV)$. Finally, the term $T(E)$ is the previously described transmission coefficient.

Using Eq. (1.4) to sum $I_{1\to2}(E) - I_{2\to1}(E)$ overall energies, the total tunneling current may be calculated. In the limit of zero temperature and small voltage V, it can be shown that only electrons at the Fermi level E_F contribute to the current. The resulting conductance is then simply proportional to the product of the densities of states at the Fermi energy in the two electrodes:

$$G_{T=0} \propto D_1(E_F) \cdot D_2(E_F). \tag{1.5}$$

1.2.2 First Approach to Tunnel Magnetoresistance: Jullière's Model

The simplified approach described in the previous section for deriving the amplitude of the tunneling current was used by Jullière in 1975 to analyze his pioneer results of tunnel magnetoresistance in a MTJ composed of two ferromagnetic thin films, iron (Fe) and cobalt (Co), separated by a thin GeO semiconducting layer (11). The ferromagnetic character of the electrodes was taken into account by introducing different densities of states $D^{\uparrow}$ for the majority and $D^{\downarrow}$ for the minority electrons, using

WD EX1057
Western Digital v IP Bridge
Page 11

the following definition for the spin polarization of a ferromagnet:

$$P_0 = \frac{D^{\uparrow}(E_F) - D^{\downarrow}(E_F)}{D^{\uparrow}(E_F) + D^{\downarrow}(E_F)}. \tag{1.6}$$

As for the GMR, the TMR can then be understood within the two-current model by summing in parallel the conductances of the spin-up and spin-down channels assuming that the tunneling process is spin-conserving. As illustrated in Fig. 1.5, in the *P* magnetic configuration, majority spin (↑) electrons from the injector tunnel

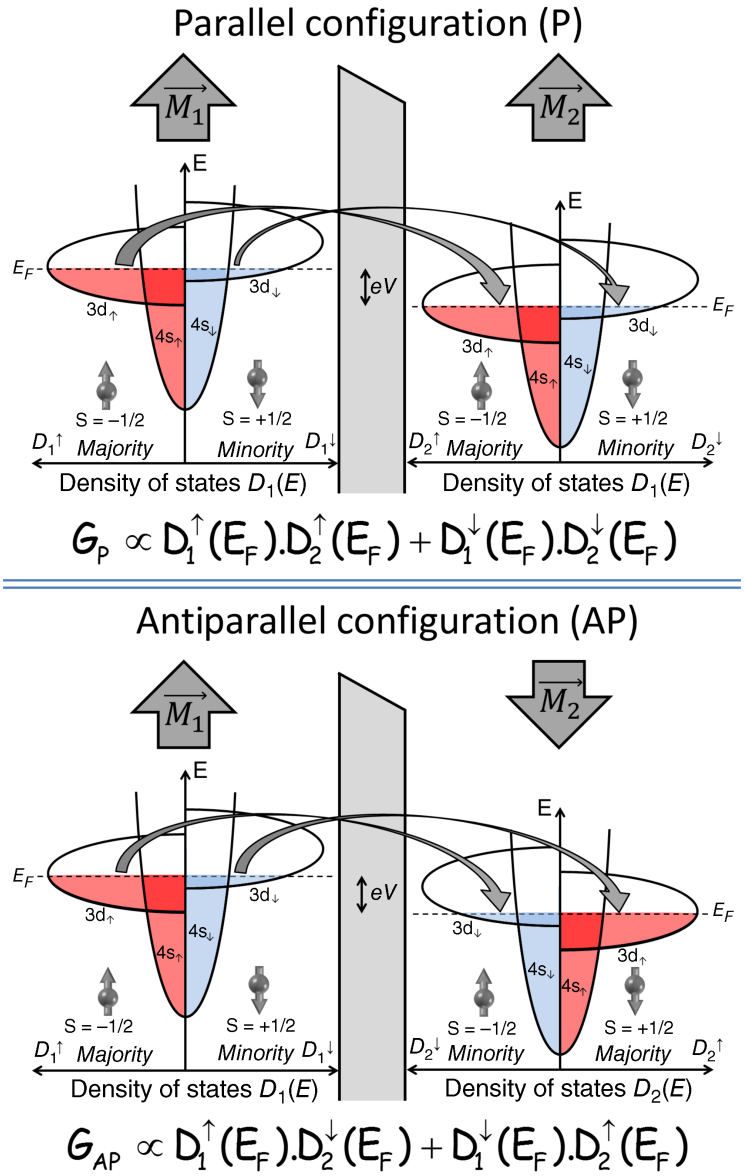


Figure 1.5 Schematics of the spin-dependent tunneling process through an insulating barrier when the magnetizations in ferromagnetic electrodes are in parallel *P* or antiparallel *AP* magnetic configurations. The process is assumed to be purely ballistic, so that no mixing of spin states occurs during the tunneling process.

WD EX1057
Western Digital v IP Bridge
Page 12

toward majority spin (↑) empty states in the collector. At the same time, minority spin (↓) electrons from the injector tunnel toward minority spin (↓) empty states in the collector. The conductance in P configuration is then written as

$$G_P \propto D_1^{\uparrow}(E_F).D_2^{\uparrow}(E_F) + D_1^{\downarrow}(E_F).D_2^{\downarrow}(E_F). \tag{1.7}$$

In case of AP magnetic configuration, majority spin (↑) electrons from the injector tunnel toward minority spin (↓) empty states of the collector. At the same time, minority spin (↓) electrons from the injector tunnel toward majority spin (↑) empty states of the collector. The conductance in AP configuration is then written as

$$G_{AP} \propto D_1^{\uparrow}(E_F).D_2^{\downarrow}(E_F) + D_1^{\downarrow}(E_F).D_2^{\uparrow}(E_F). \tag{1.8}$$

Using these expressions, the TMR ratio, which characterizes the resistance difference in P and AP configurations, may be expressed as

$$\text{TMR} = \frac{G_P - G_{AP}}{G_{AP}} = \frac{R_{AP} - R_P}{R_P} = \frac{2P_1P_2}{1 - P_1P_2}, \tag{1.9}$$

where $P_{1,2}$ are the spin polarization of electrode 1 and electrode 2 as defined in Eq. (1.6). Note that similar to the GMR case, a "pessimistic" definition of the TMR ratio can also be defined as $\text{TMR} = ((G_P - G_{AP})/G_P) < 1$.

This model is oversimplified in the sense that it neglects all band structure effects in the magnetic electrodes and in the barrier. Nevertheless, this simple model successfully predicted the amplitude of TMR (typically around 50–70% with spin polarization on the order of 50–65% in Co–Fe-based alloys) in amorphous alumina-based magnetic tunnel junctions. However, the model failed to explain the very large TMR of magnetic tunnel junctions based on epitaxial barriers, notably of magnesium oxide (MgO) barriers. A key challenge to get an accurate prediction of TMR is to properly estimate the actual amplitude and sign of spin polarization for a given ferromagnetic material. Clearly, the larger the spin polarization, the higher the TMR amplitude. To maximize this spin polarization, a significant effort in materials science has been devoted to the search for half-metals, which are expected to be conducting for one spin direction and insulating for the other, resulting in 100% spin polarization at Fermi energy ($D^{\downarrow}(E_F) = 0$). Some magnetic oxides and Heusler alloys seem to exhibit this property in bulk form, but not when integrated in MTJs at room temperature.

Several experimental techniques have been used to measure the ferromagnet's spin polarization, such as the Meservey and Tedrow technique (14), which is based on tunneling transport in FM–insulator–superconductor junctions. A list of typical values obtained for a variety of ferromagnetic materials is presented in Table 1.1.

Other experiments in 1999, involving the study of spin-dependent tunneling through transition metal oxide barriers ($SrTiO_3$), revealed that different values and even opposite signs of spin polarization of tunneling electrons could be obtained for the same ferromagnetic electrode by varying the nature of the tunneling barrier (15).

WD EX1057
Western Digital v IP Bridge
Page 13

TABLE 1.1 Values of Ferromagnet (FM) Spin Polarization P_0 Extracted from FM/Insulator/Al Tunneling Experiments, Where Al Is a Superconductor at Low Temperatures.

Ferromagnet	P_0 (%)
Ni	33
Co	42
Fe	45
$Ni_{90}Fe_{10}$	36
$Ni_{80}Fe_{20}$	48
$Co_{50}Fe_{50}$	51
$Ni_{40}Fe_{60}$	55

This technique of tunneling from a ferromagnet to a superconductor is used to determine the spin polarization in the ferromagnet (14).

These results clearly indicate that the spin polarization of the tunneling electrons is not only determined by the nature of the ferromagnetic electrodes but also by the whole trilayer ferromagnet/barrier/ferromagnet. In the following section, we introduce a more advanced model for treating the ferromagnet and the tunneling barrier configuration as a next step toward considering the whole trilayer band structure.

1.2.3 The Slonczewski Model

In 1989, Slonczewski proposed a more rigorous model based on the detailed calculations of the electron wave functions across the barrier, taking into account the exact matching conditions at the ferromagnetic/barrier and barrier/ferromagnetic interfaces (16). To derive the actual value of the transmission coefficient $T(E)$, one must consider not only the density of states of electrons at the Fermi level but also their wave vector k_F (or more simply their velocity v_F). This velocity is dependent on the type of electron one considers (s, p, and d bands). We will see below that this approach is required to understand the large values of TMR that are obtained in MgO-based MTJ devices.

1.2.3.1 The Model In Slonczewski model, several assumptions are made, similar to those of Jullière's model. First, the tunneling barrier is simply described as a square potential (energy height Φ and thickness d) above the Fermi level of the two ferromagnetic electrodes, considering the *free-electron approximation*. Second, the two ferromagnetic electrodes are taken to be identical. Finally, the model assumes that only electrons propagating perpendicular to the layers ($\vec{k} \approx \vec{k_\perp}$, $k_\parallel \approx 0$) can efficiently tunnel through the barrier. Indeed, if we consider electrons propagating in another direction, with $k_\parallel \neq 0$, then the decay coefficient inside the insulating layer becomes $\kappa(E) = \sqrt{k_\parallel^2 + \left(2m_e/\hbar^2\right)(\Phi - E)}$. Then, the higher the parallel wave vector, the lower the probability for the electron to tunnel through the barrier. By solving Schrödinger's equation in each part of the junction and applying continuity of the

wave functions at the interfaces, it was analytically demonstrated that the equivalent spin polarization of the ferromagnet/barrier couple, P, can be written as

$$P = \frac{\left(k_{F,\uparrow} - k_{F,\downarrow}\right)\left(\kappa^2 - k_{F,\uparrow}k_{F,\downarrow}\right)}{\left(k_{F,\uparrow} + k_{F,\downarrow}\right)\left(\kappa^2 + k_{F,\uparrow}k_{F,\downarrow}\right)} = P_0 \frac{\left(\kappa^2 - k_{F,\uparrow}k_{F,\downarrow}\right)}{\left(\kappa^2 + k_{F,\uparrow}k_{F,\downarrow}\right)}, \tag{1.10}$$

where $k_{F,\uparrow}$ and $k_{F,\downarrow}$ are the wave vectors for majority and minority electrons at the Fermi level, respectively, κ corresponds to the decay coefficient of the electrons' tunneling probability through the insulating barrier (see Eq. (1.3)), and P_0 corresponds to the previously defined polarization for a ferromagnet in Jullière's model (see Eq. (1.6)). Moreover, instead of defining a net polarization for the whole ferromagnetic layer, this expression highlights that the polarization actually depends on the type of electron one considers (to which band it belongs). Indeed, the values of κ, $k_{F,\uparrow}$, and $k_{F,\downarrow}$ are associated with the band one considers, and P can be derived for each of these bands.

The expression for the spin polarization P in this model reveals that the attenuation of the wave function while crossing the barrier also results in a decrease of the effective spin polarization of the total current. In the limit of large barrier height Φ, and hence large decay coefficient κ, the resulting polarization is equivalent to the one defined in the Jullière's model. This model emphasizes the importance of the electrons' properties in the calculation of the polarization. One can perform a simple calculation by considering only the contribution of the lighter (s band) electrons, but a more complete calculation would sum the contributions of each type of electrons.

1.2.3.2 Experimental Observations On the experimental side, it has been noted that TMR amplitude varies considerably depending on the nature of the electrodes and the nature of the insulating barrier and interfaces. For example, Yuasa and Djayaprawira showed that in epitaxial magnetic tunnel junctions of Fe–Al_2O_3–CoFe, the TMR amplitude changes when the crystallographic orientation is changed among (211), (110), and (100) planes (17). The major role of the interfaces between the ferromagnet and the insulating layer has been highlighted by experiments demonstrating that Co/Al_2O_3 and Co/MgO provide positive polarization of tunneling electrons, whereas Co/$SrTiO_3$ provides negative polarization of tunneling electrons, at least at low bias voltage (15). These results demonstrate that it is possible to modify the TMR amplitude by choosing different ferromagnet/barrier configurations.

1.2.3.3 About the TMR Angular Dependence Denoting θ the angle between the magnetization directions in the two ferromagnetic electrodes, Slonczewski also succeeded in deriving an expression of the tunnel conductance as a function of the angle θ in the limit of large potential barrier U:

$$G(\theta) = G_0\left(1 + P^2\cos\theta\right), \tag{1.11}$$

where the conductance in the AP configuration G_0 is given by

$$G_0 = \frac{\kappa}{\hbar d}\left[\frac{e\kappa\left(\kappa^2 + k_\uparrow k_\downarrow\right)\left(k_\uparrow + k_\downarrow\right)}{\pi\left(\kappa^2 + k_\uparrow^2\right)\left(\kappa^2 + k_\downarrow^2\right)}\right]^2 e^{-2\kappa d}, \tag{1.12}$$

WD EX1057
Western Digital v IP Bridge
Page 15

which represents the actual conductance when the quantum system is considered as a whole (i.e., the two ferromagnetic layers separated by the tunnel barrier). With the effective tunnel conductance varying as $P^2\cos\theta$, the resistance dependence is then given by $R(\theta) = R_0/\left(1 + P^2\cos\theta\right)$, which can be approximated by $R \approx R_0\left(1 - P^2\cos\theta\right)$ when the electron polarization is weak, that is, for low TMR amplitude.

1.2.4 More Complex Models: The Spin Filtering Effect

Another major breakthrough in the field of spintronics was made with the discovery of much larger TMR amplitude in MTJ based on a crystalline MgO tunnel barrier rather than an amorphous alumina barrier. These MgO-based MTJs are today's standard elements in spintronic devices, whether for MRAM, read heads, or field sensors applications. The starting point of this work was the theoretical calculations carried out by Butler and Mathon in 2001, which predicted that TMR ratios as large as 1600% could be expected for epitaxially grown Co or Fe electrodes on MgO (18,19). For instance, an epitaxial MgO(001) barrier can be easily grown on a Fe bcc layer (001) since the lattice mismatch is small (about 4%). We remind that bcc stands for body-centered cubic, relative to the arrangement of atoms in the crystal. (001) later refers to a growth direction along the cube edge direction. These calculations, performed with *ab initio* methods, derived the tunneling probability of each kind of electrons, depending on their orbital symmetry.

1.2.4.1 Incoherent Tunneling Through an Amorphous (Al_2O_3) Barrier The electrons' wave functions in crystalline materials are described by Bloch states. Bloch states are wave function solutions of the Schrödinger equation describing the quantum mechanical state of electrons in a periodic potential, for example, in a perfect, infinite atomic crystal. In crystalline ferromagnetic metals such as Fe, Ni, Co (3*d* ferromagnetic transition metals), and their alloys, these Bloch states have some specific symmetries: Δ_1 symmetry (corresponding to *spd* hybridized states), Δ_2 symmetry (*d* states), and Δ_5 symmetry (*pd* hybridized states). Bloch states with Δ_1 symmetry usually have a large positive associated polarization at E_F, but it is not the case for other symmetries (they can even have negative associated polarizations). Jullière's model (previously introduced) assumes equal tunneling probabilities independent of the electrons' Bloch states in the electrodes. This is true only if the tunneling process is *incoherent*, meaning that the coherency of the Bloch states is not conserved during tunneling.

In the case of an amorphous barrier, there is no crystallographic symmetry in the barrier. Consequently, electron wave functions from the injector, no matter their symmetry, couple identically to any *tunneling/evanescent states* in the barrier, through which they will propagate and decay. The exponential decay of the wave function throughout the barrier is then independent of the initial symmetry of the tunneling electron wave function so that the transmission probability through the barrier is itself independent on the initial electron wave function symmetry (see Fig. 1.6). This tunneling process can be regarded as an *incoherent tunneling*. It can be well described by Jullière's model introduced earlier. It leads to comparable tunneling

WD EX1057
Western Digital v IP Bridge
Page 16

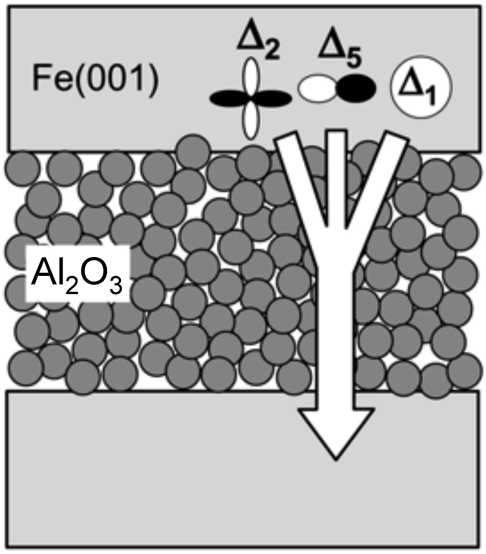


Figure 1.6 Schematic illustration of electrons tunneling through an amorphous (Al_2O_3) barrier. (From Ref. 17.)

probabilities for all Bloch states from the electrode. The *net* polarization then simply corresponds to the one calculated by summing the contributions from (↑) and (↓) DOS from all Bloch states. In this case, the net polarization is reduced due to the contributions of some Bloch states with negative spin polarization (i.e., opposite to the local magnetization).

A major difference between MTJ based on crystalline magnetic electrodes with amorphous barriers or crystalline barriers is that the symmetry of the tunneling electron wave functions may be conserved in the latter case and this symmetry can strongly influence the tunneling rates, that is, the probability of tunneling through the barrier. If one can engineer a system in which the Bloch states with large positive spin polarization have a higher tunneling probability than the Bloch states with negative spin polarization, then a very high net polarization could be expected, resulting in a very large MR ratio. This is possible in some epitaxially grown crystalline MTJs, in particular Fe/MgO/Fe, as explained in the following section.

1.2.4.2 Coherent Tunneling Through a Crystalline MgO Barrier A crystalline MgO(001) can be epitaxially grown on a bcc Fe(001) layer to prepare a crystalline Fe(001)/MgO(001)/Fe(001) MTJ. Considering the $k_{\parallel} = 0$ direction, there are three kinds of tunneling/evanescent states in crystalline MgO, with different associated symmetries: Δ_1, $\Delta_{2'}$, and Δ_5. In such systems, *coherent* tunneling is obtained: The electrons' wave functions in the ferromagnetic material couple with evanescent wave functions having the same symmetry in the barrier, so that electrons conserve their orbital symmetry as they tunnel. *Ab initio* calculations then predict that the tunneling probability of an electron strongly depends on its orbital symmetry, leading to effective possible *symmetry filtering of the tunneling current*. The mechanism of orbital selection for the tunnel conductance in Fe(001)/MgO/Fe(001) systems is presented in Fig. 1.7a.

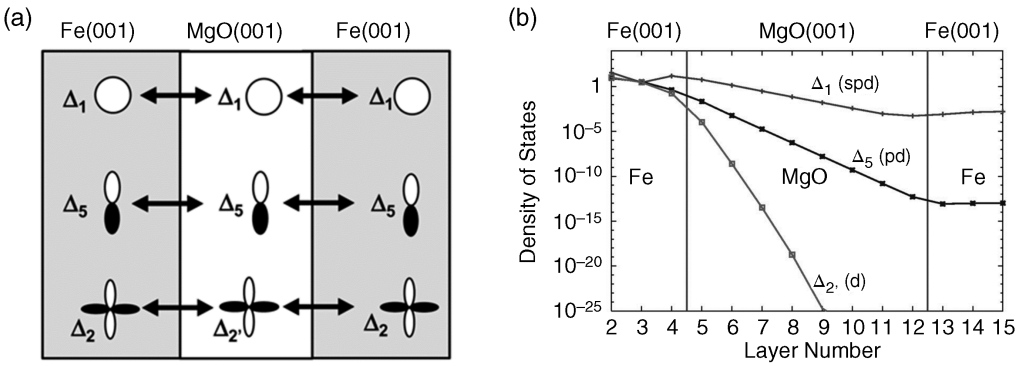


Figure 1.7 (a) Schematic illustration of the coupling between Bloch wave functions in iron and evanescent wave functions in MgO having the same symmetry. (Reproduced from Ref. 17 with permission from American Physical Society.) (b) Density of states for majority electrons tunneling ($k_{\parallel} = 0$) in a MTJ Fe(001)/MgO(001)/Fe(001) in the parallel magnetic configuration. Note the much slower decay of the DOS in the barrier for electrons with Δ_1 symmetry than for those of other symmetries. (From Ref. 17.)

In Fe, the band structure is calculated with consideration of the energy splitting between (↑) and (↓) for each Bloch state type, deducing the densities of states at the Fermi energy, and hence the polarization. Both majority and minority electrons fill many states at the Fermi energy, which corresponds to a small net polarization. But these calculations have demonstrated that only majority electrons fill Δ_1 symmetry states, implying a full polarization $P_{\Delta_1} = 1$, whereas both majority and minority Δ_2 and Δ_5 symmetry states can be found at the Fermi energy, corresponding to low polarizations. Note that for other materials such as bcc Co, only minority Δ_2 and Δ_5 symmetry states exist at the Fermi level, implying that $P_{\Delta_2} = P_{\Delta_5} = -1$.

Furthermore, calculations demonstrate that the exponential tunneling decay is much stronger for Δ_2 and Δ_5 states compared with Δ_1 states. Figure. 1.7b presents the probability for a majority electron incoming from the left electrode to propagate through the MTJ in the *P* configuration. For $d_{\mathrm{MgO}} = 8$ monolayers (ML), which is a reasonable barrier thickness, the transmitted density of Δ_1 states is larger than that of Δ_5 states by 10 orders of magnitude.

In addition, since there are no minority $\Delta_{1\downarrow}$ states to tunnel from or to, only the $\Delta_{1\uparrow} \rightarrow \Delta_{1\uparrow}$ channel has a significant contribution to the conduction. Similarly, for the *AP* configuration, $\Delta_{1\uparrow} \rightarrow \Delta_{1\downarrow}$ and $\Delta_{1\downarrow} \rightarrow \Delta_{1\uparrow}$ channels have a potentially zero tunneling probability. There is therefore here a new mechanism of *spin filtering* of the wave functions according to their symmetry, which yields a dramatic effective increase in the net spin polarization of the tunneling current. As a result, significant conduction occurs only in the *P* configuration. It is this *spin filtering effect* that explains the very large TMR magnitudes predicted and measured in epitaxial or highly textured MgO-based MTJs.

Not only bcc Fe(001) shows this high spin polarization of the Δ_1 Bloch states, but also many other bcc ferromagnetic metals, such as cobalt (Co) and alloys based on Fe and Co. Similarly, very large TMR ratios are also predicted for other crystalline barriers such as $SrTiO_3$ (20). However, so far, MgO-based MTJs still give the best results in terms of TMR. After these theoretical predictions, a strong worldwide

WD EX1057
Western Digital v IP Bridge
Page 18

research effort was made to obtain epitaxial growth of structures for Fe/MgO/Fe or CoFeB/MgO/CoFeB. These efforts resulted in an extremely large TMR of about 600% obtained in 2008 in CoFeB/MgO/CoFeB MTJs at room temperature (21). The difference between the values of experimental and theoretical TMR is mainly due to imperfections in interface quality and defects in crystal growth of materials due to dislocations, vacancies, and impurities (in particular absorbed water molecules). More details on the growth of MgO-based MTJs can be found in Chapter 2 as well as in Ref. 17.

1.2.5 Bias Dependence of Tunnel Magnetotransport

In most MTJs, the magnitude of TMR decreases markedly when the applied voltage increases. This factor is critical for applications and particularly for reading out the memory magnetic state in MRAM. This voltage-induced decrease of TMR in magnetic tunnel junctions is characterized by $V_{1/2}$, which is the voltage for which the TMR ratio is reduced to half of its amplitude in the limit of zero bias voltage. Several theories have been developed to describe this bias dependence of the magnetotransport, which is often very complex because it involves several physical mechanisms of spin depolarization, as explained below.

The first of these mechanisms is based on the emission of magnons by hot electrons. When a finite bias voltage is applied across the junction, the electrons tunnel ballistically through the barrier, that is, keeping their energy so that they arrive in the collector electrode as hot electrons (Fig. 1.4). When they penetrate the collector electrode, these hot electrons very quickly lose their excess energy by inelastic relaxation to the Fermi energy. In a normal metal, the relaxation mechanisms are via electron–electron and electron–phonon interactions. In ferromagnetic materials, electrons can also reach the Fermi energy by emission of spin waves (magnons), a process that does not preserve the spin. The higher the voltage, the greater the density of emitted magnons. Both the spin polarization of the current and the TMR, directly linked to the conservation of spin information, are then reduced.

Another mechanism of spin depolarization of the current is the presence of defects inside the insulating barrier. These defects create trap states in the barrier through which electrons can co-tunnel. This means that electrons tunnel from the injector to the trap, and then from the trap to the collector, losing their spin information in the process.

Finally, the decrease of TMR with bias voltage can be described by the voltage dependence of the electronic properties involved in the tunneling process, for example, the electron effective mass, the transmission coefficients in the barrier, and the parameter of coherent reflections at interfaces. The polarization of the tunneling electrons also depends itself on the bias voltage since at a bias voltage V, electrons within a band of width eV below the Fermi energy can tunnel through the barrier. If one considers a band structure such as the one depicted in Fig. 1.1a, it is clear that the net polarization of the tunneling electrons is expected to decrease if electrons from below the Fermi energy become allowed to tunnel through the barrier.

In MgO-based MTJs, $V_{1/2}$ is typically in the range of 0.5–0.8 V, depending on the nature of the magnetic electrodes and growth conditions. The readout in MRAMs

WD EX1057
Western Digital v IP Bridge
Page 19

is usually performed at voltages on the order of only 0.15–0.2 V for which the drop of TMR is weak.

1.3 THE SPIN-TRANSFER PHENOMENON

In the first generation of MTJ-based MRAM, the switching of the storage layer magnetization during the write process is achieved using pulses of magnetic field (4). This field is induced by a current flowing in conducting lines located above and below the MTJ. This writing process suffers both from the large energy consumption needed to generate large enough magnetic fields and from write selectivity problems due to the spatial extension of generated fields as well as dot-to-dot distribution in switching fields (variability). A new generation of magnetic memory, called spin-transfer torque magnetic random-access memory (STT-MRAM), is based on the pioneering theoretical work of Slonczewski (22) and Berger (23), which predicted that current flowing through magnetic multilayers can directly reverse the magnetization of one of the layers.

We describe below the origin and consequences of this physical phenomenon. The details of the reversal dynamics as well as the use of this new writing mode in MRAM will be described in other chapters.

1.3.1 The Concept and Origin of the Spin-Transfer Effect

The GMR and TMR magnetoresistive effects described in the previous sections correspond to a variation of the current flow in a spin-valve device or a magnetic tunnel junction (i.e., a variation in conductance) induced by a change of the magnetic configuration of the device. This change of magnetic configuration was generally mediated through the action of an external field. The spin-transfer effect may be seen in a simple description as the reciprocal effect to GMR or TMR: via the spin-transfer torque, the current, which gets spin polarized by traversing a first magnetic layer, can exert a torque on the magnetization of a second ferromagnetic layer and thereby change the magnetic configuration of the device.

The simplest system for describing this new effect is similar to the standard magnetoresistive systems described in previous sections. It consists of two thin magnetic layers separated by a nonmagnetic layer (either a normal metal NM or an insulator I). One of the two ferromagnetic layers, F1 is presumably thick and fixed, whereas the second ferromagnetic layer F2 and the nonmagnetic one are chosen to be thin in comparison to the previously introduced characteristic length of spin-polarized transport.

1.3.1.1 The "In-Plane" Torque When electrons flow through the structure perpendicularly to the interfaces, the current spin polarization evolves to remain parallel to the direction of the local magnetization. Indeed, when the electrons penetrate into a ferromagnetic material, the spins of the conduction electrons become very rapidly aligned parallel to the local magnetization direction because of a strong exchange interaction between conducting electrons (4*s*) and the more localized electrons (3*d*) responsible for the local magnetization (see Section 1.1).

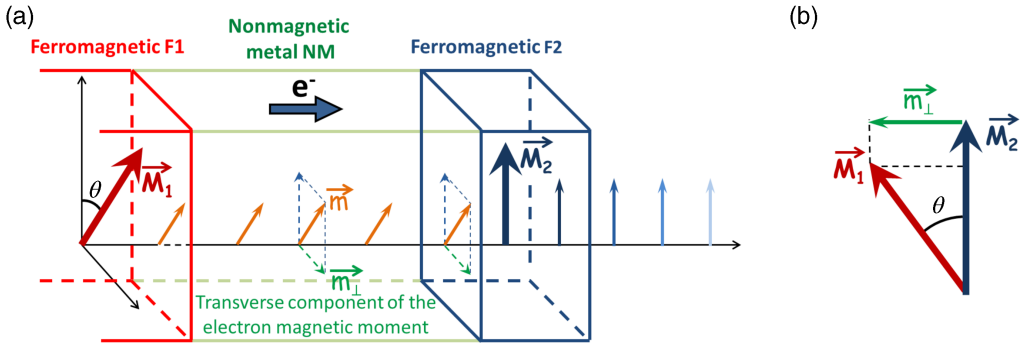


Figure 1.8 (a) Illustration of the concept of spin-transfer torque in a simple F1/NM/F2 trilayer structure; (b) Torque $\vec{m}_\perp$ exerted on the magnetization $\vec{M}_2$ of the thin magnetic layer F2, which tends to get aligned along the magnetization $\vec{M}_1$ when electrons flow from F1 to F2.

In the case where the respective magnetizations $\vec{M}_1$ and $\vec{M}_2$ are noncollinear, the spin polarization of electrons have to rotate in their paths. This occurs mainly through relaxation of the spins transverse component at the F/NM interfaces. We illustrate this phenomenon by considering the case of a spin-valve structure where the nonmagnetic spacer is metallic (NM) as illustrated in Fig. 1.8. When the electrons flow from layer F1 to F2, the current becomes spin polarized after traversing F1, through the mechanism described in Section 1.2 and thus acquires a net spin polarization along $\vec{M}_1$. This nonzero spin polarization propagates across the NM spacer as long as the spin-flip is negligible in this layer. The transmitted electrons then impinge on the NM/F2 interface with a spin polarization that is not aligned with the direction of the local magnetization $\vec{M}_2$.

If we focus on the relaxation process at the second NM/F2 interface, the incoming electrons hence have a component of their magnetic moment $\vec{m}$ transverse to the $\vec{M}_2$ direction (see Fig. 1.8a). When they penetrate into F2, their spin becomes quickly aligned toward the local magnetization direction in a very short distance after the interface (typically less than a nanometer). Hence, the electrons lose their transverse component $\vec{m}_\perp$ when they penetrate into F2 within the first nanometer from the interface. In this interaction however, the total spin angular momentum is conserved, and thus the transverse component $\vec{m}_\perp$ has been actually absorbed and transferred to the magnetization of F2.

This *transfer of spin* is therefore intrinsically an interfacial effect. For a very thick magnetic layer, with very stable magnetization, it then has a negligible influence. However, for a thin layer, this *transfer of spin* tends to modify the local magnetization direction, somehow adding the transferred spins to it. As a result, this *transfer of spin* tends to align the magnetization $\vec{M}_2$ along the direction of the spin current polarization, and hence along the magnetization $\vec{M}_1$ (see Fig. 1.9a) when electrons flow from the "reference" or "fixed" layer F1 to the "free" layer F2. It translates as a torque exerted on the magnetization $\vec{M}_2$, named *spin-transfer torque*.

If electrons now propagate in the opposite direction, that is, from layer F2 to layer F1, electrons impinging on the NM/F1 interface with spin antiparallel to the F2

WD EX1057
Western Digital v IP Bridge
Page 21

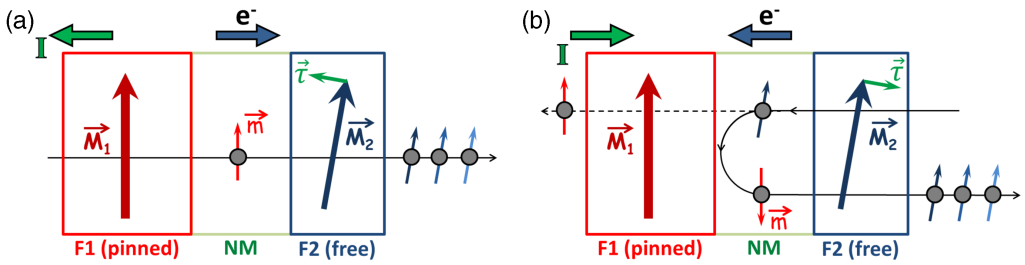


Figure 1.9 In a F1(pinned)/NM/F2(free) trilayer structure, illustration of the sign reversal of the spin-transfer torque with changing the current sign. (a) Positive current tends to align magnetization $\vec{M}_2$ parallel to $\vec{M}_1$. (b) Negative current tends to push $\vec{M}_2$ away from $\vec{M}_1$.

magnetization will have difficulty penetrating into the F1 layer or will be back-scattered because their spin is antiparallel to the local magnetization. These electrons are therefore reflected by the NM/F1 interface and impinge on the other side of the NM spacer on the NM/F2 interface with a spin antiparallel to the F1 magnetization. This flow of reflected electrons again exerts a torque on the F2 magnetization which now tends to align the F2 magnetization antiparallel to the F1 magnetization (see Fig. 1.9b). The STT therefore changes sign as a function of the current direction and can favor either *P* or *AP* magnetic configurations depending on its direction.

As the current density increases, the number of electrons crossing the magnetic layer per unit time increases, thereby proportionally increasing the spin-transfer torque. Therefore, in metallic spin valves, STT can be considered proportional to the current density.

If the system is a magnetic tunnel junction, as in STT-MRAM, the electrons are transmitted ballistically through the spacer layer (the tunnel barrier) instead of diffusely as in spin valves, but the STT effect is basically similar.

Analytically, the spin-transfer torque is equal to the sum of the absorbed transverse spin magnetic moments per unit time:

$$V\frac{d\vec{M}_2}{dt} = \text{absorbed transverse magnetic moments per unit time,} \tag{1.13}$$

considering that each electron flowing across F2 will bring a contribution $\vec{m}_\perp$ to the local magnetization:

$$\vec{m}_\perp = -\frac{g\mu_B}{2}\left(\vec{m}_2 \times \left(\vec{m}_2 \times \vec{m}_1\right)\right), \tag{1.14}$$

In this formula, the cross product $-\left(\vec{m}_2 \times \left(\vec{m}_2 \times \vec{m}_1\right)\right)$ simply corresponds to the direction of the electron's transverse magnetic moment $\vec{m}_\perp$. The free layer volume is $V = t \cdot A$ (t the thickness, A the cross section), g is the electrons Landé factor, and μ_B is the Bohr magneton. The normalized magnetization is given by $\vec{m}_i = \vec{M}_i/M_{S_i}$, where M_S is the saturation magnetization. The number of incoming electrons per second is then simply given by

$$\frac{dN}{dt} = \frac{j_{dc} \cdot A}{e}, \tag{1.15}$$

WD EX1057
Western Digital v IP Bridge
Page 22

where j_{dc} is the injected current density and e the electron's charge. By summing the contributions, and considering the current spin polarization P_{spin} at the NM/F2 interface, one obtains the expression for the spin-transfer torque as

$$\left(\frac{d\vec{m}_2}{dt}\right)_{ST} = -P_{spin}\frac{j_{dc}}{2te}g\mu_B\left(\vec{m}_2 \times \left(\vec{m}_2 \times \vec{m}_1\right)\right). \tag{1.16}$$

This torque is often labeled "Slonczewski torque" (ST) or "in-plane torque" since its direction lies in the plane defined by $\vec{M}_1$ and $\vec{M}_2$. It is proportional to the current spin polarization at the interface, and to the current density. Hence, one can directly change the magnitude or even the sign of the effect by simply tuning these two parameters. Remarkably, by changing the sign of the current, it is possible to reverse the effect. One sign of the current will make the local magnetization $\vec{M}_2$ rotate to align along the magnetization $\vec{M}_1$ (thus favoring parallel magnetizations), while the other sign will make the local magnetization rotate away from the magnetization $\vec{M}_1$ (thus favoring antiparallel magnetizations). A review on in-plane torque in metallic spin valves can be found in Ref. 24.

1.3.1.2 The "Out-of-Plane" Torque

The in-plane torque is always the dominant spin-transfer effect in junctions, and is the most significant torque in all metallic structures. However, an additional component of spin-torque can also become significant in tunnel junctions. It is referred to as field-like torque (FLT) or out-of-plane torque, and is associated to another source of spin-transfer, leading to a torque directed perpendicular to the $\left(\vec{M}_1, \vec{M}_2\right)$ plane. Its action is equivalent to applying an external magnetic field oriented along the $\vec{M}_1$ direction. The physical phenomena behind the effect are beyond the scope of this book; we will simply mention that

$$\left(\frac{d\vec{m}_2}{dt}\right)_{\text{Out-of-plane}} \propto -\left(\vec{m}_2 \times \vec{m}_1\right). \tag{1.17}$$

This out-of-plane torque is often considered through its ratio to the in-plane torque. It is usually negligible in metallic spin valves but its amplitude can reach about 30% of the in-plane STT in tunnel junctions. It is often neglected in first approximation but nevertheless can be responsible for undesirable behavior in the writing operation of STT-MRAM such as back-switching phenomena (25).

1.3.2 Spin-Transfer-Induced Magnetization Dynamics

After having introduced the spin-dependent transport mechanisms at the origin of spin-transfer torques, our aim is now to address the influence of these torques on the magnetization dynamics of F2. The dynamics of a magnetization in response to external torques in a solid is classically described by the Landau-Lifshitz-Gilbert (LLG) equation. Because of the STT, two terms associated to the in-plane and out-of-plane components of spin-transfer torques are added to this equation. The LLG equation and the detailed description of magnetization dynamics are the topic of another chapter. Here, we describe only some phenomenological aspects.

WD EX1057
Western Digital v IP Bridge
Page 23

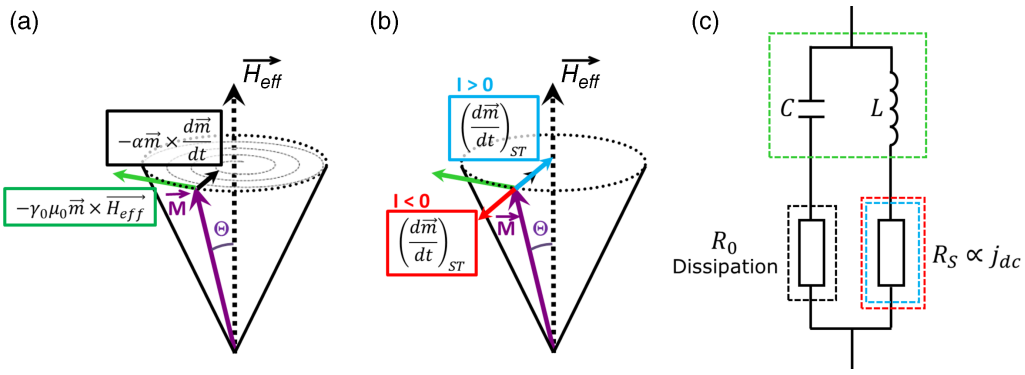


Figure 1.10 (a) Relaxation of magnetization around the effective field without spin-transfer torque. (b) Additional torque for positive or negative current. (c) Corresponding equivalent (RLC) circuit.

We return to the simple trilayer of Fig. 1.8 and consider the ferromagnetic layer F2, whose local magnetization is described by the normalized vector $\vec{m}_2$. This magnetization is aligned at equilibrium along the so-called effective field $\vec{H}_{eff}$. $\vec{H}_{eff}$ is the field resulting from the sum of all fields acting on $\vec{M}_2$, namely, the external applied magnetic field, magnetic anisotropy field, interlayer coupling field, and so on. When $\vec{M}_2$ is slightly pushed away from its stable equilibrium position, the magnetization starts precessing around the effective field $\vec{H}_{eff}$, following the differential equation:

$$\left(\frac{d\vec{m}_2}{dt}\right)_{precession} = -\gamma_0\vec{m}_2\times\mu_0\vec{H}_{eff}, \tag{1.18}$$

where γ_0 is the gyromagnetic ratio and μ_0 is the vacuum permeability. Like any other physical system with a stable equilibrium position, the magnetization will relax to this position, with a characteristic damping coefficient α, the Gilbert damping (which can range between $\sim 5\times10^{-3}$ and 0.1 for standard ferromagnets, depending on the amplitude of their spin–orbit interactions). The damping force is once again associated with a torque, written

$$\left(\frac{d\vec{m}_2}{dt}\right)_{damping} = -\alpha\vec{m}_2\times\frac{d\vec{m}_2}{dt}, \tag{1.19}$$

which tends to bring back $\vec{m}_2$ toward $\vec{H}_{eff}$ (Fig. 1.10).

1.3.2.1 A Simple Analogy A simple analogy to understand the influence of STT on magnetization dynamics is the classical RLC resonant circuit. If the circuit is initially excited, for instance by introducing a charge on the capacity, the current in the circuit exhibits damped oscillations and gradually relaxes toward the zero equilibrium value. Because of dissipation, as long as no additional energy is supplied to the

WD EX1057
Western Digital v IP Bridge
Page 24

system, it has no other choice but to relax to the closest equilibrium position. However, during this relaxation process, one can act on the system to modify the relaxation rate, by reducing or increasing the damping of the system. In the RLC analogy, this would correspond to adding a supplementary positive or negative resistance in the circuit. When dealing with magnetization, a means to do this is to use spin-transfer torque. Indeed, depending on the sign of the current, the resulting STT torque can be oriented either in the same direction or in the opposite direction to the damping torque.

This simplified description allows one to understand easily the nature of the main contribution of spin-transfer force (in-plane torque), which can be described through a non-conservative force acting in the same direction as the natural damping, that is, perpendicular to the magnetization trajectory. Depending on the relative orientation of $\vec{M}_1$ and $\vec{M}_2$, as well as the sign of the injected current, the spin-transfer torque can increase or decrease the effective damping, that is, behave as an additional damping or as an antidamping.

To continue the analogy with classical systems, like the RLC circuit, one can bring it into a regime where the effective damping around equilibrium crosses zero and becomes negative ($R_S < -R_0$). In this case, the corresponding equilibrium position is no longer stable, and any deviation from equilibrium is amplified so that the oscillations diverge. For the case of unstable local magnetization, thermal excitations are sufficient to induce a small deviation from equilibrium, further amplified by spin-transfer torque. Depending on the system configuration, the magnetic system can be designed so that the oscillation divergence drives the magnetization toward another stable minimum of energy or so that steady state excitations of the magnetization can be sustained. The first behavior is the one used to write in STT-MRAM, whereas the second behavior can yield to new types of frequency-tunable RF oscillators.

1.3.2.2 Toward MRAM Based on Spin-Transfer Torque A STT-MRAM cell is effectively composed of a MTJ consisting of a pinned ferromagnetic reference layer and a ferromagnetic storage layer separated by a tunnel barrier. This system is very similar to the one described in Fig. 1.8 where the storage layer is F2 and the reference layer is F1. The MTJ is designed in such a way that the magnetization of the storage layer has two natural equilibrium positions parallel or antiparallel to the pinned layer magnetization. Using the spin-transfer torque to destabilize either one of these positions, simply by choosing the sign of the current, it is possible to induce a reversal of the magnetization, and consequently switch the value of the memory cell. When electrons flow from the pinned layer to the storage layer, parallel alignment is favored. When electrons flow from the storage layer to the reference layer, antiparallel alignment is favored. To achieve the storage layer magnetization switching, the current density must exceed a certain threshold, which corresponds to the point where the Gilbert damping becomes balanced by the STT antidamping. This current density threshold J_c can be calculated by finding the conditions for which the net effective damping is zero. The expression of the current density for switching depends in particular on whether the layers are magnetized in-plane or out-of-plane. This will be explained in more details in

WD EX1057
Western Digital v IP Bridge
Page 25

Chapter 5. The LLG equation with Slonczewski in-plane torque yields the critical current density for switching:

$$J_c = \frac{2\alpha e \mu_0 M_S t}{\hbar P_{spin}} H_{eff}, \tag{1.20}$$

and the corresponding critical current:

$$I_c = \frac{2\alpha e \mu_0 M_S V}{\hbar P_{spin}} H_{eff}, \tag{1.21}$$

where M_s is the saturation magnetization, α is the Gilbert damping, t is the layer thickness, V is the volume, P_{spin} is the amplitude of the spin polarization, and H_{eff} is the effective field as previously defined. The other quantities are physical constants: e the electron charge, μ_0 the vacuum permeability, and $\hbar$ the reduced Planck constant. The predicted critical current densities are relatively large, in the range of a few 10^{11} A/m^2 in metallic spin valves and in the range of 1 to a few 10^{10} A/m^2 in MTJs. The higher STT efficiency in MTJs is associated with two phenomena: a higher spin polarization in particular in MgO-based MTJs, and the fact that in a MTJ, electrons impinging on the storage layer have mainly a perpendicular component of momentum. The electrons that tunnel the most easily through the barrier are those propagating perpendicular to the layers (with out-of-plane momentum $\vec{k} \approx \vec{k}_\perp,\ k_\parallel \approx 0$), whereas in metallic pillars, the electron momentum is broadly dispersed in all angular direction.

Very importantly for STT-MRAM considerations, STT switching is determined by a current density threshold. This means that the current required to write in STT-MRAM scales proportionally to the area of the device. For very small dimensions, for which thermal stability becomes a problem, a reduction in size must be compensated by an increase in the anisotropy field (and in H_{eff}) to maintain a desired thermal stability factor, that is, a given memory retention (see Chapter 5). As a consequence, the thermal stability limits the decrease of the critical current with the device dimensions. However, this minimum current value is in the range of 13 μA with known materials, which allows downsize scalability of STT-MRAM to sub-20 nm nodes.

The expression of critical current density provides paths to reduce the power consumption for spin-transfer-induced switching. In particular the Gilbert damping factor α plays a quite important role and must be minimized, and the spin polarization must be maximized. The other parameters (t, M_s, H_{eff}) also influence the thermal stability of the magnetization, so a trade-off must often be found between minimizing the write current density and maintaining sufficient thermal stability to achieve the specified memory retention. The goal of minimizing the critical current for writing has stimulated a strong research effort in the last few years, notably among two families of materials: magnetic oxides (26) and Heusler alloys (27).

1.3.3 Main Events Concerning Spin-Transfer Advances

A complete review of all the theoretical and experimental advances made in the last decade on spin-transfer is beyond the scope of this chapter (see Ref. 28 and references therein). However, it is worth mentioning a few key dates in spin-transfer torque research and development. The first experimental results to validate the

WD EX1057
Western Digital v IP Bridge
Page 26

theoretical prediction of spin-transfer torque made by Slonczewski and Berger were obtained by Tsoi et al, using a point-contact geometry for injection of a large current density into a magnetic layer (29). The experimental demonstration of the use of spin-transfer torque to reverse the magnetization of metallic spin valves without any applied field by Katine et al. in 2000 (30) showed that STT could be used as a new write scheme in MRAM instead of field-induced magnetization switching, offering a much better downsize scalability. The first demonstration of STT switching in MTJs was made in 2004 (31) once the quality of the MTJ growth became good enough to withstand the large current density required for STT switching. The first functional demonstrator of an STT-MRAM chip was developed by Sony Corp, which presented the first 4 kbit STT-RAM demonstrator in 2004 (32). A lot of further progress has been made since then on both the fundamental understanding of the STT effects as well as on the technological side (see Chapter 6). The first STT-MRAM products were announced by Everspin at the end of 2012 (see Chapter 5) and all the major microelectronic companies now have large research and development efforts, in particular aiming at DRAM replacement by STT-MRAM beyond the 20 nm technological node.

REFERENCES

1. M. Baibich, J. M. Broto, A. Fert, F. Nguyen Van Dau, F. Petroff, P. Etienne, G. Creuzet, A. Friederch, and J. Chazelas, "Giant magnetoresistance of (001)Fe/(001)Cr magnetic superlattices," *Phys. Rev. Lett.* **61**, pp. 2472–2475 (1988); doi: 10.1103/PhysRevLett.61.2472.
2. J. S. Moodera, L. R. Kinder, T. M. Wong, and R. Meservey, "Large magnetoresistance at room temperature in ferromagnetic thin film tunnel junctions," *Phys. Rev. Lett.* **74**, pp. 3273–3276 (1995); doi: 10.1103/PhysRevLett.74.3273.
3. T. Miyazaki and N. Tezuka, "Giant magnetic tunneling effect in Fe/Al_2O_3/Fe junction," *J. Magn. Magn. Mater.* **139**, pp. L231–L234 (1995); doi: 10.1016/0304-8853(95)90001-2.
4. S. Tehrani, J. M. Slaughter, E. Chen, M. Durlam, J. Shi, and M. DeHerrera, "Progress and outlook for MRAM technology," *IEEE Trans. Magn.* **35**, pp. 2814–2819 (1999); doi: 10.1109/20.800991.
5. I. A. Campbell and A. Fert, "Transport properties of ferromagnets," in *Ferromagnetic Materials*, Vol. 3, ed. E. P. Wohlfarth, North-Holland Publishing, Amsterdam, 1987, pp. 747–804.
6. A. Barthélémy, A. Fert, and F. Petroff, "Giant magnetoresistance of magnetic multilayers," in *Handbook of Magnetic Materials*, Vol. 12, ed. K. H. J. Buschow, North-Holland, Amsterdam, 1999, pp. 1–96.
7. T. Valet and A. Fert, "Theory of the perpendicular magnetoresistance in magnetic multilayers," *Phys. Rev. B* **48**, pp. 7099–7113 (1993); doi: 10.1103/PhysRevB.48.7099.
8. S. S. P. Parkin, N. More, and K. P. Roche, "Oscillations in exchange coupling and magnetoresistance in metallic superlattice structures: Co/Ru, Co/Cr, and Fe/Cr," *Phys. Rev. Lett.* **64**, pp. 2304–2307 (1990); doi: 10.1103/PhysRevLett.64.2304.
9. B. Dieny, V. S. Speriosu, S. S. P. Parkin, B. A. Gurney, D. R. Wilhoit, and D. Mauri, "Giant magnetoresistance in soft ferromagnetic multilayers," *Phys. Rev. B* **43**, pp. 1297–1300 (1991); doi: 10.1103/PhysRevB.43.1297.
10. B. Dieny, "Spin valves," in *Magnetoelectronics*, ed. M. Johnson, Elsevier, Amsterdam, 2004, pp. 67–150.
11. M. Jullière, "Tunneling between ferromagnetic films," *Phys. Lett.* **54A**, pp. 225–226 (1975); doi: 10.1016/0375-9601(75)90174-7.
12. S. Yuasa, T. Nagahama, A. Fukushima, Y. Suzuki, and K. Ando, "Giant room-temperature magnetoresistance in single-crystal Fe/MgO/Fe magnetic tunnel junctions," *Nat. Mater.* **3**, pp. 868–871 (2004); doi: 10.1038/nmat1257.

WD EX1057
Western Digital v IP Bridge
Page 27

13. S. S. P. Parkin, C. Kaiser, A. Panchula, P. M. Rice, B. Hughes, M. Samant, and S-H. Yang, "Giant tunnelling magnetoresistance at room temperature with MgO(100) tunnel barriers," *Nat. Mater.* **3**, pp. 862–867 (2004); doi: 10.1038/nmat1256.
14. R. Meservey and P. M. Tedrow, "Spin-polarized electron tunneling," *Phys. Rep.* **238**, pp. 173–243 (1994); doi: 10.1016/0370-1573(94)90105-8.
15. J. M. De Teresa, A. Barthélémy, A. Fert, J. P. Contour, F. Montaigne, and P. Seneor, "Role of metal-oxide interface in determining the spin polarization of magnetic tunnel junctions," *Science* **286**, pp. 507–509 (1999); doi: 10.1126/science.286.5439.507.
16. J. Slonczewski, "Conductance and exchange coupling of two ferromagnets separated by a tunneling barrier," *Phys. Rev. B* **39**, pp. 6995–7002 (1989); doi: 10.1103/PhysRevB.39.6995.
17. S. Yuasa and D. D. Djayaprawira, "Giant tunnel magnetoresistance in magnetic tunnel junctions with a crystalline MgO(001) barrier," *J. Phys. D Appl. Phys.* **40**, pp. R337–R354 (2007); doi: 10.1088/0022-3727/40/21/R01.
18. W. H. Butler, X.-G. Zhang, T. C. Schulthess, and J. M. MacLaren, "Spin-dependent tunneling conductance of Fe/MgO/Fe sandwiches," *Phys. Rev. B* **63** 054416 (2001); doi: 10.1103/PhysRevB.63.054416.
19. J. Mathon and A. Umerski, "Theory of tunneling magnetoresistance of an epitaxial Fe/MgO/Fe (001) junction," *Phys. Rev. B* **63**, 220403 (2001); doi: 10.1103/PhysRevB.63.220403.
20. J. P. Velev, K. D. Belashchenko, D. A. Stewart, M. van Schilfgaarde, S. S. Jaswal, and E.Y. Tsymbal, "Negative spin polarization and large tunneling magnetoresistance in epitaxial Co/SrTiO3/Co magnetic tunnel junctions," *Phys. Rev. Lett.* **95**, 216601 (2005); doi: 10.1103/PhysRevLett.95.216601.
21. S. Ikeda, J. Hayakawa, Y. Ashizawa, Y. M. Lee, K. Miura, H. Hasegawa, M. Tsunoda, F. Matsukura, and H. Ohno, "Tunnel magnetoresistance of 604% at 300 K by suppression of Ta diffusion in CoFeB/MgO/CoFeB pseudo-spin-valves annealed at high temperature," *Appl. Phys. Lett.* **93**, 082508 (2008); doi: 10.1063/1.2976435.
22. J. C. Slonczewski, "Current-driven excitation of magnetic multilayers," *J. Magn. Magn. Mater.* **159**, pp. L1–L7 (1996); doi: 10.1016/0304-8853(96)00062-5.
23. L. Berger, "Emission of spin waves by a magnetic multilayer traversed by a current," *Phys. Rev. B* **54**, pp. 9353–9358 (1996); doi: 10.1103/PhysRevB.54.9353.
24. M. D. Stiles and J. Miltat, "Spin-transfer torque and dynamics," in *Spin Dynamics in Confined Magnetic Structures III*, Topics in Applied Physics, Vol. 101, eds B. Hillebrands and A. Thiaville, Springer, pp. 225–308 (2006); doi: 10.1007/10938171_7.
25. S. C. Oh, S. Y. Park, A. Manchon, M. Chshiev, J. H. Han, H. W. Lee, J. E. Lee, K. T. Nam, Y. Jo, Y. C. Kong, B. Dieny, and K. J. Lee, "Bias-voltage dependence of perpendicular spin-transfer torque in asymmetric MgO-based magnetic tunnel junctions," *Nat. Phys.* **5**, pp. 898–902 (2009); doi: 10.1038/nphys1427.
26. M. Bibes and A. Barthélémy, "Oxide spintronics," *IEEE Trans. Electron Dev.* **54**, pp. 1003–1023 (2007); doi: 10.1109/TED.2007.894366.
27. T. Graf, C. Felser, and S. S. P. Parkin, "Simple rules for the understanding of Heusler compounds," *Prog. Solid State Chem.* **39**, pp. 1–50 (2011); doi: 10.1016/j.progsolidstchem.2011.02.001.
28. D. C. Ralph and M. D. Stiles, "Spin-transfer torques," *J. Magn. Magn. Mater.* **320**, pp. 1190–1216 (2008); doi: 10.1016/j.jmmm.2007.12.019.
29. M. Tsoi, A. G. M. Jansen, J. Bass, W. C. Chiang, M. Seck, V. Tsoi, and P. Wyder, "Excitation of a magnetic multilayer by an electric current," *Phys. Rev. Lett.* **80**, pp. 4281–4284 (1998); doi: 10.1103/PhysRevLett.80.4281.
30. J. A. Katine, F. J. Albert, R. A. Buhrman, E. B. Myers, and D.C. Ralph, "Current-driven magnetization reversal and spin-wave excitations in Co/Cu/Co pillars," *Phys. Rev. Lett.* **84**, pp. 3149 (2000); doi: 10.1103/PhysRevLett.84.3149.
31. Y. Huai, F. Albert, P. Nguyen, M. Pakala, and T. Valet, "Observation of spin-transfer switching in deep submicron-sized and low-resistance magnetic tunnel junctions," *Appl. Phys. Lett.* **84**, pp. 3118–3120 (2004); doi: 10.1063/1.1707228.
32. M. Hosomi, H. Yamagishi, T. Yamamoto, K. Bessho, Y. Higo, K. Yamane, H. Yamada, M. Shoji, H. Hachino, C. Fukumoto, H. Nagao, and H. Kano,"A novel nonvolatile memory with spin-torque transfer magnetization switching: Spin-RAM," IEEE International Electron Devices Meeting, IEDM Technical Digest, December 5–7, 2005, Washington, DC, pp. 459–462; doi: 10.1109/IEDM.2005.1609379.

WD EX1057
Western Digital v IP Bridge
Page 28

CHAPTER 2

MAGNETIC PROPERTIES OF MATERIALS FOR MRAM

Shinji Yuasa
National Institute of Advanced Industrial Science and Technology (AIST), Tsukuba, Japan

2.1 MAGNETIC TUNNEL JUNCTIONS FOR MRAM

A magnetic tunnel junction (MTJ) consists of an ultrathin insulating layer (tunnel barrier) sandwiched between two ferromagnetic (FM) metal layers (electrodes). A memory cell for magnetic random-access memory (MRAM) consists of an MTJ and a complementary metal–oxide semiconductor (CMOS) pass transistor, as shown in Fig. 2.1. The practical layer stacking structure of MTJ for MRAM and magnetic sensor applications is shown in Fig. 2.2. In the practical MTJ, the magnetization in one of the ferromagnetic electrodes can be reversed by an external magnetic field or a relatively large current passed through the MTJ. This layer is called "free layer" or "storage layer." The free layer should have a "uniaxial magnetic anisotropy" such as a shape magnetic anisotropy or magnetocrystalline anisotropy, which tends to direct the magnetization along a certain axis called the easy axis. Thanks to this uniaxial magnetic anisotropy, the free layer can store one bit of information in the form of the magnetization direction. The orientation of the magnetization of the other ferromagnetic electrode is fixed. This layer, called "reference layer" or "pinned layer," acts as a reference for readout of the stored information. In most common embodiments, the reference layer is composed of a FM/NM/FM trilayer, where NM is a nonmagnetic spacer. The two FM layers have antiparallel magnetization alignment, which is termed a synthetic antiferromagnetic (SAF) structure (see Fig. 2.2). The purpose of this structure is to increase the pinning of the reference layer magnetization and reduce the stray field that this SAF is creating on the storage layer. Furthermore, the magnetization direction of the top FM layer in the SAF structure is pinned by exchange bias from antiferromagnetic (AF) coupling to the bottom layer. These structures and their effects on magnetic properties are explained in detail in Section 2.2 of this chapter.

The magnetotransport response of the MTJ with practical stacking structure is schematically illustrated in Fig. 2.3. Whereas the magnetization of reference layer is

Introduction to Magnetic Random-Access Memory, First Edition. Edited by Bernard Dieny, Ronald B. Goldfarb, and Kyung-Jin Lee.
© 2017 The Institute of Electrical and Electronics Engineers, Inc. Published 2017 by John Wiley & Sons, Inc.

WD EX1057
Western Digital v IP Bridge
Page 29

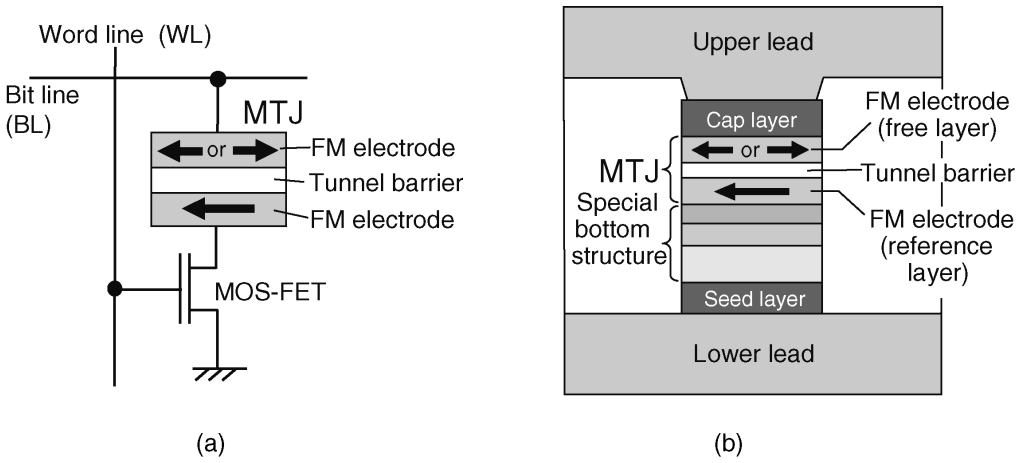


Figure 2.1 (a) Typical circuit diagram of magnetic random-access memory (MRAM). (b) Typical cross-sectional structure of magnetic tunnel junction (MTJ) with spin-valve structure.

fixed in one direction, the magnetization of the free layer can be reversed by an external magnetic field or a sufficiently large current passed through the MTJ (if spin transfer torque is used, see Chapter 1). When the free layer has a uniaxial magnetic anisotropy, the magnetization reversal process is characterized by a hysteresis loop, as shown in Fig. 2.3, which provides a nonvolatile memory function. Thus, bistable states (parallel and antiparallel magnetic alignments) appear around zero field or zero current. By applying a bipolar field or bipolar current, logic "0" or "1" can be written in the MTJ in the form of the relative orientation of the storage layer and reference layer magnetizations. The resistance of MTJ cell depends on this relative magnetization alignment (parallel or antiparallel) as a result of the tunnel magnetoresistance (TMR) effect (see Chapter 1). Thus, we can read out the bit information by passing a unipolar sense current through MTJ and measuring the MTJ resistance value. Clearly, MTJ is resistive memory, as are phase-change RAM and resistive RAM (oxide RAM, redox RAM, or conductive bridge RAM).

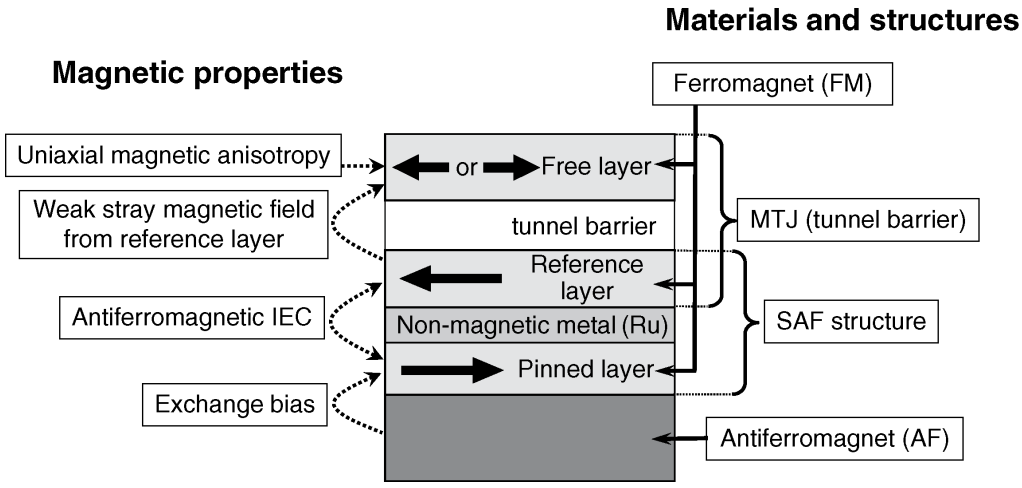


Figure 2.2 Typical stacking structure of MTJ for in-plane magnetized MRAM.

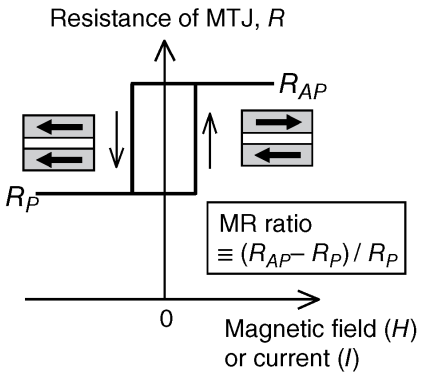


Figure 2.3 Typical magnetoresistance curve of spin-valve-type MTJ and definition of magnetoresistance (MR) ratio.

In Section 2.2, we explain basic concepts regarding magnetic materials and properties for practical MTJs, including ferromagnets, antiferromagnets, magnetic anisotropy, exchange bias, interlayer exchange coupling (IEC), and SAF structure. In Section 2.3, we explain magnetotransport properties of giant magnetoresistive device, MTJ with either amorphous aluminum oxide (AlO) or crystalline magnesium oxide (MgO) tunnel barrier.

2.2 MAGNETIC MATERIALS AND MAGNETIC PROPERTIES

2.2.1 Ferromagnet and Antiferromagnet

A ferromagnet is a material with a spontaneous magnetization (a magnetization in the absence of external magnetic field) M_s. Typical examples of ferromagnetic materials are Fe, Co, Ni (3d transition metals), Gd and Dy (rare-earth metals), and alloys mainly consisting of these ferromagnetic elements. In a ferromagnetic material, each atom of the magnetic element possesses a *localized* magnetic moment composed mainly of d or f electrons. Strictly speaking, d electrons in transition metals and alloys have itinerant nature and, therefore, are not localized exactly in an atom. However, we often use the term "localized magnetic moment" for simplicity. In ferromagnetic materials, the localized moments of the atoms tend to align parallel to each other due to a quantum mechanical ferromagnetic exchange interaction and as a result form a *net* magnetization M (magnetic moment per unit volume), as shown in Fig. 2.4a.

In an antiferromagnet, on the other hand, localized magnetic moments of neighboring atoms tend to align antiparallel because of an antiferromagnetic exchange interaction, as shown in Fig. 2.4b. An antiferromagnetic material has zero *net* magnetization.

The spontaneous magnetization in a ferromagnetic material decreases with temperature as a result of thermal activation that yields a gradual misalignment of the atomic moments. It vanishes as a result of a second-order transition from a ferromagnetic to a paramagnetic state, as shown in Fig. 2.5. The transition temperature is called the Curie temperature T_C. For a material to have stable ferromagnetic properties at room temperature (RT), its Curie temperature should be much higher than RT. For practical applications such as MRAM and magnetic sensors, stable

WD EX1057
Western Digital v IP Bridge
Page 31

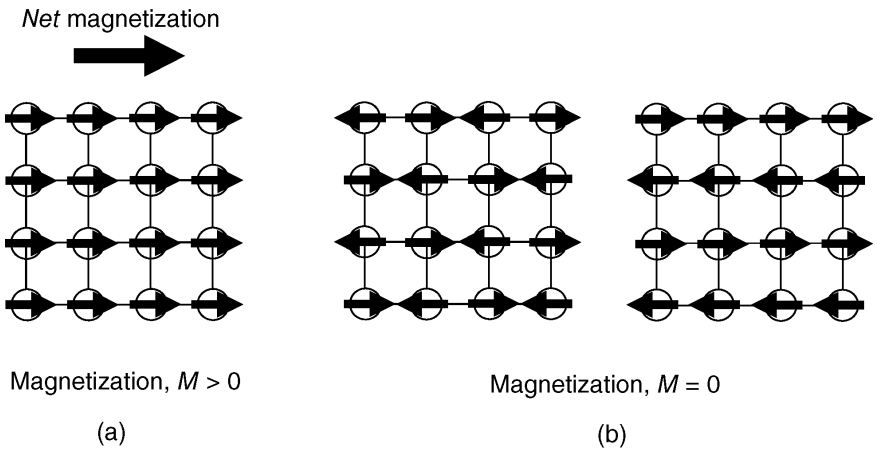


Figure 2.4 Magnetic structure of (a) ferromagnet and (b) antiferromagnet. Small arrows denote localized magnetic moments of magnetic atoms.

magnetic properties should be ensured usually for the temperature range from 0 to 80°C; this requires T_C significantly above about 300°C. Examples of Curie temperatures are 1404 K for cobalt, 1043 K for iron, and 631 K for nickel. This means that the exchange interactions are stronger in cobalt than they are in iron or nickel.

A typical magnetization process for a ferromagnet is illustrated in Fig. 2.6. Above a saturation magnetic field H_s, all the localized magnetic moments are aligned along the field direction and form a single magnetic domain (states (i) and (iii) in Fig. 2.6). The saturation magnetization is nearly equal to the spontaneous magnetization (M_s). Thus, M_s can represent both spontaneous magnetization and saturation magnetization. Below H_s, the magnetization $|M|$ can take any value between 0 and M_s because a multidomain state (state (ii) in Fig. 2.6) is formed to reduce the magnetostatic energy due to the demagnetizing field (see Section 2.2). The magnetization process in a ferromagnet is generally accompanied with a hysteresis loop. The field value for $M = 0$ is called the coercive force or the coercive field H_c. The magnetization value at zero fields is called the "remanent magnetization" M_r. When the hysteresis

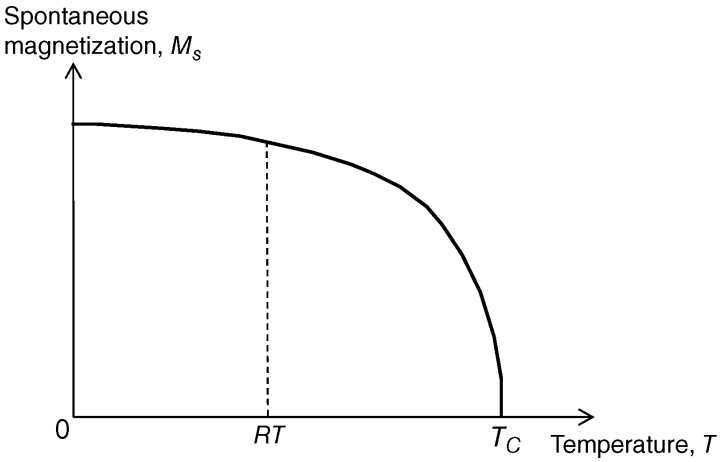


Figure 2.5 Temperature dependence of spontaneous magnetization in ferromagnet.

WD EX1057
Western Digital v IP Bridge
Page 32

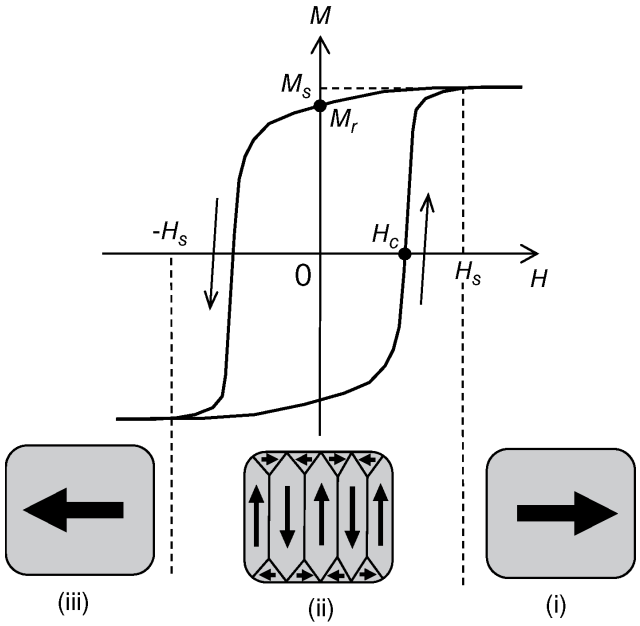


Figure 2.6 Typical magnetization process of a ferromagnet. M_s, H_s, H_c, and M_r respectively denote spontaneous (or saturation) magnetization, saturation field, coercive force, and remanent magnetization.

loop has a square shape, M_r is almost equal to M_s, and the single domain state obtained at saturation is retained even at zero field. Such a square hysteresis loop is ideal for the free layer of an MTJ in MRAM applications.

2.2.2 Demagnetizing Field and Shape Anisotropy

When the magnetization in a bulk or thin film ferromagnet is aligned parallel to an external magnetic field (H_{ext}), fictitious but mathematically described positive and negative magnetic poles are created on two sides of the ferromagnet, as shown in Fig. 2.7. These magnetic poles generate a demagnetizing field H_d, whose direction is opposite to M and H_{ext}. The effective magnetic field (H_{eff}) acting inside the ferromagnet is therefore expressed as $H_{eff} = H_{ext} - H_d$.

The following discussion is rigorously correct only for spheres and ellipsoids. Here, we approximate a rectangular thin film as an ellipsoid with a very small z-axis. A complete discussion of demagnetizing fields may be found in the work of Chen et al. (1). When the magnetization is aligned along x-axis (Fig. 2.8a), the demagnetizing field $H_d = -N_x M$. Here, N_x is the demagnetizing factor for the x-axis. For

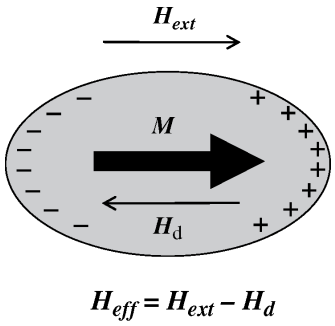


Figure 2.7 Demagnetizing field in a ferromagnet. Symbols + and – denote positive and negative magnetic charges.

WD EX1057
Western Digital v IP Bridge
Page 33

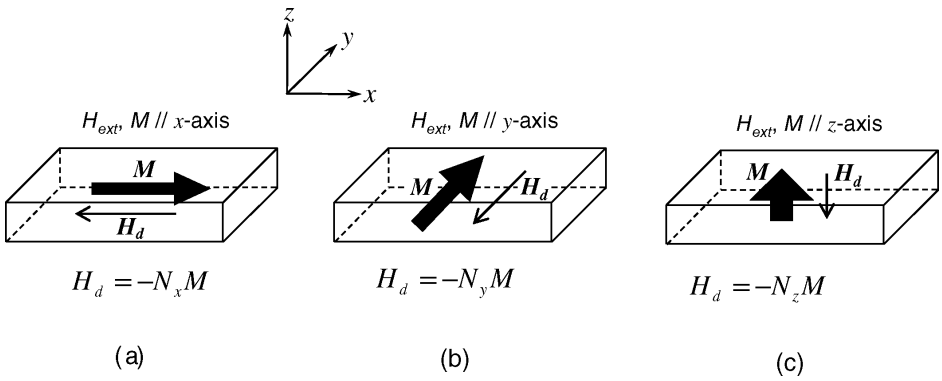


Figure 2.8 Demagnetizing field H_d for magnetization directed along (a) x-axis, (b) y-axis, and (c) z-axis.

M parallel to the y-axis (Fig. 2.8b) and M parallel to the z-axis (Fig. 2.8c), $H_d = -N_y M$ and $H_d = -N_z M$, respectively. Here, $0 < N_\alpha < 1$ ($\alpha = x, y, z$) and $N_x + N_y + N_z = 1$ in the ellipsoidal approximation. If the shape of ferromagnet is a sphere, $N_x = N_y = N_z = 1/3$. If the ferromagnet is a thin film in x–y plane, whose lateral size is much larger than the film thickness, $N_x \approx N_y \approx 0$ and $N_z \approx 1$.

Figure 2.9 shows a free layer shape in MTJ cell for MRAM. The free layer consists of a thin film with a typical thickness of a few nanometers. The free layer is usually fabricated into an ellipse or circular shape with a typical lateral size from micrometer down to a few tens of nanometers. In Fig. 2.9a, the long axis of ellipse is along x-axis. The typical dimensions $d_x > d_y \gg d_z$ yields $0 < N_x < N_y \ll N_z < 1$. The magnetostatic energy due to the demagnetizing field, E_d, when the magnetization is pointing in the direction α ($\alpha = x, y, z$) is expressed as

$$E_{d\alpha} = -\mu_0 \cdot M_s \cdot H_{d\alpha}/2 = \mu_0 \cdot N_\alpha \cdot M_s^2/2. \tag{2.1}$$

Because the magnetostatic energy is proportional to the demagnetizing factor N_α, the energy is the lowest when M is aligned to the film plane and parallel to the long axis of the ellipse (Fig. 2.9b), and the energy is the highest when M is perpendicular to the film plane (Fig. 2.9c). If the single domain state is retained at $H_{ext} = 0$, the magnetization is aligned to the long axis of ellipse due to the lowest demagnetizing energy. This axis is called "easy axis." On the other hand, it is usually hard to direct the

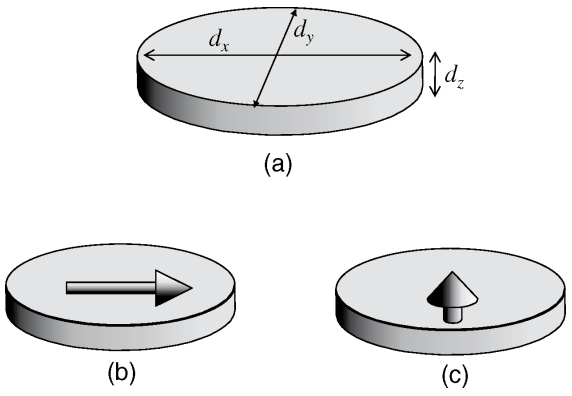


Figure 2.9 (a) Ellipse-shaped magnetic cell with the x-axis corresponding to the long axis and the z-axis corresponding to the out-of-plane axis. (b) In-plane magnetization along the long axis of ellipse (easy axis). (c) Perpendicular magnetization.

WD EX1057
Western Digital v IP Bridge
Page 34

magnetization perpendicular to the plane because of the large demagnetizing energy. The perpendicular axis in this case is called "hard axis." The shape of ferromagnet yields a magnetic anisotropy energy called "shape magnetic anisotropy" and is expressed as $E_{shape} = \mu_0(N_y - N_x)M_s^2/2$.

2.2.3 Magnetocrystalline Anisotropy, Interface Magnetic Anisotropy, and Perpendicular Magnetic Anisotropy

When the effective magnetic field $H_{eff} = H_{ext} - H_d$ is used for the magnetization curve (M–H curve), we exclude the effects of shape and discuss the intrinsic magnetic properties of a ferromagnet. Typical examples of intrinsic magnetization curves are shown in Fig. 2.10. In isotropic "soft" ferromagnetic materials, the magnetization can be easily aligned parallel to the field direction and as a result can be saturated at a small magnetic field (Fig. 2.10a). A typical example of a soft ferromagnet is fcc $Ni_{0.81}Fe_{0.19}$ (Permalloy). When the magnetic energy depends on the magnetization direction, the directional dependence is called "magnetic anisotropy." In most common cases, the magnetic anisotropy energy (E_{MA}) can be expressed as

$$E_{MA} = K_u \sin^2 \theta, \tag{2.2}$$

where θ is the angle between the magnetization direction and a certain crystalline axis called the anisotropy axis. Such magnetic anisotropy is called "uniaxial magnetic anisotropy." When $K_u > 0$, the energy is the lowest for $\theta = 0$, and the magnetization tends to be directed along this axis, which corresponds to the easy axis of magnetization. Figure 2.10b schematically shows typical magnetization curves for the "easy" and "hard" axes in a ferromagnet with uniaxial anisotropy. The hard-axis magnetization curve shows a high saturation field (H_s), whereas the easy-axis magnetization curve exhibits a square hysteresis loop with a high coercive force (H_c).

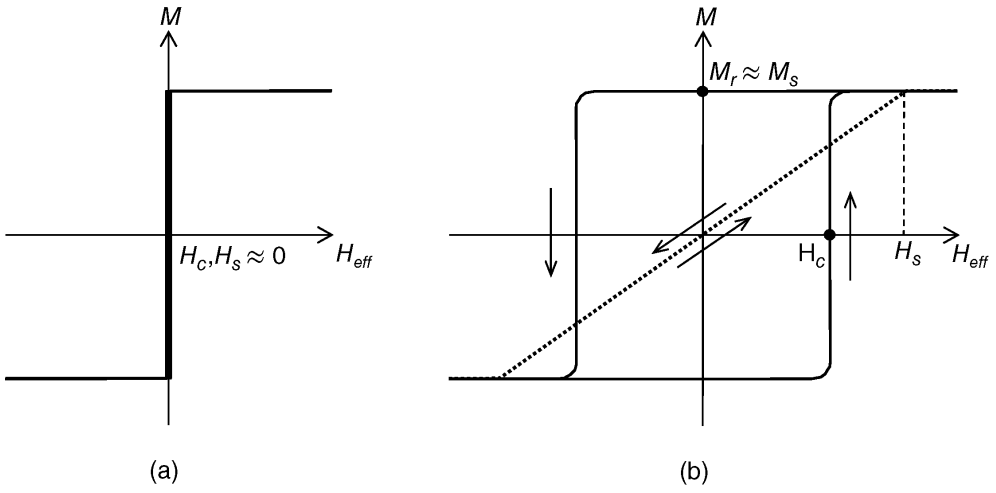


Figure 2.10 (a) Typical magnetization curve for soft, isotropic ferromagnet. (b) Typical magnetization curves for anisotropic ferromagnet. Solid and dotted lines represent magnetization curves for the easy and hard axes, respectively.

WD EX1057
Western Digital v IP Bridge
Page 35

Magnetic anisotropy has several possible origins. Shape anisotropy is important in in-plane magnetized MRAM. In contrast, in out-of-plane magnetized MRAM, the two most important sources of anisotropy are (i) magnetocrystalline anisotropy and (ii) interfacial magnetic anisotropy.

(i) *Magnetocrystalline Anisotropy:* The anisotropy of crystalline lattice is usually reflected in the magnetic anisotropy. This is called magnetocrystalline anisotropy. When the lattice has a cubic crystallographic symmetry, the magnetocrystalline anisotropy also has cubic symmetry. When the lattice has a uniaxial symmetry (e.g., body-centered tetragonal (bct), face-centered tetragonal (fct), hexagonal close-packed (hcp), $L1_0$-type ordered structure), the magnetocrystalline anisotropy is often a uniaxial magnetic anisotropy. Some $L1_0$-ordered alloys such as $Fe_{50}Pt_{50}$ are known to have very high uniaxial magnetic anisotropy with the easy axis along [0 0 1] direction. When the easy axis of uniaxial anisotropy for a thin film ferromagnet is perpendicular to the film plane, the anisotropy is called "perpendicular magnetic anisotropy" (PMA).

(ii) *Interfacial Magnetic Anisotropy:* In a magnetic multilayer structure consisting of two or more materials, in which at least one of the materials is ferromagnetic, the interfaces can exhibit a magnetic anisotropy. This is called interfacial magnetic anisotropy. For some combinations of two materials, the interface yields a perpendicular magnetic anisotropy with the easy axis perpendicular to the plane. Co/Pt and Co/Pd interfaces are known to exhibit such strong perpendicular magnetic anisotropy.

The perpendicular magnetic anisotropy due to magnetocrystalline and/or interfacial anisotropy competes with the shape magnetic anisotropy of the thin film ferromagnet. If the perpendicular magnetic anisotropy is stronger than the shape magnetic anisotropy, the film can be magnetized out-of-plane at zero magnetic fields (Fig. 2.9c and Fig. 2.10b). Typical examples of such perpendicularly magnetized thin films are $L1_0$-type ordered FePt(0 0 1) and $Fe_{50}Pd_{50}$(0 0 1), Co/Pt and Co/Pd multilayers, and Co-based hcp alloys with [0 0 0 1] axis (*c*-axis) oriented perpendicular to plane.

2.2.4 Exchange Bias

When a ferromagnetic layer (F) is adjacent to an AF layer, a "unidirectional" magnetic anisotropy can be induced at the interface because of the exchange coupling between the two layers at the interface (2), as schematically illustrated in Fig. 2.11a. This unidirectional anisotropy energy induces a shift of the center of hysteresis loop (Fig. 2.11b). This property is called "exchange bias." The basic principle of exchange bias is the following: Since the AF layer has no net magnetization, its spin lattice is not directly coupled to the applied magnetic field and tends to remain fixed in its initial structure. In contrast, the ferromagnet magnetization is coupled to the field and tends to align with the field direction. However, due to the interfacial coupling between the AF spin lattice and the F magnetization, the last interfacial AF layer in contact with the F layer tends to exert a torque on its magnetization that hinders the switching of the F magnetization.

WD EX1057
Western Digital v IP Bridge
Page 36

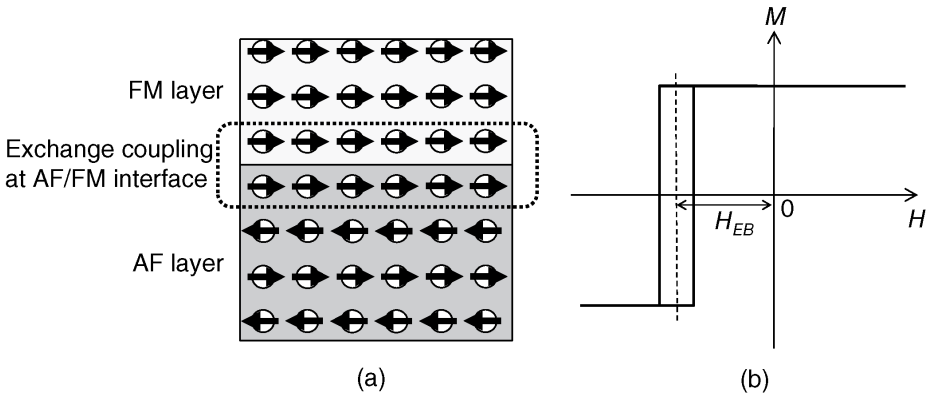


Figure 2.11 (a) Magnetic structure of a ferromagnet/antiferromagnet (FM/AF) bilayer. (b) Typical magnetization curve with exchange bias field, H_{EB}.

As a result, the magnetization of the ferromagnetic layer is pinned in a certain direction. To have a strong exchange bias, the bilayer AF/F structure must be deposited in a magnetic field and/or annealed and cooled down under a magnetic field from a temperature close to the ordering temperature of the AF material (T_N). Then, the magnetization is pinned along the cooling field direction. Typical AF materials used for exchange bias are $Ir_{20}Mn_{80}$ or $Pt_{50}Mn_{50}$ alloys.

2.2.5 Interlayer Exchange Coupling and Synthetic Antiferromagnetic Structure

When two ferromagnetic metal layers are separated by a nonmagnetic (NM) metal layer with a typical thickness of nanometer, an exchange coupling between the ferromagnetic layers is often observed. This coupling is called "interlayer exchange coupling". The coupling energy can be expressed as $E_{IEC} = -J_{IEC} \cdot \cos\theta$, where θ is the angle between the magnetizations and J_{IEC} is the exchange coupling constant. $J_{IEC} > 0$ ($J_{IEC} < 0$) corresponds to ferromagnetic (antiferromagnetic) IEC.

In the late 1980s, Grünberg et al. discovered the existence of an antiferromagnetic IEC in Fe/Cr/Fe structure and that this IEC could be used to change the relative orientation of the magnetization in the Fe layers from an antiparallel alignment at zero field to a parallel alignment under a saturating magnetic field (3). Fert (4) and Grünberg (3) then independently discovered a large change in the sheet resistance of the film associated with this change in the magnetization alignment. As explained in Chapter 1, this new phenomenon, known as the giant magnetoresistance (GMR) effect, triggered the development of this new field of electronics called spintronics. Because of the discovery of GMR, Fert and Grünberg were awarded the Nobel Prize in physics in 2007 (5). More details on GMR effect can be found in Chapter 1.

In 1990, Parkin et al. discovered an oscillatory IEC with respect to the thickness of nonmagnetic layer for various combinations of ferromagnetic and nonmagnetic materials (6). As schematically illustrated in Fig. 2.12, the IEC often shows a damped oscillatory character (7). The physical origin of IEC is interpreted as RKKY-type

WD EX1057
Western Digital v IP Bridge
Page 37

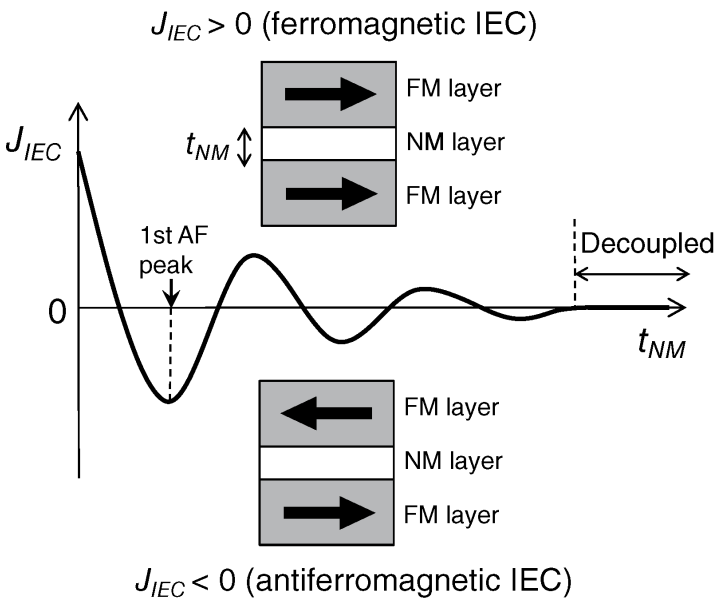


Figure 2.12 Schematic illustration of oscillatory interlayer exchange coupling (IEC).

interaction between two ferromagnetic layers or a formation of spin-polarized quantum well states (8,9). Nonmagnetic layer thickness (t_{NM}) > 5 nm is usually necessary to decouple the two FM layers. On the other hand, at the first peak of antiferromagnetic coupling (Fig. 2.12), the strongest AF coupling is attained. For example, a nonmagnetic Ru spacer layer combined with Co or Co–Fe alloys exhibit a very strong antiferromagnetic IEC at the first AF peak of about 0.4 nm. This type of strongly antiferromagnetically coupled FM/NM/FM structure is referred to as a "synthetic antiferromagnetic" structure. The SAF structure with Ru spacer is used as a building block in MTJs for device applications, as explained in the following section.

2.2.6 Spin-Valve Structure

An AF/FM/NM/FM structure, where NM denotes a "normal metal," meaning a "nonmagnetic" metal, or a tunnel barrier (Fig. 2.13a) is called "spin-valve" (10). Magnetization of the top FM layer (the "free layer") can be reversed by an external magnetic field or a current (via spin-transfer torque). Magnetization of the bottom FM layer (the "reference layer") is pinned via the exchange bias with the AF layer. This spin-valve-type magnetoresistive device can act as a magnetic sensor or as a memory cell for MRAM. The spin-valve structure shown in Fig. 2.13a, however, has a problem of unwanted stray magnetic field (H_{str}) from the reference layer. The stray field acting on the free layer induces an offset of the center of the free layer hysteresis loop, which causes various problems in magnetic sensor and memory applications. To minimize the unwanted stray field, a spin-valve device with a SAF type of reference layer (Fig. 2.13b) has been developed (11). Because the SAF trilayer forms a *flux closure* structure, most of the flux from the reference layer is absorbed in the pinned layer. This results in a suppression of the stray field and as a result induces a negligibly

WD EX1057
Western Digital v IP Bridge
Page 38

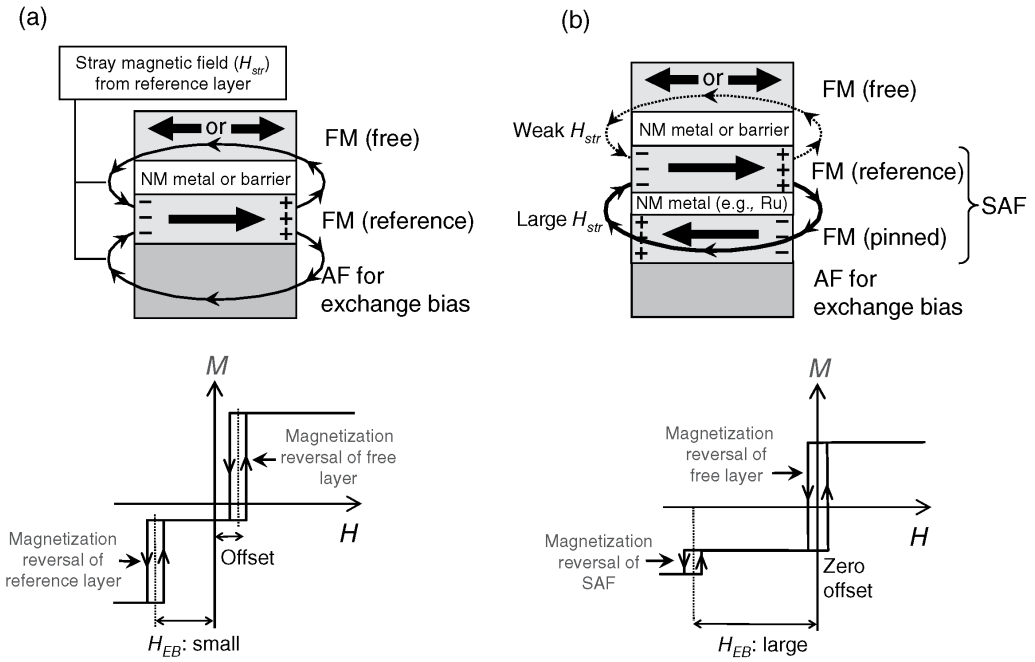


Figure 2.13 Typical spin-valve structures and magnetization curves. (a) Simple spin-valve structure with a single pinned layer. (b) Spin-valve structure with synthetic antiferromagnetic (SAF)-type pinned layer.

small offset of the free layer hysteresis loop. The SAF-type reference layer also enlarges the exchange bias field because of the smaller (or nearly zero) *net* magnetic moment in the SAF structure. The spin-valve-type MTJ with a SAF-type reference layer exhibits an ideal magnetization curve shown in Fig. 2.13b.

2.3 BASIC MATERIALS AND MAGNETOTRANSPORT PROPERTIES

2.3.1 Metallic Nonmagnetic Spacer for GMR Spin-Valve

In 1988, Baibich et al. fabricated a metallic magnetic multilayer consisting of Fe and Cr layers and obtained the GMR effect, in which electric resistance of the multilayer film changes by a few tens of percent due to the change in magnetization alignment (parallel or antiparallel), as shown in Fig. 2.14 (4). This new magnetoresistive effect was named *giant* magnetoresistance because the magnetoresistance (MR) ratio in GMR was more than 10 times than that in conventional anisotropic magnetoresistance (AMR), where the MR ratio is about 1% at ambient temperature.

The origin of the GMR effect is spin-dependent scattering of conduction electrons in the bulk of the FM layers and/or at FM/NM interfaces, as schematically illustrated in Fig. 2.15. Supposing that the conduction electrons with majority spin (spin parallel to magnetization of ferromagnetic layer) have lower probability to be scattered in the FM layers than the conduction electrons with minority spin (spin antiparallel to magnetization of ferromagnetic layer), the majority spin electrons can

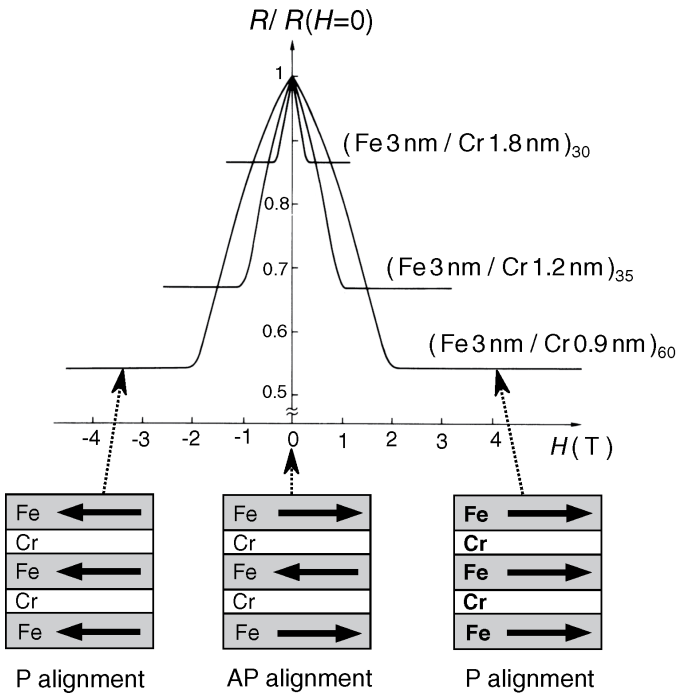


Figure 2.14 Giant magnetoresistance (GMR) effect in Fe/Cr multilayers. (Adapted from Ref. 4 with permission from American Physical Society.).

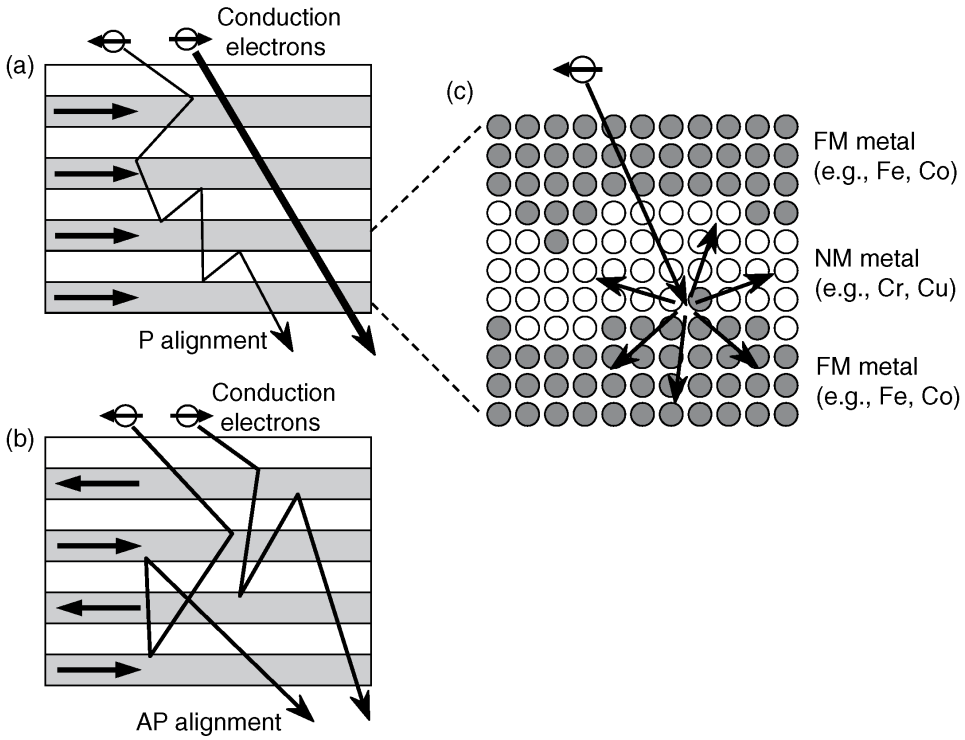


Figure 2.15 Schematic illustration of scattering of conduction electrons in magnetic multilayers. (a) Parallel (P) magnetization alignment. (b) Antiparallel (AP) magnetization alignment.

WD EX1057
Western Digital v IP Bridge
Page 40

travel for a long distance without scattering in the parallel magnetization alignment, and, as a result, the total electric resistance of the film for the parallel alignment becomes smaller than that for the antiparallel alignment.

In principle, a finite GMR effect can occur for any combinations of ferromagnetic and nonmagnetic metals and alloys. High MR ratios, however, are obtained for certain material combinations such as Fe–Cr (3,4) and Co–Cu (12). This is because the electron scatterings at Fe–Cr and Co–Cu interfaces are largely spin dependent. At Fe–Cr interfaces, for example, scattering probability for minority-spin electrons is much smaller than that for majority-spin electrons because of the good matching between the Fe minority-spin band and the Cr band at the Fermi energy. At Co–Cu interfaces, on the other hand, the scattering probability is much smaller for majority-spin electrons.

For device applications such as magnetic sensors, the spin-valve structure (Fig. 2.13) with basically zero interlayer exchange coupling (the decoupled region in Fig. 2.12) is important. Such zero IEC is easily obtained in the Co/Cu/Co system with Cu thicker than 5 nm. (The Fe/Cr/Fe system usually exhibits much stronger IEC.) The Co/Cu/Co system is therefore useful in device applications such as magnetic sensors.

The GMR effect was originally measured with a current flowing parallel to the film plane (Fig. 2.16a). This geometry is called the "current-in-plane" (CIP) geometry. It is also possible to flow the current perpendicular to the layers by fabricating the multilayer film into a nanopillar junction structure. This geometry is called "current-perpendicular-to-plane" (CPP) geometry (13,14).

2.3.2 Magnetic Tunnel Junction with Amorphous AlO Tunnel Barrier

As explained in Section 2.1, a FM/NM/FM trilayer structure with an insulating NM spacer layer (tunnel barrier) is called a magnetic tunnel junction. The resistance of an MTJ depends on the relative magnetization alignment (parallel or antiparallel) of the electrodes. The tunnel resistance R of an MTJ is usually lower when the magnetizations are parallel than it is when the magnetizations are antiparallel, as shown in Fig. 2.3. That is, $R_P < R_{AP}$. This change in resistance with the relative orientation of

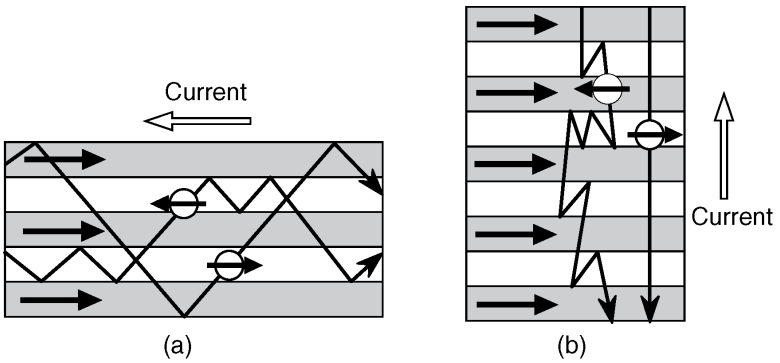


Figure 2.16 (a) Current-in-plane (CIP) GMR. (b) Current-perpendicular-to-plane (CPP) GMR.

the two magnetic layers, called the tunnel magnetoresistance effect, is one of the most important phenomena in spintronics. The size of this effect is measured by the fractional change in resistance $(R_{AP} - R_P)/R_P \times 100(\%)$, which is called the magnetoresistance ratio.

The TMR effect was first discovered in 1975 by Jullière (15), who found that a Fe/Ge-O/Co MTJ exhibited an MR ratio of 14% at 4.2 K. Although it received little attention for more than a decade because the TMR effect was not obtained at RT, it attracted renewed attention after the discovery of giant magnetoresistance in metallic magnetic multilayers in the late 1980s (3,4). Because researchers recognized that the GMR effect could be applied to magnetic sensor devices such as the read heads of hard disk drives (HDDs), extensive experimental and theoretical efforts were devoted to increasing the MR ratio at RT as well as to understanding the physics of spin-dependent transport. In 1995, Miyazaki and Tezuka (16) and Moodera et al. (17) made MTJs with amorphous aluminum oxide tunnel barriers and 3d transition metal ferromagnetic electrodes such as Fe and Co and obtained MR ratios above 10% at RT. Because these MR ratios were the highest then reported for a practical spin-valve structure, the TMR effect attracted a great deal of attention.

The origin of the TMR effect is tunneling of spin-polarized electrons. Jullière (15) proposed a simple phenomenological model (Fig. 2.17). According to this model, the MR ratio of an MTJ could be expressed in terms of the tunneling spin polarizations (TSP) P of the ferromagnetic electrodes:

$$MR = 2P_1P_2/(1 - P_1P_2), \tag{2.3}$$

where

$$P_\alpha \equiv [D_{\alpha\uparrow}(E_\mathrm{F}) - D_{\alpha\downarrow}(E_\mathrm{F})]/[D_{\alpha\uparrow}(E_F) + D_{\alpha\downarrow}(E_F)]; \quad \alpha = 1, 2. \tag{2.4}$$

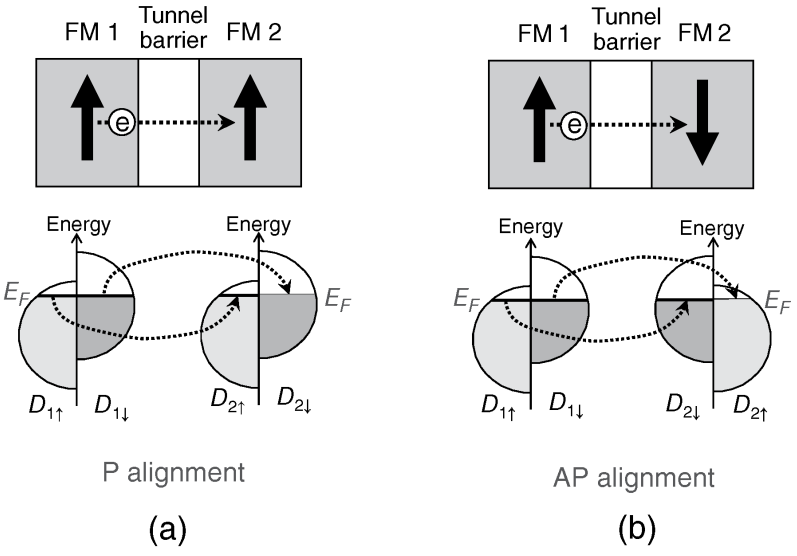


Figure 2.17 Schematic illustrations of spin-dependent tunneling in magnetic tunnel junction (MTJ). (a) Parallel (P) magnetization alignment. (b) Antiparallel (AP) magnetization alignment.

WD EX1057
Western Digital v IP Bridge
Page 42

Here P_α is the spin polarization of a ferromagnetic electrode, and $D_{\alpha\uparrow}(E_F)$ and $D_{\alpha\downarrow}(E_F)$ correspond to the densities of states (DOS) of the electrode at the Fermi energy (E_F) for the majority-spin and minority-spin bands. In Jullière's model, spin polarization is an intrinsic property of an electrode material. When an electrode material is nonmagnetic, $P = 0$. When the DOS of the electrode material is fully spin-polarized at E_F, $|P| = 1$.

Since 1995, extensive experimental effort has been made on MTJs with amorphous AlO barriers and ferromagnetic electrode materials so that conditions for fabricating the AlO barrier could be optimized. As a result, RT MR ratios have been increased to about 70%, as shown in Fig. 2.18. These MR ratios of up to 70%, however, are still lower than those needed for many applications of spintronic devices. High-density spin-transfer torque MRAM (STT-MRAM, STT-RAM, or Spin-RAM), for example, will need to have MR ratios higher than 150% at RT, and the read head in next-generation ultrahigh-density HDDs will need to have both a high MR ratio and an ultralow tunneling resistance. The MR ratios of conventional AlO-based MTJs are simply not high enough for applications to next-generation devices.

One way to obtain an MR ratio significantly higher than 70% at RT is to use special kinds of ferromagnetic materials called *half-metals* as electrodes, which have full tunneling spin polarization ($|P| = 1$) and are therefore theoretically expected to yield MTJs with huge MR ratios (up to infinity, according to Jullière's model). Some candidate half-metals are CrO_2, Heusler alloys such as Co_2MnSi, Fe_3O_4, and manganese perovskite oxides such as $La_{1-x}Sr_xMnO_3$. Very high MR ratios, above several hundred percent, have been obtained at low temperatures in $La_{1-x}Sr_xMnO_3$/$SrTiO_3$/$La_{1-x}Sr_xMnO_3$ MTJs (18) and Co_2MnSi/AlO/Co_2MnSi MTJs (19). However,

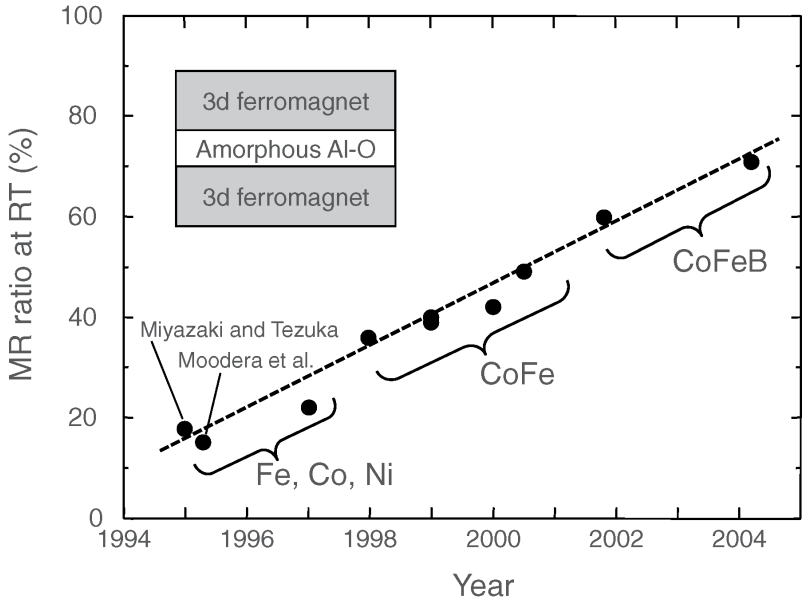


Figure 2.18 History of improvement in magnetoresistance (MR) ratio at room temperature (RT) for MTJs with amorphous AlO tunnel barriers. Early work by Miyazaki and Tezuka (16) and Moodera et al. (17) are indicated. (Reproduced from Ref. 17 with permission from American Physical Society.)

WD EX1057
Western Digital v IP Bridge
Page 43

such high MR ratios have never been obtained at RT for half-metal electrodes when combined with amorphous tunnel barriers.

Another way to obtain a very high MR ratio is to use coherent spin-dependent tunneling in an epitaxial MTJ with a crystalline tunnel barrier such as MgO(0 0 1). This is explained in the following sections.

2.3.3 Magnetic Tunnel Junction with Crystalline MgO(0 0 1) Tunnel Barrier

In 2001, theoretical calculations predicted that epitaxial MTJs with a crystalline magnesium oxide tunnel barrier would have MR ratios of over 1000% (20,21). In 2004, huge MR ratios of about 200% were obtained at RT in MTJs with a crystalline MgO(0 0 1) barrier (22–24). The huge TMR effect in MgO-based MTJs is now called the *giant TMR effect* and is one of the most important technologies for device applications of spintronics.

2.3.3.1 Epitaxial MTJ with a Single-Crystal MgO(0 0 1) Barrier Before discussing the crystalline MgO(0 0 1) barrier, we will briefly review the tunneling process through an amorphous tunnel barrier (25). Tunneling in an MTJ with an amorphous AlO barrier is schematically illustrated in Fig. 2.19a, where the top electrode layer is Fe(0 0 1), being an example of a 3d ferromagnet. Various Bloch states with different symmetries of wave functions exist in the electrode. Because the tunnel barrier is amorphous, there is no crystallographic symmetry in the tunnel barrier. Because of this nonsymmetric structure, Bloch states with various orbital symmetries can couple with evanescent states in AlO and therefore have finite tunneling probabilities. This tunneling process can be regarded as *incoherent* tunneling through an amorphous barrier. In Fe- and/or Co-based ferromagnetic metals and alloys with bcc(0 0 1) structure, Bloch states with Δ_1 symmetry (spd hybridized states) usually have a full spin polarization at E_F ($P = +1$), whereas Bloch states with Δ_5 and Δ_2 symmetry (d states) usually have a much smaller or even

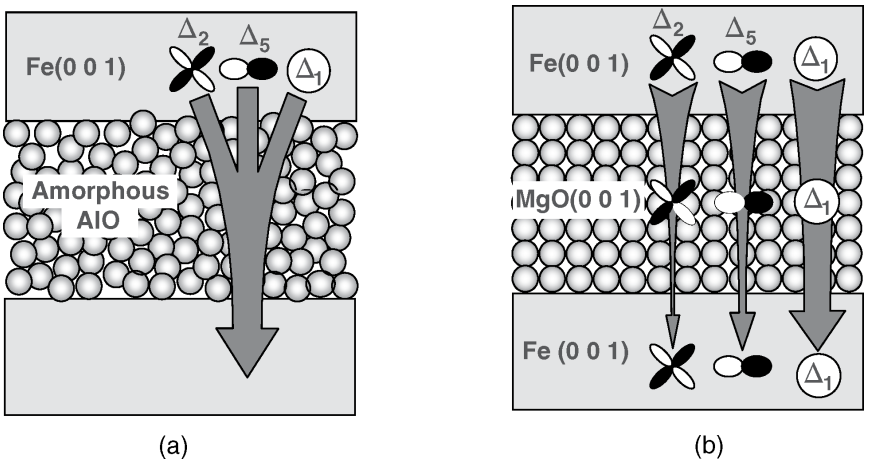


Figure 2.19 Schematic of electron tunneling through (a) an amorphous AlO barrier and (b) a crystalline MgO(0 0 1) barrier.

negative spin polarization at E_F. Because Bloch states with various spin polarizations contribute to the tunneling current, the tunneling spin polarization of the electrode is usually reduced below 0.6 for 3d ferromagnetic metals and alloys, which results in MR ratio below about 70% at RT (below about 100% at low temperature).

If only fully spin-polarized Δ_1 states coherently tunnel through a barrier, as illustrated in Fig. 2.19b, a very high spin polarization of tunneling current and thus a very high MR ratio are expected. Such ideal coherent tunneling is theoretically expected in an epitaxial Fe/MgO/Fe MTJ with a crystalline MgO(0 0 1) tunnel barrier (20,21). It should be noted that the Δ_1 Bloch states are highly spin-polarized not only in bcc Fe(0 0 1) but also in many other bcc ferromagnetic metals and alloys that are based on Fe and Co (e.g., bcc Fe–Co, bcc CoFeB, and some of the Heusler alloys). According to first-principles calculations, the TMR of a Co(0 0 1)/MgO(0 0 1)/Co(0 0 1) MTJ is even larger than that of a Fe(0 0 1)/MgO(0 0 1)/Fe(0 0 1) MTJ (26). A very large TMR should be characteristic of MTJs with 3d ferromagnetic alloy electrodes with a bcc (0 0 1) structure based on Fe and Co. Note also that very large TMR is theoretically expected not only for the MgO(0 0 1) barrier but also for other crystalline tunnel barriers such as ZnSe(0 0 1) (27) and $SrTiO_3$(0 0 1) (28). Large TMR has, however, never been obtained in MTJs with crystalline ZnSe(0 0 1) or $SrTiO_3$(0 0 1) barriers because of experimental difficulties in fabricating high-quality MTJs without pinholes in the barriers and interdiffusion at the interfaces.

Since the theoretical predictions of very large TMR effects in Fe/MgO/Fe MTJs, several experimental attempts have been made to fabricate fully epitaxial Fe(0 0 1)/MgO(0 0 1)/Fe(0 0 1) MTJs (29–31). Bowen et al. were the first to obtain a relatively high MR ratio in Fe(0 0 1)/MgO(0 0 1)/Fe(0 0 1) MTJs (30% at RT and 60% at 30 K), (30), but the RT MR ratios obtained in MgO-based MTJs did not exceed the highest of 70% obtained in AlO-based MTJs. In 2004, Yuasa et al. fabricated high-quality fully epitaxial Fe(0 0 1)/MgO(0 0 1)/Fe(0 0 1) MTJs with a single-crystal MgO (0 0 1) tunnel barrier by using molecular beam epitaxial (MBE) growth under an ultrahigh vacuum and attained RT MR ratios that were significantly higher than those of conventional AlO-based MTJs (Fig. 2.21) (23,24). A cross-sectional transmission electron microscope (TEM) image of an epitaxial MTJ is shown in Fig. 2.20 in which

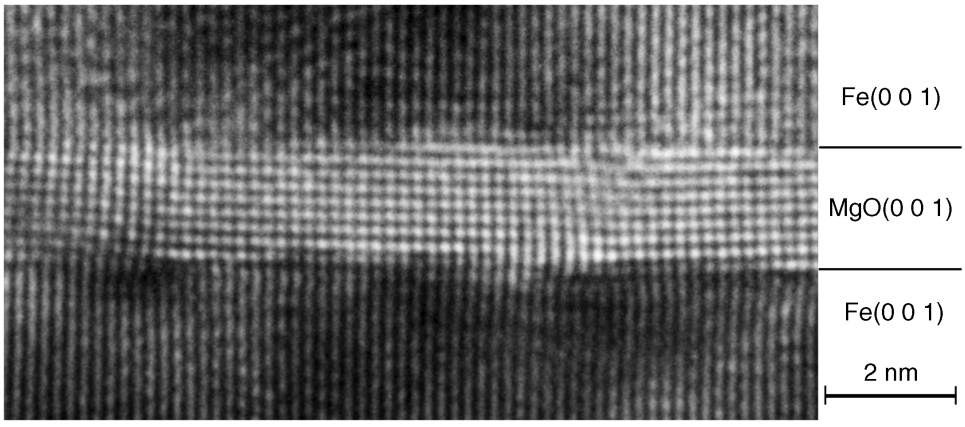


Figure 2.20 Cross-sectional transmission electron microscope (TEM) image of epitaxial Fe (0 0 1)/MgO(0 0 1) (1.8 nm)/Fe(0 0 1) MTJ. (Adapted from Ref. 24 with permission from Nature Publishing Group.)

WD EX1057
Western Digital v IP Bridge
Page 45

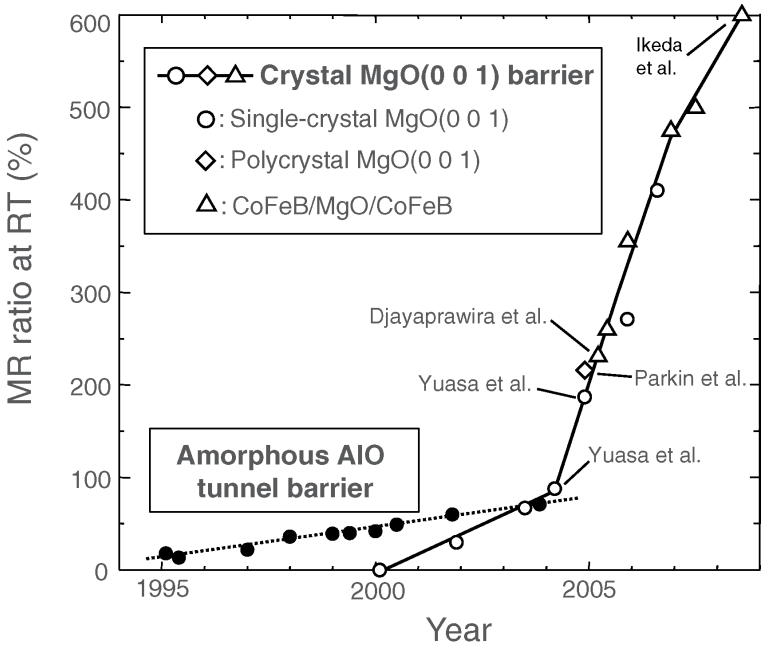


Figure 2.21 History of improvement in MR ratio at RT for MTJs with amorphous AlO barrier (solid circles) or crystalline MgO(0 0 1) barrier (open symbols). Data are shown for work by Yuasa et al. (22,23), Parkin et al. (24) Djayaprawira et al. (33), and Ikeda et al. (36).

single-crystal lattices of MgO(0 0 1) and Fe(0 0 1) are clearly evident. During the same period, Parkin et al. fabricated highly oriented polycrystalline (or textured) FeCo (0 0 1)/MgO(0 0 1)/FeCo(0 0 1) MTJs with a textured MgO(0 0 1) tunnel barrier by using sputtering deposition on an SiO_2 substrate. A tantalum nitrate seed layer was used to orient the entire MTJ stack in the (0 0 1) plane and obtained a giant MR ratio of up to 220% at RT (Fig. 2.21) (24). These were the first RT MR ratios that were higher than the highest MR ratios obtained with an AlO-based MTJ.

Fully epitaxial MTJs and textured MTJs are basically the same from a microscopic point of view if structural defects such as grain boundaries do not strongly influence the tunneling properties. It is therefore considered that the giant MR ratios in the epitaxial and textured MTJs originate from the same mechanism. Even higher MR ratios (above 400% at RT) have been attained by using FeCo and bcc Co electrodes (Fig. 2.21) (32).

2.3.3.2 CoFeB/MgO/CoFeB MTJ with a (0 0 1)-Textured MgO Barrier for Device Applications As explained above, epitaxial MTJs with a single-crystal MgO(0 0 1) barrier or textured MTJs with a polycrystalline MgO(0 0 1) barrier exhibit the giant TMR effect at RT. Although giant TMR is an attractive property for device applications such as spin-transfer torque MRAM, these MTJ structures cannot be applied to practical devices because of a problem concerning crystal growth. As explained in Section 2.1, MTJs for practical applications need to have the stacking structure shown in Fig. 2.2. Ir–Mn or Pt–Mn is used as the antiferromagnetic layer, and Co–Fe/Ru/Co–Fe trilayer is used as the SAF structure to attain an exchange bias

WD EX1057
Western Digital v IP Bridge
Page 46

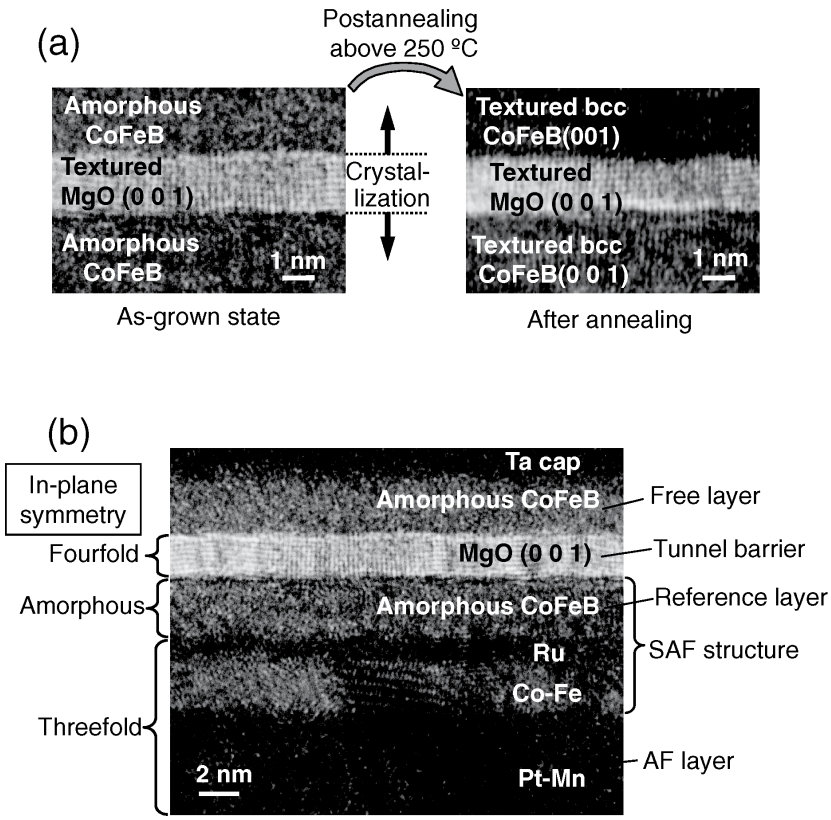


Figure 2.22 Cross-sectional TEM image of CoFeB/MgO/CoFeB MTJ (a) in as-grown state and (b) after postannealing. Cross-sectional TEM image of CoFeB/MgO/CoFeB MTJ with practical AF/SAF structure underneath MTJ part. (Courtesy of Canon-Anelva Corporation.)

that is strong enough for commercial devices. This type of reliable AF/SAF structure is based on an fcc structure with (1 1 1)-orientation.

A fundamental problem with this structure is that an NaCl-type MgO(0 0 1) tunnel barrier and a bcc(0 0 1) ferromagnetic electrode, both of which have fourfold in-plane crystallographic symmetry, cannot be grown on the fcc(1 1 1)-oriented AF/SAF structure, which has threefold in-plane crystallographic symmetry, because of the lattice mismatch. We could theoretically solve this problem by developing a new pinned layer structure with fourfold in-plane symmetry. This solution, however, is not generally acceptable to the electronics industry because it has spent more than a decade in developing the reliable pinned layer structure. The reliability of practical devices is determined by the reliability of the pinned layer.

To solve this problem concerning crystal growth, Djayaprawira et al. developed a new MTJ structure, CoFeB/MgO/CoFeB, by using a sputtering deposition technique (33). Figure 2.22a shows a cross-sectional TEM image of such a MTJ in an *as-grown* state. As can be seen in the figure, the bottom and top CoFeB electrode layers have an amorphous structure in the as-grown state. Surprisingly, the MgO barrier layer grown on the amorphous CoFeB is a (0 0 1)-oriented polycrystal (textured structure). Because the bottom CoFeB electrode is amorphous, this CoFeB/MgO/CoFeB MTJ can theoretically be grown on all kinds of underlayers. For practical

applications, the CoFeB/MgO/CoFeB MTJ can be grown on the standard AF/SAF structure, as shown in Fig. 2.22b. Thus, it is possible to grow the MgO(0 0 1) barrier with fourfold symmetry on the practical pinned layer with threefold symmetry by inserting an amorphous CoFeB bottom electrode layer between them. During annealing above 250°C, the amorphous CoFeB electrode layers crystallize in the bcc(0 0 1) structure (Fig. 2.22b) (34,35). It should be noted that a $Co_{60}Fe_{20}B_{20}$ layer adjacent to an MgO(0 0 1) layer crystallizes in a bcc(0 0 1) structure, although the stable structure of $Co_{60}Fe_{20}B_{20}$ is not bcc but fcc (34). This clearly indicates that the MgO(0 0 1) layer acts as a template for crystallizing the amorphous CoFeB layers because of the good lattice match between MgO(0 0 1) and bcc CoFeB(0 0 1). This type of crystallization process is known as *solid-phase epitaxy*. Because the bcc CoFeB(0 0 1) has a fully spin-polarized Δ_1 Bloch state at the Fermi energy, the (0 0 1)-textured CoFeB/MgO/CoFeB MTJs exhibits a giant TMR effect of up to 600% at RT (Fig. 2.21) (33–36).

2.3.3.3 Device Applications of MgO-Based MTJs The history of magnetoresistance and its device applications are summarized in Fig. 2.23. GMR spin-valve devices have MR ratios of 5–15% at RT and have been used in the read heads of HDDs. AlO-based MTJs have MR ratios of 20–70% at RT and have been used not only in HDD read heads but also in MRAM cells. MgO-based MTJs have MR ratios of 150–600% at RT and are expected to be used in various spintronic devices such as HDD read heads, spin-transfer MRAM cells, and novel microwave devices. Here, we briefly describe recent developments in these applications.

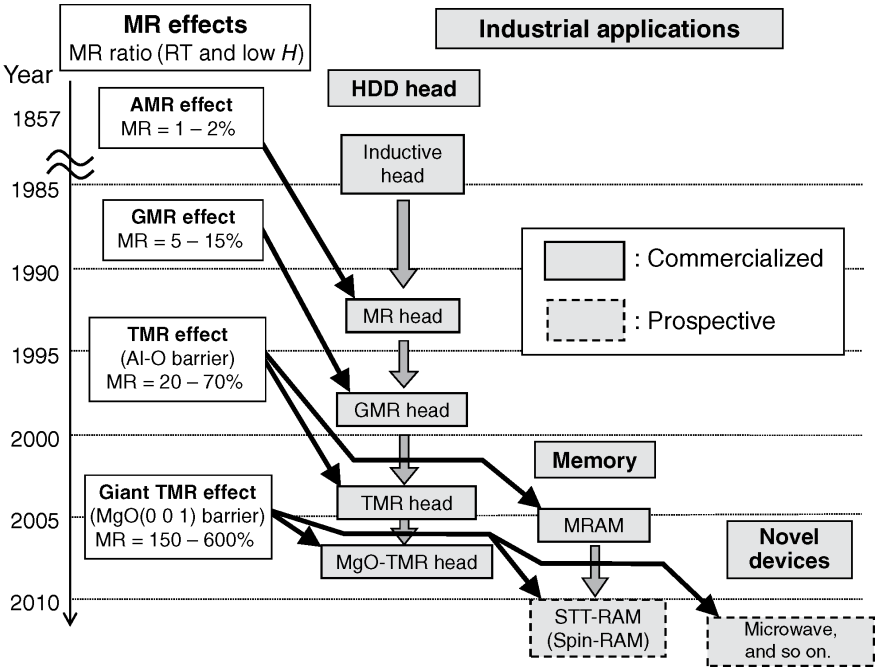


Figure 2.23 Historical and prospective magnetoresistive effects, MR ratios at RT and applications of MR effects in spintronic devices.

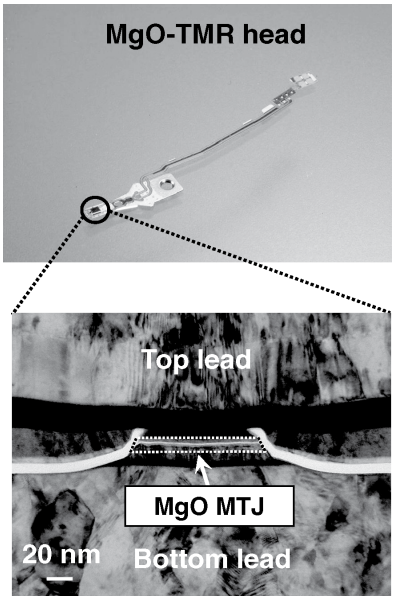


Figure 2.24 Photograph and cross-sectional TEM image of MgO-TMR read head for HDD with recording density of 250 Gbit/in^2. (Courtesy of Fujitsu Corp.)

(i) *Read Heads of High-Density HDDs*

MTJs with an amorphous AlO or TiO barrier have been used in the TMR read heads for HDDs with areal recording densities of 100–150 Gbit/in^2 since 2004 (37). These MTJs have low *RA* products (about 3 Ω μm^2) and MR ratios of 20–30% at RT. Although these properties are sufficient for recording densities of 100–150 Gbit/in^2, even lower *RA* products and much higher MR ratios are needed for recording densities above 200 Gbit/in^2.

By using ultralow-resistance CoFeB/MgO/CoFeB MTJs (38,39), HDD manufacturers were able to commercialize TMR read heads for ultrahigh-density HDDs in 2007 (35). For example, Fujitsu Corp. commercialized TMR read heads for ultrahigh-density HDDs in 2007 (Fig. 2.24). MgO-TMR heads have already been used for HDDs with recording densities of 250–800 Gbit/in^2. This means a factor of 5 increase in the recording density of HDDs, thanks to MgO-TMR heads combined with perpendicular magnetic recording media. MgO-TMR heads currently represent the mainstream technology for HDD read heads and are also expected to be applied to recording densities of up to about 1–2 Tbit/in^2.

(ii) *Spin-Transfer Torque MRAM*

The giant TMR effect in MgO-based MTJs is also useful in the development of spin-transfer torque MRAM (variously referred to as STT-MRAM, STT-RAM, or Spin-RAM). In 2005, Sony Corporation developed the 4-kbit prototype STT-MRAM based on CoFeB/MgO/CoFeB MTJs with in-plane magnetization (Fig. 2.25) and demonstrated reliable write and read operations (40). With the in-plane magnetized MTJs, however, high thermal stability, which is necessary to retain data for more than 10 years, is very difficult to achieve when the lateral size of MTJ cells is smaller than about 50 nm, which is a typical cell size in gigabit-scale STT-MRAM.

A solution to achieving gigabit-scale STT-MRAM is to use MTJs with perpendicularly magnetized electrodes (see Chapter 5). It is theoretically possible

WD EX1057
Western Digital v IP Bridge
Page 49

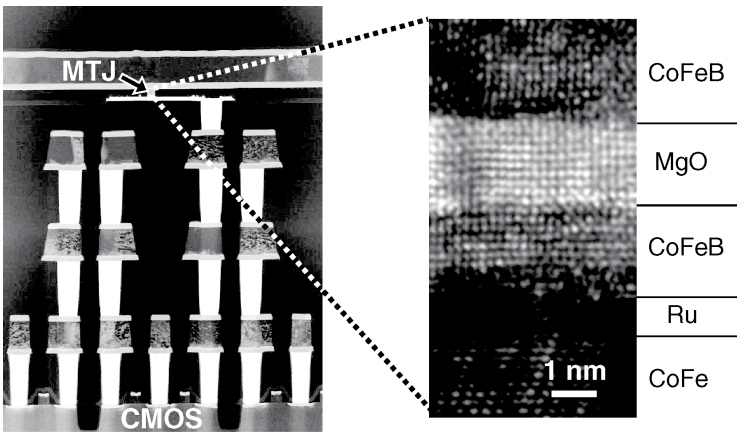


Figure 2.25 Cross-sectional TEM images of 4-kbit spin torque MRAM (Spin-RAM) using CoFeB/MgO/CoFeB MTJs. (Courtesy of Sony Corporation, redrawn from Ref. 40).

to simultaneously have high thermal stability in 50 nm-sized MTJ cells and a small write current density by using perpendicularly magnetized electrodes with a high perpendicular magnetic anisotropy, K_u. Since 2008, Toshiba Corporation and AIST have developed a prototype STT-MRAM using 30–50 nm-sized MgO-based MTJs with perpendicularly magnetized electrodes (Fig. 2.26) (41,42). The perpendicularly magnetized MgO-based MTJs are now the mainstream technology to achieve gigabit-scale STT-MRAM.

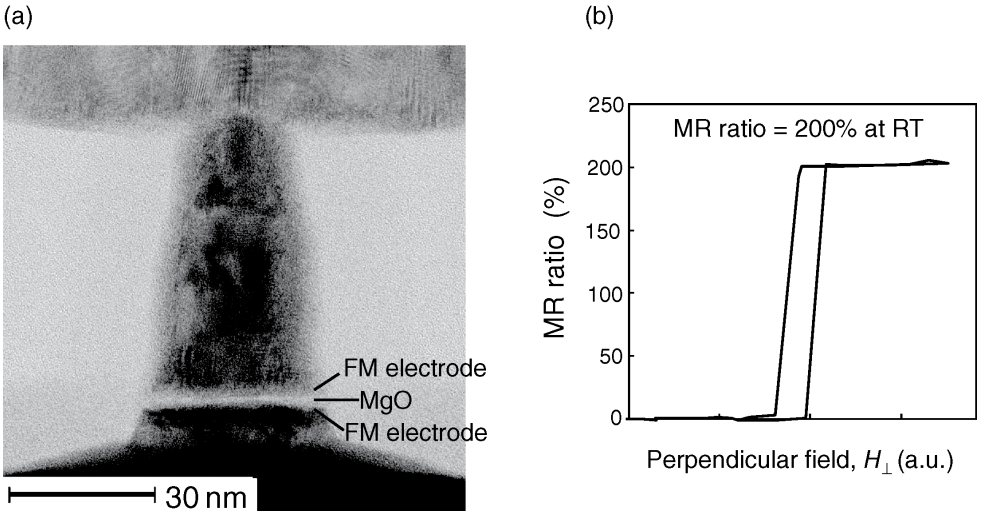


Figure 2.26 (a) Cross-sectional TEM image of MgO-based MTJ with perpendicularly magnetized electrodes with lateral diameter of 30 nm. (Courtesy of Toshiba Corporation.) (b) Typical magnetoresistance curve for perpendicular magnetic field. (Reproduced with permission from IEEE.)

WD EX1057
Western Digital v IP Bridge
Page 50

REFERENCES

1. D.-X. Chen, J. A. Brug, and R. B. Goldfarb, "Demagnetizing factors for cylinders," *IEEE Trans. Magn.* **27**, pp. 3601–3619 (1991); doi: 10.1109/20.102932.
2. W. H. Meiklejohn and C. P. Bean, "A new magnetic anisotropy," *IEEE Trans. Magn.* **37**, pp. 3866–3876 (2002); doi: 10.1109/20.966120.
3. G. Binasch, P. Grünberg, F. Saurenbach, and W. Zinn, "Enhanced magnetoresistance in layered magnetic structures with antiferromagnetic interlayer exchange," *Phys. Rev. B* **39**, pp. 4828–4830 (1989); doi: http://dx.doi.org/10.1103/PhysRevB.39.4828.
4. M. N. Baibich, J. M. Broto, A. Fert, F. Nguyen Van Dau, F. Petroff, P. Etienne, G. Creuzet, A. Friederich, and J. Chazelas, "Giant magnetoresistance of (0 0 1)Fe/(0 0 1)Cr magnetic superlattices," *Phys. Rev. Lett.* **61**, pp. 2472–2475 (1988); doi: 10.1103/PhysRevLett.61.2472.
5. "The Nobel Prize in Physics 2007," www.nobelprize.org/nobel_prizes/physics/laureates/2007/.
6. S. S. P. Parkin, N. More, and K. P. Roche, "Oscillations in exchange coupling and magnetoresistance in metallic superlattice structures: Co/Ru, Co/Cr, and Fe/Cr," *Phys. Rev. Lett.* **64**, pp. 2304–2308 (1990); doi: 10.1103/PhysRevLett.64.2304.
7. J. Unguris, D. T. Pierce, R. J. Celotta, and J. A. Stroscio, "SEMPA studies of oscillatory exchange coupling," in *Magnetism and Structure in Systems of Reduced Dimension*, NATO ASI Series, Vol. **309**, eds. R. F. C. Farrow, B. Dieny, M. Donath, A. Fert, and B. D. Hermsmeier, Springer, 1993, pp. 101–112.
8. P. Bruno and C. Chappert, "Oscillatory coupling between ferromagnetic layers separated by a nonmagnetic metal spacer," *Phys. Rev. Lett.* **67**, pp. 1602–1605 (1991); doi: 10.1103/PhysRevLett.67.2592.
9. D. M. Edwards, J. Mathon, R. B. Muniz, and M. S. Phan, "Oscillations of the exchange in magnetic multilayers as an analog of de Haas–van Alphen effect," *Phys. Rev. Lett.* **67**, pp. 493–496 and 1467 (1991); doi: 10.1103/PhysRevLett.67.493 and 10.1103/PhysRevLett.67.1476.
10. B. Dieny, V. S. Speriosu, S. S. P. Parkin, B. A. Gurney, D. R. Wilhoit, and D. Mauri, "Giant magnetoresistance in soft ferromagnetic multilayers," *Phys. Rev. B* **43**, pp. 1297–1300 (1991); doi: 10.1103/PhysRevB.43.1297.
11. D. Heim, R. Fontana, C. Tsang, V. S. Speriosu, B. Gurney, and M. Williams, "Design and operation of spin valve sensors," *IEEE Trans. Magn.* **MAG-30**, pp. 316–321 (1994); doi: 10.1109/20.312279.
12. D. H. Mosca, F. Petroff, A. Fert, P. A. Schroeder, W. P. Pratt, and R. Loloee, "Oscillatory interlayer coupling and giant magnetoresistance in Co/Cu multilayers," *J. Magn. Magn. Mater.* **94**, pp. L1–L5 (1991); doi: 10.1016/0304-8853(91)90102-G.
13. W. P. Pratt, S.-F. Lee, J. M. Slaughter, R. Loloee, P. A. Schroeder, and J. Bass, "Perpendicular giant magnetoresistances of Ag/Co multilayers," *Phys. Rev. Lett.* **66**, pp. 3060–3063 (1991); doi: http://dx.doi.org/10.1103/PhysRevLett.66.3060
14. E. Tsymbal and D. G. Pettifor, "Perspectives of giant magnetoresistance," in *Solid State Physics*, Vol. **56**, ed. H. Ehrenreich and F. Spaepen, Academic Press, San Diego, CA, 2001, pp. 113–237.
15. M. Jullière, "Tunneling between ferromagnetic films," *Phys. Lett. A* **54**, pp. 225–226 (1975); doi: 10.1016/0375-9601(75)90174-7.
16. T. Miyazaki and N. Tezuka, "Giant magnetic tunneling effect in Fe/Al_2O_3/Fe junction," *J. Magn. Magn. Mater.* **139**, pp. L231–L234 (1995); doi: 10.1016/0304-8853(95)90001-2.
17. J. S. Moodera, L. R. Kinder, T. M. Wong, and R. Meservey, "Large magnetoresistance at room temperature in ferromagnetic thin film tunnel junctions," *Phys. Rev. Lett.* **74**, pp. 3273–3276 (1995); doi: 10.1103/PhysRevLett.74.3273.
18. M. Bowen, M. Bibes, A. Barthélémy, J.-P. Contour, A. Anane, Y. Lemaître, and A. Fert, "Nearly total spin polarization in $La_{2/3}$ $Sr_{1/3}$ MnO_3 from tunneling experiments," *Appl. Phys. Lett.* **82**, pp. 233–235 (2003); doi: 10.1063/1.1534619.
19. Y. Sakuraba, M. Hattori, M. Oogane, Y. Ando, H. Kato, A. Sakuma, T. Miyazaki, and H. Kubota, "Giant tunneling magnetoresistance in Co_2MnSi/Al–O/Co_2MnSi magnetic tunnel junctions," *Appl. Phys. Lett.* **88**, 192508 (2006); doi: 10.1063/1.2202724.
20. W. H. Butler, X.-G. Zhang, T. C. Schulthess, and J. M. MacLaren, "Spin-dependent tunneling conductance of Fe/MgO/Fe sandwiches," *Phys. Rev. B* **63**, 054416 (2001); doi: 10.1103/PhysRevB.63.054416.

21. J. Mathon and A. Umersky, "Theory of tunneling magnetoresistance of an epitaxial Fe/MgO/Fe(0 0 1) junction," *Phys. Rev. B* **63**, 220403 (2001); doi: 10.1103/PhysRevB.63.220403.
22. S. Yuasa, A. Fukushima, T. Nagahama, K. Ando, and Y. Suzuki, "High tunnel magnetoresistance at room temperature in fully epitaxial Fe/MgO/Fe tunnel junctions due to coherent spin-polarized tunneling," *Jpn. J. Appl. Phys.* **43**, pp. L588–L590 (2004); doi: 10.1143/JJAP.43.L588.
23. S. Yuasa, T. Nagahama, A. Fukushima, Y. Suzuki, and K. Ando, "Giant room-temperature magnetoresistance in single-crystal Fe/MgO/Fe magnetic tunnel junctions," *Nat. Mater.* **3**, pp. 868–871 (2004); doi: 10.1038/nmat1257.
24. S. S. P. Parkin, C. Kaiser, A. Panchula, P. M. Rice, B. Hughes, M. Samant, and S.-H. Yang, "Giant tunnelling magnetoresistance at room temperature with MgO (1 0 0) tunnel barriers," *Nat. Mater.* **3**, pp. 862–867 (2004); doi: 10.1038/nmat1256.
25. W. H. Butler, "Tunneling magnetoresistance from a symmetry filtering effect," *Sci. Technol. Adv. Mater.* **9**, pp. 014106 (2008); doi: 10.1088/1468-6996/9/1/014106.
26. X.-G. Zhang and W. H. Butler, "Large magnetoresistance in bcc Co/MgO/Co and FeCo/MgO/FeCo tunnel junctions," *Phys. Rev. B* **70**, 172407 (2004); doi: 10.1103/PhysRevB.70.172407.
27. Ph. Mavropoulos, N. Papanikolaou, and P. H. Dederichs, "Complex band structure and tunneling through ferromagnet/insulator/ferromagnet junctions," *Phys. Rev. Lett.* **85**, pp. 1088–1091 (2000); doi: 10.1103/PhysRevLett.85.1088.
28. J. P. Velev, K. D. Belashchenko, D. A. Stewart, M. Van Schilfgaarde, S. S. Jaswal, and E. Y. Tsymbal, "Negative spin polarization and large tunneling magnetoresistance in epitaxial Co/$SrTiO_3$/Co magnetic tunnel junctions," *Phys. Rev. Lett.* **95**, pp. 216601 (2005); doi: 10.1103/PhysRevLett.95.216601.
29. W. Wulfhekel, M. Klaua, D. Ullmann, F. Zavaliche, J. Kirschner, R. Urban, T. Monchesky, and B. Heinrich, "Single-crystal magnetotunnel junctions," *Appl. Phys. Lett.* **78**, pp. 509–511 (2001); doi: 10.1063/1.1342778.
30. M. Bowen, V. Cros, F. Petroff, A. Fert, C. Martinez Boubeta, J. L. Costa-Krämer, J. V. Anguita, A. Cebollada, F. Briones, J. M. de Teresa, L. Morellon, M. R. Ibarra Large, F. Güell, F. Peiró, and A. Cornet, "Large magnetoresistance in Fe/MgO/FeCo(0 0 1) epitaxial tunnel junctions on GaAs(0 0 1)," *Appl. Phys. Lett.* **79**, pp. 1655–1657 (2001); doi: 10.1063/1.1404125.
31. J. Faure-Vincent, C. Tiusan, E. Jouguelet, F. Canet, M. Sajieddine, C. Bellouard, E. Popova, M. Hehn, F. Montaigne, and A. Schuhl, "High tunnel magnetoresistance in epitaxial Fe/MgO/Fe tunnel junctions," *Appl. Phys. Lett.* **82**, pp. 4507–4509 (2003); doi: 10.1063/1.1586785.
32. S. Yuasa, A. Fukushima, H. Kubota, Y. Suzuki, and K. Ando, "Giant tunneling magnetoresistance up to 410% at room temperature in fully epitaxial Co/MgO/Co magnetic tunnel junctions with bcc Co(0 0 1) electrodes," *Appl. Phys. Lett.* **89**, 042505 (2006); doi: 10.1063/1.2236268.
33. D. D. Djayaprawira, K. Tsunekawa, M. Nagai, H. Maehara, S. Yamagata, N. Watanabe, S. Yuasa, Y. Suzuki, and K. Ando, "230% room-temperature magnetoresistance in CoFeB/MgO/CoFeB magnetic tunnel junctions," *Appl. Phys. Lett.* **86**, 092502 (2005); doi: 10.1063/1.1871344.
34. S. Yuasa, Y. Suzuki, T. Katayama, and K. Ando, "Characterization of growth and crystallization processes in CoFeB/MgO/CoFeB magnetic tunnel junction structure by reflective high-energy electron diffraction," *Appl. Phys. Lett.* **87**, pp. 242503 (2005); doi: 10.1063/1.2140612.
35. S. Yuasa and D. D. Djayaprawira, "Giant tunnel magnetoresistance in magnetic tunnel junctions with a crystalline MgO(0 0 1) barrier," *J. Phys. D Appl. Phys.* **40**, pp. R337–R354 (2007); doi: 10.1088/0022-3727/40/21/R01.
36. S. Ikeda, J. Hayakawa, Y. Ashizawa, Y. M. Lee, K. Miura, H. Hasegawa, M. Tsunoda, F. Matsukura, and H. Ohno, "Tunnel magnetoresistance of 604% at 300 K by suppression of Ta diffusion in CoFeB/MgO/CoFeB pseudo-spin-valves annealed at high temperature," *Appl. Phys. Lett.* **93**, pp. 082508 (2008); doi: 10.1063/1.2976435.
37. J.-G. Zhu and C. Park, "Magnetic tunnel junctions," *Mater. Today* **9**, pp. 36–45 (2006); doi: 10.1016/S1369-7021(06)71693-5.
38. K. Tsunekawa, D. D. Djayaprawira, M. Nagai, H. Maehara, S. Yamagata, N. Watanabe, S. Yuasa, Y. Suzuki, and K. Ando, "Giant tunneling magnetoresistance effect in low-resistance CoFeB/MgO(0 0 1)/CoFeB magnetic tunnel junctions for read-head applications," *Appl. Phys. Lett.* **87**, pp. 072503 (2005); doi: 10.1063/1.2012525.
39. Y. Nagamine, H. Maehara, K. Tsunekawa, D. D. Djayaprawira, N. Watanabe, S. Yuasac, and K. Ando, "Ultralow resistance-area product of 0.4 Ω $(\mu m)^2$ and high magnetoresistance above 50% in CoFeB/

WD EX1057
Western Digital v IP Bridge
Page 52

MgO/CoFeB magnetic tunnel junctions," *Appl. Phys. Lett.* **89**, pp. 162507 (2006); doi: 10.1063/1.2352046.

40. M. Hosomi, H. Yamagishi, T. Yamamoto, K. Bessho, Y. Higo, K. Yamane, H. Yamada, M. Shoji, H. Hachino, C. Fukumoto, H. Nagao, and H. Kano,"A novel nonvolatile memory with spin torque transfer magnetization switching: Spin-RAM," *IEEE International Electron Devices Meeting, IEDM Technical Digest 19.1*, December 2005; doi: 10.1109/IEDM.2005.1609379.
41. T. Kishi, H. Yoda, T. Kai, T. Nagase, E. Kitagawa, M. Yoshikawa, K. Nishiyama, T. Daibou, M. Nagamine, M. Amano, S. Takahashi, M. Nakayama, N. Shimomura, H. Aikawa, S. Ikegawa, S. Yuasa, S. K. Yakushiji, H. Kubota, A. Fukushima, M. Oogane, T. Miyazaki, T. K. Ando,"Lower-current and fast switching of a perpendicular TMR for high speed and high density spin-transfer-torque MRAM," *IEEE International Electron Devices Meeting, IEDM Technical Digest 12.6*, December 2008; doi: 10.1109/IEDM.2008.4796680.
42. H. Yoda, T. Kishi, T. Nagase, M. Yoshikawa, K. Nishiyama, E. Kitagawa, T. Daibou, M. Amano, N. Shimomura, S. Takahashi, T. Kai, M. Nakayama, H. Aikawa, S. Ikegawa, M. Nagamine, J. Ozeki, S. Mizukami, M. Oogane, Y. Ando, S. Yuasa, K. Yakushiji, H. Kubota, Y. Suzuki, Y. Nakatani, T. Miyazaki, and K. Ando, "High efficient spin transfer torque writing on perpendicular magnetic tunnel junctions for high density MRAMs," *Curr. Appl. Phys.* **10**, pp. E87–E89 (2010); doi: 10.1016/j.cap.2009.12.021.

CHAPTER 5

MAGNETIC RANDOM-ACCESS MEMORY

Bernard Dieny[1,2,3] *and I. Lucian Prejbeanu*[1,2,3]
[1]INAC-SPINTEC, Université Grenoble Alpes, Grenoble, France
[2]INAC-SPINTEC, CEA, Grenoble, France
[3]SPINTEC, CNRS, Grenoble, France

5.1 INTRODUCTION TO MAGNETIC RANDOM-ACCESS MEMORY (MRAM)

5.1.1 Historical Perspective

Magnetism has been used for a long time to store information in the form of a magnetization orientation in magnetic materials. This has been used in tape recording since 1928, in magnetic hard disk drives since 1956, and in a number of magnetic solid-state memory devices, starting with magnetic core memory (1955–1975), bubble memory in the 1970s and early 1980s, followed by several magnetoresistive memory technologies. The latter were first based on the anisotropic magnetoresistance phenomenon (variation of resistivity of a few percent at room temperature in magnetic transition metals as a function of the angle between magnetization and current) and subsequently on the giant magnetoresistance (GMR) effect, following its discovery in 1988 (magnetoresistance amplitude in the range 15–20% in GMR structures of practical interest).

The interest in magnetic random-access memory (MRAM) was renewed after the first successful attempts in 1995 to fabricate magnetic tunnel junctions (MTJs) that exhibit large tunneling magnetoresistance (TMR) amplitude of several tens of percentages at room temperature using amorphous AlO_x barriers (see Chapters 1 and 2). Besides their larger magnetoresistance amplitude, MTJs are more suitable than GMR metallic structures for memory applications due to their larger impedance (adjustable to several kilohms), which allows an easier integration with complementary metal–oxide–semiconductor (CMOS) components.

Two other breakthroughs further boosted research and development in MRAM. The first was the discovery that MTJs based on crystalline MgO barriers associated with crystalline magnetic electrodes exhibit much larger TMR amplitude, in the range

Introduction to Magnetic Random-Access Memory, First Edition. Edited by Bernard Dieny, Ronald B. Goldfarb, and Kyung-Jin Lee.
© 2017 The Institute of Electrical and Electronics Engineers, Inc. Published 2017 by John Wiley & Sons, Inc.

WD EX1057
Western Digital v IP Bridge
Page 101

of 150–600% at room temperature (1,2), than their counterparts based on amorphous alumina tunnel barriers. This larger TMR provides a much improved read margin and faster read in memory devices. The second was the possibility to switch the magnetization of a magnetic nanostructure by a spin-polarized current, thanks to the spin-transfer torque (STT) effect. This effect was first measured in metallic structures (3) and later in magnetic tunnel junctions (4). It provided a new write scheme in MRAM with much better downsize scalability than in the first generations of MRAM, as will be explained later in this chapter. Currently, most of research and development in MRAM are focused on STT-MRAM with perpendicular anisotropy (i.e., the magnetization in the ferromagnetic electrodes is oriented out of the plane of the layers) since STT-MRAM seems to be the most promising in terms of scalability down to and beyond the 16 nm technological node. Thermal assistance during the write process is an additional factor also used in other magnetic storage technology, in particular in heat-assisted magnetic recording (HAMR) in hard disk drive technology. Thermal assistance allows magnetization to switch easily during the write process while achieving a very good thermal stability of the magnetization in standby mode. Besides extending the downsize scalability, this technology also offers new functionalities (see Section 5.6).

5.1.2 Various Categories of MRAM

Since 1996, various families of MRAM have been developed, benefiting from the progress in spintronics research, particularly the giant TMR of MgO tunnel junctions and the STT phenomenon (see Fig. 5.1). All of these MRAM use MTJs as elementary

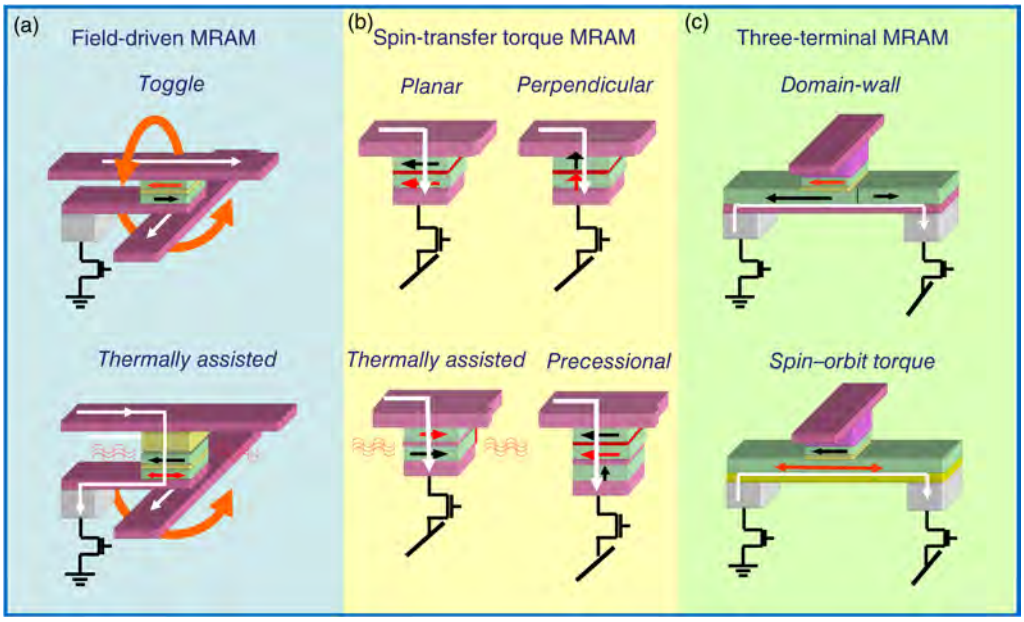


Figure 5.1 Various categories of MRAM developed since 1996. (a) This column corresponds to MRAM written by magnetic fields. (b) This column illustrates MRAM based on STT writing. (c) This column contains three-terminal MRAM based on domain wall propagation or spin–orbit torque switching.

storage cells. MTJs essentially consist of two ferromagnetic layers (typically 1–2.5 nm thick) separated by a thin insulating barrier (typically 1–1.5 nm thick). The resistance of the MTJ in the direction perpendicular to the plane of the layers depends on the relative orientation of the magnetization in these two ferromagnetic layers. The amplitude of the resistance change between the antiparallel magnetic configuration (high resistance state) and the parallel magnetic configuration (low resistance state) defines the TMR amplitude. In most MRAM embodiments, the magnetization of one of the ferromagnetic layers is fixed in a predetermined direction to provide a reference direction for the spin of the electrons. This layer is called the reference layer. The magnetization of the other layer, called the storage layer, can be switched between two stable states: Its magnetization can be set either parallel or antiparallel to that of the reference layer. As illustrated in Fig. 5.1, the magnetization in the ferromagnetic electrodes can lie in the plane of the layers or point perpendicular to the plane depending on the particular choice of materials. For small devices, typically below 50 nm, MTJs with perpendicular magnetization are preferred because their higher magnetic anisotropy provides better stability of the written information (see Section 5.2). However, these perpendicular-to-the-plane magnetized materials are generally more difficult to grow than the in-plane magnetized materials.

In most embodiments, each MTJ is connected in series with a selection transistor used as a switch, which controls the current through the MTJ. During read, a moderate current is sent through the MTJ (corresponding to a bias voltage across the MTJ on the order of 0.1–0.2 V). The change of resistance between parallel and antiparallel magnetic configurations allows the magnetic state of the storage layer to be sensed and, therefore, the stored information to be read (see Section 5.3). The various families of MRAM displayed in Fig. 5.1 differ by the way the information is written in the memory.

Between 1996 and 2004, most research and development focused on MRAM written by field (Fig. 5.1a). Until the discovery of STT switching and its gradual implementation in MTJ after 2004, the only known way to manipulate the magnetization of a magnetic nanostructure (here the MTJ storage layer) was indeed with use of a magnetic field. The magnetic field is created by pulses of current flowing in conducting lines located below and above the MTJ. These approaches, which will be described in more detail in Section 5.4, actually resulted in the commercialization of the first MRAM products (1, 4, 8, and 16 Mbit MRAM chips) by Freescale Semiconductor and its spin-off Everspin Technologies in 2006. An extension of field-written MRAM is represented by thermally-assisted MRAM (TA-MRAM) mainly developed by Crocus Technology. In the latter, the write selectivity is achieved by a combination of temporary heating of the selected cell produced by the tunneling current flowing through the cell and a single pulse of magnetic field. The power consumption to write these memory elements is significantly reduced compared to conventional field-written MRAM, thanks to the possibility of using lower magnetic fields and of sharing each field pulse among several cells so as to write several bits at once (see Section 5.6). Field-written technology is robust and is already used in a variety of applications where reliability, endurance, and resistance to radiation are important features, such as in automotive and space applications. However, the downsize scalability provided by field-writing in conventional technology is limited to MTJ dimensions on the order of 60 nm × 120 nm due to

WD EX1057
Western Digital v IP Bridge
Page 103

electromigration in the conducting lines used to generate the field. In addition, in field-writing, the write field extends all along the conducting line where it is produced and decreases relatively gradually in space, inversely proportional to the distance to this line. As a result, unselected bits adjacent to selected bits may sense a significant fraction of the write field, which may yield accidental switching of these unselected bits. In TA-MRAM, smaller dimensions can be reached, thanks to the field sharing approach, the lower required amplitude of the write field, and the different mechanism of write selectivity (see Section 5.6).

Since the first observation of STT-induced switching in GMR metallic spin-valve pillars (3), the interest in using STT as a new write approach in MRAM has increased, motivated by the fact that STT-writing (middle column in Fig. 5.1) offers a much better downsize scalability than field-writing. This is due to the fact that the critical current required to write by STT decreases in proportion to the cell area, whereas it tends to increase in the case of field-writing. Furthermore, STT provides very good write selectivity since the STT current flows through only the selected cells. As will be explained in Section 5.5, the greatest interest in STT-MRAM is now focused on out-of-plane magnetized STT-MRAM because it requires significantly less write current than its in-plane counterparts for a given criterion of memory retention.

Thermal assistance can also be combined with the STT write approach. In this case, one takes advantage of the Joule heating produced by the STT write current flowing through the MTJ tunnel barrier to facilitate the magnetization switching (see Section 5.6). This allows circumvention of a classical difficulty in data storage: the trade-off between the memory writability and retention.

A third category of MRAM under research and development is represented in Fig. 5.1c. These are three-terminal MRAM cells (see Section 5.7). The purpose of these embodiments is to separate the write and read current paths and thereby increase the reliability of the memory. These approaches open new possibilities in the design of the memory architecture or for logic applications. The writing is here based on current induced domain wall propagation or another phenomenon called spin–orbit -torque (see Section 5.7).

The two following sections discuss two common functions of the various categories of MTJ-based MRAM shown in Fig. 5.1: the storage function (Section 5.2) and the read function (Section 5.3).

5.2 STORAGE FUNCTION: MRAM RETENTION

5.2.1 Key Role of the Thermal Stability Factor

In memory applications, a key characteristic is the retention of the memory, that is, how long the memory chip is capable of keeping the information that has been written in it. The specification depends on the application but is, for instance, on the order of 10 years for mass storage application such as in hard disk drives (HDD). In MRAM, the information may get corrupted by unintended switching of the magnetization of the storage layer due to thermal fluctuations. The failure rate in an MRAM chip of N bits in standby mode can be estimated as follows. The magnetization of the storage

WD EX1057
Western Digital v IP Bridge
Page 104

layer of the memory cell can be described as a bistable system, the two stable states being separated by an energy barrier ΔE. ΔE is determined by the magnetic material's properties and the shape and dimensions of the magnetic element, that is, the MTJ storage layer, as is explained immediately below. At a temperature T, the characteristic thermally activated switching time is given by an Arrhenius law:

$$\tau = \tau_0 \exp\left(\frac{\Delta E}{k_B T}\right), \tag{5.1}$$

where k_B is the Boltzmann constant and τ_0 is an attempt time of the order of 1 ns (see Chapter 3). For a given bit, the probability of not having accidentally switched after a time t is

$$P_{noswitch}(t) = \exp(-t/\tau). \tag{5.2}$$

For N bits, the probability for the set of N bits of not having experienced any switching event after a time t is

$$P^N_{noswitch}(t) = [P_{noswitch}(t)]^N = \exp(-Nt/\tau). \tag{5.3}$$

Consequently, the probability of having experienced at least one switching event after a time t, that is, the failure rate in standby mode, is given by

$$F(t) = 1 - \exp(-Nt/\tau) = 1 - \exp\left[\frac{-Nt}{\tau_0}\exp\left(-\frac{\Delta E}{k_B T}\right)\right]. \tag{5.4}$$

This expression clearly shows that the factor $\Delta = \Delta E/k_B T$, often called the thermal stability factor, plays a key role in the failure rate of MRAM chips in standby mode, that is, memory retention failure. Figure 5.2 shows the variation of the failure rate

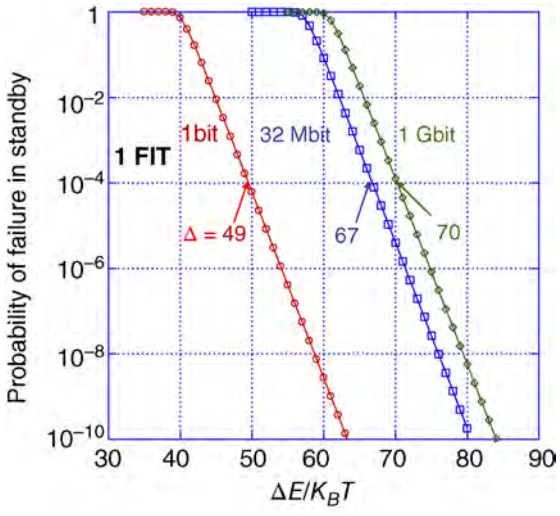


Figure 5.2 Failure rate during 10 years in standby mode for MRAM chips of 1 bit, 32 Mbit, or 1 Gbit as a function of thermal stability factor.

WD EX1057
Western Digital v IP Bridge
Page 105

during 10 years in standby mode (not during a write or read operation) as a function of the thermal stability factor ($\boldsymbol{\Delta}$) for a 32 Mbit and a 1 Gbit MRAM chip. In order for the probability of experiencing one failure in time (FIT) during 10 years in standby mode to be below an acceptable level of 10^{-4} (this number depends on whether the application is memory or logic, and on the possible use of error correction codes), the thermal stability factor must be greater than 67 for the 32 Mbit chip and greater than 70 for the 1 Gbit chip. The higher the memory capacity, the larger the thermal stability factor has to be.

5.2.2 Thermal Stability Factor for In-Plane and Out-of-Plane Magnetized Storage Layer

In magnetic materials, the barrier height ΔE, which determines the thermal stability factor, is most often created by a magnetic anisotropy that can have different origins. This anisotropy can be of magnetocrystalline origin or can be due to stress or to some electronic hybridization effects taking place at the interfaces in magnetic multilayers. It can be also due to the shape of the patterned magnetic element: a magnetic nanostructure having an elongated shape has an easy axis of magnetization along the long dimension of the structure (see Chapter 3). Whatever the origin of this anisotropy, it can generally be described by an energy per unit volume $E_{anisotropy} = -K\left(\hat{n}\cdot\hat{M}\right)^2$, where $\hat{n}$ is a unit vector along the easy axis of magnetization and $\hat{M}$ is a unit vector parallel to the magnetization direction. The barrier height separating the two opposite stable states along the easy axis direction is then given by $\Delta E = KV$, where V is the volume of the magnetic nanostructure, that is, the volume of the storage layer in a considered memory cell.

Commonly used in-plane magnetized materials in MRAM have in general a relatively weak magnetocrystalline anisotropy. Their magnetic anisotropy mostly originates from their shape. The MTJs, and in particular their storage layers, are patterned in the form of elliptical elements. With the notation given in Fig. 5.3a, the barrier height is given by

$$\Delta E = \frac{1}{2}\mu_0\left(N_y - N_x\right)M_s^2 V, \tag{5.5}$$

where N_x and N_y are the storage layer demagnetizing coefficients, respectively, along the short and long axis of the ellipse, M_s is the storage layer magnetization, and μ_0 is the vacuum permeability equal to $4\pi\ 10^{-7}$ H/m (SI).

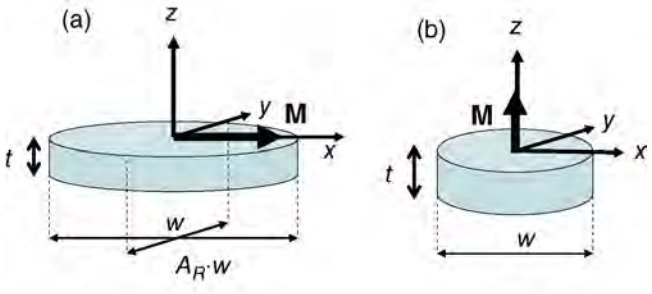


Figure 5.3 Schematic representation of a storage layer with its characteristic dimensions. (a) Case of an in-plane magnetized storage layer with an elliptical prism shape. (b) Case of an out-of-plane magnetized storage layer having the shape of a flat cylinder.

WD EX1057
Western Digital v IP Bridge
Page 106

Unfortunately, there are no simple expressions for the demagnetizing coefficients N_x and N_y of an elliptical cylinder as a function of its characteristic dimensions (thickness t, width w, length $A_R \cdot w$, where A_R is the in-plane aspect ratio). These coefficients are functions of elliptic integrals and must be tabulated or numerically calculated (5,6). Let's mention that for elliptical cylinders with small t, the structure is often approximated as a uniformly magnetized ellipsoid, for which closed-form solutions exist. Qualitatively, for the purpose of understanding the general influence of the storage layer dimensions, the thermal stability factor Δ of in-plane magnetized storage layer can be approximated by

$$\Delta = \frac{\Delta E}{k_B T} = \frac{\mu_0}{2} \frac{M_s^2 t^2 (A_R - 1) w}{k_B T}. \tag{5.6}$$

The Δ values given by Eq. (5.6) only differs by a few percent from those provided by the more exact expressions from Ref. 6. Equation (5.6) shows that for in-plane magnetized system, Δ scales with the lateral dimension w (typically the technological node), aspect ratio as $(A_R - 1)$, square of saturation magnetization M_s,, and square of thickness t. Practically, aspect ratios between 1.5 and 2.5 are used. For larger aspect ratio, the magnetization switching no longer occurs via a coherent rotation of the magnetization (i.e., as a whole magnetic block) but proceeds via nucleation of a reversed domain and propagation of domain wall. Therefore, there is no benefit in terms of thermal stability of the magnetization in increasing the aspect ratio above ~2.5. From Eq. (5.6), one can estimate that the smallest dimensions that an in-plane CoFeB storage layer ($M_s \approx 10^6$ A/m) 2.5 nm thick can have while keeping a thermal stability factor above 70 is of the order of 60 nm × 150 nm.

Perpendicular-to-plane magnetized storage layer can in general have better thermal stability than their in-plane counterparts at smaller dimensions because of their much larger intrinsic anisotropy. This is actually one of the reasons why the hard disk drive industry switched from in-plane magnetized magnetic media to perpendicular media in 2004. The perpendicular magnetic anisotropy (PMA) in thin film magnetic materials can have different origins. It can originate from the bulk of the material as in FePt or FePd $L1_0$ ordered alloys due to a tetragonal distortion of the lattice cell along the growth direction. This bulk anisotropy is usually described by a characteristic energy per unit volume (in J/m^3)

$$E_{anisotropy}^{Bulk} = -K_V (\hat{n} \cdot M)^2, \tag{5.7}$$

where $\hat{n}$ is a unit vector normal to the plane of the layer. The PMA may also be of interfacial origin due to interfacial electron hybridization or interfacial stress (for instance at Co–Pd, Co–Pt, or CoFe–MgO interfaces, see Section 5.5.5.3). This interfacial PMA is usually expressed in terms of a volume energy (in J/m^3) as

$$E_{anisotropy}^{Interface} = -\frac{K_S}{t} \left(\hat{n} \cdot \hat{M}\right)^2, \tag{5.8}$$

where K_S is the surface energy (J/m^2) and t the thickness of the storage layer. However, this PMA is partially counterbalanced by the demagnetizing energy, that is, the cost of magnetostatic energy required to pull the magnetization of a thin film out of

WD EX1057
Western Digital v IP Bridge
Page 107

the plane. Indeed, from a pure magnetostatic viewpoint, the thickness of a magnetic thin film is most often its smallest dimension. The direction along the thickness is therefore usually the hard axis of magnetization (in terms of magnetostatics). If the magnetization is nevertheless pulled out of plane by other sources of anisotropy, these other sources must overcome the demagnetizing energy. For an extended thin film, the demagnetizing energy per unit volume is written as

$$E_{demagnetizing} = +\frac{1}{2}\mu_0 M_s^2 \left(\hat{n}\cdot\hat{M}\right)^2. \tag{5.9}$$

In perpendicular STT-MRAM, the MTJ and therefore its storage layer is usually patterned in the form of a flat cylinder, since there is no longer a need for in-plane shape anisotropy to insure thermal stability of the magnetization. A cylindrical shape allows an increase in areal density. If the width of the cell is larger than 50 nm, the demagnetizing energy expression Eq. (5.9) is a sufficiently good approximation. However, for smaller dimensions, it is necessary to take into account the exact values of N_x, N_y, N_z demagnetizing coefficients. Since $N_x + N_y + N_z \approx 1$ (see Chapter 3) and $N_x = N_y$ due to the cylindrical shape, the demagnetizing energy is expressed as

$$E_{demagnetizing} = +\frac{1}{4}\mu_0 (3N_z - 1) M_s^2 \left(\hat{n}\cdot\hat{M}\right)^2. \tag{5.10}$$

The expression of N_z can be found for instance in Ref. 6 for flat disks. It can be approximated to 1 for storage layer of diameter larger than ~50 nm.

The total magnetic anisotropy energy per unit volume of the patterned storage layer is then the sum of these various anisotropy contributions:

$$\begin{aligned} E_{anisotropy} &= E_{anisotropy}^{Bulk} + E_{anisotropy}^{Interface} + E_{demagnetizing} \\ &= -\left[K_V - \frac{1}{4}\mu_0 (3N_z - 1) M_s^2 + \frac{K_s}{t}\right] \left(\hat{n}\cdot\hat{M}\right)^2. \end{aligned} \tag{5.11}$$

For the storage layer magnetization to remain stable in the out-of-plane direction, the term

$$K_{eff} = K_V - \frac{1}{4}\mu_0 (3N_z - 1) M_s^2 + \frac{K_s}{t} \tag{5.12}$$

called the effective anisotropy, must be positive, meaning that the bulk and interfacial perpendicular anisotropy must exceed the demagnetizing energy. To estimate the thermal stability factor of the storage layer, a cylindrical storage layer of diameter w in a perpendicular MTJ, one must consider which magnetization switching process prevails. As explained in Chapter 3, in out-of-plane magnetized nanostructures of dimensions typically >40 nm, magnetization reversal tends to proceed by nucleation of a reversed domain, most often at the edge of the nanostructures and propagation of the domain wall throughout the nanostructure. In this case, the barrier height for reversal is determined by the energy required for the nucleation of the reversed domain. In contrast, for smaller structures (typically <30 nm in diameter), the magnetization does not have enough space to nucleate a reversed domain and consequently switches as a rigid magnetic block (often called a "macrospin"). In

WD EX1057
Western Digital v IP Bridge
Page 108

this macrospin approximation, which is valid for technological node below ~30 nm, the thermal stability factor of a cylindrical storage layer of diameter w in a perpendicular MTJ is expressed as

$$\Delta = \frac{\Delta E}{k_B T} = \frac{\left[\left(K_V - (1/4)\mu_0(3N_z - 1)M_s^2\right)t + K_s\right]\frac{\pi}{4}w^2}{k_B T}. \tag{5.13}$$

As an example, for a CoFeB storage layer, 1.2 nm thick, with typical CoFeB/MgO interfacial anisotropy of 1.2×10^{-3} J/m^2 (see Section 5.5.3), and a magnetization on the order of 1000 kA/m: $\Delta = 107$ for $w = 30$ nm, $\Delta = 77$ for $w = 25$ nm, $\Delta = 52$ for $w = 20$ nm, and $\Delta = 32$ for $w = 15$ nm. A 10-year retention for a MTJ with $w \leq 20$ nm therefore requires an increase in the interfacial anisotropy, a decrease in the storage layer thickness while maintaining its TMR amplitude, or a decrease in its saturation magnetization.

For larger structures, as mentioned above, the magnetization switching proceeds by nucleation of a reversed domain and propagation of a domain wall. In this case, the thermal stability factor weakly depends on the cell area as illustrated in the right part of Fig. 5.4. Figure 5.4 clearly shows the crossover from the macrospin regime (coherent switching of the storage layer magnetization) at cell width below ~30 nm to the regime of nucleation of reversed domain and propagation of domain wall above ~40 nm. High density p-STT-MRAM (perpendicular, that is, out-of-plane magnetized STT-MRAM) cells of sub-25 nm diameter will likely switch in the macrospin switching mode, also called the coherent rotation regime.

Finally, another factor that can influence the thermal stability factor of a MRAM cell is the presence of a static field, which, depending on its direction relative to the storage layer magnetization, can further stabilize or on the contrary destabilize the magnetization. Of particular relevance is the stray field from the reference layer. To minimize it, synthetic antiferromagnetic reference layers are often used. These consist of two ferromagnetic layers antiferromagnetically coupled through a Ru spacer layer (see Chapter 2). Thanks to the partial compensation of the magnetic moment of these

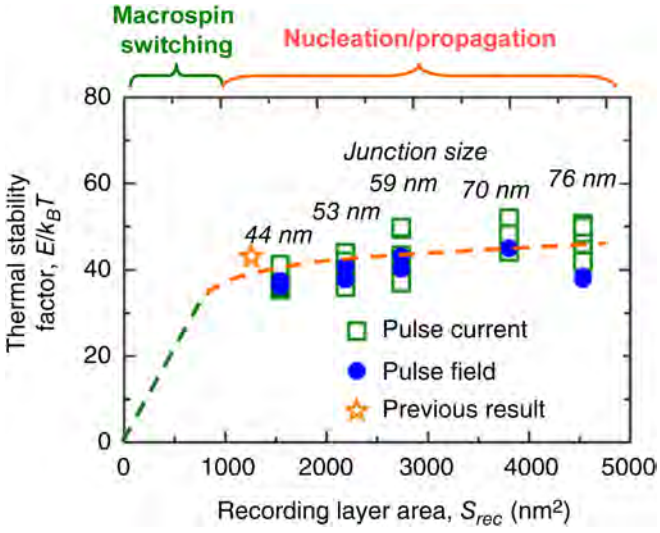


Figure 5.4 Experimentally measured thermal stability factor of the storage layer in perpendicular MTJ of composition Ta 5 nm/$Co_{20}Fe_{60}B_{20}$ 0.9 nm (reference layer)/MgO 0.9 nm/$Co_{20}Fe_{60}B_{20}$ 1.5 nm (storage layer)/Ta 5 nm. (Adapted from Ref. 7 with permission from AIP Publishing LLC.)

WD EX1057
Western Digital v IP Bridge
Page 109

two antiparallel coupled layers (i.e., a path of flux closure), their overall stray field on the storage layer is reduced. Quantitatively, if H_s is the static field acting on the storage layer magnetization, then the thermal stability factor is enhanced or reduced as

$$\Delta_{H_s} = \Delta\left(1 \pm \frac{H_s}{H_k^{eff}}\right)^2, \tag{5.14}$$

where H_k^{eff} is the effective anisotropy field related to the effective anisotropy by (8) $H_k^{eff} = 2(K_{eff}/(\mu_0 M_s))$. K_{eff} is mainly determined by the shape anisotropy for in-plane magnetized systems and is given by Eq. (5.12) for out-of-plane magnetized systems. The static field H_s acting on the storage layer can be determined by performing a minor hysteresis loop measurement on the storage layer. In the presence of a nonzero H_s, the storage layer hysteresis loop is shifted along the field axis by the quantity H_s (see Figure 2.13).

5.3 READ FUNCTION

5.3.1 Principle of Read Operation

The general principle of the read operation in MTJ-based MRAM consists in exploiting the change of resistance between P and AP magnetic configurations to determine the magnetic state of the junction and therefore the written information. This principle is illustrated in Fig. 5.5. During read, a read current flows through the MTJ to sense its magnetic state from the value of the cell resistance. Usually, the output resistance value is compared to a reference cell whose resistance is the average value of the low- and high-resistance state (Fig. 5.5c). To discriminate between the two possible MTJ states in a fast and reliable way, the cell-to-cell distribution of low resistance and high-resistance states must be separated by at least $6\left(\sigma_{low} + \sigma_{high}\right)$, where σ_{low} and σ_{high} are, respectively, the half-width of the distributions of low- and high-resistance states over an MRAM chip (Fig. 5.5b).

During read, the read current is chosen so that the voltage across the MTJ during read is in the range 0.1–0.2 V. This choice is motivated by two reasons:

1. In MTJs in general and in MgO-based MTJ in particular, the TMR amplitude decreases with bias voltage. As an example, this is illustrated in Fig. 5.6. This TMR decrease versus V is explained by a reduction of the spin polarization as the bias voltage increases due to the fact that the spin filtering mechanism associated with the symmetry of the wave becomes less effective at higher voltage (see Chapters 1 and 2). Also, hot tunneling electrons injected in the receiving electrode after tunneling generate magnetic excitations in the ferromagnetic electrodes, which can contribute to depolarize the tunneling current. With read voltage in the range of 0.1–0.2 V, the decrease of TMR compared to the maximum amplitude at very low voltage is no more than 10% in relative value.
2. The second reason for which the reading is performed at relatively low voltage is to avoid spin-transfer torque disturbance of the storage layer magnetic state by the read current as explained in the following section.

WD EX1057
Western Digital v IP Bridge
Page 110

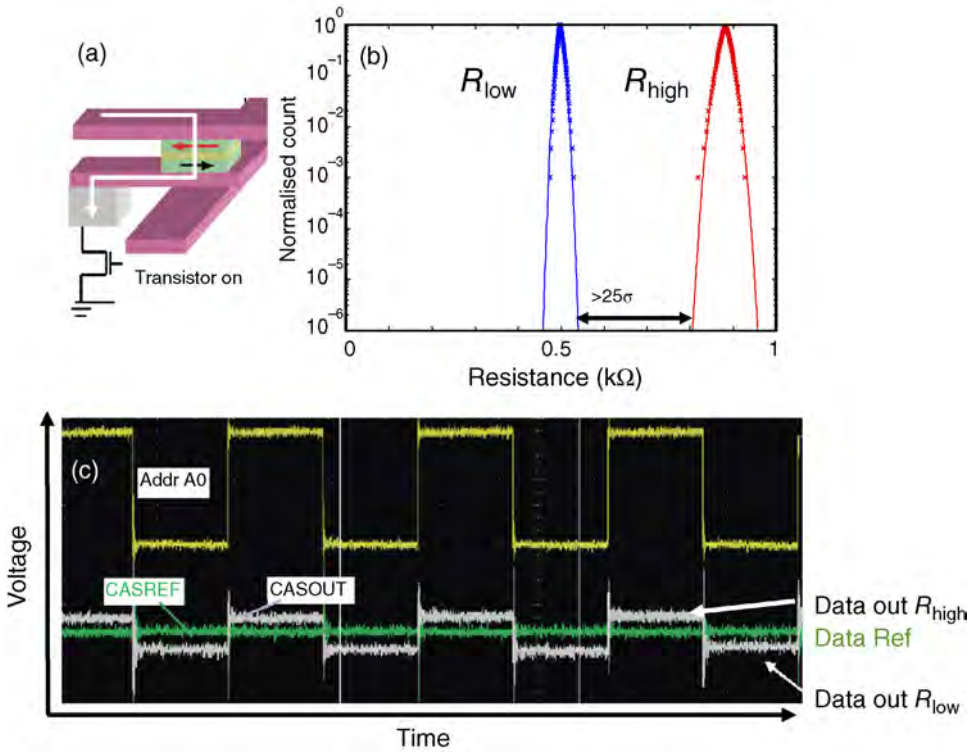


Figure 5.5 Principle of read operation. (a) During read, a current flows through the MTJ to determine the resistance state. (b) The distributions of R_{low} corresponding to P state and R_{high} corresponding to AP state must be sufficiently separated to allow fast and reliable discrimination between the two memory states. Here, data from Crocus Technology on a 1 Mbit TA-MRAM chip in 130 nm technology. (c) Example of readout signal from the same 1 Mbit chip as in part (b): top curve, address signal switching between two cells in opposite magnetic states; low curves, comparison of the readout signal from the read cells with a reference cell having an intermediate resistance $(R_{low} + R_{high})/2$.

5.3.2 STT-Induced Disturbance of the Storage Layer Magnetic State During Read

Since during read a current flows throughout the MTJ, it exerts a STT on the storage layer magnetization very similar to the write current in STT-MRAM. In order to avoid writing during read, the read current must be low enough compared to the STT critical current for switching. The failure rate during read associated with accidental STT switching of the storage layer magnetization during read can be estimated as follows. Let I_0^{STT} indicate the critical current for switching by STT. The barrier height for magnetization switching under a read current $I_{read} < I_0^{STT}$ is decreased due to the STT influence according to

$$\Delta E = \Delta E_0 \left(1 - \frac{I_{read}}{I_0^{STT}}\right)^{\delta}, \tag{5.15}$$

where ΔE_0 is the barrier height at zero current, as given by Eqs. (5.5) or (5.13). The exponent δ is usually taken equal to 1. However, recent experimental studies and

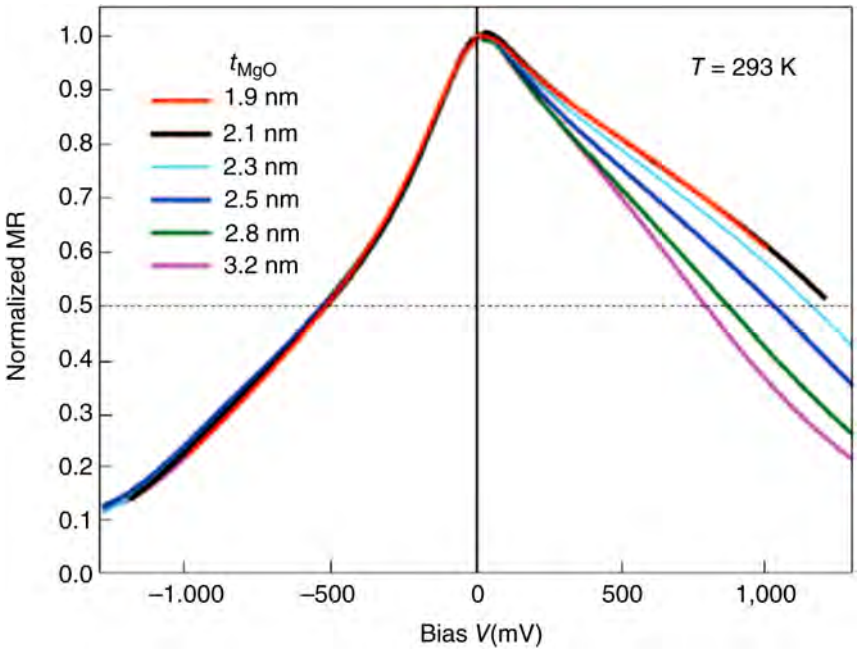


Figure 5.6 Dependence of the TMR amplitude in Fe(0 0 1)/MgO(0 0 1)/Fe(0 0 1) tunnel junctions with various MgO thicknesses t_{MgO}. The direction of bias voltage is defined with respect to the top electrode. (From Ref. 1 with permission from Nature Publishing Group.)

theories based on the Fokker–Planck equation (9) have concluded that δ should be taken equal to 2. With the same notation as for expression (5.4), this yields the following failure rate during read:

$$F(t) = 1 - \exp(-Nt/\tau) = 1 - \exp\left[\frac{-Nt}{\tau_0}\exp\left(-\frac{\Delta E}{k_B T}\left(1 - \frac{I_{read}}{I_0^{STT}}\right)^{\delta}\right)\right]. \qquad (5.16)$$

Figure 5.7 shows how the read current has to be adjusted with respect to the STT critical current for switching depending on the storage layer thermal stability factor and on the required failure rate. In STT-MRAM, the write voltage on the order of 0.5 V and the read voltage on the order of 0.15 V are typically used, corresponding to a I_{read}/I_0^{STT} ratio between 1/3 and 1/4.

5.4 FIELD-WRITTEN MRAM (FIMS-MRAM)

Two categories of field-induced magnetic switching MRAM (FIMS-MRAM) are described in this section. These are MRAM based on the Stoner–Wohlfarth model and an improved version: the "toggle" MRAM, which reached the market in 2006.

5.4.1 Stoner–Wohlfarth MRAM

The Stoner–Wohlfarth MRAM (SW-MRAM) was the first developed category of MTJ-based MRAM. The research and development in this area has been very useful

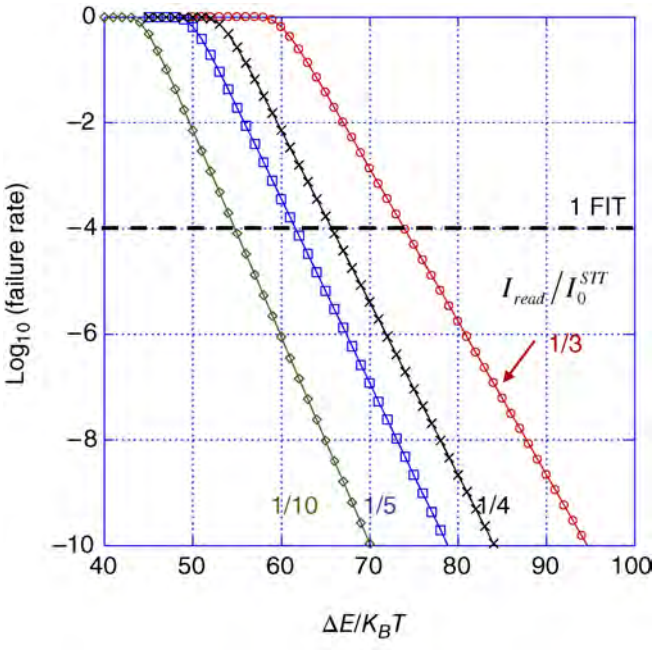


Figure 5.7 Calculated failure rate during read as a function of the thermal stability factor in standby for several values of the I_{read}/I_0^{STT} ratio (assumption $\delta = 1$). The plot assumes that 8 bits are read simultaneously during 10% of the time for 10 years. The dashed line corresponds to an example situation where one FIT would happen in 10 years with a probability of 10^{-4}.

in starting the development of hybrid CMOS/MTJ technology but it did not yield a product because of write selectivity problems and poor downsize scalability, as explained below.

SW-MRAM consists of an array of MTJs in which each MTJ is connected in series with a selection transistor (Fig. 5.8). The MTJs are sandwiched between two

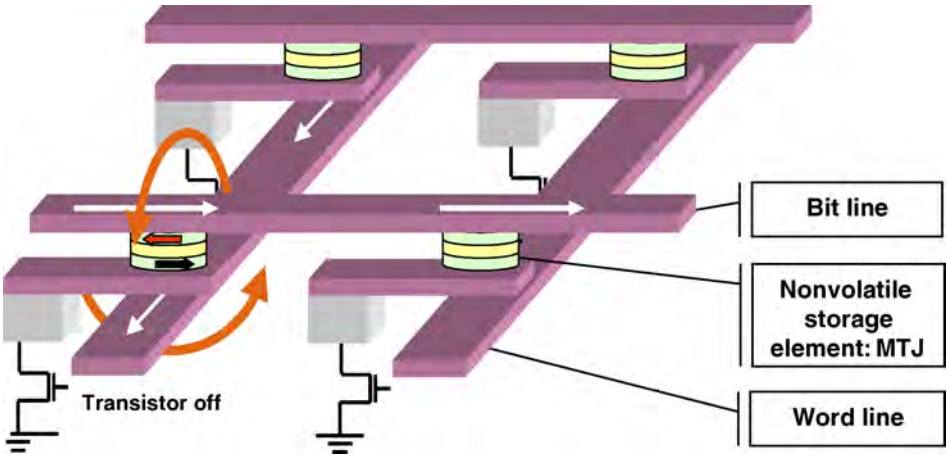


Figure 5.8 Schematic representation of a SW-MRAM array. The MTJs are patterned as elliptical cylinders. They are in-plane magnetized with one layer of fixed magnetization pinned along the ellipse long axis ("reference layer," black arrow) and one layer of switchable magnetization having two stable states along the ellipse long axis ("storage layer," red arrow). To address the memory element located at the front left of the array, two pulses of current (represented by white arrows) are simultaneously sent in the bit line and word line that cross each other at the addressed memory point. These pulses generate two perpendicular magnetic fields (represented by orange arrows), which add as two vectors at the addressed memory point.

WD EX1057
Western Digital v IP Bridge
Page 113

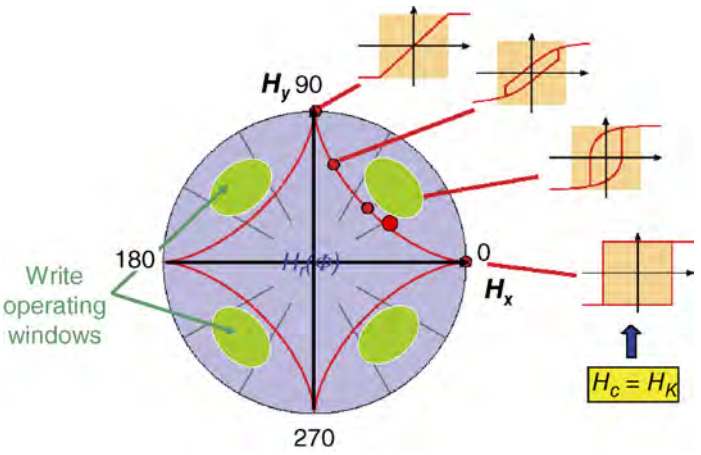


Figure 5.9 Stoner–Wohlfarth astroid (in red). Examples of hysteresis loops measured for various directions of field in the (x, y) plane. The operating windows for SW-MRAM are indicated in green.

sets of orthogonal conducting lines (bit lines and word lines) aimed at creating local magnetic fields on the MTJ's storage layer when current flows are sent along them. To write at a particular addressed cell, two simultaneous pulses of current are sent in the bit line and world line, which cross each other at the addressed MTJ cell. These currents must be adjusted so that the resulting field at the addressed cell is locally large enough to switch its storage layer magnetization in the desired direction while not switching the storage layer magnetization in the other memory points located further along the same bit line or the same world line. Indeed these other memory cells also feel the field created by the current pulse but not the two perpendicular fields simultaneously. They are called half-selected bits.

In these SW-MRAMs, the write selectivity is thus based on the combination of two orthogonal magnetic fields, one along the easy axis of magnetization, the other along the hard axis. This write principle is described in more detail in Chapter 4. It is based on the so-called Stoner–Wohlfarth switching astroid (Fig. 5.9) that provides a quantitative criterion for magnetization switching in a magnetic nanostructure with uniaxial anisotropy. To review the principle, a magnetic nanostructure of magnetization M_s has a uniaxial anisotropy described by an anisotropy energy per unit volume K_u. This nanostructure is assumed to be sufficiently small so that its magnetization remains homogeneous and therefore can be described in the macrospin approximation. We now assume that the magnetization is initially oriented in one direction along the easy axis of magnetization and that we want to switch it in the opposite direction. This is achieved by applying simultaneously a field along the easy axis of magnetization (H_x) and another one in the orthogonal direction, that is, along the hard axis of magnetization (H_y). It was demonstrated that in this situation, the condition for switching is that the total field vector of components (H_x, H_y) must fall out of the Stoner–Wohlfarth astroid, which is defined by the relationship

$$H_x^{2/3} + H_Y^{2/3} = \left(\frac{2K_u}{M_s}\right)^{2/3}. \tag{5.17}$$

This sets a lower limit to the amplitude of the write field in a SW-MRAM chip.

WD EX1057
Western Digital v IP Bridge
Page 114

In order to avoid half-selected bits to switch, the easy axis field must be lower than the anisotropy field H_k given by $H_K = (2K_u/M_s)$, otherwise this field alone would switch all bits located along the corresponding word line. Thus, taking into account the lower limit set by the SW astroid and upper limit set by the anisotropy field, this defines the ideal operating window for SW-MRAM. However, in practical devices, several factors actually restrain the size of this operating window:

1. The SW astroid in elliptic MTJ of typical dimensions 100 nm × 200 nm is often distorted due to micromagnetic distortions of the magnetization.
2. The switching criterion given by the SW astroid is actually valid only at 0 K. For devices operating at ambient temperature, thermal activation can significantly assist the magnetic switching so that the operating window must be pushed further away from the theroretical astroid.
3. Due to variability in the patterning process, cell-to-cell distributions in effective anisotropy field lead to cell-to-cell distribution in the shape and size of the SW astroid. As a result of these phenomena, it was very difficult to find any write operating window in SW-MRAM chips, even those of moderate capacity (e.g., 1 Mbit). That is, no write conditions exist in which all bits could be properly written without writing any half-selected bits.

Fortunately, a solution to this problem was found by Savtchenko et al. from Freescale Technologies called "toggle writing (10)."

5.4.2 Toggle MRAM

5.4.2.1 Toggle Write Principle Toggle MRAM are also written with magnetic fields but the structure of the MTJ storage layer and the synchronization of the two orthogonal pulses of magnetic field differ from SW-MRAM. The magnetization in the MTJ ferromagnetic layers is still in-plane and the cells are patterned in elliptical shape, providing a uniaxial shape anisotropy with easy axis along the long axis of the ellipse. In toggle MRAM, the ellipses are oriented at 45° with respect to the bit lines and word lines to optimize the write process, as explained below. Concerning the storage layer composition, the latter consists of a compensated synthetic antiferromagnet, that is, two ferromagnetic layers of same magnetic moment antiferromagnetically coupled through a thin Ru spacer layer. At rest, the magnetic moments of these two layers lie antiparallel along their easy axis of magnetization. In toggle-MRAM, the resistance state is determined by the magnetic orientation of the magnetic layer, which is in contact with the tunnel barrier.

When a moderate field is applied to such a structure, a magnetic transition takes place at a field called "spin–flop field" between a configuration at low fields, wherein the magnetic moments of the two layers lie antiparallel along their common anisotropy axis, and a configuration above the spin–flop field, where they lie symmetrically with respect to the field direction in a scissor configuration (see Fig. 5.10). This scissor configuration is called the spin–flop configuration. As a result, at low fields, the system has no net magnetic moment, whereas above the spin–flop field, it acquires a net magnetic moment.

WD EX1057
Western Digital v IP Bridge
Page 115

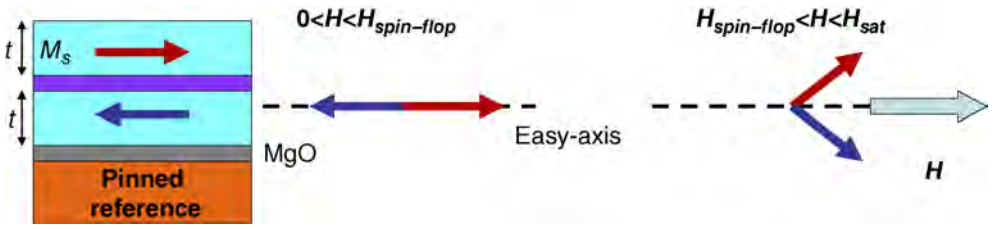


Figure 5.10 Schematic explanation of the spin–flop transition that takes place in the synthetic antiferromagnetic storage layer of a toggle MRAM cell.

The spin–flop field $H_{spin-flop}$ is given by the following expression (11):

$$\mu_0 M_s H_{spin-flop} = 2\sqrt{K_{eff}\left(\frac{A}{t} + K_{eff}\right)}, \tag{5.18}$$

where M_s (A/m) is the saturation magnetization of the two ferromagnetic layers (assumed here to be identical), t (m) is their thickness, K_{eff} (J/m^3) is their effective anisotropy per unit volume mainly of shape origin, and A (J/m^2) is the amplitude of the interfacial antiferromagnetic coupling through the Ru spacer. Therefore, the spin–flop field can be adjusted by varying the cell aspect ratio, which determines K_{eff} or the ferromagnetic layers thickness or the Ru thickness, which determines the amplitude of the antiferromagnetic coupling. Typical values of this spin–flop field in toggle MRAM are on the order of $\mu_0 H_{spin-flop} = 5$ mT. The write toggle operation then proceeds as represented in Fig. 5.11.

In the initial state, the two ferromagnetic layers are in antiparallel magnetic configuration along the long axis of the elliptical cell. At t_1, a current is sent in the x-line generating a magnetic field on the storage layer in the y-direction. This field is typically on the order of 7–10 mT, above the spin–flop transition. The two magnetizations then scissor in the direction of this field and get in spin–flop configuration. The applied field is then gradually rotated by two steps of 45°. This is achieved by applying simultaneously a current along the x-line and y-line between t_2 and t_3, then only along the y-line between t_3 and t_4. During these steps, the spin–flop magnetic configuration rotates with the field. The y-current is then stopped. Since no more magnetic field is applied, the magnetization of the ferromagnetic magnetic layers then

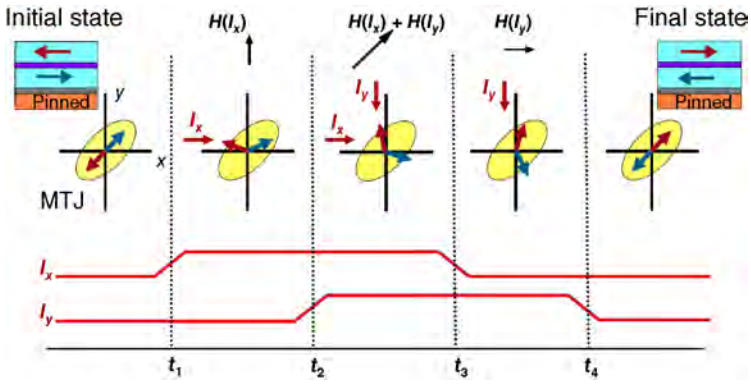


Figure 5.11 Toggle write operation sequence. (After Ref. 12 with permission from IEEE.)

WD EX1057
Western Digital v IP Bridge
Page 116

relax back to the antiparallel configuration along their easy axis of magnetization. In the final state, both layers have rotated by 180°. This writing process takes between 10 and 20 ns (12).

In order to maximize the field produced by a given current in the word and bit lines and better confine the field at the memory element, these lines are coated on their faces opposite to the memory element with a soft magnetic material (cladding) (13). This material gets polarized by the Ampere field created by the current flowing in the line and helps focus the field on the storage layer. Typically, a factor 2 gain in field amplitude is obtained, thanks to the cladding. The application of this sequence of current pulses systematically rotates the storage layer magnetization by 180° whatever the initial state of the system (i.e., independent of whether a "0" or a "1" is written in the memory element). Therefore, it is necessary to read before write to determine whether the magnetic state has to be changed or not.

5.4.2.2 Improved Write Margin Toggle writing provides a much wider operation window than SW writing as illustrated in Fig. 5.12 on a 4 Mbit toggle chip from Everspin Technologies. In toggle writing, the energy barrier to switch half-selected bits is many times larger than for switching fully selected bits (14). Thanks to these improved write performances, Everspin Technologies succeeded in launching the first MRAM products in 2006 (15).

5.4.2.3 Applications of Toggle MRAM Toggle MRAM have many interesting features that combine the advantages of static random-access memory (SRAM) and Flash memory. Toggle MRAM is nonvolatile as in the case of Flash, with a projected retention of more than 10 years. Their read–write cycle is on the order of 35 ns. They can work in applications at various ranges of temperature: commercial (0–70 °C), industrial (−40–85 °C), extended (−40–105 °C), and automotive AEC-Q100 Grade 1 (−40–125 °C). They occupy a relatively small surface area, for a capacity of up to 16 Mbit in one chip. They combine the functions of several types of memory: Flash, SRAM, EEPROM, nvRAM, and battery-backed SRAM. Their radiation hardness makes them interesting for space and avionic applications. Toggle MRAM is already

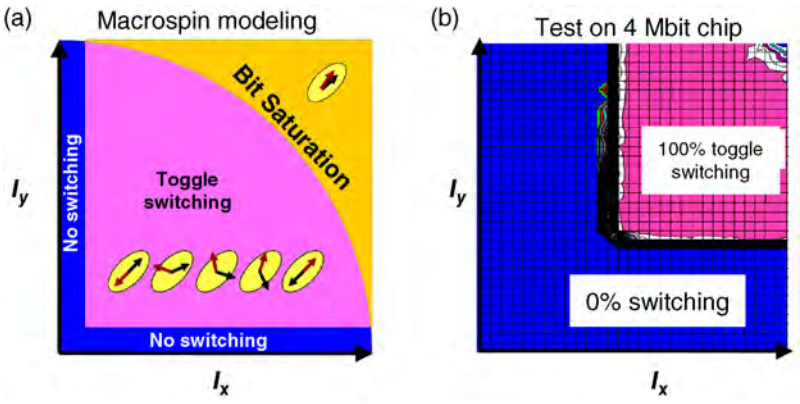


Figure 5.12 Toggle operation windows determined from macrospin modeling (a) and from testing a 4 Mbit chip (b). (After Ref. 12 with permission from IEEE.)

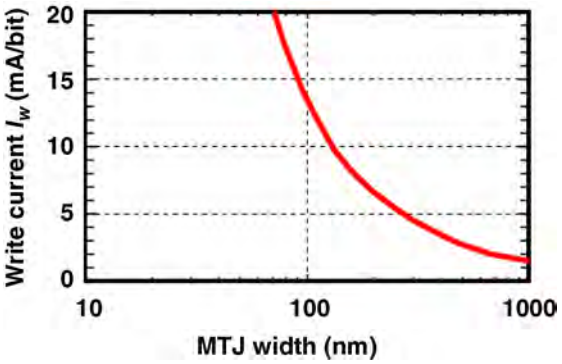


Figure 5.13 Write current versus MTJ short axis dimension (aspect ratio is typically between 2 and 2.5). The write current is here defined as the sum: $I_w = I_{word\ line} + I_{bit\ line}$.

used in a variety of applications: microcontrollers, automotive industry, motorcycles, slot machines, satellites, airplanes, and so on. However, their power consumption remains relatively large due to the large current required to generate the pulses of magnetic field (~10 mA).

5.4.3 Limitation in Downsize Scalability

In field-written MRAM, downsize scaling is mainly limited by electromigration taking place in the field-generation word and bit lines. This can be understood as follows: In order to ensure sufficient memory retention, the volume of the storage layer must fulfill the relationship $K_{eff}V > \sim 70\, k_B T$, in which V is the volume of the storage layer and K_{eff} is its effective anisotropy (see Section 5.2.2). As the feature size F decreases, the volume of the storage layer decreases as F^2 so that the effective anisotropy must be increased as F^{-2}. In toggle writing, the spin–flop field given by Eq. (5.18) roughly scales as $(K_{eff})^{1/2}$, that is, as F^{-1}. This spin–flop field is the lower limit of the write field in toggle MRAM. Because the distance between the center of the field-generating line and the storage layer does not vary significantly as the technology shrinks, the current required to generate the write field is proportional to the write field amplitude and therefore roughly scales as F^{-1}, as illustrated in Fig. 5.13. In terms of current density, if only the width of the field generating lines decreases while their height is approximately constant, the current density in these lines increases as F^{-2} when F itself decreases. Since the electromigration threshold in Cu is $\sim 10^7$ A/cm^2, this limits the MTJ width to dimensions above 100 nm. Therefore, the downsize scalability of toggle MRAM and of other types of field-written MRAM is limited by this consideration.

5.5 SPIN-TRANSFER TORQUE MRAM (STT-MRAM)

In STT writing, a polarized electrical current exerts a torque called spin-transfer torque on the magnetization of the storage magnetic layer, which can switch its direction for a large enough current density. For high density and fast read–write operation, STT-MRAM provides a good alternative to FIMS-MRAM. The STT-MRAM cell is simplified in comparison to FIMS-MRAM cell since no field lines are

WD EX1057
Western Digital v IP Bridge
Page 118

required. Each cell consists of only a MTJ connected in series with a selection transistor. The writing is performed with bipolar pulses of current. The reading is performed at lower current to avoid write errors during read.

Writing a "0" (i.e., a parallel configuration of the magnetization in the storage and pinned layers) can be achieved by sending a current pulse through the stack, the electrons flowing from the pinned layer to the storage layer. Writing a "1" can be achieved by sending a pulse of current of opposite polarity. This approach clearly solves the write selectivity problem of the SW-MRAM since the write current flows only through the addressed cell so there is no risk of writing an unselected cell. Another major advantage of the STT write approach is the downsize scalability. Indeed, the critical current for which the magnetization switches due to the STT influence is determined by a critical current density (3) so that the total current required to write a memory cell scales as the area of the cell, assuming a constant free layer thickness. As a result, the STT writing approach offers much better downsize scalability than FIMS-MRAM. However, at very small dimensions, there are still problems concerning the thermal stability of the information written in the cell, as explained in Section 5.4.1. These limit the downsize scalability of in-plane magnetized STT-MRAM down to about 60 nm × 150 nm and for out-of-plane magnetized STT-MRAM to dimension on the order of 20 nm as explained further.

5.5.1 Principle of STT Writing

When a spin-polarized current flows through a magnetic nanostructure, the STT results from the interaction between the spin of the conduction electrons and those responsible for the nanostructure magnetization. This torque is exerted on the local magnetization and tends to switch it toward a direction parallel or antiparallel to that of the spin polarizing layer depending on the current direction. The physical origin of the STT was explained in detail in Chapter 1. It can be summarized as follows: Each conduction electron has angular momentum $\hbar/2$. Considering that the current has a finite spin polarization (typically between 40 and 80%), and taking into account the details of the interactions between the conduction electrons and the local magnetization, yields a STT efficiency coefficient η $(0 < \eta < 1)$ so that the average angular momentum carried by each electron becomes $\eta(\hbar/2)$. In a multilayered pillar geometry, the number of electrons per unit time and unit area flowing perpendicular to the plane of the layers is given by J/e (J being the current density and e the absolute value of the electron charge) so that the corresponding flow of angular momentum per unit area is $\eta(J/e)(\hbar/2)$. When such a spin-polarized incoming flow of electrons penetrates in a magnetic layer, the spin of these electrons gets reoriented in the direction parallel to the local magnetization within ~1 nm. This corresponds to an interfacial absorption of the incoming flow of transverse angular momentum. By conservation of overall angular momentum, this absorption results in a torque exerted on the local magnetization, the spin-transfer torque given by

$$\Gamma_{STT} = -\gamma\eta\frac{J}{e}\frac{\hbar}{2}\frac{1}{\mu_0 M_s d}\hat{m}\times(\hat{m}\times\hat{p}), \tag{5.19}$$

WD EX1057
Western Digital v IP Bridge
Page 119

where $\hat{m}$ and $\hat{p}$ are unit vectors, respectively, along the magnetic nanostructure magnetization and incoming spin polarization (often set by the direction of magnetization of the reference layer in a MTJ), d is the nanostructure thickness along the current direction, M_s its magnetization, γ is the gyromagnetic ratio, and μ_0 the vacuum permeability. This expression was first established by Slonczewski in 1996 (16,17). This term is often called Slonczewski torque or in-plane torque (since it lies in the plane defined by $\hat{m}$ and $\hat{p}$) or damping-like torque (since it has the same form as the damping term in the LLG equation, see below). In magnetic tunnel junctions, it was shown that the STT also introduces a second term called field-like term, but which has an amplitude of only 10–25% of the Slonczewski STT torque. This second term most often is considered as having a negligible role in the design of STT-MRAM (18).

As explained in Chapter 2, taking into account the STT, the general equation governing the dynamics of magnetization of the magnetic nanostructure is written as

$$\frac{d\hat{m}}{dt} = -\gamma\left(\hat{m}\times\vec{H}_{eff}\right) + \alpha\left(\hat{m}\times\frac{d\hat{m}}{dt}\right) - \frac{\gamma\hbar}{2\mu_0 M_s}\frac{1}{d}\frac{\eta J}{e}\hat{m}\times(\hat{m}\times\hat{p}). \tag{5.20}$$

In this equation, an extension of the famous Landau–Lifshitz–Gilbert (LLG) equation (see Chapter 3), the first term describes a precessional motion of the magnetization around the local effective field $\vec{H}_{eff}$, which contains contributions from the applied field, the demagnetizing field, the anisotropy field, and the STT field-like term (if it is taken into account). This first term is conservative, that is, conserves energy. The second term is the Gilbert damping term that describes the magnetic dissipation in the system, that is, the fact that in the absence of STT influence, the magnetization tends to gradually relax toward the local effective field. This term always dissipates energy. The third term is the STT previously discussed. Interestingly, this term is also nonconservative. Furthermore, depending on the current direction through the magnetic nanostructure (e.g., the storage layer in a STT-MRAM cell), this term can absorb or dissipate energy, which means that it either behaves as a damping or antidamping term. If the current has the proper direction and the current density is large enough, the STT antidamping effect can exceed the natural Gilbert damping. Very peculiar magnetization dynamics effects then arise, such as STT-induced magnetization switching (3,4) or magnetization steady-state oscillations (19). STT offers a new way to manipulate the magnetization of magnetic nanostructures. STT-induced magnetization switching provides a new way to write the information in MRAM or logic devices. STT-induced steady-state magnetic oscillations allow the generation of RF voltage and thus new types of frequency-tunable RF oscillators.

The possibility to use the STT to switch the magnetization of a free layer in a magnetoresistive stack was first demonstrated in metallic pillars called spin-valves[3] traversed by a current flowing perpendicular to the plane of the layers. The latter comprise a thick magnetic layer of fixed magnetization acting as a current polarizer and a second magnetic layer of switchable magnetization that reacts to the STT influence from the fixed layer magnetization. These two magnetic layers are magnetically decoupled, thanks to a thin, nonmagnetic, metallic spacer, typically Cu 3–5 nm thick. The current density required to switch the magnetization in these metallic pillars was on the order of 2×10^7 A/cm^2. A few years later, thanks to the progress made in

WD EX1057
Western Digital v IP Bridge
Page 120

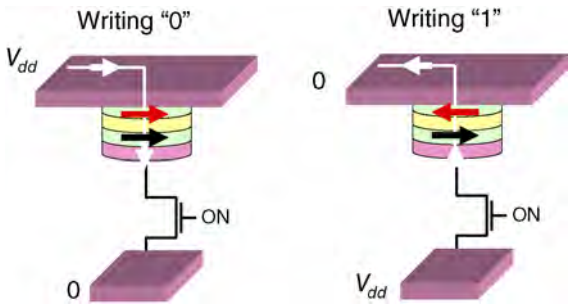


Figure 5.14 Principle of writing in STT-MRAM. Each STT-MRAM cell consists of an MTJ connected in series with a transistor. To write the parallel magnetic configuration, a current flow of density larger than $j_{cAP\to P}$ is sent through the MTJ from the storage layer (red arrow) to the pinned reference layer (black arrow) (i.e., electrons tunnel from the pinned reference layer to the free layer). To write the antiparallel magnetic configuration, a current flow of density larger than $j_{cP\to AP}$ is sent through the MTJ from the reference layer (red arrow) to the storage layer.

the development of low *RA* (resistance × area product) magnetic tunnel junctions, magnetization switching induced by STT was also observed (4). Interestingly, the current density required to write in MTJ was lower than in metallic pillars (in the range $2–6 \times 10^6$ A/cm^2 in MTJ) mainly due to a higher effective spin polarization in MTJ compared to spin-valves. Since then, the interest in STT in MTJs for STT-MRAM applications has kept on increasing. STT indeed provides a powerful write scheme in MRAM for several reasons:

- In STT-MRAM there is no need to create pulses of magnetic field. Each cell is directly written by the current flowing through the stack. As a result, the cells are much more compact than in field-written MRAM, as illustrated in Fig. 5.14.
- During write of a selected cell, the corresponding selection transistor in series with the MTJ is closed so that the write current flows only through the selected cell. This provides excellent write selectivity, much better than in field-written MRAM.
- As explained in Chapter 1, in STT writing, the condition for magnetization switching is set by a critical current density j_c (actually two critical current densities, $j_c^{P\to AP}$ and $j_c^{AP\to P}$, as will be explained later). The magnetization of the storage layer switches if the current density of proper direction exceeds j_c. This provides very good downsize scalability since the total current required to write scales like the cell area down to very small dimensions where it becomes limited by the thermal stability factor.

One can define switching voltages associated with the critical switching current densities. They are given by $V_c^{P\to AP} = (RA)_P(V) j_c^{P\to AP}$ and $V_c^{AP\to P} = (RA)_{AP}(V) j_c^{AP\to P}$, where *RA* is voltage-dependent resistance × area product of the MTJ in the corresponding magnetic configuration. Interestingly, in MTJ, whereas the critical current $j_c^{P\to AP}$ can be typically twice the critical current $j_c^{AP\to P}$ due to a weaker STT efficiency in P than in AP configuration, the critical voltage for switching from P to AP and from AP to P: $V_c^{P\to AP}$ and $V_c^{AP\to P}$ are very close in absolute values due to the larger *RA* value in the AP than in the P configuration.

WD EX1057
Western Digital v IP Bridge
Page 121

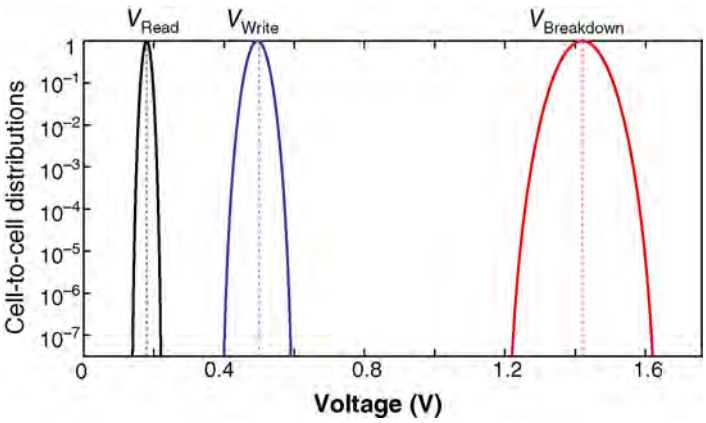


Figure 5.15 Schematic representation of the three voltage distributions (read, write, and breakdown) specific for STT-MRAM functioning.

5.5.2 Considerations of Breakdown, Write, Read Voltage Distributions

In conventional STT-MRAM, the write and read current paths are the same. In order to avoid write disturbance during read, the read voltage must be chosen low enough compared to the critical write voltage. There are therefore three voltage cell-to-cell distributions in an MRAM chip that need to be well separated for proper functioning and reliability of the chip. This is schematically illustrated in Fig. 5.15. These three distributions are as follows:

1. *The breakdown voltage distribution.* The MTJ tunnel barrier is a thin dielectric oxide layer (MgO ~1 nm thick). When exposed to an excessively large voltage, this barrier may experience dielectric breakdown. The breakdown voltage in the MTJ depends on the voltage pulse duration, the number of pulses, and even on the delay between pulses (20). Compared to CMOS dielectrics, these ultrathin MgO barriers are relatively resistant to breakdown. This mainly comes from the fact that the tunneling through the barrier is direct in normal working conditions, in contrast to Fowler-Nordheim tunneling as in Flash memories. As a result, upon cycling, less defects are generated in the MgO barrier than in CMOS oxides for Flash memory. For voltage pulse width in the range of 10 ns, the voltage breakdown is usually larger than 1.2 V even for $RA \sim 5\,\Omega{\cdot}\mu m^2$.
2. *The write voltage distribution.* At each write event (and to lesser extend read event), the tunnel barrier is exposed to an electrical stress that may cause electrical breakdown. To avoid breakdown failure, the highest write voltage in the distribution must be sufficiently low compared to the weakest MTJ in terms of breakdown. By adjusting the MTJ's stack composition and their *RA*, one tries to get this write voltage distribution centered around 0.5 V and be as narrow as possible (typical width as illustrated in Fig. 5.15). The distribution width mainly originates from fluctuations in the shape and particularly in edge defects associated with the patterning process.

WD EX1057
Western Digital v IP Bridge
Page 122

3. *The read voltage distribution.* The read voltage distribution originates from the variation in the resistance of the selection transistor that is connected in series with the MTJ. The read voltage across the MTJ is typically in the range 0.1–0.15 V. As explained in Section 5.3, it must be low enough compared to the write voltage in order to avoid any write disturbance during read caused by the STT from the read current. However, the lower the read voltage, the slower the read-out process. Therefore, a trade-off must be found.

5.5.3 Influence of STT Write Pulse Duration

The global picture of STT switching versus the current pulse width is shown in Fig. 5.16. As commonly observed in microelectronics, the larger the voltage (i.e., the current density), the faster the operation. Two distinct switching modes have been found, namely, thermal activation and precessional switching (21,22) (Fig. 16) (23). At finite temperature, thermal activation plays an important role in reducing the switching current at long current pulses (>10 ns). In this slow thermally activated switching regime, the switching current depends on the current pulse width τ and thermal stability factor $\Delta = K_u V/k_B T$ of the free layer (24,25):

$$J_c(\tau) = J_{c0}\left[1 - \frac{k_B T}{K_u V}\ln\left(\frac{\tau}{\tau_0}\right)\right], \tag{5.21}$$

where $\tau_0 \sim 1$ ns is the inverse of the attempt frequency and $K_u V$ is the anisotropy energy.

J_{c0} is the so-called critical current that corresponds to the linearly extrapolated value of the switching current density for a pulse duration of 1 ns.

For fast precessional switching in the nanosecond regime (less than a few nanoseconds), the required switching current is several times greater than the critical

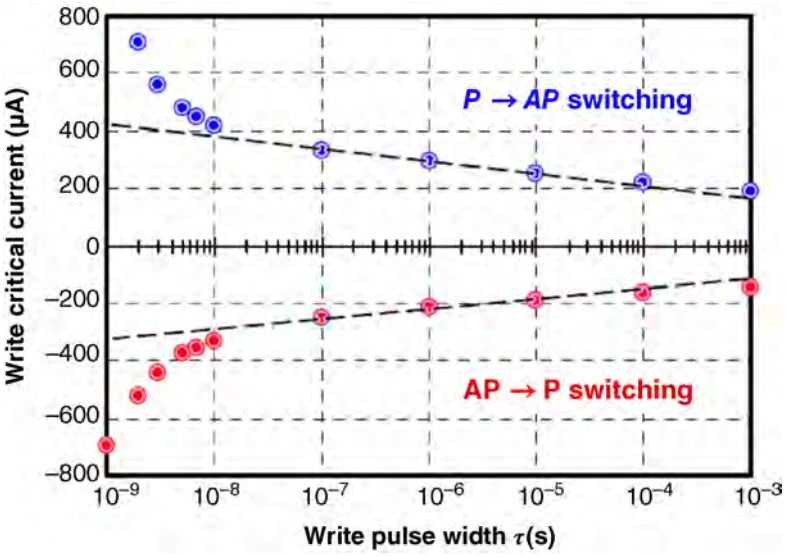


Figure 5.16 Typical values of STT switching current density (normalized by J_{c0}) as a function of write pulse width (After Ref. 23 with permission from IEEE).

WD EX1057
Western Digital v IP Bridge
Page 123

current. In this regime, the switching time varies as (24)

$$\tau_{switching} = \frac{(1+\alpha^2)}{\gamma H_K} J_{c0} \frac{Ln(\pi/\theta_0)}{((J/J_{c0})-1)}, \tag{5.22}$$

where α is the Gilbert damping, H_k the anisotropy field, γ the gyromagnetic ratio, and θ_0 is the angle between the storage layer magnetization and the current spin polarization at the onset of the current pulse. This initial angle is often due to random thermal fluctuations that may cause stochasticity in the magnetization switching and slow down the write process. Some particular embodiments such as one with orthogonal polarizers, as described in Section "Perpendicular Polarizer," may help to improve the reproducibility (deterministic character) of the switching dynamics. Equation (5.22) illustrates that the larger the current density, the faster the switching, that is, the shorter the write current pulse. In this regime, the tunnel barrier may however be exposed to a too large electrical stress that may result in accidental electrical breakdown.

Typical write speeds in operation in STT-MRAM are around 5–10 ns, which corresponds to the intermediate regime between thermally activated and precessional switching.

5.5.4 In-Plane STT-MRAM

The first investigated MTJs for STT-MRAM were in-plane magnetized MTJ, meaning that both magnetic electrodes have in-plane magnetization. The reason is mainly historical since, besides the tunnel barrier itself, their configuration is fairly close to that of spin-valves that had been developed for hard disk drive magnetoresistive heads since 1991. However, as will be explained further, their performance and downsize scalability is not as good as for STT-MRAM based on out-of-plane magnetized MTJ. But the latter are more difficult to prepare so that their optimization is still on-going.

5.5.4.1 Critical Current for Switching The expression of the critical current for switching obtained in a macrospin model and at zero temperature is (26) given as

$$J_{c0} = \frac{2e\alpha\mu_0 M_s t_F (H + H_k + (M_s/2))}{\hbar\eta}, \tag{5.23}$$

where H is the applied field along the easy axis, M_s and t_F the magnetization and the thickness of the storage layer, α is the damping constant, H_k the in-plane anisotropy field (magnetocrystalline and shape), η the spin-transfer efficiency. This relationship is derived by analyzing the stability of the solution of the LLG Eq. (5.20) under STT influence. When the injected current has the proper direction (see caption of Fig. 5.14) and is larger than $J_c(\tau)$ (Section 5.5.3), τ being the pulse duration, the magnetization reverses. In this expression, the term $M_s/2$ is usually much larger than $(H + H_k)$ by one or two orders of magnitude. This dominant role of the demagnetizing field term ($\mu_0 M_s/2$) comes from the fact that during the STT-induced switching of the magnetization of the in-plane magnetized layer, the magnetization has to precess out-of-plane, which increases the demagnetizing energy. As a result, a good approximation of J_{c0} is given

WD EX1057
Western Digital v IP Bridge
Page 124

by $J_{c0} = (e\alpha\mu_0 M_s^2 t_F)/\hbar\eta$. It is also important to note that because of the dominance of the demagnetizing field term in (5.23), the critical current for STT writing weakly depends on H_k, the in-plane anisotropy field that determines the thermal stability of the magnetization at rest. In other words, in in-plane magnetized MTJs, the barrier for STT switching is mainly related to the demagnetizing energy, whereas the barrier for thermal stability of the magnetization, that is, the memory retention, is determined by the in-plane shape anisotropy. The first barrier is usually much larger than the second one, which means that the in-plane magnetized configuration is not efficient in terms of compromise between thermal stability and writability. This is the reason why the out-of plane magnetized MTJ is more favorable, as will be explained in Section 5.5.

5.5.4.2 Minimization of Critical Current for Writing The reduction of the intrinsic critical switching current J_{c0} can be realized by materials and magnetic anisotropy engineering (lower M_s, higher spin polarization factor η, and perpendicular anisotropy) and MTJ and free layer structures improvement (dual stack, perpendicular polarizer). The main challenge is to reduce the critical current while maintaining a large enough thermal stability.

Dual Magnetic Tunnel Junction Dual MTJs consist of two MgO tunnel barriers of different resistances, two pinned reference layers aligned antiparallel, and a free storage layer sandwiched between the two tunnel barriers. In such dual structure, STT effect is enlarged by the double spin-torque current acting on both sides of the free layer (21). Moreover, this type of structure reduces the asymmetry of the writing current, which is helpful for a wider read–write margin.

Perpendicular Polarizer The efforts to reduce the energy to write one cell have mostly concentrated on reducing the threshold of critical current density. This reduction also reduces the current value that the selection transistor has to sink/drive, and therefore smaller transistor sizes can be achieved. Another possibility to reduce the energy used to write one bit is to shorten the time that current/power needs to be applied to switch the magnetic configuration of the storage element. To achieve sub-nanosecond switching times, it is possible to take advantage of the precessional motion of the magnetization around the effective field direction before it aligns itself with this direction. The precession frequency can be calculated from Kittel's formula, $(2\pi f/\gamma\mu_0)^2 = H_{eff}(M_s + H_{eff})$, where f is the frequency, γ the gyromagnetic ratio, and M_s the saturation magnetization assumed to be parallel to the effective field H_{eff}. Typically, f is in the gigahertz frequency range for common ferromagnetic materials.

The precessional switching approach has already been explored in magnetic field driven switching concepts (27,28). In this case, a magnetic field pulse is applied in the hard axis direction. The magnetization starts precessing around the hard axis direction and, by doing so, acquires an out-of-plane component. Even at small angles, this out-of-plane magnetization generates a large demagnetizing field in the out-of-plane direction, becoming the new dominant field direction. The magnetization then precesses around this out-of-plane field direction. At each half-precession period the magnetization rotates by 180° and therefore changes from the initial magnetization

WD EX1057
Western Digital v IP Bridge
Page 125

direction to the opposite direction, all this at gigahertz frequencies. By properly timing the field pulse duration to stop at a half precession, it is possible to achieve sub-nanosecond switching of the magnetization. In magnetic field-driven precessional switching, this half precession corresponded to 140 ps. Field precessional switching was not pursued in actual MRAM demonstrations because the currents required to generate the hard axis field are large and cannot be scaled down by cell size reduction. Another problem is the need to accurately control the pulse duration with an accuracy of typically ±50 ps in a large capacity chip.

A more promising way to achieve precessional switching in the sub-nanosecond range with real scaling possibilities was proposed (29,30) in parallel to studies on spin-transfer oscillators. These spin-transfer oscillators use a perpendicular spin polarizer to induce the precession of the magnetization of an in-plane ferromagnetic layer, without an external applied field (Fig. 5.17) (31). In this case, the precession frequency can be controlled by the current density flowing through the device. The first demonstrations of precessional switching were realized in full metallic current-perpendicular-to-plane GMR systems (32,33). The structure in this case corresponded to a bottom perpendicular spin polarizer based on a Co/Pt multilayer separated from a NiFe 3/Co 0.5 nm storage layer by a Cu spacer. The reference layer was Co 3 nm pinned by an IrMn layer. The storage layer magnetization precesses around the normal to the layers for current densities higher than $j_c = (2e/\hbar)(M_s t/g)(H_k/2)$, H_k being the in-plane anisotropy field (32). The precession frequency increases linearly with the current density up to a maximum equal to $2\gamma M_s$. Figure 5.17 illustrates this concept of the spin-transfer precessional switching.

The storage layer changes its magnetic orientation from the initial direction to the opposite 180° direction within 250 ps and back to the initial direction after 500 ps. The switching probability of the initial precession is 100%, while for subsequent precessions there is a gradual lack of precession coherence due to thermal

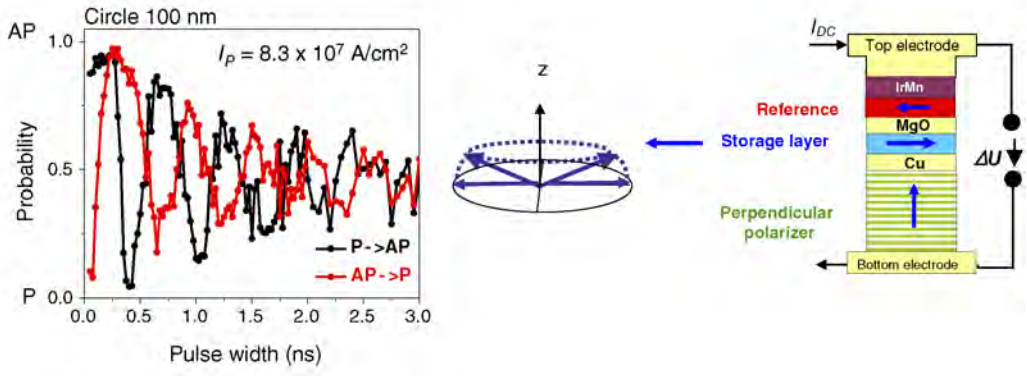


Figure 5.17 Illustration of the concept of spin-transfer precessional switching. The stack (right) includes a perpendicular spin polarizer, the precessing storage layer, and the reference layer. This latter layer is aimed to convert the storage layer direction change into a resistance change. The graph shows how the probability of magnetic switching of the storage layer oscillates between parallel and antiparallel alignment as a function of current pulse duration with a frequency of ~1 GHz for a current density of 8×10^7 A/cm^2. (After Ref. 32 with permission from AIP Publishing LCC.)

WD EX1057
Western Digital v IP Bridge
Page 126

fluctuations, which is not detrimental to the application, since only the initial half precession is actually required to realize the switching. The precession can be induced by a current density of $\sim 8 \times 10^7$ A/cm^2 and it is actually independent of the current direction. This is shown by the two different traces, one starting at the parallel configuration, while the other starts in the antiparallel configuration. This is important, since the transistor to be connected to these cells can be optimized for one current polarity. This means that higher currents per transistor lateral size has also been achieved, ultimately allowing for smaller cells. The same switching process has also been used with magnetic tunnel junction cells (34–36). In these studies, swithing in less than 200ps were demonstrated with associated energy down to about 200fJ. The remaining difficulties with this technology are associated with i) the write endurance since pulses of voltage around 0.7 - 1V are used for ultrafast switching, ii) the assymetry between the P to AP and AP to P transition due to the STT from the in-plane analyzer, iii) improve the write error rate by an accurate control of the precessional motion of the storage layer magnetization.

Reduced Demagnetizing Field In the case of thin films with in-plane magnetization, the shape anisotropy energy that determines the value of the critical STT current can be reduced by adding an interface anisotropy term to the volume anisotropy term (37). This interface term can even be the leading term, thus spontaneously orienting the magnetization out-of-plane below a critical magnetic thickness. This phenomenon can be used to develop planar MTJ's with reduced demagnetizing field using magnetic metal-oxide combinations. In conventional MTJ, the demagnetizing field of the magnetic layer is $-\mu_0 M_s$. As explained earlier, it is usually the dominant contribution to the critical STT switching current linked to the in-plane anisotropy. However, the relative role of demagnetizing and anisotropy energy can be strongly modified in the presence of either volume or interfacial PMA. Indeed, in that case, the demagnetizing and anisotropy terms have opposite signs, leading to an expected significant reduction in critical current density (38,39). Since there are different ways to obtain interfacial out-of-plane anisotropy, several research teams have proposed structures based on this concept (40–42).

The first low demagnetizing structure was a spin-valve (40) that used interfacial anisotropy from Co/Ni multilayers, a very versatile system in which the PMA can be tuned over a wide range by changing the thickness of each layer and/or the number of repeats. The zero-thermal-fluctuation critical current Jc_0 is reduced by a factor of 5–6 ($Jc_0 = 2 \times 10^6$ A/cm^2) compared to control samples with high demagnetizing energy and the same total magnetic moment, while the thermal stability was almost the same. Further reduction in critical current is expected by optimizing the spin polarization using a magnetic tunnel junction rather than a spin-valve. The same team (43) fabricated MgO magnetic tunnel junctions using similar Co/Ni switching layers combined with a FeCoB insertion layer to reduce the effective demagnetizing field (thanks to interface anisotropy) to 0.2 T, still keeping the tunnel magnetoresistance ratio as high as 106%. However, the use of Co/Ni or Pt/Co materials in the switching layer is not recommended because of increased damping and difficulties in maintaining high TMR in MTJs because such materials with fcc (1 1 1) texture are incompatible with the (1 0 0) texture of the MgO barrier.

WD EX1057
Western Digital v IP Bridge
Page 127

Large interfacial out-of-plane anisotropy has also been evidenced at Co(Fe)–oxide interfaces (44–46). This interfacial anisotropy is able to orient the magnetization of a 1 nm thick CoFeB layer out-of-plane (47). This makes it possible to obtain a free layer with a low effective demagnetizing field in planar MTJ just by increasing the layer thickness in order to decrease the relative anisotropy contribution of the CoFeB–MgO interface. The effect of the CoFeB composition on device characteristics (anisotropy and critical thickness) was investigated in full MTJ stacks with bottom pinned $Co_{80-x1}Fe_{x1}B_{20}$ and top free $Co_{80-x2}Fe_{x2}B_{20}$ electrodes with $x_1 = 20$, 40, 60, and $x_2 = 20$, 60 (41). MTJs with a free layer thickness of 1.8 nm were compared with standard devices, resulting in a 40% reduction in the average quasi-static switching current density from 2.8 to 1.6 MA/cm^2 when the free layer was changed from a Co-rich ($x_1 = 40$ and $x_2 = 20$) to a Fe-rich ($x_1 = 40$ and $x_2 = 60$) composition. It was believed that the reduction of current density by a factor 2.4 was related to the interfacial anisotropy increase since the layer thickness was reduced only by a factor of 1.2 (from 2.03 to 1.69 nm). For a 1.8 nm free layer thickness of Fe-rich CoFeB, the TMR ratio obtained was still high, around 120%.

Work on STT spin-valves (40) or classical STT-MTJ (41) showed that PMA contribution greatly reduces the required switching current by decreasing the demagnetizing field effect. Switching current densities and perpendicular anisotropy are strongly dependent on the free layer thickness for in-plane magnetized structures with PMA contribution (41). Critical current densities as low as 2×10^6 A/cm^2 were obtained in planar MTJ with low demagnetizing field. Fast switching, of the order of hundreds of picoseconds, was observed in in-plane systems comprising an additional perpendicular polarizer (32–35) or with reduced demagnetizing field (40). At the end of 2012, based on these results, the company EVERSPIN Technologies released a 64Mbit STT-MRAM product implementing such in-plane magnetized MTJs with reduced demagnetizing field in the storage layer (48).

5.5.5 Out-of-Plane STT-MRAM

Devices that show a magnetic anisotropy normal to the film surface hold great promise for faster and smaller magnetic bits in data-storage applications. They have many advantages compared to in-plane magnetized MTJs:

1. The switching current density is expected to be significantly reduced because the two terms present in the expression of the critical current density partially cancel each other (49).
2. The thermal energy barrier is provided by this large effective perpendicular anisotropy instead of in-plane shape anisotropy (47,50). For comparison, in MRAM systems based on field induced magnetic switching, high coercive fields and large anisotropy were problematic. However, in STT-MRAM, these same properties become an advantage, since they enable thermally stable elements beyond the 45 nm technology node. As a consequence, elongated cell shapes are no longer needed and the perpendicular MTJs can be patterned in circular shape. This facilitates manufacturability at smaller technology nodes and leads to lower switching current for a given memory retention.

WD EX1057
Western Digital v IP Bridge
Page 128

3. Finally, dipole field interaction between neighboring cells can also be reduced in high bit density layouts.

The perpendicular magnetic anisotropy can have different origins, either bulk (in hcp CoCrPt, heavy rare-earth–transition metal, or $L1_0$ FePt ordered alloys) or interfacial (in Pt/Co, Pd/Co, or Co/Ni multilayers). Besides, a quite large PMA can be induced at the interface between a ferromagnetic electrode and an oxide (44–46).

The growth of good quality perpendicular MTJs is a more difficult task than for their in-plane counterparts for reasons that will be explained below.

The first report on perpendicular magnetic tunnel junctions dates from 2002 (51). In this publication, the authors presented results on electrodes made of rare-earth–transition metal (RE-TM) alloys exchange-coupled to a 1.0 nm thick CoFe layer, separated by an Al_2O_3 barrier. In pillars 300 nm in size, they obtained a TMR ratio of up to 55%. At that time, RE-TM alloys were probably the best choice, since alumina barriers require only moderate annealing to optimize their transport properties. The first results on TMR properties in MgO-based structures (64% TMR) were published in 2008 (52), with electrodes made of RE-TM alloys exchange-coupled to a Fe layer. The same year, Toshiba presented the first STT switching results in MTJs with perpendicular anisotropy having a typical stack composed of TbCoFe/CoFeB/MgO/CoFeB/TbCoFe (as shown in Fig. 5.18) and patterned into a circular shape (50). Electrical measurements have shown a low 15% TMR, while the critical current densities extracted from switching curves at current pulse width from 30–100 ns were in the range of 5×10^6 A/cm^2. Coercive fields of 0.12 T yield a thermal stability factor $\Delta = 107$, large compared to less than $40k_BT$ in in-plane anisotropy cells at similar critical current densities.

Since 2009, different materials have been tested in order to induce perpendicular anisotropy in the magnetic electrodes on both sides of the MgO barrier (RE-TM alloys, CoCrPt alloys, ordered $L1_0$ alloys, and (Co/Pt) and (Co/Pd) multilayers) (53). All materials have both their advantages and their disadvantages. RE-TM alloys can be relatively easily fabricated, but their anisotropy properties greatly depend on alloy

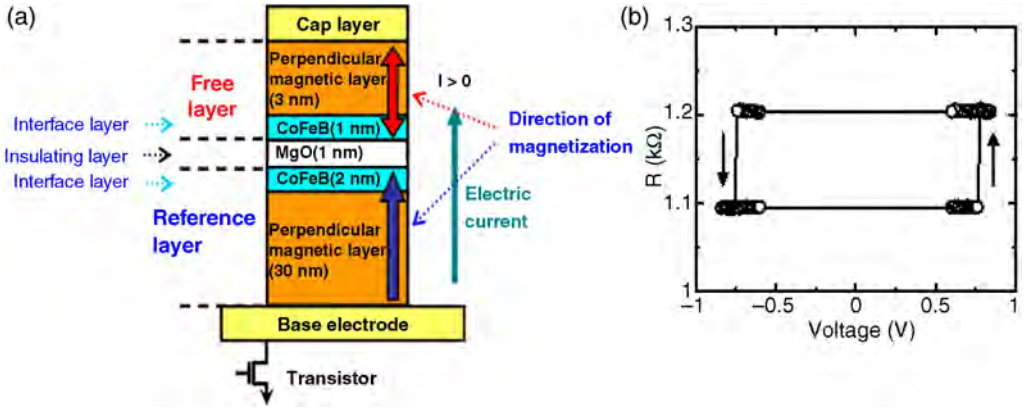


Figure 5.18 Cell structure of TbCoFe/CoFeB-based perpendicular MTJs (a) resistance versus voltage pulses for the perpendicular MTJ structure schematically shown (b). (From Ref. 50 with permission from AIP Publishing LLC.)

WD EX1057
Western Digital v IP Bridge
Page 129

composition, annealing temperature and operation temperature, which makes their optimization rather difficult. Furthermore, they are rather susceptible to corrosion.

Nevertheless (54), critical switching current densities as low as 5×10^5 A/cm^2 have been reported in TbCoFe/CoFeB/MgO/CoFeB/$L1_0$-FePd structures. These results show that critical current densities smaller than those in in-plane magnetized MTJ can be achieved in such out-of-plane magnetized junctions.

The great breakthrough came in 2010 when structures based on interfacial magnetic metal/oxide perpendicular anisotropy (44–46) with Ta/CoFeB electrodes were proposed (47), very similar to their in-plane counterparts but with thinner storage layer. The problem of the bcc (1 0 0) texturation of the CoFeB electrode upon crystallization was thus solved. In these structures, the perpendicular anisotropy mainly arises from the CoFeB–MgO interface. After patterning into sub-micrometer pillars, two well-separated parallel and antiparallel states were obtained, leading to simultaneously high TMR ratio (120%), low *RA* product (18 Ω μm^2) and low STT switching current density (4 MA/cm^2). It is important to emphasize that this approach based on the interfacial PMA at magnetic metal/ oxide interface (see section 5.5.5.3) has now become the mainstream one in the development of perpendicular MTJ for STT-MRAM.

5.5.5.1 Benefit of Out-of-Plane Configuration in Terms of Write Current The critical current for spin-transfer reversal of the storage layer obtained from the LLG equation (Eq. 5.20) in the out-of-plane configuration is given by

$$I_{c0} = \frac{2 \cdot e}{\hbar} \cdot \frac{\alpha \cdot A \cdot t \cdot \mu_0 M_s}{\eta} \cdot H_{eff}, \tag{5.24}$$

where A is the area of the magnetic element, e is the electron charge, $\hbar$ is the reduced Planck constant, μ_0 the vacuum permeability, α is the Gilbert damping coefficient, M_s and t are the saturation magnetization and thickness of the storage layer, η the spin-transfer torque efficiency that depends on the relative orientation of the magnetizations ($\theta = 0$ or π) and on the polarization P, and H_{eff} the effective switching field.

In magnetic junctions with out-of-plane magnetization, the effective field is given by

$$H_{eff} = H_{K\perp} - M_s, \tag{5.25}$$

where $H_{K\perp}$ is the perpendicular anisotropy field that pulls the magnetization out-of-plane ($H_{K\perp} > M_s$). In contrast to the in-plane magnetized case, the energy barriers to overcome to switch by STT during write or to switch by thermal fluctuations in standby are here identical. Therefore, for a given memory retention, the critical switching current can thus be much smaller than for in-plane magnetized electrodes. In addition, since shape anisotropy does not play a role anymore in the thermal stability, magnetic cells can be made circular instead of elliptical, which makes downsize scaling easier. Several papers addressed the advantages of perpendicular magnetic tunnel junctions (48,55–57). By introducing the thermal stability factor

$$\Delta = \frac{KV}{k_B T} = \frac{\mu_0 M_s H_{eff} A t}{2 k_B T}, \tag{5.26}$$

WD EX1057
Western Digital v IP Bridge
Page 130

where K is the anisotropy, $V = A \cdot t$ is the volume of the storage layer, k_B is the Boltzmann's constant, and T is the absolute temperature, Eq. (5.23) can be rewritten as

$$I_{c0} = \frac{4 \cdot e}{\hbar} \cdot \frac{\alpha \cdot k_B T}{\eta} \cdot \Delta. \tag{5.27}$$

This relation expresses that in the macrospin approximation (valid at dimensions below typically 40 nm, as discussed regarding Fig. 5.4), a direct proportionality exists between the thermal stability factor (i.e., the memory retention) and the write critical current. This is the classical dilemma between retention and writability often encountered in memory technology: the more stable the information, the more difficult it is to change it. To account for Eq. (5.27), a figure of merit has been proposed (58), which is the ratio of the thermal stability factor to the critical switching current, Δ/I_{C0}. Following the discussion of Section 5.4.1 and of this section, the figures of merit obtained with out-of-plane magnetized MTJ are expected to be much better (larger Δ/I_{C0}) than with in-plane magnetized MTJs. This is however true only if the Gilbert damping constant α, to which I_{c0} is proportional can be maintained as low as in in-plane magnetized material, which is not easy, as explained below.

5.5.5.2 Trade-off Between Strong Perpendicular Anisotropy and Low Gilbert Damping

With perpendicular MTJ, current density on the order of 5×10^5 A/cm^2 to 3×10^6 A/cm^2 were obtained, values of the same order of magnitude as the values obtained for in-plane switching ($\sim 2 \times 10^6$ A/cm^2). These rather large values are associated to the large perpendicular anisotropy of the investigated materials (e.g. Rare-Earth/transition metal alloys, FePt or FePd ordered alloys) but also to the relatively large values of the Gilbert damping constant commonly obtained in these materials (59). Indeed, both Gilbert damping and magnetic anisotropy derive from the spin–orbit interactions that basically couple the electron spin to the lattice. As a result, materials that exhibit large anisotropy (for instance FePt ordered alloys, CoPt multilayers and alloys) also exhibit large Gilbert damping constant α (in the range 0.05–0.2). In contrast, in-plane magnetized materials such as CoFeB have weak anisotropy and low damping (in the range 0.007–0.01).

A promising route to circumvent the problem of large damping in out-of-plane magnetized materials consists in using a storage layer where the perpendicular anisotropy does not arise from a bulk contribution as in Co/Pd or Co/Pt multilayers or as in FePt ordered alloys, but from a large interfacial perpendicular anisotropy that exists at the interface between the magnetic electrode and the tunnel barrier, as explained below.

5.5.5.3 Benefit from Magnetic Metal/Oxide Perpendicular Anisotropy

In magnetic thin films, the interfaces have in general a high impact on their magnetic properties. This is particularly the case in some systems wherein a very strong perpendicular magnetic anisotropy can originate from the interface between a magnetic and a nonmagnetic layer, as predicted by Néel (60) and experimentally observed several years later (61). In a very simple picture, the measured effective anisotropy energy (K_{eff})

WD EX1057
Western Digital v IP Bridge
Page 131

has two major contributions: a volume anisotropy (K_V), which itself can have different origins (magnetocrystalline, magnetoelastic, demagnetizing), and a surface–interface anisotropy (K_S), whose relative contribution increases as the thickness t of the magnetic film decreases. Taking into account these different contributions, the effective anisotropy per unit volume is given as $K_{eff} = K_V + \frac{K_s}{t}$.

Remarkably, a strong PMA interfacial contribution exists at magnetic metal–oxide interfaces (Co–AlO_x, CoFe–MgO, and Co–CrO_x) (45–47) despite the weak spin–orbit coupling of the involved materials. Experiments showed that this phenomenon is quite general (44–46,62,63) since it was obtained at the interface between various magnetic transition metals and oxide layers and is independent of the crystalline structure of the oxide layers (amorphous as alumina tunnel barriers or crystalline as MgO barriers). In addition, X-ray photoemission spectroscopy (63) showed that oxygen plays an essential role in the PMA at the magnetic metal–oxide interface by the formation of Fe(Co)–oxygen bonds. For a better understanding of the PMA origin at the magnetic metal–oxide interfaces, an *ab initio* study was realized taking into account the weak spin–orbit coupling (64). The origin of the large PMA is ascribed to the combination of several factors:

1. Lift of degeneracy of out-of-plane 3d orbitals due to the spin–orbit coupling,
2. Hybridizations between dz^2 and dxz and dyz 3d orbitals induced by spin–orbit interactions
3. Hybridizations between Fe(Co)-3d and O-2p orbitals at the interface between the transition metal and the insulator.

This interfacial anisotropy makes possible to pull out-of-plane the magnetization of materials having low Gilbert damping such as CoFeB alloys ($\alpha_{\mathrm{CoFeB}} \sim 0.01$, (65) compared with $\alpha_{(\mathrm{Co/Pd})} \sim 0.1$ and $\alpha_{(\mathrm{Co/Pt})} \sim 0.2$). Using the interfacial anisotropy therefore makes it possible to achieve simultaneously large perpendicular anisotropy required for high thermal stability of the magnetization and the weak Gilbert damping required for low STT switching current density. The interdiffusion between layers, caused by the nature of the materials (immiscibility) or by annealing, is always detrimental to the interface anisotropy. For example, it was experimentally observed (45,66) and calculated (64) that over/under-oxidation of the magnetic material–oxide interface strongly reduces the interface anisotropy. The remaining presence of B along the CoFe–MgO interface after annealing is also detrimental for the interfacial PMA. A lot of care must therefore be taken in the growth, oxidation and annealing conditions of these out-of-plane magnetized MTJ. Since the first demonstrations of STT switching in MTJ with large TMR using CoFeB/MgO interface anisotropy (48), tremendous progress have been made in the development of these MTJs to reach the specifications required in practical products (67), in particular sufficiently low bit-error rates (68,69). To further take advantage of the magnetic metal/oxide interface anisotropy, it was proposed to sandwich the storage layer between two oxide layers thus benefiting from two metal/oxide interfaces (70). The storage layer typically consists of a CoFeB 1.5 nm/Ta0.4 nm/CoFeB 1.2 nm composite structure sandwiched between two MgO layers wherein the thin Ta layer is intended to absorb the B away from the MgO interfaces upon annealing thus allowing the crystallization of the

WD EX1057
Western Digital v IP Bridge
Page 132

CoFeB layers into bcc structure and increasing the interface PMA at MgO/CoFe and CoFe/MgO interfaces (70,71). In these double barrier MTJs, the top electrode is usually non-magnetic so that there is no TMR associated with the top MgO barrier. The bottom MgO barrier provides the TMR signal required to determine the magnetic state of the storage layer. It is made thicker (i.e. has a higher RA product) than the top MgO layer to minimize the TMR decrease associated with the serial resistance of the top MgO layer. Very successful demonstrations of fully functional STT-MRAM chips were made following the optimization of these stacks (72–74). In 2016, the company EVERSPIN Technologies announced the launching of 256Mbit STT-MRAM products based on this technology. In 2016, other companies made also announcements on their move towards embedded Flash or SRAM replacement by this type of perpendicular STT-MRAM.

5.5.5.4 Downsize Scalability of Perpendicular STT-MRAM For high-density applications, below the 45 nm technological node and *a fortiori* at even more advanced nodes, it is mandatory to use out-of-plane magnetized MTJ to get long enough memory retention in STT-MRAM. But how small can we hope to go? With presently known materials, the optimized structures should look like the one represented in Fig. 5.19.

The general structure of this stack is a double tunnel junction with out-of-plane magnetization wherein the storage layer is sandwiched between two tunnel barriers of different *RA* product, themselves sandwiched between two polarizers of opposite magnetization. This dual configuration has three main advantages:

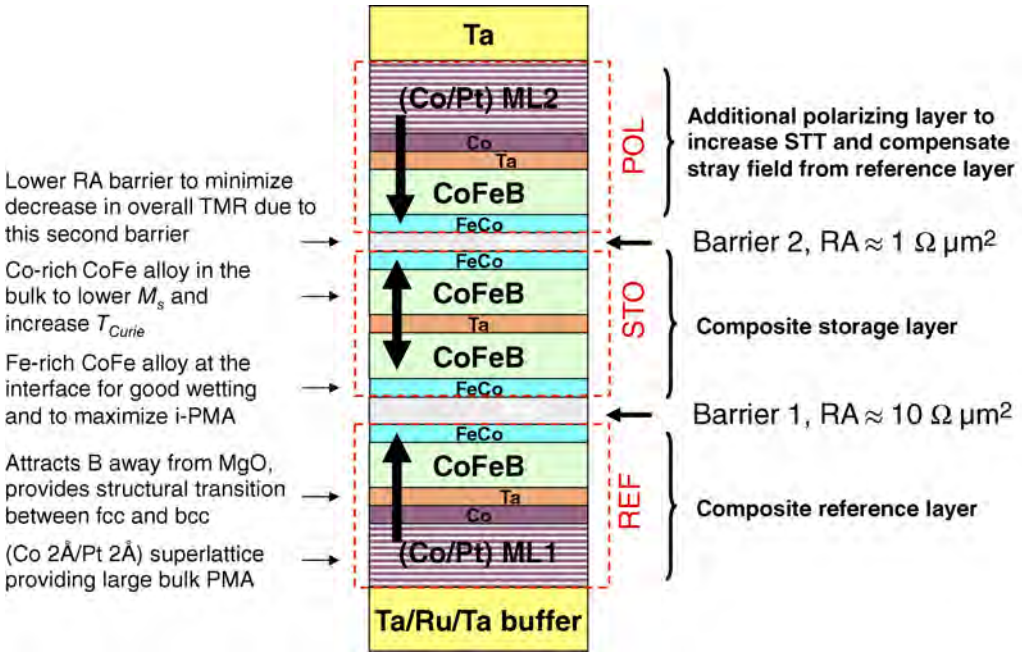


Figure 5.19 Expected optimized stack for downsize scalability of STT-MRAM to sub-20 nm node (75,76).

WD EX1057
Western Digital v IP Bridge
Page 133

1. The STT efficiency on the storage layer magnetization is more than doubled, thanks to the additive contributions from the two antiparallel polarizing layers.
2. The interfacial PMA on the storage layer magnetization is doubled by the presence of two CoFeB–MgO interfaces instead of only one in single MTJ stacks.
3. The stray field from the two polarizing layers on the storage layer magnetization is cancelled due to the antiparallel alignment of the two polarizing layers so that both states of the storage layer have the same thermal stability.

Since the antiparallel orientation of the two polarizing layers is rather unstable, the stability of this configuration can be improved by pinning the magnetization of these layers by antiferromagnetic layers (on both layers or one or the other only).

To further optimize the stack, each layer has a composite structure. The thin Ta insertions are intended to attract the B away from the MgO–CoFeB interfaces since B next to the MgO interface reduces the TMR as well as the PMA. The Co/Pt superlattices in the polarizing layers are increasing the overall PMA of these layers and thereby their magnetic stability. The storage layer is also composed of several layers. The bulk of the storage layer is made of a Co-rich CoFeB alloy to lower its magnetization (compared to Fe-rich alloys) and increase its exchange stiffness, thanks to the higher Curie temperature of Co than of Fe. This layer can be doped with some V to further lower its magnetization, thereby reducing its demagnetizing energy and thus increasing the effective perpendicular anisotropy of this layer. The layers in contact with the MgO barrier is Fe-rich to maximize the interfacial PMA and to allow good wetting of this layer during growth.

From the known properties of the involved materials, we can estimate that the magnetization of the storage layer should be stable with a thermal stability factor above 70 at RT down to diameter on the order of 10 nm (assuming interfacial anisotropy of 1.45 mJ/m^2 at FeCo–MgO interfaces, average $\mu_0 M_s = 0.75$ T in the storage layer). The current required to switch the magnetization calculated from Eq. (5.27) should be on the order of 13 μA (assuming a Gilbert damping constant $\alpha \sim 0.01$and a current spin polarization P ~80%). This current could be delivered by a transistor of a bit more than 10 nm in width. This means that from both magnetic and electrical points of view, this stack should be scalable to dimension down to about 10 nm (77,78).

In the past few years, the interest of the microelectronics industry for MRAM technology has tremendously increased. Among the various technologies of non-volatile memories (PCRAM, ReRAM, MRAM), MRAM and particularly STT-MRAM is the only one which combines density, speed and long endurance making it so promissing for e-Flash and SRAM applications. In the longer term, DRAM may also be replaced by STT-MRAM. However, the main difficulty remains the etching of the MTJ stacks at small feature size (sub-20 nm dimensions) and small pitch for this type of high density application. The edge damages and redeposition on sidewalls due to etching affect the transport and magnetic properties of the stack. Indeed, etch damages yield cell-to-cell dispersion (variability) in *RA*, TMR, and switching current as well as in retention and endurance. These distributions need to be further reduced. The reliability associated with resistance to electrical breakdown needs also to be further improved. Cyclability in STT-MRAM of 10^{12} cycles has already been demonstrated (79) and studies in accelerated conditions have shown that 10^{16} cycles

WD EX1057
Western Digital v IP Bridge
Page 134

can be achieved provided the density of electron trapping sites in the barrier is reduced (20,80). These trapping sites can be oxygen or Mg vacancies in the MgO barrier, dislocations associated with the 4% crystallographic mismatch between CoFe and MgO, BO formation along the MgO interface if the diffusion of B away from the interface during annealing is not properly controlled, or water molecules absorbed in the MgO barrier if the water partial pressure during MgO growth is not low enough. These various challenges can be met by an optimization of the growth and oxidation conditions of the stack. The objective is to bring the write endurance above 10^{16} cycles so that MRAM could become a universal memory, combining the advantages of DRAM (density), SRAM (speed), and Flash (nonvolatility).

In order to obtain minimal power consumption and optimized reliability, many tricks have been proposed (21). For example, subnanosecond switching with optimized power consumption can be achieved by tuning the switching current pulse width (81). Resonant STT switching was proposed to increase the reliability of the writing: (82) a weak microwave signal is applied to the junction in combination with the switching DC pulse. Such a microwave signal triggers the magnetization reversal by exciting its main precession modes, decreasing thus the writing consumption. Other assistance methods have been proposed, such as electric field (83–85), or thermal assistance (86,87). The idea is to decrease the anisotropy of the storage layer during write, either by radio-frequency fields or heating, so that it becomes easier to switch the junction either by magnetic field or spin-transfer torque. By disconnecting the anisotropy requirements under standby and writing conditions, it becomes possible to scale down to even smaller dimensions. Thermally-assisted MRAM are described in detail in the next section. In addition to allowing further downsize scalability, thermal assistance during write opens new functionalities particularly interesting for security or router applications.

5.6 THERMALLY-ASSISTED MRAM (TA-MRAM)

5.6.1 Trade-off Between Retention and Writability; General Idea of Thermally-Assisted Writing

It was shown in the previous sections that if writing is performed by field, then the field required to switch the magnetization of an element of anisotropy K and saturation magnetization M_s is $\mu_0 H_{write} = 2K/M_s$. Therefore, the larger the anisotropy, the larger the write field and therefore the larger the current required to create this magnetic field, meaning larger write power consumption. Now, if the writing is performed by spin-transfer torque, a similar problem occurs. Indeed, for spin-transfer writing, it is preferable to use magnetic tunnel junctions that are magnetized in the out-of-plane direction since these junctions require less current density to switch the magnetization by STT than their in-plane magnetized counterparts. In these perpendicular MTJs, the switching current is directly proportional to the thermal stability factor Δ, which controls the memory retention (Eq. 5.27). Therefore, both for field and STT writing, increasing the memory retention of the cell systematically yields an increase in the energy required to write.

WD EX1057
Western Digital v IP Bridge
Page 135

The same problem is actually also encountered in magnetic HDD technology, wherein the increase in areal density of information stored on HDD requires a reduction in the grain size in the storage media in order to maintain a sufficiently large signal-to-noise ratio. However, to maintain sufficient stability of the magnetization of the grains, their anisotropy must be increased. But then the required field to write becomes too large to be produced by the magnetic pole of the write head. This is known as the magnetic storage "trilemma."

This general difficulty validates the interest in using a thermally-assisted write approach. Indeed, in magnetic materials, it is known that, in the vast majority of cases, it is easier to switch the magnetization of a magnetic element at elevated temperature than at low temperature. This originates from the fact that the magnetic anisotropy decreases with temperature so that the barrier height for switching (ΔE) decreases with temperature. Furthermore, the higher thermal activation itself may help the magnetization to switch above the barrier. The concept of thermally-assisted writing thus consists in storing the information at a standby temperature at which the anisotropy and therefore the thermal stability factor are very large, thereby temporarily increasing the temperature of the magnetic element during each write event to reduce the barrier height and ease the switching of the magnetization.

5.6.2 Self-Heating in MTJ Due to High-Density Tunneling Current

In MRAM, the heating of the storage layer can be produced in a simple way by taking advantage of the Joule dissipation around the tunnel barrier. Actually the heating in MTJ is not a simple Joule heating as in metallic systems because we are here dealing with tunneling instead of ohmic transport. Rather, the heating in MTJ is due to the inelastic relaxation of tunneling hot electrons, which takes place when the tunneling electrons penetrate in the receiving electrode after their ballistic tunneling across the tunnel barrier. However, the heating power per unit area has the same expression as usual Joule heating: $P = jV$, where j is the current density flowing through the tunnel barrier and V the bias voltage across the barrier. In MTJs having RA product on the order of $30\,\Omega\,\mu m^2$, with heating current density on the order of 10^6 A/cm^2, a rise in temperature ΔT on the order of 200 °C within 5 ns is typically achieved (88).

5.6.3 In-Plane TA-MRAM

5.6.3.1 Write Selectivity Due to a Combination of Heating and Field In 2001, a thermally-assisted switching (TAS) MRAM concept (TA-MRAM) was proposed to improve the thermal stability, write selectivity, and power consumption of MRAM cells (89). A convenient approach to TA-MRAM is to heat directly with a current flow through the MRAM cell. In this scheme, a conventional MRAM junction is modified by replacing the simple ferromagnetic storage layer by an exchange-biased storage layer, that is, a ferromagnetic storage layer exchange coupled to an antiferromagnetic layer (89). The write procedure requires heating above the storage

WD EX1057
Western Digital v IP Bridge
Page 136

layer blocking temperature and cooling in the presence of a magnetic field. We remind here that the blocking temperature in a ferromagnetic/antiferromagnetic bilayer is the temperature at which the loop shift induced by the exchange coupling across the interface between these two layers vanishes. This temperature is usually slightly below the Néel temperature of the antiferromagnet (see Chapter 2). In TA-MRAM, the reference and the storage layer must be exchange-biased with antiferromagnets having sufficiently different blocking temperatures. Typically, PtMn with blocking temperature of 350 °C is used in the reference layer, whereas the storage layer antiferromagnet is chosen with a blocking temperature in the range 180–250 °C depending on the requirements on the device operating temperature range. The main advantages of this scheme are (i) the use of a single field selection line instead of two for toggle writing, (ii) an important reduction in write power consumption as will be explained later, and (iii) realization of cell with high thermal stability, that is, much improved retention due to the exchange pinning. For a given heating pulse duration, the temperature increase in the TA-MRAM cell is proportional to the dissipated power density P_d. The temperature increase can actually be directly derived experimentally from the measurements of the storage layer exchange bias field versus heating current. The total power density is effectively determined by the RA product (resistance × area product) of the junction and the current density j as $P_d = RA\ j^2$. Typical RA used in TA-MRAM are in the range 20–30 $\Omega\,\mu m^2$ and heating current density around 10^6 A/cm^2 comparable to the lowest used in STT writing. One way to increase the heating efficiency and reduce the power density is to insert low-thermal conductivity materials at both ends of the magnetic tunnel junction stack, serving as thermal barriers between the junction and the electrical leads. This confines the heat to the junction volume, preventing lead heating and possible thermal crosstalk (90). Typical heating time in TA-MRAM are in the range 3–10 ns. This heating time is primarily influenced by the heating power dissipated at the tunnel barrier. The cooling rate depends on the heat diffusion constant toward the top and bottom of the MTJ stack and on the specific heat of the MTJ. It is typically in the range 10–20 ns (91).

A bit write sequence, illustrated in the bottom drawing in Fig. 5.20, starts from a given initial orientation of the magnetization of the exchange-biased storage layer, for instance representing a low resistance state "0". The corresponding storage layer loop is shifted around a negative field, as seen in Fig. 5.20 in the hysteresis cycle before the heating pulse is applied (red curve). The reversal of the storage layer bias is achieved by heating the AF layer above its blocking temperature with a current pulse and applying simultaneously an external magnetic field H_{sw} larger than the coercive field of the storage layer. The field is applied in the direction parallel or antiparallel to the reference layer magnetization depending on whether a "0" or a "1" is to be written. In the example of Fig. 5.20, a "0" is written. The heating current pulse is then stopped so that the storage layer cools in a magnetic field. This maintains the storage layer magnetization in the field-cooling direction during its freezing. The result is a reversal of the pinning orientation of the storage layer magnetization and a bit state change to a low resistance "0". As a result, the storage layer loop is now shifted toward positive values as shown in Fig. 5.20 (blue curve).

WD EX1057
Western Digital v IP Bridge
Page 137

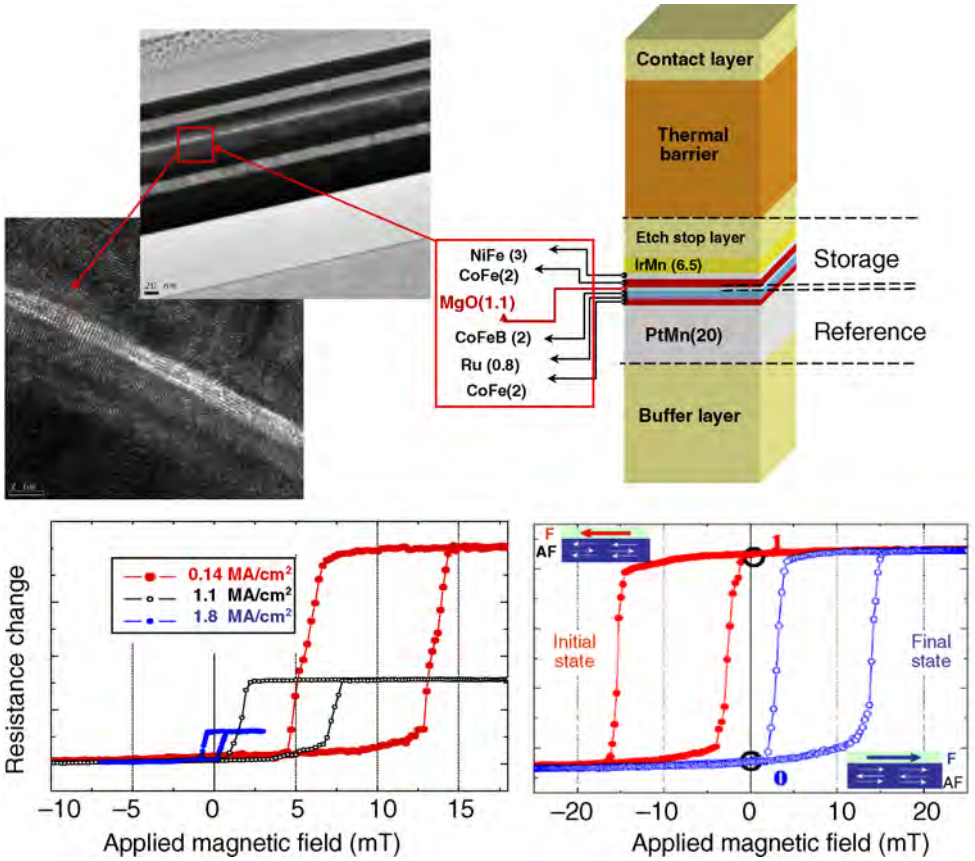


Figure 5.20 *Top:* Composition of the stack and cross-sectional transmission electron microscopy images of the MTJs. *Bottom left:* Hysteresis loops of the storage layer for various heating current density showing the decrease in the pinning as the heating current increases. At the highest heating current density, the loop is centered, meaning that the exchange bias has vanished and low fields of a few millitesla are then sufficient to switch the storage layer magnetization. The drop in amplitude of the hysteresis loop is due to the dependence of the TMR on heating bias voltage. *Bottom right:* Resistance hysteresis loops of the exchange-biased storage layer before (red) and after (blue) writing, showing the inversion of the hysteresis loop shift. Note that in both cases, only one remanent state is stable at zero field: either the low or the high resistance state, meaning that the memory is very stable against perturbing external fields (92).

Several demonstrations of TA-MRAM were realized first in micrometer-size junctions ($2\,\mu m \times 2\,\mu m$) under DC currents (93), then on submicrometer cells using heating pulses down to 10 ns (94). The company Crocus Technology in collaboration with TowerJazz has produced fully functional 1 Mbit demonstrators using this technology.

5.6.3.2 Reduced Power Consumption, Thanks to Low Write Field and Field Sharing In conventional TA-MRAM, the write selectivity is achieved by a combination of temporary heating of the storage layer that lowers its magnetic pinning energy together with the application of a pulse of magnetic field. The efficiency of this write selectivity scheme is illustrated in Fig. 5.21. Repeated successful writing can be achieved only when heating and field pulse are combined. This therefore solves the write selectivity problems that were present in Stoner–Wohlfarth first MRAM.

WD EX1057
Western Digital v IP Bridge
Page 138

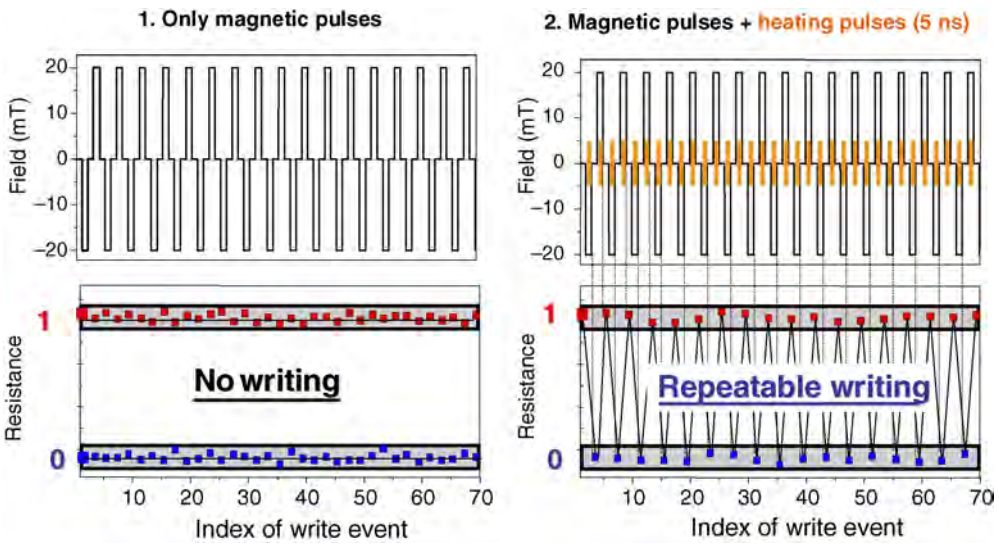


Figure 5.21 Illustration of the write selectivity in TA-MRAM resulting from the combination of heating pulse and application of a magnetic field. *Left:* Application of pulses of magnetic field alone (no writing). *Right:* Combination of heating pulses and alternating pulses of magnetic field (repeatable writing of *P* and *AP* (0 and 1) magnetic states).

Another advantage of this write scheme is the protection against field erasure in standby. As seen in Fig. 5.20 (right), in standby, only one state of the storage layer is stable at zero field. This means that even if the TA-MRAM chip is exposed to a perturbation field, this field may temporarily switch the magnetic configuration of the memory but the latter will spontaneously return to its original state before perturbation once the perturbation disappears (92). This, however, would not be true during write. If a perturbation field that is a significant fraction of the write field is applied during write, a write error may occur. A read-after-write scheme may be used to verify that no such error has occurred during write.

Field writing combined with thermal assistance is also quite advantageous in terms of power consumption in MRAM chips by offering the possibility to share the pulse of magnetic field among numerous bits. Indeed, in a RAM, the bits are usually not written randomly one by one but word by word. Each word may contain 32 or 64 bits. In TA-MRAM, to write a full word, only two pulses of magnetic field are required. The scheme for writing a word is illustrated on Fig. 5.22. In a first step, all bits in the word that have to be written to "0" are heated simultaneously by sending a heating current through the corresponding MTJ. The "0" field is then applied and the heating currents are switched off so that the heated cells cool down in the "0" magnetic field. As a result, these cells freeze in the "0" configuration. The cells that are not heated do not switch so that they remain in their original state. In a second step, all bits that have to be written to "1" are heated simultaneously and the "1" magnetic field is applied by sending a current in the corresponding word line (Fig. 5.22). The heating currents are then switched off, while the "1" field is still on so that the heated cells now freeze in the "1" configuration. At the end, the whole word has been written with 32 pulses of heating current (assuming a 32-bit word). The corresponding energy is ~1 pJ per dot plus two pulses of magnetic field.

WD EX1057
Western Digital v IP Bridge
Page 139

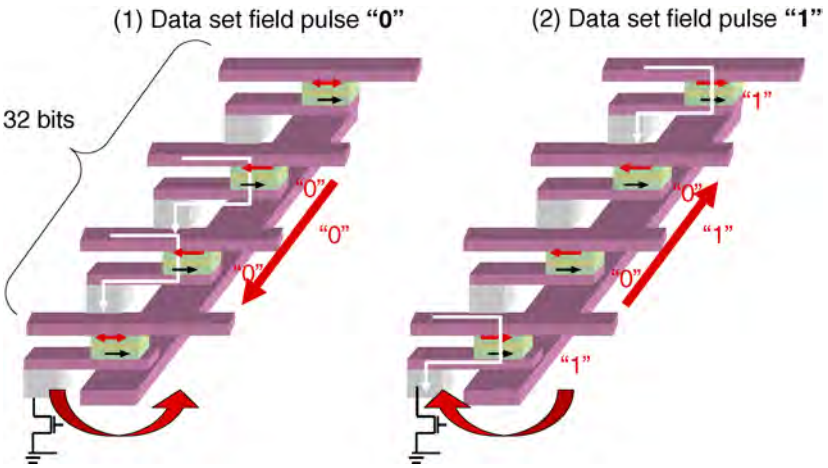


Figure 5.22 Illustration of write scheme with field sharing in TA-MRAM. A whole word can be written with only two pulses of magnetic fields.

Furthermore, in TA-MRAM, since the thermal stability of the storage layer magnetization in standby is provided by exchange coupling to an adjacent antiferromagnetic layer, the cell can have a circular shape. As a result, once the writing is enabled by heating the cell above the blocking temperature of the antiferromagnetic layer, only a low field of a few millitesla (2–5 mT) is sufficient to switch the storage layer magnetization since the cell has no shape anisotropy.

For comparison, consider the case of toggle MRAM. Writing a bit in a toggle MRAM requires two orthogonal pulses of magnetic fields. To write a 32 bits word, one of these pulses can be shared by the 32 bits of the same word by sending a pulse of current along the corresponding word line. However, 32 pulses of magnetic field must be independently generated along the corresponding 32 bit lines. This means that 33 pulses of magnetic field of about 10 mT each must be generated in toggle MRAM instead of two pulses of about 5 mT for TA-MRAM.

5.6.4 TA-MRAM with Soft Reference: Magnetic Logic Unit (MLU)

In a second possible implementation of TA-MRAM, a soft reference (SR) layer is made of a material with easily switchable magnetization. The storage layer is still exchange-biased by an adjacent antiferromagnetic layer as in standard TA-MRAM (see Fig. 5.23). The writing of the storage layer is achieved similar to the thermally-assisted MRAM devices by the application of a combination of an external field and a heating pulse that allows the storage layer to be switched and then pinned in the opposite direction as the system cools back below its antiferromagnetic blocking temperature. The reading is performed in two steps: the SR magnetization is set in a first direction, and the MTJ resistance is measured. The SR magnetization is then switched to the opposite direction and the new resistance is measured. The resistance variation between the two measurements yields the magnetic orientation of the storage layer. In this approach, the read cycle is longer (~50 ns) but the tolerance to process variation is greatly enhanced since each bit is self-referenced. Indeed, for the standard reading scheme, the two resistance state distributions have to be well separated in order to avoid read errors. This implies good dot size and shape control.

WD EX1057
Western Digital v IP Bridge
Page 140

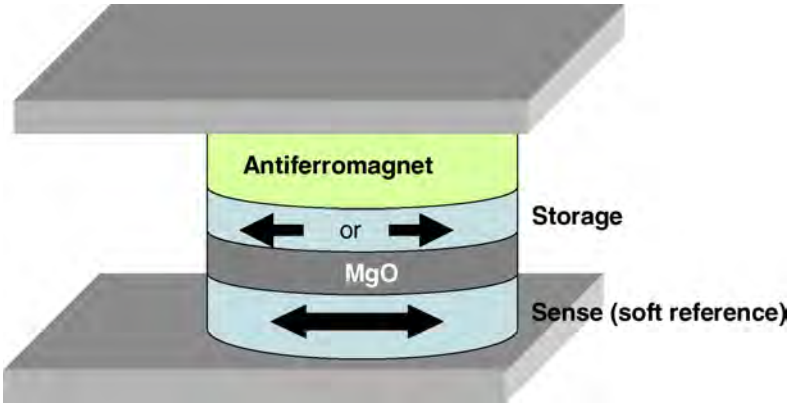


Figure 5.23 Schematic representation of a self-referenced MRAM with thermally-assisted write.

In contrast, for the SR reading scheme, the difference of resistance between the two states is used to read the junction, and is thus not sensitive to dot size variation. This is particularly useful for small technological nodes where the dot to dot resistance and magnetoresistance variability tend to significantly increase.

5.6.4.1 Principle of Reading with Soft Reference The reading scheme consists in switching the free layer in a first predetermined direction (along the stable directions of storage layer magnetization) and then in the opposite direction. The change of resistance associated with these two states due to the TMR effect, either increasing or decreasing, is used to infer the storage layer magnetization direction. A typical normalized R(H) cycle is shown in Fig. 5.24. This reading can be performed

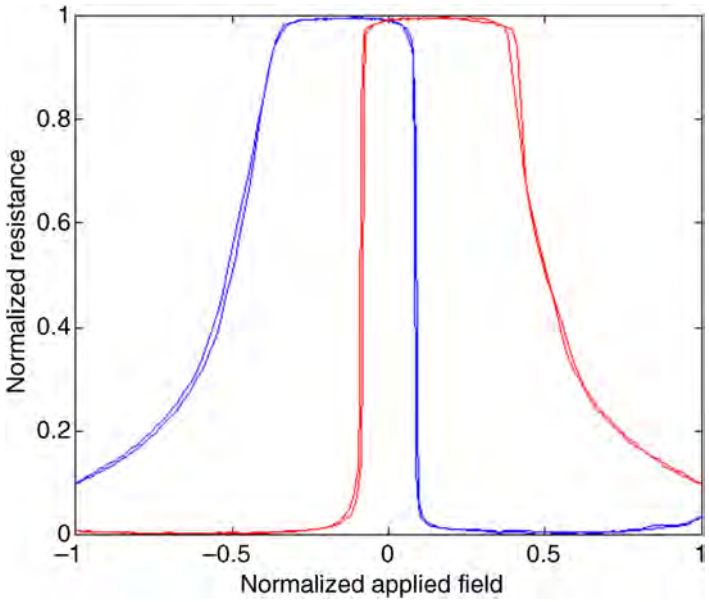


Figure 5.24 Normalized resistance response as a function of the external field for a self-referenced MRAM at standby temperature in state “0” (blue) and “1” (red). The resistance transition at low field is associated with the switching of the sense layer magnetization.

in a two-step quasi-static way or dynamically with an oscillation of the sense layer magnetization away from a 90° orientation, with the storage layer magnetization yielding an upward or downward oscillation of the MTJ resistance. Thanks to this self-referenced readout scheme, a major advantage of these devices is that they are much more tolerant of process variation and cell-to-cell variation. Since each cell is self-referenced, the constrains on homogeneity of cell-to-cell resistance and magnetoresistance amplitude are much released. The drawback of this self-referenced scheme is a slower readout process.

Besides its MRAM application, this self-referenced cell can be used to perform logic operations with particularly interesting applications in security. Indeed, these devices combine memory and logic (XOR) functions. For this reason, they are called Magnetic Logic Units (MLU™) (95). In addition to being storage devices, self-referenced MRAM intrinsically allows performing logic comparison functions. Considering the storage and the sense layer magnetizations as two inputs, this magnetic stack outputs the exclusive OR function of these logic inputs through the magnetoresistance level. Both inputs are set using pulses of magnetic field, with first the storage layer being written with a heating pulse and then the sense layer switched at room temperature. By using a set of self-referenced MRAM cells connected in series to form a NAND chain, a Match-In-Place™ engine can be created, as illustrated in Fig. 5.25, wherein a pattern applied to the sense layers is compared to the written pattern stored in the storage layers (96). Any mismatch between the two patterns systematically results in a higher resistance than for a perfect match. The expected advantages of this architecture are as follows:

- The stored patterns are never read, and never exposed to potential hackers.
- The matching cycles are very quick and could be orders of magnitude faster than existing methods and use less power.
- Match-In-Place engines could act as a hardware accelerator, and simplify the overall chip.
- The cost structures of the secure chips are considerably reduced.

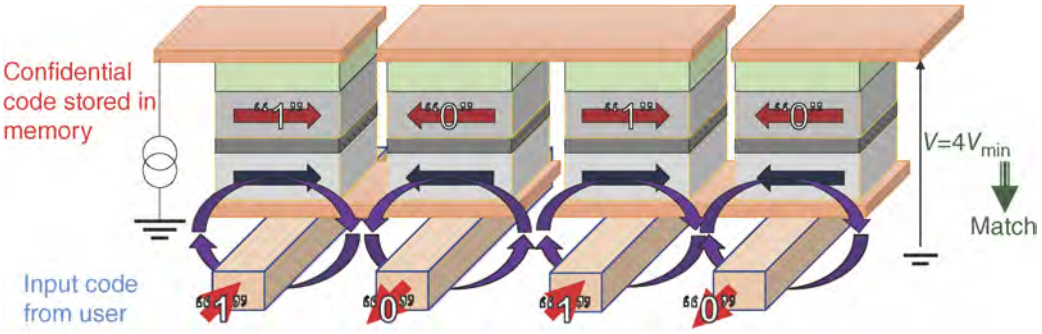


Figure 5.25 Example of a Match-In-Place™ (MIP) engine made by the serial connection of four MLUs in a NAND chain. The input binary pattern "1 0 1 0" is compared with the stored binary pattern "1 0 1 0". When the input pattern matches the stored pattern, the serial resistance of the chain is at its minimum level. If the input pattern does not perfectly match the stored pattern, the resistance of the MIP is larger.

The basic Match-In-Place architecture can be built at three levels: The single cell for direct matching at the bit level, NAND chains that combine multiple individual cells in series for linear Match-In-Place engines, and a matrix that combines multiple NAND chains in parallel to match one input pattern to a stack of stored patterns.

When the input bit matches a stored bit (a "0" with a "0" or "1" with a "1"), the cell measures a match. Conversely, if the input data do not match the cell's contents (a "0" with a "1" or "1" with a "0"), the cell measures a mismatch. Unlike a RAM-based content-addressable memory (CAM), an MLU-based Match-In-Place cell retains the stored bit when power is removed. This avoids any need to reload the stored information, a step that exposes the information to hacking. An MLU-based Match-In-Place engine can handle unlimited write cycles, and a read or match cycle does not disturb the stored information. The read cycle of an individual cell is extremely fast; a compare can occur in as little as 5 ns. Program cycles can be implemented through a separate path with a cycle time of about 20 ns.

5.6.4.2 Content-Addressable Memory These Match-In-Place engines can be assembled to design fast associative memories and notably CAM, which have applications in search engines and routers for instance, where incoming data packets are directly routed to the recipient address. An example of such a CAM is illustrated in Fig. 5.26. Fields of use of these new architectures are quite wide and include secure microcontrollers, subscriber identity module (SIM) cards, banking cards, biometric authentication chips, near-field communication, and hardware acceleration. Expected benefits are enhanced security, lower cost, and faster response time.

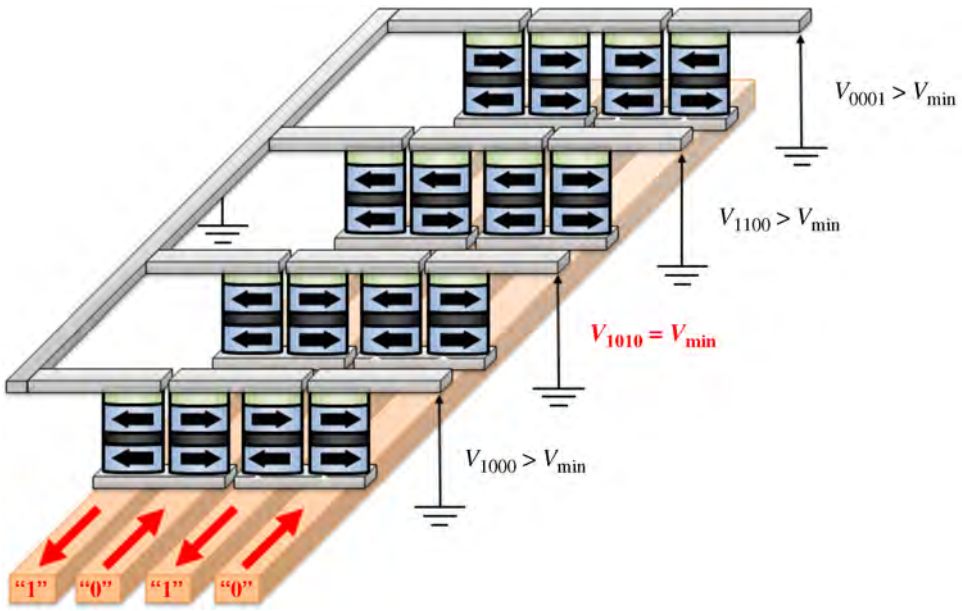


Figure 5.26 Example of a content-addressable memory (CAM) with four Match-In-Place engines. The input binary pattern "'1 0 1 0" is compared with the memory content and matched with the lowest voltage for a set reading current value.

WD EX1057
Western Digital v IP Bridge
Page 143

5.6.5 Thermally-Assisted STT-MRAM

So far in Section 5.6, MRAM using write scheme based on thermal assistance combined with pulses of magnetic field have been described. Alternatively, thermal assistance can also be used in combination with spin-transfer torque to extend the scalability of STT-MRAM both with in-plane and out-of-plane magnetized materials. This is explained in the following sections.

5.6.5.1 In-Plane STT Plus TA-MRAM As explained earlier, there are several advantages in using a thermally-assisted MRAM concept, the main one being the decoupling of the thermal stability (memory retention) and the write power consumption (writeability), since the bit can have simultaneously a low write field at the write temperature and be stable in standby in the whole operating temperature range. The problem with the field-driven writing of TA-MRAM cells is still that the magnetic field needs to be generated by a current line with current pulses of a few milliamperes. TA-MRAM requires a single magnetic field and lower field values compared to the toggle MRAM approach, thus lowering the total power consumption. However, the write field does not scale with cell size and can be at best kept constant, unlike STT-MRAM where the write current scales with cell size. In TA-MRAM, the heating current is not the bottleneck, since the use of thermal barriers has already demonstrated a heating current density in the $1–2 \times 10^6$ A/cm^2 range, similar to low values of spin-transfer torque MRAM cells (STT-MRAM). Alternatively, it is possible to get rid of the field line by still using the thermally-assisted concept but combining it with spin-transfer torque to switch an exchange-biased storage layer (89). In this case, the same current flowing through the cell is used both to heat up the cell and switch the storage layer magnetization by STT. It is thus possible to combine the added stability obtained from the exchange biasing to retain the information with the reduction of the current through cell size scaling, since the cell switching occurs at a constant current density, typically in the 10^6 A/cm^2 range.

With in-plane magnetized materials, structures similar to those used for TA-FIMS-MRAM, comprising an exchange-biased storage layer, can be used (Fig. 5.27). Since the current density required for heating the storage layer to 200 °C in 5 ns is comparable to the current density required for STT switching with in-plane magnetized materials (both $\sim 2–4 \times 10^6$ A/cm^2), the same current flowing through the MTJ, downward or upward, can be used to simultaneously heat the cell that enables the writing by reaching the AFM blocking temperature and to switch the storage layer magnetization. The first implementation of the thermal assistance combined with STT (TAS + STT) with in-plane magnetized MTJ was realized in 2009 (97). The magnetic stack was Ta 3/CuN 30/Ta 5/PtMn 20/CoFe 2/Ru 0.74/CoFeB 2/MgO 1.1 natural oxidation/CoFeB 2/NiFe 3/IrMn 6.5/Ta 5 (thicknesses in nanometers) patterned to 140 nm diameter circular cells. The storage layer is pinned by IrMn and the hysteresis cycles show a pinning field of ~5 mT, as shown in Fig. 5.28. The resistance state was switched between the low- and high-resistance states by applying current pulses of alternating polarity across the junction. Each pulse first creates a temperature increase above the antiferromagnet blocking temperature. With the ferromagnetic layer no longer pinned, the spin-polarized current simultaneously exerts a torque on the

WD EX1057
Western Digital v IP Bridge
Page 144

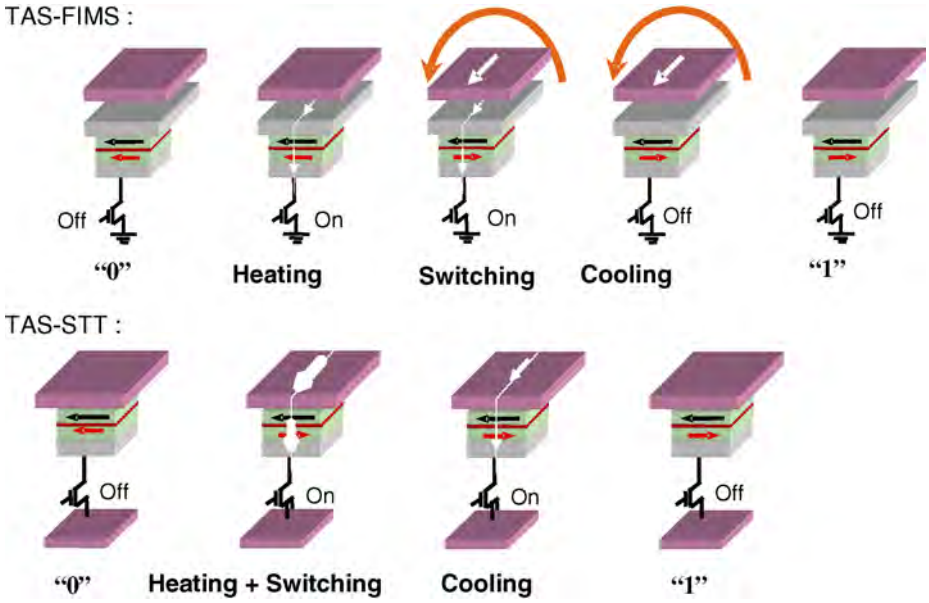


Figure 5.27 TA write principle combined with FIMS or STT. In TA-FIMS, the temporary heating of the MTJ is combined with a pulse of magnetic field. In TA-STT, the current flowing through the MTJ both heats the MTJ and exerts the magnetic torque that switches the magnetization.

ferromagnetic storage layer, reversing its magnetization direction depending on the current direction. The write voltage is then gradually decreased to zero so that the junction cools down while STT is still on. The antiferromagnet then freezes the new storage layer magnetization direction. Figure 5.28 shows this writing process with 30 ns pulses applied in a sequence of positive and negative polarity resulting in a zero-field resistance that is alternating between the low- and high-resistance states. Additionally, there is also a change in the storage layer pinning direction as can be seen from the alternating positive and negative exchange bias field values. The critical current density required for switching the exchange pinned layer was 8×10^6 A/cm^2 and 13×10^6 A/cm^2, respectively, for the antiparallel to parallel and the parallel to antiparallel transitions. Similar structures without exchange biasing resulted in critical current densities of 8×10^6 A/cm^2 and 13×10^6 A/cm^2, virtually identical to thermally-assisted cells, meaning that the heating is not the limiting factor and that the exchange pinning does not increase the critical current density for STT switching. This shows how the thermally-assisted approach can benefit the STT-MRAM concept.

5.6.5.2 Out-of-Plane STT Plus TA-MRAM Ultimately, thermally induced anisotropy reorientation (TIAR) (86) can be used to assist the spin-transfer torque switching in perpendicular magnetic tunnel junctions. The TIAR provides a way to reorient the direction of the free layer magnetization with heating. Indeed, the magnetization of an out-of-plane magnetized layer at room temperature can reorient in the thin film plane when heated due to the different temperature dependence of the out-of-plane anisotropy and demagnetizing energy (98). One should notice that

WD EX1057
Western Digital v IP Bridge
Page 145

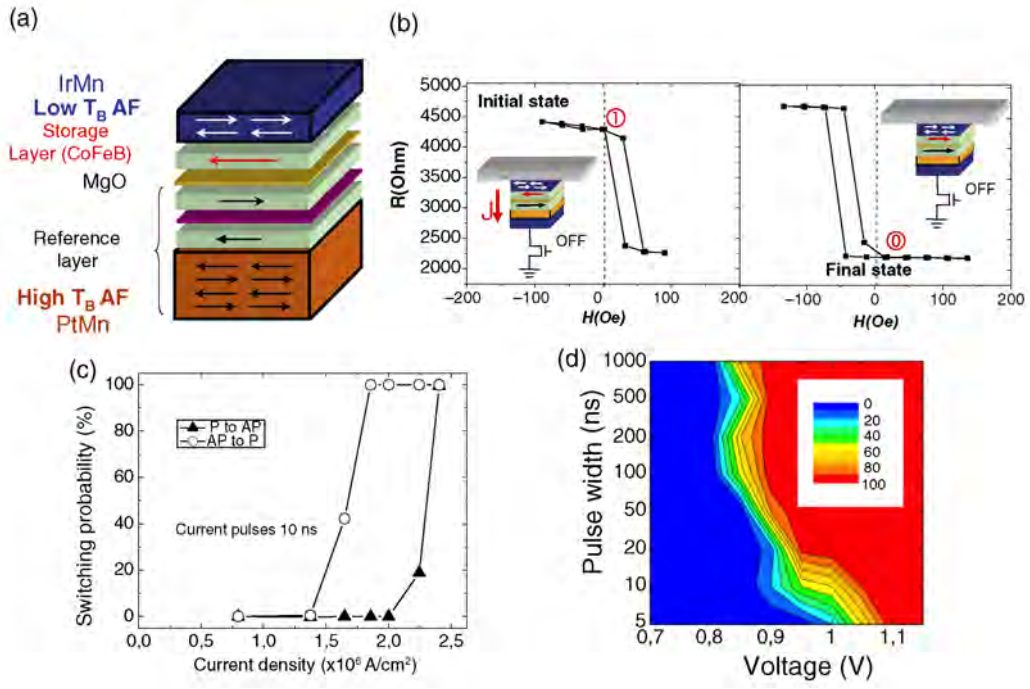


Figure 5.28 Illustration of STT + TA switching using exchange-biased in-plane magnetized storage layer. (a) Stack used. (b) Magnetoresistance loops showing the reversal of the exchange pinning direction after applying 30 ns pulses. The inset represents the exchange bias field after pulses of alternating current direction. (c): Switching probability from *P* to *AP* and *AP* to *P* versus current density for current pulses 10 ns long. (d) Color map showing the switching probability versus voltage pulse amplitude and voltage pulse duration.

heating is always occurring when a current is injected in a MTJ during writing. This heating assists STT switching, but materials used in MTJ are usually not optimized to take advantage of this effect. Oppositely, TIAR-assisted switching consists in optimizing the temperature dependence of the MTJ magnetic properties to decrease the STT critical current while keeping a satisfying thermal stability under standby conditions. In that latter case, the current is responsible for three phenomena: STT, heating, and TIAR. Such a switching method is promising to achieve highly scalable MRAM cells with low power consumption and reliable writing.

Figure 5.29 presents the proposed writing scheme: the MTJ exhibits a large thermal stability factor in standby on the operating temperature window. During write, a current pulse is sent through the junction. Due to the inelastic relaxation of tunneling electrons, heating occurs so that the PMA decreases. As a result, the free layer magnetization falls into the thin film plane, while the reference layer is engineered so as to keep its out-of-plane magnetization. This latter electrode polarizes the current in the out-of-plane direction. The STT, due to this spin-polarized current, pulls the free layer magnetization in the upper or lower hemispheres depending on the current direction and induces large angle out-of-plane precessions (31). In such a configuration, the STT effect is highest since the spin polarization is almost perpendicular to the magnetization. It results in a more reproducible switching since no thermal fluctuations are required to initiate the reversal. The injected current is then

WD EX1057
Western Digital v IP Bridge
Page 146

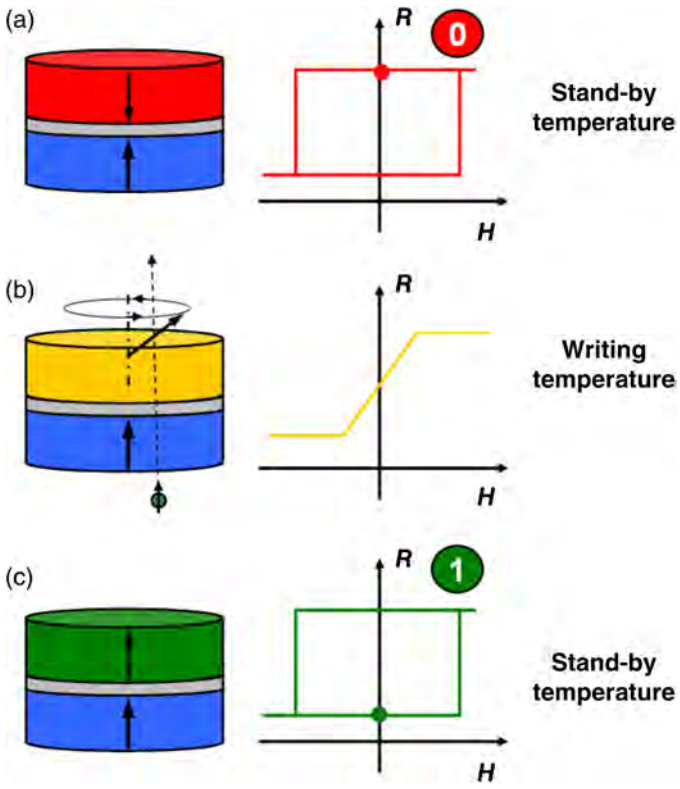


Figure 5.29 Principle of TIAR-assisted switching. (a) The junction exhibits a large PMA at standby temperature. (b) A current is sent through the junction. The FL magnetization undergoes a TIAR due to the heating. The STT induces a large-angle precessional motion of the FL magnetization and pulls it upward or downward depending on the current direction. (c) The FL recovers its PMA during the cooling when the current is gradually decreased to zero. Its magnetization rotates out-of-plane in the direction corresponding to the hemisphere in which it was pulled in by STT.

gradually decreased so that the junction cools while STT is still effective. The free layer recovers its PMA, and its magnetization gets reoriented out-of-plane, in the direction defined by the hemisphere into which it was previously pulled by STT. This switching approach reduces the write consumption as soon as the required current to heat the junction to the anisotropy reorientation temperature T_K is lower than the critical switching current in a standard MTJ (typically a few 10^6 A/cm^2). This condition is fulfilled in most common cases. In addition, the heating current density can be further reduced by adding in-stack thermal barriers on both sides of the MTJ.

In this particular writing scheme, the voltage required to switch the junction is mainly determined by the anisotropy reorientation temperature T_K, which sets the lower limit of the writing window. T_K can be estimated theoretically by calculating K^{eff} as a function of temperature. For a cubic or uniaxial anisotropy, it can be written to first order as

$$K(T) = K_{\perp}(0)\left(\frac{M_s(T)}{M_s(0)}\right)^m - (N_{perp} - N_{plan})\frac{\mu_0}{2}M_s(T)^2, \tag{5.28}$$

where $K_{\perp}(0)$ is the perpendicular magnetic anisotropy constant at 0 K, $M_S(T)$ is the free layer magnetization, and $-(N_{perp} - N_{plan})(\mu_0/2)M_s(T)^2$ is the demagnetizing energy, N_{perp} and N_{plan} being the demagnetizing factors of the pillar. The exponent m depends on the origin of the PMA. For a single ion bulk anisotropy, $m = i(i+1)/2$, where i denotes the anisotropy constant order, equal to 2 to first order in the most common case of a uniaxial anisotropy so that $m = 3$. However, this exponent can

WD EX1057
Western Digital v IP Bridge
Page 147

differ in the case of an anisotropy of interfacial origin such as at CoFeB/MgO interface. From this equation, the K^{eff} sign changes beyond T_K, where T_K is the temperature where $K^{eff} = 0$. In that situation, the in-plane anisotropy induced by the demagnetizing energy becomes larger than the PMA, so that the free layer magnetization falls into the thin film plane. In order to tune T_K, Eq. (5.25) shows that the evolution of M_S as a function of T has to be controlled. This can be achieved by tuning the Curie temperature T_C of the magnetic material. (Co/NM) multilayers, where NM is a nonmagnetic metal, provide a wide range of T_C, and exhibit PMA at room temperature when NM is a noble metal such as Pt, Pd, or Au (37). In those systems, the T_C can be easily tuned by changing the Co or NM thickness, or by doping Co with Ni or nonmagnetic elements (99–101).

However, such multilayers cannot be used alone as magnetic electrodes in MTJ for MRAM applications, which require relatively high TMR ratio. Indeed, (Co/NM) multilayers present an fcc (1 1 1) texture that does not match the bcc (0 0 1) MgO texture (102). This problem can be solved by inserting a thin CoFeB layer at the MgO interface: the (Co/NM) multilayer together with the interfacial anisotropy at the CoFeB–MgO interface provides a sufficiently large PMA to pull the CoFeB magnetization out-of-plane, while the CoFeB layer provides the appropriate bcc texture required to obtain large TMR ratio (103). In such structures, TIAR can still be obtained by tuning the (Co/NM) multilayer properties.

Figure 5.30 illustrates the TIAR phenomenon in a multilayer of MgO/CoFeB1.5/Ta0.2/(Pd1.2/Co0.3)×3 (thickness in nanometers). In this figure, hysteresis loops have been measured on a full sheet sample by polar magneto-optical Kerr effect as a function of temperature, with an out-of-plane applied field. At room temperature, the loops have square-loop and coercive behavior, indicating out-of-plane magnetization. When the temperature increases, the coercivity decreases while the signal amplitude decreases due to the decrease of magnetization. At 150 °C, perpendicular domains appear, leading to a loop with no remanence. The anisotropy reorientation occurs at 175 (±20) °C. Above this temperature, the loops exhibit the reversible linear behavior expected from a measurement along the hard axis direction. When the sample is cooled down, the loop recovers its squareness and coercivity, indicating that the TIAR phenomenon is reversible.

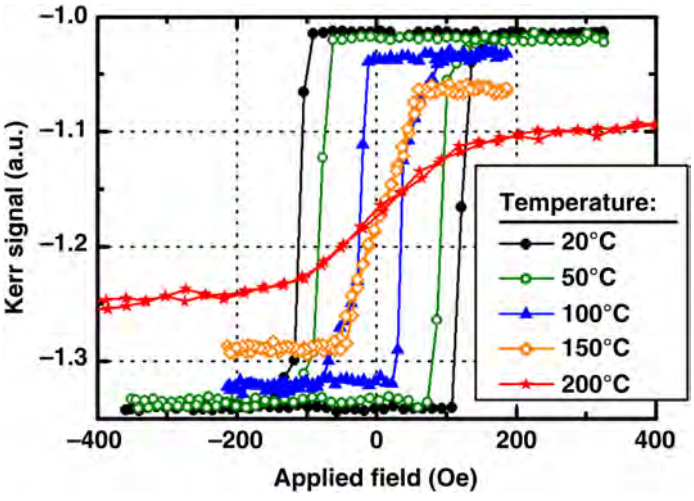


Figure 5.30 Hysteresis loops of CoFeB 1.5/Ta0.2/(Pd 1.2/Co 0.3)×3/Pd 2 for different measurement temperatures with out-of-plane applied field.

WD EX1057
Western Digital v IP Bridge
Page 148

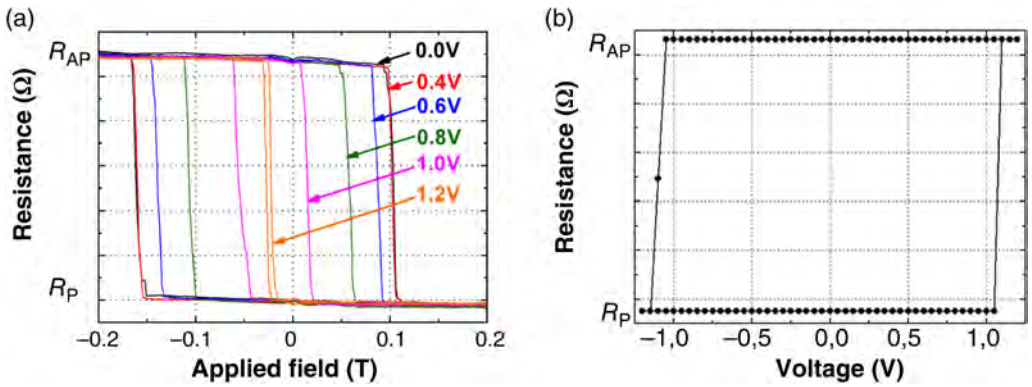


Figure 5.31 (a) Hysteresis loop of a 110 nm diameter pillar with 30 ns-long applied pulses of various amplitudes. (b) STT + TAS resistance switching.

The magnetic tunnel junction also requires a reference electrode. For that electrode, a (Co/Pt)-based synthetic antiferromagnet (SAF) can be used. Such a SAF is important for MRAM technologies, since they create a reduced stray field on the storage layer magnetization, thus avoiding different thermal stabilities Δ in the P and AP magnetic configurations as well as asymmetric P to AP and AP to P write currents (104,105). In order to study the effect of heating, the hysteresis loops were then measured while applying 30 ns long pulses of square shape of increasing voltage at each field step (0.2 mT). The resistance of the junction was measured after each pulse (see Fig. 5.31a). Figure 5.31 illustrates the very strong decrease in switching field associated with the heating of the storage layer due to the voltage pulse. The possibility to switch the magnetization without field just by combining spin-transfer torque with heating is then shown in Fig. 5.31b (86). With 30 ns long pulses, the switching voltage is 1.15 ($\pm$0.05) V, corresponding to a current density of $j_w = 4.6 \times 10^6$ A/cm^2. At the time of this study (2011), this current was of the same order as the values reported in the literature using a standard Ta/CoFeB/MgO free layer and no thermal writing assistance. However, in order to calculate the switching efficiency, the figure of merit Δ/I_{c0} gives a better idea of the writing efficiency as discussed for Eq. (5.27).

Table 5.1 gives a comparison of this figure of merit Δ/I_{c0} between the standard STT switching in perpendicular MTJ and the TIAR-assisted switching at the time of this study. This table shows reported write current densities corresponding to 30 ns long pulses. The thermal stability at 300 K given here are extrapolated for $d = 40$ nm diameter junctions and 30 ns pulse width (47,86,106).

Under these assumptions, it is clear that TIAR-assisted STT switching has improved efficiency compared to the standard STT switching. This is even more striking regarding the damping constant α of the different kinds of free layer: whereas it is equal to 0.013–0.03 in a Ta/CoFeB/MgO stack, it is of about 0.15 in a CoFeB/(Pd/Co) stack (107). The efficiency of the TIAR-assisted STT writing could be further optimized by implementing thermal barriers in the stack. It has been shown that with this kind of barriers, a temperature of about 200 °C can be obtained with an RA product of about 30 $\Omega \cdot \mu$m^2 and a current density of about 10^6 A.cm^{-2} (97,108). The thermal stability Δ at operating temperature could be enhanced,

WD EX1057
Western Digital v IP Bridge
Page 149

TABLE 5.1 Comparison of Writing Current Densities at 30 ns, j_{write}; Corresponding Current I_c for 40 nm Diameter Cell, Thermal Stability Factor Δ at 300 K for 40 nm Large Devices and Figure of Merit Δ/I_c of Standard STT Switching (47,106) and TIAR-Assisted STT Switching (86).

Reference	Material	Writing principle	j_{write} (MA/cm^2)	I_c(30 ns) (μA)	Δ(300 K)	Δ/I_c (μA^{-1})
106	Ta/CoFeB/MgO	STT	3.8	48	43	0.89
47	Ta/CoFeB/MgO	STT	7.4	93	50	0.54
86	CoFeB/(Pd/Co)	TIAR + STT	4.6	58	73	1.26

keeping a constant writing consumption by controlling T_K, leading to even more scalable MTJ.

In conclusion, TIAR plus STT writing could help to extend the downsize scalability of perpendicular STT-MRAM to even smaller dimensions than discussed in Section 5.5.5.4.

5.7 THREE-TERMINAL MRAM DEVICES

Among recent emerging nonvolatile memory, spin-transfer torque magnetic random-access memory (STT-MRAM) has been identified by the ITRS as one of the two most credible candidates. However, STT-MRAM still suffers from a lack of speed for the fastest cache applications and from potential endurance limitations due to the large current injected through the tunnel barrier for switching the magnetization. Indeed, at each write event, the tunnel barrier is submitted to a pulse of voltage on the order of 0.5 V, 10 ns long in conventional STT-MRAM, 0.7–1 V in thermally-assisted schemes that use larger *RA* than STT-MRAM. Since the barrier is typically 1 nm thick, this represents an electrical field across the oxide barrier on the order of 10^9 V/m, which is approaching the values for which electrical breakdown of the barrier may occur. In order to circumvent this problem, several groups have proposed concepts of three-terminal STT-MRAM cells (represented in Fig. 5.1c) in which the write current does not flow across the tunnel barrier, thereby limiting the electrical stress during write. These approaches also open new possibilities in the design of the memory architecture or for logic applications since the write and read current paths are different.

5.7.1 Field versus Current-Induced Domain Wall Propagation

Figure 5.32 gives an experimental comparison of the domain wall (DW) dynamics that can be induced in a magnetic stripe by application of a magnetic field or by a current flowing in the stripe. The blue and red colors correspond to magnetic domains magnetized in opposite direction along the wire. In Fig. 5.32b, a field is applied parallel to the magnetization of the blue colored domains and correspondingly antiparallel to the red colored domain. The field therefore favors the blue domain magnetic orientation. As a result, the blue domains expand as a function of

WD EX1057
Western Digital v IP Bridge
Page 150

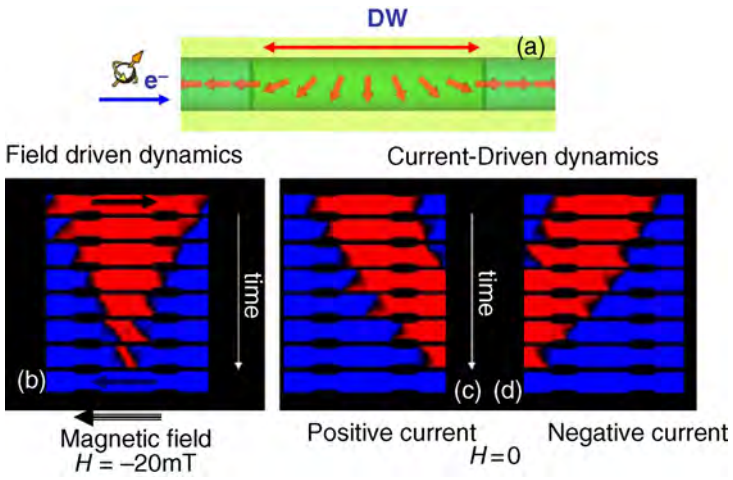


Figure 5.32 (a) A domain wall is a transition region separating two magnetic domains magnetized in different directions. The wall has a certain width to minimize the cost in exchange energy associated with the change in the direction of the magnetization. The domain wall width is determined by a balance between exchange energy and anisotropy energy. (b–d) The blue and red regions represent domains of opposite magnetization along a magnetic stripe. Part (b) illustrates the domain wall dynamics induced by a pulse of magnetic field. Parts (c and d) illustrate the dynamics induced by a current flowing through the magnetic stripe. (Courtesy of Stuart Parkin, IBM, unpublished.)

time, while the red domain shrinks to the point where the red domain disappears. The domain size is therefore not conserved under field induced dynamics. In contrast, Fig. 32c and d illustrate the domain wall dynamics induced by a positive or a negative current flowing through the magnetic stripe. The current gets spin polarized when traversing the domains and exert a spin-torque on the walls separating the domains. The spin-transfer torque on the domain wall contains two terms called adiabatic STT and nonadiabatic STT. The adiabatic STT corresponds to the situation where the spin of the electrons continuously follow the local magnetization direction (dominant for large walls and strong exchange interaction between the spin of the conduction electrons and the spin of the electrons responsible for the local magnetization), whereas the nonadiabatic STT corresponds to situation where the spin of the conduction electrons gets re-oriented on a length scale much longer than the domain wall width. The dominant effect of the adiabatic STT term is to distort the shape of the domain wall, whereas the effect of the nonadiabatic term is effectively to exert a pressure on the wall and induce its motion. Quite interestingly, all the walls located along the wires are submitted to the same pressure so that they move coherently in the same direction determined by the current direction. This is illustrated in Fig. 32c and d for two opposite current directions. Remarkably, because the walls move at the same speed under the current flow, the size of the domains does not vary and the whole domain pattern shifts coherently along the magnetic stripe. Domain wall speeds on the order of a hundred to several hundreds of meters per second (i.e., nanometers per nanosecond) are achieved with current density on the order of 1 to a few 10^7 A/cm^2.

WD EX1057
Western Digital v IP Bridge
Page 151

5.7.2 Principle of Writing

One of the proposed concepts of three-terminal MRAM based on DW propagation is illustrated in Fig. 5.33: Each MRAM cell consists of a magnetic tunnel junction having three electrical connections. One of the connections (named bottom electrode in Fig. 5.33) is, as usual, at the bottom of the cell, and most often connects the bottom part of the MTJ (i.e., the underlayer of the antiferromagnetic pinning layer) to a selection transistor. In addition, two other contacts are connecting the top part of the MTJ, that is, its storage layer. One of the contacts is made of a Cu spacer plus another pinned ferromagnetic layer. This contact together with the free layer of the MTJ constitutes a so-called spin-valve stack. The pinned ferromagnetic layer of the spin-valve is used to inject an in-plane spin-polarized current into the storage layer to switch its magnetization upon write. This spin-valve stack is connected to the so-called top electrode (see Fig. 5.33a and b). The second top contact to the middle electrode is made of a simple nonmagnetic metal such as Cu or Al. Writing an information in the memory means, as for conventional MRAM cell, orientating the

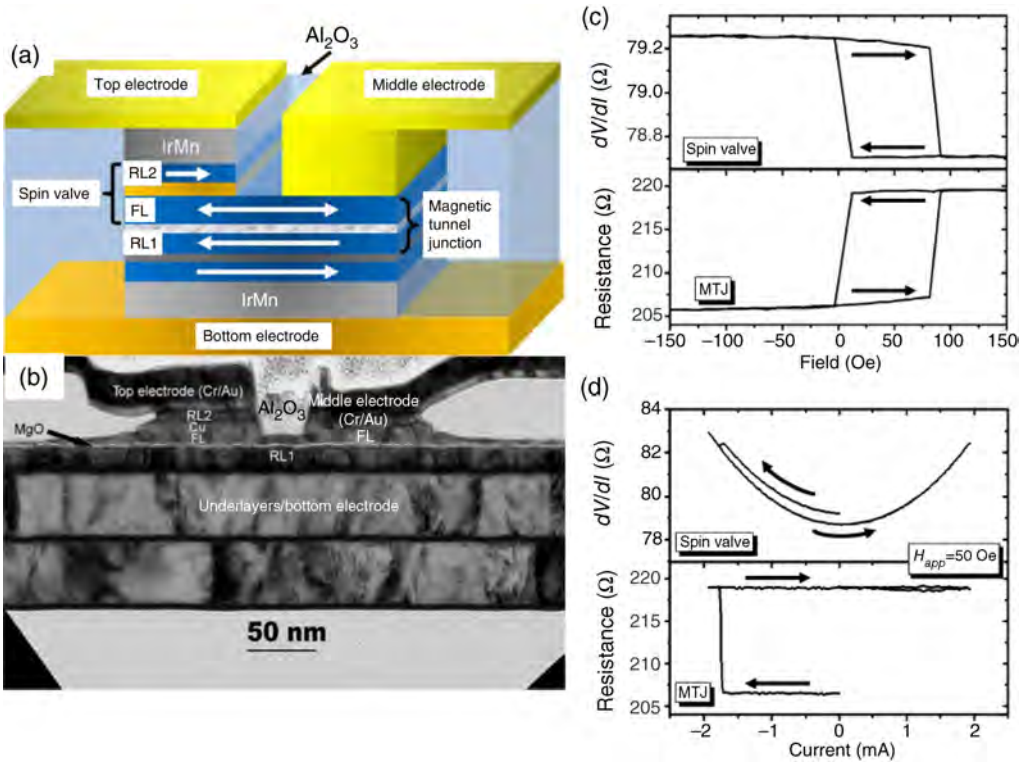


Figure 5.33 Example of three-terminal MRAM cell proposed by HGST (109). (a) Schematic representation of the MRAM cell. (b) Cross-sectional transmission electron microscopy view of the device. (c) Simultaneous measurements of the spin-valve differential resistance response versus field (measured between top and middle electrodes) and of the tunnel junction response (measured between the top and bottom electrodes). (d) Simultaneous measurements of the spin-valve differential resistance response versus current flowing from top and middle electrodes (measured between top and middle electrodes) and magnetoresistance of the tunnel junction response (measured between the top and bottom electrodes).

WD EX1057
Western Digital v IP Bridge
Page 152

magnetization of the storage layer (FL in Fig. 5.33) parallel or antiparallel to that of the reference layer (RL1 in Fig. 5.33) of the MTJ. This is achieved by sending a pulse of current between the top electrode and the middle electrode. This current flows through the top contact, then in the plane of the storage layer, then in the middle contact to the middle electrode. By traversing the pinned layer of top contact, the conduction electrons become spin polarized. They then exert a spin-transfer torque on the left extremity of the storage layer which nucleates a reversed domain underneath the contact. At this point, the storage layer is divided into two magnetic domains, one nucleated underneath the top contact, and one in the original magnetization direction. These two domains are separated by a domain wall. Still, due to the spin-transfer effect, the current flowing in the free layer exerts a pressure on this domain wall, which then propagates across the entire free layer leading to a complete switching of its magnetization. The magnetization can then be switched back by using a write current of opposite polarity. By this mechanism, the free layer magnetization can be switched without current flowing through the barrier.

More recently, novel three-terminal memory concepts, called "spin–orbit torque" MRAM (SOT-MRAM) (109–113), were proposed and demonstrated. A current flowing in the plane of a magnetic multilayer with structural inversion asymmetry, such as Pt/Co (0.6 nm)/AlO_x, exerts a torque on the magnetization, due to the spin–orbit coupling. This torque can lead to magnetization reversal, with a switching time shorter than 500 ps (114) and a writing energy one tenth that in current STT-MRAM. The key advantage of the SOT-MRAM is that write and read are decoupled due to independent current paths. The SOT-MRAM thus naturally solves the reliability problems in current STT-MRAM with a potentially infinite endurance. This new concept is particularly interesting for cache-compatible high-speed applications (SRAM-type) for which density is not the primary concern. As future objectives, writing current needs to be further lowered to match advanced transistor outputs and remain much below electromigration threshold.

5.7.3 Advantages and Drawbacks of Three-Terminal Devices

The readout is performed as usual by sending a current from the top contact to the bottom contact and thereby measuring the resistance of the tunnel junction. This approach therefore allows for an SOT writing scheme without tunnel barrier wear-out issues while retaining the benefits for read-out of the large TMR signals from MTJs. In this approach, write and read current paths are separated which is not the case in STT-MRAM. The drawback is the increased cell size due to the requirement of making two isolated contacts with associated interconnects on top or bottom of each memory cell.

5.8 COMPARISON OF MRAM WITH OTHER NONVOLATILE MEMORY TECHNOLOGIES

5.8.1 MRAM in the International Technology Roadmap for Semiconductors (ITRS)

From an application perspective, the demand for on-chip memories has been increasing both on an absolute basis and relative to overall chip transistor counts.

WD EX1057
Western Digital v IP Bridge
Page 153

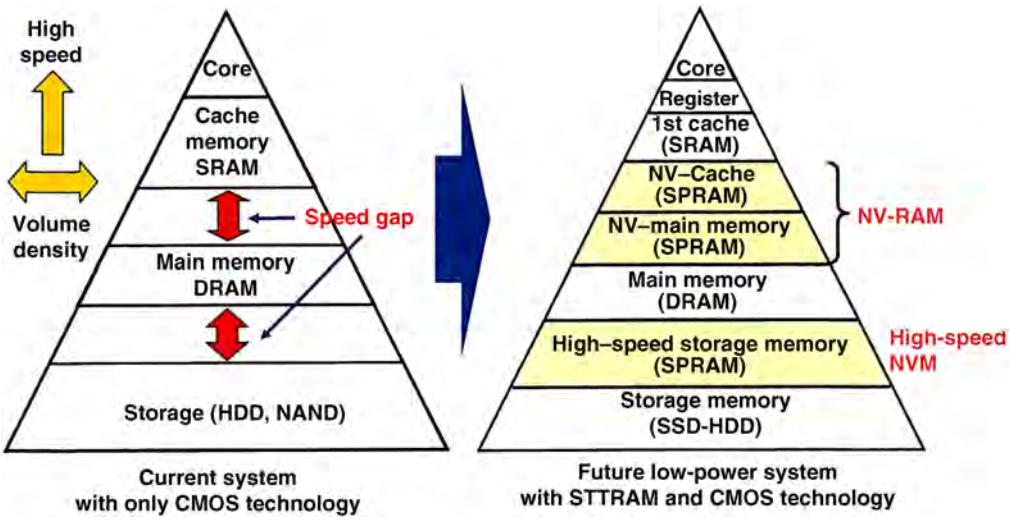


Figure 5.34 Need for introducing nonvolatility in the memory hierarchy (SPRAM stands for STT-MRAM) (115).

This is due to a confluence of factors such as the growth in demand for data storage and the increasing gap between processor and off-chip memory speeds. The move to multicore processors few years ago has only accelerated the demand for on-chip memory. As pointed out in the ITRS, one of the best solutions to limit power consumption and to fill the memory gap is the modification of the memory hierarchy by the integration of nonvolatility (NV) at different levels (storage-class memories, DRAM main working memory, SRAM cache memory), which would immediately minimize static power as well as pave the way toward normally off/instant-on computing (see Fig. 5.34).

The International Technology Roadmap for Semiconductors (ITRS) Emerging Research Devices and Emerging Research Materials Working Groups met in 2010 to evaluate eight emerging research memory technologies proposed to scale nonvolatile memory technology to and beyond the 16 nm node (ferroelectric gate field-effect transistor, nano-electromechanical switch, STT-MRAM, various types of resistive RAM, in particular redox RAM, nanothermal phase change RAM, electronic effects RAM, macromolecular memories, and molecular RAM). In conclusion, the ERD/ERM working groups "identified spin-transfer torque MRAM and redox RRAM as emerging memory technologies recommended for accelerated research and development leading to scaling and commercialization of nonvolatile RAM to and beyond the 16 nm generation (116)." Currently, there is an intense research and development effort in microelectronics on these two technologies, one based on spintronic phenomena, the other based on migration of vacancies or ions in an insulating matrix driven by oxidoreduction potentials. Both technologies could be used for standalone or embedded applications.

The potential benefits of spin-based memories are especially appealing when viewed in light of the exploding demand for on-chip memories. However, spin-based chips are still in an early stage of volume production. In order to realize their potential, there is a need to strengthen the technology maturity and for advances in circuit designs and innovative architectures.

WD EX1057
Western Digital v IP Bridge
Page 154

5.8.2 Comparison of MRAM and Redox-RAM

The redox RAM combines good potential for scaling below 10 nm generation, fast read and write times, (<10 ns), and relatively low write current (in the microampere range). They should be stackable in three-dimensional architectures called cross-bar architectures and offer multilevel capabilities, thanks to the possibility to control the growth/dissolution of the conducting filaments, which determines the cell resistance level. However, the underlying physical mechanisms are based on statistical phenomena rather difficult to control at the scale of each dot leading to relatively large dot to dot variability. Predictive model of reliability are more difficult to establish for this technology. Finally, their endurance ($\sim 10^8$ cycles) is sufficient for Flash type applications but not enough for the working memory in microprocessors (which require $>10^{15}$ cycles). Therefore, these memory elements seem to be most suited for storage class memory applications (intermediate level between hard disk drives, solid-state drives (SSD), and DRAM) and memristor applications, thanks to the possibility that they offer to continuously vary their resistance between a minimum and a maximum value in a hysteretic way. This may open the path to neuromorphic architectures that mimic the working principle of the human brain.

The STT-MRAM appears today as the most credible candidate for embedded FLASH and SRAM replacement as it combines CMOS compatibility, high retention time (10 years), large endurance ($>10^{15}$ cycles), and fast write/read time (1–30 ns depending on the embodiments). A further goal is also DRAM replacement. However, this technology is still not yet mature enough for this high density application. The main difficulty remains associated with the difficulty to etch the MTJ stacks at small pitch (sub-20 nm) and with the related cell-to-cell variability. This variability is mainly caused by the edge defects generated during patterning of the cells. Whenever the MgO barrier is damaged by the patterning, this yields local changes in the barrier resistance, tunnel magnetoresistance, magnetic anisotropy, and correlatively, cell retention. Redeposition on the MTJ sidewalls during etching also contributes to the variability. Now that the number of laboratories (including major equipment suppliers) working on this technology has substantially increased, technological progress are much faster.

5.8.3 Main Applications of MRAM

According to recent market research reports, solid-state memory constitutes a market of over $50 billion, while the nonvolatile memory (NVM) segment is much smaller. Most laptops nowadays use NVMs, which retain data when the power is off, in the form of a solid-state drive in place of an HDD. The now ubiquitous smart cell (mobile) phones and other handheld devices also use NVM, but there is a trade-off between cost and performance. The cheapest NVM is Flash memory, which, among other uses, is the basis of small, portable Flash memory sticks. Flash memory, however, is slow and has a limited cyclability of 10^5 cycles, sufficient for a large number of storage applications ranging from memory sticks to digital camera memory to SSDs, but much lower than that of redox RAM or STT-MRAM.

WD EX1057
Western Digital v IP Bridge
Page 155

Besides computers, today's portable electronics have become intensively computational devices as the user interface has migrated to a full multimedia experience. To provide the performance required for these applications, the portable electronics designer uses multiple types of memory: a medium-speed random-access memory for continuously changing data, a high-speed memory for caching instructions to the CPU, and a slower NVM for long-term information storage when the power is removed. Combining all of these memory types into a single memory has been a long-standing goal of the semiconductor industry. With such a memory, computing devices would become much simpler and smaller, more reliable, faster, and less energy-consuming.

As a result, advanced NVM chips are expected to see phenomenal growth in the next few years, with the global market increasing from $209 million in 2012 to $2,028 million by 2018 (117). This will occur in a number of applications: embedded system-on-chip (SOC) cards; radio-frequency identification (RFID) tags used in goods transported by high-speed detection conveyors; smart airbags used in automobiles; radiation-hardened memory in aerospace and nuclear installations; printed memory platforms (such as smart cards, games, sensors, display, storage-class memory network); and high-end smart mobile phones.

MRAM has the potential to become a "universal" memory device applicable to a wide variety of functions. As a matter of fact, MRAM can have similar performance to SRAM Cache 3 (switching time ~5 ns) but is nonvolatile. It has also similar density to DRAM but at lower power consumption since there is no need to refresh and with reduced leakage since MRAM can be powered off on standby. Besides, it is nonvolatile as Flash memory but much faster and suffers no degradation over time. It is this combination of features that makes it so attractive. Some suggest that it could replace SRAM, e-FLASH, DRAM, in embedded and standalone forms, some storage class memories, resulting in instant-on nonvolatile computers and tiny, super-fast and reliable portable devices.

In cell phones, handheld tablet computers, notebooks, personal digital assistants (PDAs), and other forms of mobile computing, MRAM is an attractive alternative to deploying both Flash and DRAM since it can save money and space. With software applications residing in memory, mobile devices could be instantaneously repowered up to exactly the same state in which they were when they were turned off. In general computing and networking, MRAM can be used to avoid boot-up delays and to provide faster access to hard drives and nonvolatile backup capabilities. At present, BIOS tend to use high-cost, low-density EEPROM or battery-backed-up SRAM—and volatile memory is used to alleviate I/O bottlenecks. In such applications, MRAM could prove much more economical.

In factory automation systems, microcontrollers and robots typically employ both RAM and PROMs/Flash. Lower costs will be achieved by replacing these two chips with one MRAM device. RFID tags need low-cost NVM, and a price point that makes MRAM economically viable for RFID applications will almost certainly push MRAM into other cost-sensitive areas. For aerospace use, MRAMs are radiation-hard, meaning that they can withstand ionizing radiation in contrast to most of semiconductor memories based on capacitor charge. This makes them suitable for use in airplanes (already in Airbus flight controllers), in satellites, and in spacecraft. They

WD EX1057
Western Digital v IP Bridge
Page 156

could also be used in nuclear environment such as nuclear power plants where conventional CMOS electronics devices fail when exposed to radiation.

5.9 CONCLUSION

MRAMs are expected to combine nonvolatility, high speed, moderate power consumption, infinite endurance, and radiation hardness, all at moderate cost and be easy to embed in devices. However, since its inception in the late 1990s, and the launching of Toggle MRAM products by EVERSPIN Technologies in 2006, MRAM has not yet reached large volume applications. The more recent advent of giant tunnel magnetoresistance in MgO-based MTJs and of spin-transfer torque, however, has shed a new light on MRAM with the promise of much improved performance and greater scalability to very advanced technology nodes. As a consequence, MRAM is now viewed as a credible replacement for existing technologies for applications where the combination of nonvolatility, speed, and endurance is key. Several start-up companies (e.g., Everspin Technologies, Crocus Technology, Avalanche, and Spin-Transfer Technology), large integrated device manufacturers (e.g., IBM, NEC, Toshiba, Hynix, TDK, TSMC, Renesas, Micron, Intel, and Samsung), and equipment suppliers (e.g., Canon Anelva, Applied Materials, Singulus, LAM, TEL and Keysight Technologies) are now actively developing STT-MRAM technology. The launch of 64 Mbit in-plane magnetized STT-MRAM products was announced by EVERSPIN Technologies at the end of 2012 as well as the forthcoming launch of 256 Mbit out-of-plane magnetized STT-MRAM products in 2016.

STT-MRAM has the potential of delivering the high density (stacking the magnetic cell with the selection transistor) and a scalable technology down to ~10 nm by using out-of-plane magnetized MTJs, taking advantage of the perpendicular magnetic anisotropy that exists at the CoFeB–MgO interface. The main difficulty for high density MRAM products currently remains the eching of the MTJ stack at small feature size and small pitch. Progress is also steadily being made in the composition of the stack to maximize the TMR amplitude, particularly in the perpendicular MTJ configuration (now above 240%), and in improvements in the temperature operating range (to minimize the decrease of the PMA with operating temperature).

Further downsize scalability in MRAM could be provided by combining thermally-assisted switching and spin-transfer torque writing to achieve the benefits of both: the stability of TAS and the full scalability of STT. This approach is promising for high-density, low-energy consumption, such as DRAM replacement.

Longer term approaches to reduce the power consumption in MRAM are envisioned based on a different write approach which relies on the voltage control of interface anisotropy but this is still at the research level (118,119).

ACKNOWLEDGMENTS

We thank all our colleagues from Crocus Technology and SPINTEC for fruitful discussions and for their contributions to some of the results presented in this chapter:

WD EX1057
Western Digital v IP Bridge
Page 157

Stéphane Auffret, Sebastien Bandiera, Bertrand Cambou, Yann Conraux, Marie-Thérèse Delaye, Clarisse Ducruet, Erwan Gapihan, Ken Mackay, Lucien Lombard, Jean-Pierre Nozieres, Céline Portemont, Liliana Buda-Prejbeanu, Bernard Rodmacq, Quentin Stainer, and Maria Souza. Some of the results presented in this chapter were obtained in projects supported by the French *Agence Nationale de la Recherche* (ANR SPIN, RAMAC, and PATHOS) and the European Commission (ERC Adv Grant HYMAGINE n° 246942, ERC Adv Grant MAGICAL n° 669204).

REFERENCES

1. S. Yuasa, T. Nagahama, A. Fukushima, Y. Suzuki, and K. Ando, "Giant room temperature magnetoresistance in single-crystal Fe/MgO/Fe magnetic tunnel junctions," *Nat. Mater.* **3**, pp. 868–871 (2004); doi: 10.1038/nmat1257.
2. S. S. P. Parkin, C. Kaiser, A. Panchula, P. M. Rice, B. Hughes, M. Samant, and S.-H. Yang, "Giant tunnel magnetoresistance at room temperature with MgO (1 0 0) tunnel barriers," *Nat. Mater.* **3**, pp. 862–867 (2004); doi: 10.1038/nmat1256.
3. J. A. Katine, F. J. Albert, R. A. Buhrman, E. B. Myers, and D. C. Ralph, "Current-driven magnetization reversal and spin-wave excitations in Co/Cu/Co pillars," *Phys. Rev. Lett.* **84**, pp. 3149–3152 (2000); doi: 10.1103/PhysRevLett.84.3149.
4. Y. Huai, F. Albert, P. Nguyen, M. Pakala, and T. Valet, "Observation of spin-transfer switching in deep submicron-sized and low-resistance magnetic tunnel junctions," *Appl. Phys. Lett.* **84**, pp. 3118–3120 (2004); doi: 10.1063/1.1707228.
5. J. A. Osborn, "Demagnetizing factors of the general ellipsoid," *Phys. Rev.* **67**, pp. 351–357 (1945); doi: 10.1103/PhysRev.67.351.
6. M. Beleggia, M. De Graef, Y. T. Millev, D. A. Goode, and G. Rowlands, "Demagnetization factors for elliptic cylinders," *J. Phys. D Appl. Phys.* **38**, pp. 3333–3342 (2005); doi: 10.1088/0022-3727/38/18/001.
7. H. Sato, M. Yamanouchi, K. Miura, S. Ikeda, H. D. Gan, K. Mizunuma, R. Koizumi, F. Matsukura, and H. Ohno, "Junction size effect on switching current and thermal stability in CoFeB/MgO perpendicular magnetic tunnel junctions," *Appl. Phys. Lett.* **99**, 042501 (2011); doi: 10.1063/1.3617429.
8. H. Sato, M. Yamagouchi, S. Ikeda, S. Fukami, F. Matsukura, and H. Ohno, "Perpendicular anisotropy CoFeB-MgO magnetic tunnel junctions with a MgO/CoFeB/Ta/CoFeB/MgO recording structure," *Appl. Phys. Lett.* **101**, 022414 (2012); doi: 10.1063/1.4736727.
9. H. Tomita, S. Miwa, T. Nozaki, S. Yamashita, T. Nagase, K. Nishiyama, E. Kitagawa, M. Yoshikawa, T. Daibou, M. Nagamine, T. Kishi, S. Ikegawa, N. Shimomura, H. Yoda, and Y. Suzuki, "Unified understanding of both thermally-assisted and precessional spin-transfer switching in perpendicularly magnetized giant magnetoresistive nanopillars," *Appl. Phys. Lett.* **102**, 042409 (2013); doi: http://dx.doi.org/10.1063/1.4789879.
10. L. Savtchenko, B. Engel, N. Rizzo, M. DeHerrera, and J. A. Janesky, "Method of writing to scalable magnetoresistance random access memory element," U.S. Patent 6,545,906 (2001).
11. B. Dieny, J. P. Gavigan, and J. P. Rebouillat, "Magnetisation processes, hysteresis and finite-size effects in model multilayer systems of cubic or uniaxial anisotropy with antiferromagnetic coupling between adjacent ferromagnetic layers," *J. Phys. Condens. Matter* **2**, pp. 159–185 (1990); doi: 10.1088/0953-8984/2/1/013.
12. B. N. Engel, J. Åkerman, B. Butcher, R. W. Dave, M. DeHerrera, M. Durlam, G. Grynkewich, J. Janesky, S. V. Pietambaram, N. D. Rizzo, J. M. Slaughter, K. Smith, J. J. Sun, and S. Tehrani, "A 4-Mb toggle MRAM based on a novel bit and switching method," *IEEE Trans. Magn.* **41**, pp. 132–136 (2005); doi: 10.1109/TMAG.2004.840847.
13. N. D. Rizzo, "Narrow gap cladding field enhancement for low power programming of a MRAM device," U.S. Patent 6,559,511B1 (2001).
14. D. C. Worledge, "Spin–flop switching for magnetic random access memory," *Appl. Phys. Lett.* **84**, pp. 4559–4561 (2004); doi: 10.1063/1.1759376.

WD EX1057
Western Digital v IP Bridge
Page 158

15. Everspin Technologies, Chandler, Arizona; www.everspin.com.
16. J. Slonczewski, "Currents and torques in metallic magnetic multilayers," *J. Magn. Magn. Mater.* **159**, pp. L1–L7 (1996); doi: 10.1016/0304-8853(96)00062-5.
17. J. Slonczewski, "Excitation of spin waves by an electric current," *J. Magn. Magn. Mater.* **195**, pp. L261–L268 (1999); doi: 10.1016/S0304-8853(99)00043-8.
18. D. E. Nikonov, G. I. Bourianoff, G. Rowland, and I. N. Krivorotov, "Strategies and tolerances of spin-transfer torque switching," *J. Appl. Phys.* **107**, 113910 (2010); doi: 10.1063/1.3429250.
19. W. H. Rippard, M. R. Pufall, S. Kaka, S. E. Russek, and T. J. Silva, "Direct-current induced dynamics in $Co_{90}Fe_{10}/Ni_{80}Fe_{20}$ point contacts," *Phys. Rev. Lett.* **92**, 027201 (2004); doi: 10.1103/PhysRevLett.92.027201.
20. S. Amara-Dababi, R. C. Sousa, M. Chshiev, H. Béa, J. Alvarez-Hérault, L. Lombard, I. L. Prejbeanu, K. Mackay, and B. Dieny, "Charge trapping–detrapping mechanism of barrier breakdown in MgO magnetic tunnel junctions," *Appl. Phys. Lett.* **99**, 083501 (2011); doi: 10.1063/1.3615654.
21. Z. Diao, Z. Li, S. Wang, Y. Ding, A. Panchula, E. Chen, L.-C. Wang, and Y. Huai, "Spin-transfer torque switching in magnetic tunnel junctions and spin-transfer-torque random access memory," *J. Phys. Condens. Matter* **19**, 165209 (2007); doi: 10.1088/0953-8984/19/16/165209.
22. J. Z. Sun, "Spin angular momentum transfer in current–perpendicular nanomagnetic junctions," *IBM J. Res. Dev.* **50**, pp. 81–100 (2006); doi: 10.1147/rd.501.0081.
23. M. Hosomi, H. Yamagishi, T. Yamamoto, K. Bessho, Y. Higo, K. Yamane, H. Yamada, M. Shoji, H. Hachino, C. Fukumoto, H. Nagao, and H. Kano, "A novel nonvolatile memory with spin-torque transfer magnetization switching: spin-RAM," *IEEE International Electron Devices Meeting, IEDM Technical Digest*, pp. 459–462 (2005); doi: 10.1109/IEDM.2005.1609379.
24. J. Z. Sun, "Spin–current interaction with a monodomain magnetic body: a model study," *Phys. Rev. B* **62**, pp. 570–578 (2000); doi: 10.1103/PhysRevB.62.570.
25. R. Heindl, W. H. Rippard, S. E. Russek, M. R. Pufall, and A. B. Kos, "Validity of the thermal activation model for spin-transfer torque switching in magnetic tunnel junctions," *J. Appl. Phys.* **109**, 073910 (2011); doi: 10.1063/1.3562136.
26. Y. Huai, "Spin-transfer-torque MRAM (STT-MRAM): Challenges and prospects," *AAPPS Bull.* **18** (6), pp. 33–40 (2008).
27. H. W. Schumacher, C. Chappert, P. Crozat, R. C. Sousa, P. P. Freitas, J. Miltat, J. Fassbender, and B. Hillebrands, "Phase coherent precessional magnetization reversal in microscopic spin-valve elements," *Phys. Rev. Lett.* **90**, 017201 (2003); doi: 10.1103/PhysRevLett.90.017201.
28. S. Kaka and S. E. Russek, "Precessional switching of submicrometer spin-valves," *Appl. Phys. Lett.* **80**, pp. 2958–2960 (2002); doi: 10.1063/1.1470704.
29. O. Redon, B. Dieny, and B. Rodmacq, "Magnetic device with polarization of spin incorporating a three-layer stack with two magnetic layers separated by a non-magnetic conducting layer for the realization of magnetic memory," France Patent 2,817,999A1 (2000).
30. A.D. Kent, B. Özyilmaz, and E. del Barco, "Spin-transfer-induced precessional magnetization reversal," Appl. Phys. Lett. **84**, pp. 3897–3899 (2004); doi: 10.1063/1.1739271.
31. D. Houssameddine, U. Ebels, B. Delaet, B. Rodmacq, I. Firastrau, F. Ponthenier, M. Brunet, C. Thirion, J.-P. Michel, L. Prejbeanu-Buda, M.-C. Cyrille, O. Redon, and B. Dieny, "Spin-torque oscillator using a perpendicular polarizer and a planar free layer," *Nat. Mater.* **6**, pp. 447–453 (2007); doi: 10.1038/nmat1905.
32. C. Papusoi, B. Delaët, B. Rodmacq, D. Houssameddine, J.-P. Michel, U. Ebels, R. C. Sousa, L. Buda-Prejbeanu, and B. Dieny, "100 ps precessional spin-transfer switching of a planar magnetic random access memory cell with perpendicular spin-polarizer," *Appl. Phys. Lett.* **95**, 072506 (2009); doi: 10.1063/1.3206919.
33. O.J. Lee, V.S. Pribiag, P.M. Braganca, P.G. Gowtham, D.C. Ralph, and R.A. Buhrman, "Ultrafast switching of a nanomagnet by a combined out-of-plane and in-plane polarized spin current pulse," Appl. Phys. Lett **95**, 012506 (2009); doi: 10.1063/1.3176938.
34. H. Liu, D. Bedau, D. Backes, J. A. Katine, J. Langer, and A. D. Kent, "Ultrafast switching in magnetic tunnel junction based orthogonal spin-transfer devices," *Appl. Phys. Lett.* **97**, 242510 (2010); doi: 10.1063/1.3527962.
35. H. Liu, D. Bedau, D. Backes, J. A. Katine, and A. D. Kent, "Precessional reversal in orthogonal spin-transfer magnetic random access memory devices," *Appl. Phys. Lett.* **101**, 032403 (2012); doi: 10.1063/1.4737010.

36. B. Lacoste, M. Marins de Castro, T. Devolder, R. C. Sousa, L. D. Buda-Prejbeanu, S. Auffret, U. Ebels, C. Ducruet, I. L. Prejbeanu, L. Vila, B. Rodmacq, and B. Dieny, "Modulating spin-transfer torque switching dynamics with two orthogonal spin-polarizers by varying the cell aspect ratio," *Phys. Rev. B.* **90**, 224404 (2014); doi: 10.1103/PhysRevB.90.224404.
37. M. T. Johnson, P. J. H. Bloemen, F. J. A. den Broeder, and J. J. de Vries, "Magnetic anisotropy in metallic multilayers," *Rep. Prog. Phys.* **59**, pp. 1409–1458 (1996); doi: 10.1088/0034-4885/59/11/002.
38. P. P. Nguyen and Y. Huai, "Spin transfer magnetic element with free layers having high perpendicular anisotropy and in-plane equilibrium magnetization," U.S. Patent 7,531,882B2 (2009).
39. B.Rodmacq, B.Dieny, "Thin-film magnetic device with strong spin polarization perpendicular to the plane of the layers, magnetic tunnel junction and spin-valve using such device," U.S. patent US 7,813,202 B2 (2010)
40. L. Liu, T. Moriyama, D. C. Ralph, and R. A. Buhrman, "Reduction of the spin-torque critical current by partially cancelling the free layer demagnetization field," *Appl. Phys. Lett.* **94**, 122508 (2009); doi: 10.1063/1.3107262.
41. P. K. Amiri, Z. M. Zeng, J. Langer, H. Zhao, G. Rowlands, Y.-J. Chen, I. N. Krivorotov, J.-P. Wang, H. W. Jiang, J. A. Katine, Y. Huai, K. Galatsis, and K. L. Wang, "Switching current reduction using perpendicular anisotropy in CoFeB–MgO magnetic tunnel junctions," *Appl. Phys. Lett.* **98**, 112507 (2011); doi: 10.1063/1.3567780.
42. L. E. Nistor, B. Rodmacq, S. Auffret, and B. Dieny, "Low effective demagnetizing field in magnetic tunnel junctions," *INTERMAG Conference, Taipei (Taiwan)*, April 25–29, HE-07 (2011).
43. T. Moriyama, T. J. Gudmundsen, P. Y. Huang, L. Liu, D. A. Muller, D. C. Ralph, and R. A. Buhrman, "Tunnel magnetoresistance and spin-torque-switching in MgO-based magnetic tunnel junctions with a Co/Ni multilayer electrode," *Appl. Phys. Lett.* **97**, 072513 (2010); doi: 10.1063/1.3481798.
44. S. Monso, B. Rodmacq, S. Auffret, G. Casali, F. Fettar, B. Gilles, B. Dieny, and P. Boyer, "Crossover from in-plane to perpendicular anisotropy in Pt/CoFe/AlO_x sandwiches as a function of Al oxidation: a very accurate control of the oxidation of tunnel barriers," *Appl. Phys. Lett.* **80**, pp. 4157–4159 (2002); doi: 10.1063/1.1483122.
45. B. Rodmacq, A. Manchon, C. Ducruet, S. Auffret, and B. Dieny, "Influence of thermal annealing on the perpendicular magnetic anisotropy of Pt/Co/AlO_x trilayers," *Phys. Rev. B*, **79**, 024423 (2009); doi: 10.1103/PhysRevB.79.024423.
46. L. E. Nistor, B. Rodmacq, S. Auffret, and B. Dieny, "Pt/Co/oxide and oxide/Co/Pt electrodes for perpendicular magnetic tunnel junctions," *Appl. Phys. Lett.* **94**, 012512 (2009); doi: 10.1063/1.3064162.
47. S. Ikeda, K. Miura, H. Yamamoto, K. Mizunuma, H. D. Gan, M. Endo, S. Kanai, J. Hayakawa, F. Matsukura, and H. Ohno, "A perpendicular-anisotropy CoFeB–MgO magnetic tunnel junction," *Nat. Mater.* **9**, pp. 721–724 (2010); doi: 10.1038/nmat2804.
48. N. D. Rizzo, D. Houssameddine, J. Janesky, R. Whig, F. B. Mancoff, M. L. Schneider, M. DeHerrera, J. J. Sun, K. Nagel, S. Deshpande, H.-J. Chia, S. M. Alam, T. Andre, S. Aggarwal, and J. M. Slaughter, "A Fully Functional 64 Mb DDR3 ST-MRAM Built on 90 nm CMOS Technology," *IEEE Trans. Mag.* **49**, 4441–4446 (2013); doi: 10.1109/TMAG.2013.2243133.
49. S. Mangin, D. Ravelosona, J. A. Katine, M. J. Carey, B. D. Terris, and E. E. Fullerton, "Current-induced magnetization reversal in nanopillars with perpendicular anisotropy," *Nat. Mater.* **5**, pp. 210–215 (2006); doi: 10.1038/nmat1595.
50. M. Nakayama, T. Kai, N. Shimomura, M. Amano, E. Kitagawa, T. Nagase, M. Yoshikawa, T. Kishi, S. Ikegawa, and H. Yoda, "Spin-transfer-switching in TbCoFe/CoFeB/MgO/CoFeB/TbCoFe magnetic tunnel junctions with perpendicular magnetic anisotropy," *J. Appl. Phys.* **103**, 07A710 (2008); doi: 10.1063/1.2838335.
51. N. Nishimura, T. Hirai, A. Koganei, T. Ikeda, K. Okano, Y. Sekiguchi, and Y. Osada, "Magnetic tunnel junction device with perpendicular magnetization films for high-density magnetic random access memory," *J. Appl. Phys.* **91**, pp. 5246–5249 (2002); doi: 10.1063/1.1459605.
52. H. Ohmori, T. Hatori, and S. Nakagawa, "Fabrication of MgO barrier for a magnetic tunnel junction in as-deposited state using amorphous RE–TM alloy," *J. Magn. Magn. Mater.* **320**, pp. 2963–2966 (2008); doi: 10.1016/j.jmmm.2008.08.005.
53. B. Carvello, C. Ducruet, B. Rodmacq, S. Auffret, E. Gautier, G. Gaudin, and B. Dieny, "Sizable roomtemperature magnetoresistance in cobalt based magnetic tunnel junctions with out-of-plane anisotropy," *Appl. Phys. Lett.* **92**, 102508 (2008); doi: 10.1063/1.2894198.

WD EX1057
Western Digital v IP Bridge
Page 160

54. H. Yoda, T. Kishi, T. Nagase, M. Yoshikawa, K. Nishiyama, E. Kitagawa, T. Daibou, M. Amano, N. Shimomura, S. Takahashi, T. Kai, M. Nakayama, H. Aikawa, S. Ikegawa, M. Nagamine, J. Ozeki, S. Mizukami, M. Oogane, Y. Ando, S. Yuasa, K. Yakushiji, H. Kubota, Y. Suzuki, Y. Nakatani, T. Miyazaki, and K. Ando, "High efficient spin-transfer-torque writing of perpendicular magnetic tunnel junctions for high density MRAMs," *Curr. Appl. Phys.* **10** (Suppl. 1), pp. e87–e89 (2010); doi: 10.1016/j.cap.2009.12.021.
55. O. G. Heinonen and D. V. Dimitrov, "Switching-current reduction in perpendicular-anisotropy spin-torque magnetic tunnel junctions," *J. Appl. Phys.* **108**, 014305 (2010); doi: 10.1063/1.3457327.
56. S. A. Wolf, J. Lu, M. R. Stan, E. Chen and D. M. Treger, "The promise of nanomagnetics and spintronics for future logic and universal memory," *Proc. IEEE* **98**, pp. 2155–2168 (2010); doi: 10.1109/JPROC.2010.2064150.
57. A. V Khvalkovskiy, D. Apalkov, S. Watts, R. Chepulskii, R. S. Beach,A. Ong, X. Tang, A. Driskill-Smith, W.H. Butler, P. B. Visscher, D. Lottis, E. Chen, V. Nikitin and M. Krounbi, "Basic principles of STT-MRAM cell operation in memory arrays," *J. Phys. D: Appl. Phys.* **46**, 074001 (2013); doi: 10.1088/0022-3727/46/7/074001.
58. T. Kishi, H. Yoda, T. Kai, T. Nagase, E. Kitagawa, M. Yoshikawa, K. Nishiyama, T. Daibou, M. Nagamine, M. Amano, S. Takahashi, M. Nakayama, N. Shimomura, H. Aikawa, S. Ikegawa, S. Yuasa, K. Yakushiji, H. Kubota, A. Fukushima, M. Oogane, T. Miyazaki, and K. Ando, "Lower-current and fast switching of a perpendicular TMR for high speed and high density spin-transfer-torque MRAM," *IEEE International Electron Devices Meeting, IEDM Technical Digest*, vol. 4, pp. (2008), doi: 10.1109/IEDM.2008.4796680.
59. J. M. Shaw, H. T. Nembach, and T. J. Silva, "Measurement of orbital asymmetry and strain in $Co_{90}Fe_{10}$/Ni multilayers and alloys: origins of perpendicular anisotropy," *Phys. Rev. B* **87**, 054416 (2013); doi: 10.1103/PhysRevB.87.054416.
60. L. Néel, "Anisotropie magnétique superficielle et surstructures d'orientation," *J. Phys. Radium* **15**, pp. 225–239 (1954); doi: 10.1051/jphysrad:01954001504022500.
61. U. Gradmann and J. Müller, "Flat ferromagnetic epitaxial 48Ni/52Fe(1 1 1) films of few atomic layers," *Phys. Stat. Solidi* **27**, pp. 313–324 (1968); doi: 10.1002/pssb.19680270133.
62. A. Manchon, C. Ducruet, L. Lombard, S. Auffret, B. Rodmacq, B. Dieny, S. Pizzini, J. Vogel, V. Uhlir, M. Hochstrasser, and G. Panaccione, "Analysis of oxygen induced anisotropy crossover in Pt/Co/MO_x trilayers," *J. Appl. Phys.* **104**, 043914 (2008); doi: 10.1063/1.2969711.
63. A. Manchon, S. Pizzini, J. Vogel, V. Uhlir, L. Lombard, C. Ducruet, S. Auffret, B. Rodmacq, B. Dieny, M. Hochstrasser, and G. Panaccione, "X-ray analysis of oxygen-induced perpendicular magnetic anisotropy in Pt/Co/AlO_x trilayers," *J. Magn. Magn. Mater.* **320**, pp. 1889–1892 (2008); doi: 10.1063/1.2969711.
64. H. X. Yang, M. Chshiev, B. Dieny, J. H. Lee, A. Manchon, and K. H. Shin, "First-principles investigation of the very large perpendicular magnetic anisotropy at Fe|MgO interfaces," *Phys. Rev. B* **84**, 054401 (2011); doi: 10.1103/PhysRevB.84.054401.
65. T. Devolder, P.-H. Ducrot, J.-P. Adam, I. Barisic, N. Vernier, Joo-Von Kim, B. Ockert, and D. Ravelosona, "Damping of CoxFe80-2xB20 ultrathin films with perpendicular magnetic anisotropy," *Appl. Phys. Lett.* **102**, 022407 (2013); doi: 10.1063/1.4775684.
66. L. E. Nistor, B. Rodmacq, S. Auffret, A. Schuhl, M. Chshiev, and B. Dieny, "Oscillatory interlayer exchange coupling in MgO tunnel junctions with perpendicular magnetic anisotropy," *Phys. Rev. B* **81**, 220407 (2010); doi: 10.1103/PhysRevB.81.220407.
67. T. Kawahara, K. Ito, R. Takemura, H. Ohno, "Spin-transfer torque RAM technology: Review and prospect," *Microelectron. Reliab.* **52**, 613–627 (2012); DOI: 10.1016/j.microrel.2011.09.028
68. J. J. Nowak, R. P. Robertazzi, J. Z. Sun, G. Hu, David W. Abraham, P. L. Trouilloud, S. Brown, M. C. Gaidis, E. J. O'Sullivan, W. J. Gallagher, and D. C. Worledge, "Demonstration of ultralow bit error rates for spin-torque magnetic random-access memory with perpendicular magnetic anisotropy," *IEEE Magn. Lett.* **2**, 2–5 (2011); DOI: 10.1109/LMAG.2011.2155625
69. J.J. Nowak, R.P. Robertazzi, J.Z. Sun, G. Hu, J.H. Park, J. Lee, A.J. Annunziata, G.P. Lauer, R. Kothandaraman, E.J. O'Sullivan, P.L. Trouilloud, Y. Kim, and D.C. Worledge, "Dependence of Voltage and Size on Write Error Rates in Spin-Transfer Torque Magnetic Random-Access Memory", *IEEE Mag. Lett.* **7**, 3102604 (2016); DOI: 10.1109/LMAG.2016.2539256

70. B. Rodmacq, S. Auffret, B. Dieny, L. Nistor,"Three-layer magnetic element, magnetic field sensor, magnetic memory and magnetic logic gate using such an element," U.S. Patent 8,513,944 B2 (2008).
71. H. Sato, M. Yamanouchi, S. Ikeda, S. Fukami, F. Matsukura, and H. Ohno, "Perpendicular-anisotropy CoFeB-MgO magnetic tunnel junctions with a MgO/CoFeB/Ta/CoFeB/MgO recording structure," *Appl. Phys. Lett.* **101**, 022414 (2012); DOI: 10.1063/1.4736727
72. G. Jan, L. Thomas, S. Le, Y.J. Lee, H. Liu, J. Zhu, R.Y. Tong, K. Pi, Y.J. Wang, D. Shen, R. He, J. Haq, J. Teng, V. Lam, K. Huang, T. Zhong, T. Torng, and P.K. Wang,"Demonstration of fully functional 8 Mb perpendicular STT-MRAM chips with sub-5 ns writing for non-volatile embedded memories," *Proc. Symp. VLSI Technol. Dig. Tech. Papers*, 42–43 (2014).
73. L. Thomas, G. Jan, J. Zhu, H. Liu, Y.J. Lee, S. Le, R.Y. Tong, K. Pi, Y.J. Wang, D. Shen, R. He, J. Haq, J. Teng, V. Lam, K. Huang, T. Zhong, T. Torng and P.K. Wang, "Perpendicular spin-transfer torque magnetic random access memories with high spin-torque efficiency and thermal stability for embedded applications (invited)," *J. Appl. Phys.* **115**, 172615 (2014); DOI: 10.1063/1.4870917
74. C. Park, J.J. Kan, C. Ching, J. Ahn, L. Xue, R. Wang, A. Kontos, S. Liang, M. Bangar, H. Chen, S. Hassan, M. Gottwald, X. Zhu, M. Pakala, and S. H. Kang,"Systematic Optimization of 1 Gbit Perpendicular Magnetic Tunnel Junction Arrays for 28 nm Embedded STT- MRAM and Beyond," *Proc. Int. Elect. Devices Meet (IEDM 2015)*, 26.2.1 (2015); DOI: 10.1109/IEDM.2015.7409771.
75. B. Dieny and O. Redon, "Magnetic tunnel junction magnetic device, memory and writing and reading methods using said device," U.S. Patent 6,950,335B2 (2005), Fig. 8.
76. K. Yakushiji, T. Saruya, H. Kubota, A. Fukushima, T. Nayahama, S. Yuasa, and K. Ando, "Ultrathin Co/Pt and Co/Pd superlattice films for MgO-based perpendicular magnetic tunnel junctions," *Appl. Phys. Lett.* **97**, 232508 (2010); doi: 10.1063/1.3524230.
77. G. Hu, J. H. Lee, J. J. Nowak, J. Z. Sun, J. Harms, A. Annunziata, S. Brown, W. Chen, Y. H. Kim, G. Lauer, L. Liu, N. Marchack, S. Murthy, E. J. O'Sullivan, J. H. Park, M. Reuter, R. P. Robertazzi, P. L. Trouilloud, Y. Zhu and D. C. Worledge,"STT-MRAM with double magnetic tunnel junctions," *Proc. Int. Electron. Devices Meeting Dig., 2015*, 26.3.1–26.3.4. (2015).
78. L. Cuchet, B. Rodmacq, S. Auffret, R.C. Sousa, I.L. Prejbeanu, B. Dieny, "Perpendicular magnetic tunnel junctions with a synthetic storage or reference layer: A new route towards Pt- and Pd-free junctions", *Scient. Rep.* **6**, 21246 (2016); DOI: 10.1038/srep21246.
79. D. Apalkov, A. Khvalkovskiy, and S. Watts, "Spin-transfer torque magnetic random access memory (stt-mram)," *ACM J. Emerg. Technol. Comput. Syst.*, **9**, 13:1–13:35 (2013); DOI: 10.1145/2463585.2463589
80. S. Amara, R. C. Sousa, H. Bea, C. Baraduc, and B. Dieny, "Barrier breakdown mechanisms in MgO-based magnetic tunnel junctions and correlation with low-frequency noise," *IEEE Trans. Magn.* **48**, pp. 4340–4343 (2012); doi: 10.1109/TMAG.2012.2200243.
81. H. Zhao, A. Lyle, Y. Zhang, P. K. Amiri, G. Rowlands, Z. Zeng, J. Katine, H. Jiang, K. Galatsis, K. L. Wang, I. N. Krivorotov, and J.-P. Wang, "Low writing energy and sub-nanosecond spin-torque transfer switching of in-plane magnetic tunnel junction for spin-torque transfer random access memory," *J. Appl. Phys.* **109**, 07C720 (2011); doi: 10.1063/1.3556784.
82. M. Carpentieri, M. Ricci, P. Burrascano, and L. Torres, "Spreading sequences for fast switching process in spin-valve nanopillars," *Appl. Phys. Lett.* **98**, 122504 (2011); doi: 10.1063/1.3569947.
83. T. Nozaki, Y. Shiota, M. Shiraishi, T. Shinjo, and Y. Suzuki, "Voltage-induced perpendicular magnetic anisotropy change in magnetic tunnel junctions," *Appl. Phys. Lett.* **96**, 022506 (2010); doi: 10.1063/1.3279157.
84. Y. Shiota, T. Maruyama, T. Nozaki, T. Shinjo, M. Shiraishi, and Y. Suzuki, "Voltage-assisted magnetization switching in ultrathin $Fe_{80}Co_{20}$ alloy layers," *Appl. Phys. Express* **2**, 063001 (2009); doi: 10.1143/APEX.2.063001.
85. F. Bonell, S. Murakami, Y. Shiota, T. Nozaki, T. Shinjo, and Y. Suzuki, "Large change in perpendicular magnetic anisotropy induced by an electric field in FePd ultrathin films," *Appl. Phys. Lett.* **98**, 232510 (2011); doi: 10.1063/1.3599492.
86. S. Bandiera, R. C. Sousa, M. Marins de Castro, C. Ducruet, C. Portemont, S. Auffret, L. Vila, I. L. Prejbeanu, B. Rodmacq, and B. Dieny, "Spin-transfer-torque switching assisted by thermally induced

WD EX1057
Western Digital v IP Bridge
Page 162

anisotropy reorientation in perpendicular magnetic tunnel junctions," *Appl. Phys. Lett.* **99**, 202507 (2011); doi: 10.1063/1.3662971.

87. W. Zhao, J. Duval, J.-O. Klein, and C. Chappert, "A compact model for magnetic tunnel junction (MTJ) switched by thermally-assisted spin-transfer-torque (TAS + STT)," *Nanoscale Res. Lett.* **6**, p. 368 (2011); doi: 10.1186/1556-276X-6-368.
88. R. C. Sousa and I. L. Prejbeanu, "Non-volatile magnetic random access memories (MRAM)," *Compt. Rend. Phys.* **6**, pp. 1013–1021 (2005); doi: 10.1016/j.crhy.2005.10.007.
89. B. Dieny and O. Redon, "Magnetic device with magnetic tunnel junction, memory array and read/write methods using same," Patent US6950335 (B2) (2003).
90. S. S. Cardoso, R. Ferreira, F. Silva, P. P. Freitas, L. V. Melo, R. C. Sousa, O. Redon, M. MacKenzie, and J. N. Chapman, "Double-barrier magnetic tunnel junctions with GeSbTe thermal barriers for improved thermally-assisted magnetoresistive random access memory cells," *J. Appl. Phys.* **99**, 08N901 (2006); doi: 10.1063/1.2162813.
91. C. Papusoi, R. Sousa, J. Herault, I. L. Prejbeanu, and B. Dieny, "Probing fast heating in magnetic tunnel junction structures with exchange bias," *New J. Phys.* **10**, 103006 (2008); doi: 10.1088/1367-2630/10/10/103006.
92. I. L. Prejbeanu, M. Kerekes, R. C. Sousa, H. Sibuet, O. Redon, B. Dieny, and J.-P. Nozières, "Thermally-assisted MRAM," *J. Phys. Cond. Mater* **19**, 165218 (2007); doi: 10.1088/0953-8984/19/16/165218.
93. I. L. Prejbeanu, W. Kula, K. Ounadjela, R. C. Sousa, O. Redon, B. Dieny, and J.-P. Nozières, "Thermally-assisted switching in exchange-biased storage layer magnetic tunnel junctions," *IEEE Trans. Magn.* **40**, pp. 2625–2627 (2004); doi: 10.1109/TMAG.2004.830395.
94. J. Wang and P. P. Freitas, "Low-current blocking temperature writing of double barrier magnetic random access memory cells," *Appl. Phys. Lett.* **84**, pp. 945–947 (2004); doi: 10.1063/1.1646211.
95. B. F. Cambou, "Multilevel magnetic element," U.S. Patent 8,630,112 (2014). B. F. Cambou, D. J. Lee, and K. Mackay, "Magnetic logic units configured as an amplifier," U.S. Patent 8,933,750 (2015).
96. B. F. Cambou, *Match-In-Place™: A Novel Way to Perform Secure and Fast User's Authentication*, Crocus Technology, Santa Clara, CA (2012).
97. E. Gapihan, R. C. Sousa, J. Herault, C. Papusoi, M. T. Delaye, B. Dieny, I. L. Prejbeanu, C. Ducruet, C. Portemont, K. Mackay, and J.-P. Nozières, "FeMn exchange biased storage layer for thermally-assisted MRAM," *IEEE Trans. Magn.* **46**, pp. 2486–2488 (2010); doi: 10.1109/TMAG.2010.2041198.
98. E. R. Callen and H. B. Callen, "Anisotropic magnetization," *J. Phys. Chem. Solids* **16**, pp. 310–328 (1960); doi: 10.1016/0022-3697(60)90161-X.
99. H. W. van Kesteren and W. B. Zeper, "Controlling the Curie temperature of magneto-optical recording media of Co/Pt multilayer," *J. Magn. Magn. Mater.* **120**, pp. 271–273 (1993); doi: 10.1016/0304-8853(93)91339-9.
100. P. Poulopoulos and K. Baberschke, "Magnetism in thin films," *J. Phys. Condens. Matter* **11**, pp. 9495–9515 (1999); doi: 10.1088/0953-8984/11/48/310.
101. Q. Meng, W. P. van Drent, J. C. Lodder, and Th. J. A. Popma, "Curie temperature dependence of magnetic properties of CoNi/Pt multilayer films," *J. Magn. Magn. Mater.*, **156**, pp. 296–298 (1999); doi: 10.1016/0304-8853(95)00875-6.
102. S. Yuasa and D. D. Djayaprawira, "Giant tunnel magnetoresistance in magnetic tunnel junctions with a crystalline MgO(0 0 1) barrier," *J. Phys. D Appl. Phys.* **40**, pp. R337–R354 (2007); doi: 10.1088/0022-3727/40/21/R01.
103. K. Mizunuma, S. Ikeda, J. H. Park, H. Yamamoto, H. Gan, K. Miura, H. Hasegawa, J. Hayakawa, F. Matsukura, and H. Ohno, "MgO barrier-perpendicular magnetic tunnel junctions with CoFe/Pd multilayers and ferromagnetic insertion layers," *Appl. Phys. Lett.* **95**, 232516 (2009); doi: 10.1063/1.3265740.
104. S. Bandiera, R. C. Sousa, Y. Dahmane, C. Ducruet, C. Portemont, V. Baltz, S. Auffret, I. L. Prejbeanu, and B. Dieny, "Comparison of synthetic antiferromagnets and hard ferromagnets as reference layer in magnetic tunnel junctions with perpendicular magnetic anisotropy," *IEEE Magn. Lett.* **1**, 3000204 (2010); doi: 10.1109/LMAG.2010.2052238.
105. K. Mizunuma, S. Ikeda, H. Sato, M. Yamanouchi, H. D. Gan, K. Miura, H. Yamamoto, J. Hayakawa, F. Matsukura, and H. Ohno, "Tunnel magnetoresistance properties and annealing stability in

perpendicular anisotropy MgO-based magnetic tunnel junctions with different stack structures," *J. Appl. Phys.* **109**, 07C711 (2011); doi: +10.1063/1.3554092.

106. M. Gajek, J. J. Nowak, J. Z. Sun, P. L. Trouilloud, E. J. O'Sullivan, D. W. Abraham, M. C. Gaidis, G. Hu, S. Brown, Y. Zhu, R. P. Robertazzi, W. J. Gallagher, and D. C. Worledge, "Spin-torque switching of 20 nm magnetic tunnel junctions with perpendicular anisotropy," *Appl. Phys. Lett.* **100**, 132408 (2012); doi: 10.1063/1.3694270.
107. E. P. Sajitha, J. Walowski, D. Watanabe, S. Mizukami, F. Wu, H. Naganuma, M. Oogane, Y. Ando, and T. Miyazaki, "Magnetization dynamics in CoFeB buffered perpendicularly magnetized Co/Pd multilayer," *IEEE Trans. Magn.* **46**, pp. 2056–2059 (2010); doi: 10.1109/TMAG.2009.2038929.
108. L. Lombard, E. Gapihan, R. C. Sousa, Y. Dahmane, Y. Conraux, C. Portemont, C. Ducruet, C. Papusoi, I. L. Prejbeanu, J. P. Nozières, B. Dieny, and A. Schuhl, "IrMn and FeMn blocking temperature dependence on heating pulse width," *J. Appl. Phys.* **107**, 09D728 *(2100);* doi: 10.1063/1.3340452.
109. P. M. Braganca, J. A. Katine, N. C. Emley, D. Mauri, J. R. Childress, P. M. Rice, E. Delenia, D. C. Ralph, and R. A. Buhrman, "A three-terminal approach to developing spin-torque written magnetic random access memory cells," *IEEE Trans. Nanotech.* **8**, pp. 190–195 (2009); doi: 10.1109/TNANO.20A08.2005187.
110. I. M. Miron, K. Garello, G. Gaudin, P.-J. Zermatten, M. V. Costache, S. Auffret, S. Bandiera, B. Rodmacq, A. Schuhl, and P. Gambardella, "Perpendicular switching of a single ferromagnetic layer induced by in-plane current injection," *Nature* **476**, pp. 189–194 (2011); doi: 10.1038/nature10309.
111. I. M. Miron, G. Gaudin, S. Auffret, B. Rodmacq, A. Schuhl, S. Pizzini, J. Vogel, and P. Gambardella, "Current-driven spin-torque induced by the Rashba effect in a ferromagnetic metal layer," *Nat. Mater.* **9**, pp. 230–234 (2010); doi: 10.1038/nmat2613.
112. L.Q. Liu, O.J. Lee, T.J. Gudmundsen, D.C. Ralph, R.A. Buhrman, "Current-Induced Switching of Perpendicularly Magnetized Magnetic Layers Using Spin Torque from the Spin Hall Effect", *Phys. Rev. Lett.* **109**, 096602 (2012); DOI: 10.1103/PhysRevLett.109.096602
113. S. Fukami, T. Anekawa, C. Zhang, H. Ohno, "A spin–orbit torque switching scheme with collinear magnetic easy axis and current configuration," *Nat. Nanotec.* **11**, 621 (2016); DOI: 10.1038/NNANO.2016.29
114. K. Garello, C.O. Avci, I.M. Miron, M. Baumgartner, A. Ghosh, S. Auffret, O. Boulle, G. Gaudin and P. Gambardella, "Ultrafast magnetization switching by spin–orbit torques," *Appl. Phys. Lett.* **105**, 212402 (2014); DOI: 10.1063/1.4902443
115. T. Endoh, "Spin-transfer torque MRAM (SPRAM) and its applications," ITRS Emerging Research Memory Technologies Workshop (2010).
116. J. Hutchby and M. Garner, Assessment of the Potential & Maturity of Selected Emerging Research Memory Technologies Workshop & ERD/ERM Working Group Meeting (April 6–7, 2010).
117. Y. de Charentenay, *Emerging Non Volatile Memory (NVM) Technology & Market Trends Report*, Yole Développement, Lyon-Villeurbanne, France (2015). www.i-micronews.com/component/hikashop/product/emerging-non-volatile-memory-nvm-technology-market-trends-report-launch-offer.html
118. Y. Shiota, T. Nozaki, F. Bonell, S. Murakami, T. Shinjo and Y. Suzuki, "Induction of coherent magnetization switching in a few atomic layers of FeCo using voltage pulses," *Nat. Mater.*, **11**, 39 (2012); DOI: 10.1038/nmat3172
119. S. Kanai, M. Yamanouchi, S. Ikeda, Y. Nakatani, F. Matsukura, and H. Ohno, "Electric field-induced magnetization reversal in a perpendicular anisotropy CoFeB–MgO magnetic tunnel junction," *Appl. Phys. Lett.* **101**, 122403 (2012); DOI: 10.1063/1.4753816

WD EX1057
Western Digital v IP Bridge
Page 164